

Development of a Confocal Line Scanning Sensor

Vom Naturwissenschaftlich-Technische Fakultät der
Universität Siegen
zur Erlangung des akademischen Grades

**Doktor der Ingenieurwissenschaften
(Dr.-Ing.)**

genehmigte Dissertation

von

M.Sc. Sirichanok Chanbai

1. Gutachter: Prof. Dr.-Ing. Hubert Roth
2. Gutachter: Prof. Dr.-Ing. Peter Haring Bolívar
Vorsitzender: Prof. Dr.-Ing. Markus Böhm

Tag der mündlichen Prüfung : 22 October 2012

Gedruckt auf alterungsbeständigem holz- und säurefreiem Papier.
Printed on aging resistant wood- and acid free paper.

Zusammenfassung

Die Oberflächeneigenschaften eines Produktes sind genauso entscheidend für die Vorhersage der Produktlebensdauer und der Oberflächenfunktionalität wie für die Optimierung des Herstellungsprozesses. Daher befasst sich diese Arbeit mit der berührungslosen Oberflächenmesstechnik.

Das Prinzip der Konfokalmikroskopie (CM) ermöglicht es dank seiner tiefendiskriminierenden Eigenschaften mit Lichtmikroskopen Tiefeninformation zu erhalten. Die Konfokalmikroskopie erlaubt die Entwicklung einer parallelen statischen Tiefenabtastung ohne bewegte Teile. Chromatische-konfokale Punktsensoren sind ein bekanntes Beispiel hierfür. Sie benötigen jedoch ein separates Spektrometer zur Analyse der verschiedenen Wellenlängenanteile. Dessen komplexer Aufbau und die relativ geringe Lichtausbeute je Wellenlänge macht es schwierig einfache und preiswerte Produkte zu entwickeln.

Daher wird in dieser Arbeit ein neuer Ansatz unter Verwendung der Scheimpflug-Technik in einem konfokalen Abbildungssystem, einen sogenannten konfokalen Zeilenscanner (CLSS), vorgestellt. Eine parallele statische Tiefenabtastung wird hier mit einer kostengünstigeren Technologie und einem robusteren Aufbau erreicht.

Ein neuer Ansatz zur Erklärung und Korrektur der Vergrößerungsvariation, auch als Keystone-Verzeichnung bekannt, wird vorgestellt. Desweiteren werden Verfahren zur Datenauswertung und Kalibrierung entwickelt. Das Scheimpflug-Prinzip wird erstmals auf die Konfokalmikroskopie angewandt.

Schließlich wird experimentell gezeigt, dass die Scheimpflugtechnik erfolgreich in einem Konfokalsystem eingesetzt werden kann. Die Eigenschaften des Verfahrens werden experimentell evaluiert.

Abstract

Surface characteristics are of vital importance for predicting the product life time and surface functionality, or even improving the manufacturing procedure. In consequence, this thesis focuses on the surface inspection using a non-contact technique.

The principle of Confocal Microscopy(CM) enables light microscopes to gain depth information through what is known as *depth discrimination* ability. Among the other optical inspection techniques, the principle of confocal microscopy allows a parallel and motionless depth scanning scheme to be developed. The chromatic confocal point sensor is one prominent example of a parallel depth scanning scheme. However, this technique requires a separate analysis unit to analyze light of different wavelengths. The complication and relatively low efficiency of light per wavelength can pose a limit on developing a simplified configuration and a cost effective unit.

Therefore, a novel approach to incorporate a tilted plane technique in a confocal imaging system is proposed in this thesis, namely a *Confocal Line Scanning Sensor* (CLSS). A parallel and motionless depth scanning scheme is then achieved with a cost-effective technique, resulting in a greatly simplified and robust configuration.

This thesis is devoted to establish new knowledge on incorporating a tilted plane technique in a confocal imaging system. A novel approach to explain and to correct the variation of the magnification inherent in a tilted plane system, known as *keystone distortion*, is proposed. Moreover, particular data processing and calibrations are developed to support the new concept. Here, the Scheimpflug's principle is first applied with confocal microscopy, whereas selected well-known theories are also used to support the system design and construction.

Finally, the experiments demonstrate that a tilted plane technique can successfully be incorporated in a confocal imaging system. In addition, the performance of the CLSS is evaluated through a series of experiments.

Acknowledgments

A thesis is not the product of one person's ideas or efforts. Many people have contributed their time and effort to this work. Foremost among these is my advisor, Prof. Dr.-Ing. Hubert Roth. His faith in me and priceless support encouraged me to pursue my doctoral study at the University of Siegen. I would also like to express my sincere and deep sense of gratitude to my supervisor, Dr. Georg Wiora, who provided valuable input at all stages of this work. I am most grateful for his enthusiasm, creative suggestions, faith and smile, motivation and exemplary guidance throughout the course of my doctoral research. Apart from the subject of my research, I have learned a lot from him, which I am sure will be useful in different stages of my life.

Prof. Dr.-Ing. Peter Haring Bolívar and Prof. Dr.-Ing. Markus Böhm generously took the role of my thesis committee and shared their expertise, enlightening discussions, and invaluable suggestions. Their insightful questions and constructive advices have been very helpful for me to build a perspective in the research field. I would also extend my thanks to Assoc. Prof. Veera Chanvattana for running through the manuscript at the last minute, and for his continuous encouragement and endless support that keep me inspired and motivated.

Many of my thanks goes to members of the research and development department of NanoFocus AG. The inspiring and collaborative atmosphere in our department allowed me to learn the joy of sharing expertise and knowledge. I would like to thank Dr.-Ing. Gerd Jakob and Dr. Mark A. Weber for providing a wonderful environment within the department. PhD. Ijaz Zafarullah helped me not only with experiments and simulations but also with sparkling discussions, and with proofreading many of my papers including this thesis. I feel particularly indebted to Lukas Wewer, who never hesitated to lend a hand and for his invaluable discussions. Ronny Lobeda proved to be an excellent helper for many experiments, who also designed the mechanics which made the measurements possible. Thomas Rymarczyk, David Knochenhauer, and Peter Schreuder were always around when I needed them and never too busy to listen or lend a helping hand, and gave invaluable software support. Time spent with all of my work colleagues, those who shared academic and nonacademic interest together, was enjoyable and rewarding.

It has been a great pleasure for me to have the chance to work with Prof.Dr.-Ing. Jörg Seewig and Dipl.-Ing. Qiang Hao at IMR, University of Hannover,

Germany, and with Dr. Remigiusz Michalczewski, Dr. Waldemar Tuszynski and Dr. Mihaela Vald at ITEE, Poland. Interacting and working with them have been fun and gratifying. I have been nourished with their broad knowledge of surface characteristics.

In addition, I would also like to thank and acknowledge WEMESURF research network and NanoFocus AG for the financial and equipment support, in the form of an ESR Fellowship. The support received under contract MRTN CT 2006 035589, the Sixth Framework Programme of the European Commission and Marie Curie Action. During these three years, I have received both academic and nonacademic support for my graduate studies and for developing my career path. Through these activities and networking, the WEMESURF fellows have added vitality in my graduate life. In particular, I appreciate their friendship.

I would like to thank to all members of International Postgraduate Programme (IPP), University of Siegen. In particular, I would like to thank Dr.-Ing. Stefan Knedlik and Dr.-Ing. Holger Nies for numerous advices and support on both scientific and non-scientific matters. I am also grateful to Silvia Niet-Wunram, Birgit Hoffmann, and Judith Düber for their excellent administrative services.

Finally, I am very much grateful to all the people who have contributed many useful materials to complete my thesis and who also offered many useful ideas and suggestion.

The hard work of reviewing the manuscript was done by David Matthews. In this regard, I sincerely appreciate his thorough and meticulous support.

This thesis would not have been possible without my family's unconditional love and caring support. I would like to thank our parents and my only brother, Sirinwat, for their faith and encouragement, and I dedicate this thesis to them.

Contents

Zusammenfassung	i
Abstract	iii
Acknowledgments	v
Table of Contents	viii
Symbols and Acronyms	ix
1 Introduction	1
1.1 Motivation	1
1.2 Goals	3
1.3 Organization of the thesis	3
2 Background of Confocal Microscopy	5
2.1 The advent of Confocal Microscopy (CM)	5
2.2 The evolution of the Nipkow disk based confocal microscopes	8
2.3 The <i>pinhole disk based</i> confocal microscope	9
2.4 Optical resolution	11
2.5 Surface inspection application	14
2.6 Conclusion	15
3 Theory of the Confocal Line Scanning Sensor (CLSS)	17
3.1 System overview	17
3.2 Keystone distortion	21
3.3 Intensity responses and criteria to define the pinhole size	24
3.4 Pinhole mask design	27
3.5 Imaging characteristics of the CLSS	37
3.6 Conclusion	47
4 System Design Description	49
4.1 CLSS' configuration	49
4.2 System alignment	57

4.3	Process control and data acquisition	61
4.4	Errors and noises in the CLSS	64
4.5	Conclusion	69
5	Data Processing and Calibrations	71
5.1	Conceptual data processing	71
5.2	Calibrations	79
5.3	One-dimensional roughness parameters	92
5.4	Conclusion	94
6	Experimental Results and Discussions	97
6.1	Calibrated standards	97
6.2	Axial resolution beyond the FWHM	103
6.3	Lateral resolution improved with a finer sampling interval	108
6.4	Sampling focal-line in the CLSS	110
6.5	Uncertainty in the lateral scan direction	110
6.6	Aberrations in the CLSS	112
6.7	The effect of tilted specimens on the axial response	117
6.8	Conclusion	118
7	Conclusions and Future Work	123
7.1	Conclusions	123
7.2	Future Work	125
A	Point Spread Function	127
A.1	Amplitude point spread function	127
A.2	Intensity point spread function	129
B	Principal planes shifting in a simple compound lens system	135
C	Geometry Approach for Pinhole Design	139
D	Gaussian-Lens-Equation Approach for Pinhole Design	143
	Bibliography	157

Symbols and Acronyms

List of Symbols

a	semi-major axis
b	semi-minor axis
d	distance
D	detection sensitivity
e	eccentricity of an ellipse
f	focal length
g_i	image distance measured from the effective focus
g_o	object distance measured from the effective focus
G	gain of the CCD signal
h	absolute coordinates of the focal points
h_1	distance measured from the first principal plane
h_2	distance measured from the second principal plane
h_{groove}	known groove depth
h_p	absolute coordinates of the foci
$h_{x,y}$	amplitude point spread function at the (x, y) plane
H	absolute coordinates of the pinhole apertures
I	intensity
J_0	the Bessel function of the zero order of the first kind
J_1	the Bessel function of the first order of the first kind
k	wave number
m	magnification
m_0	lateral magnification on the optical axis
M	lateral magnification
n	refractive index
n_{pix}	number of pixels
N_*	total number of photons collected per pixel
n_B	background noise on the CCD
N_D	total number of dark current electrons per pixel
N_R^2	read noise in terms of the total number of electrons per pixel

List of Symbols (cont.)

N_S	background noise in terms of the total number of photons per pixel
P	known period of an ultra high-resolution target
$P(\rho)$	pupil function of a lens as a function of the radius ρ
$P(\theta)$	apodization function as a function of the angle θ
$PP1$	the first principal plane
$PP2$	the second principal plane
r	radial coordinate
R	effective radius of the pinhole
R_a	arithmetic mean roughness parameter
R_{ku}	kurtosis roughness parameter
R_q	root mean square roughness parameter
R_{sk}	skewness roughness parameter
R_t	maximum peak to valley
R_z	ten points average of height differences
s	signal output per pixel
s, s_o	object distance
s', s_i	image distance
t, T	dummy variables
t_1, t_2	time
t_a	acquisition time
t_e	exposure time
t_r	remaining delay time
t_s	scanning time
u	normalized axial optical coordinate
v	normalized lateral optical coordinate
x	x coordinate
y	y coordinate
z	z coordinate

List of Symbols (cont.)

α	half aperture angle of an imaging lens
λ	wavelength
δ	dummy error
φ	tilt angle of the detection arm
ΔF	step size
Δx	lateral sampling interval
$\Delta x, \Delta z$	sampling interval between foci
$\Delta x', \Delta z'$	spacing interval between pinholes
$\Delta x'', \Delta z''$	spacing intervals between pinhole images
$\Delta z(3\text{ dB})$	the half power width of the optical axial resolution
Φ	tilt angle of the focal plane
ρ	radial coordinate
σ_f	estimation of 1 sigma error
Θ	tilt angle of the pinhole mask plane
ζ	correction factor

List of Acronyms

2D	Two Dimensions/Dimensional
3D	Three Dimensions/Dimensional
AMR	Axial Measurement Range
A/D	Analog to Digital
CCD	Charge Coupled Device
CLSS	Confocal Line Scanning Sensor
CM	Confocal Microscope
CSOM	Confocal Scanning Optical Microscope
FOV	Field of View
FWHM	Full Width at Half Maximum
fps	frames per second
HWHM	Half Width at Half Maximum
LED	Light Emitting Diode
MTF	modulation transfer function
NA	Numerical Aperture
PSF	Point Spread Function
RMS	Root Mean Square
PTB	Physikalisch Technische Bundesanstalt
SNR	Signal to Noise Ratio
TSCM	Tandem-Scanning Confocal Microscope

Chapter 1

Introduction

1.1 Motivation

The growth of interest in Confocal Microscopy (CM) lies in the unique property of *optical sectioning* or *depth discrimination* [55]. This property ensures that only the in-focus object is imaged efficiently at a time. Due to the improved contrast and depth discrimination capability, the early interests in the confocal microscopes are related to three-dimensional imaging applications. These microscopes are used in widespread areas ranging from metallography [26, 58, 102, 104, 119], geology [3], semiconductor devices [19], biology to medicine [20, 45, 46, 49, 51, 66]. However, the focusing area of interest in this thesis is the surface characterization.

The confocal point sensor developed by Minsky [55] in 1961 needs be scanned in three-dimensions to measure surface topography. In consequence, several techniques have been developed to enhance the scan, for example, a raster scanning using a Nipkow disk, applied in a confocal microscope [69, 70]. The Nipkow disk is rotated, however, to facilitate the raster scanning only in the lateral plane.

It was not until the invention of the *chromatic principle*, developed by Molesini *et al.* [57] in 1984, that a motionless parallel depth scanning scheme was viable. Therefore, this technique gains a significant interest for a high speed measurement. The *chromatic principle* uses chromatic aberration to create wavelength-to-depth coding technique to focus light of different wavelengths at different depths, as shown in Figure 1.1 (a). Therefore, fast measurement with a slight reduction in resolution is obtained by using the chromatic principle with a white light source and a color CCD camera [104]. The notable developments based on the chromatic principle include, for instance, single-shot depth-section imaging system [46] and non-translational three-dimensional profilometry [102].

However, this technique introduces certain complication and increases cost of the data processing, since a spectrometer per sampling channel of a specific wavelength is required to evaluate the intensity output [76]. Thus, spectrometers equivalent to the number of the sampling channels are necessitated, that drasti-

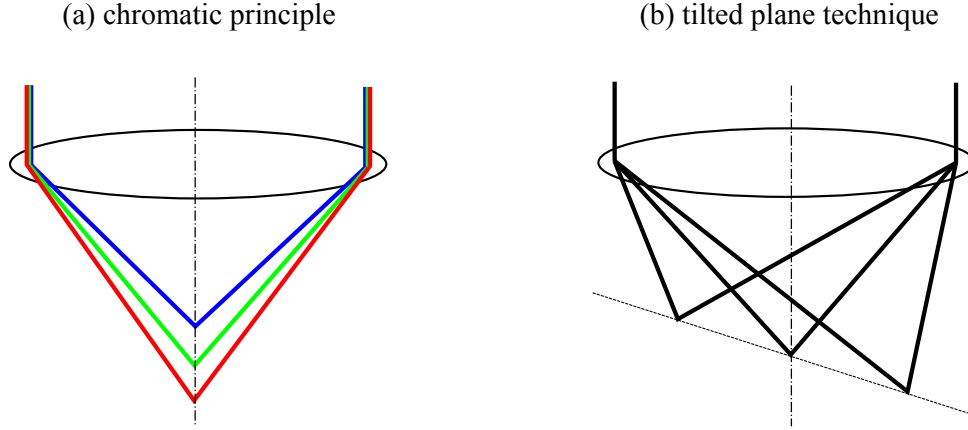


Figure 1.1: Simplified schematic of the parallel depth scanning schemes based on: (a) chromatic principle, (b) a tilted plane technique.

cally increases cost of the system. In addition, focusing dispersed light at different depths will degrade the light budget efficiency per wavelength per sampling point [93]. High linearity in the wavelength-to-depth coding characteristic of supercontinuum light is also required for evenly sampling in the axial direction [46]. Thus, to replace a single sampling point, an array of multiple focal points can be formed using diffractive microlenses to cover the whole lateral *field of view* and using chromatic aberration [101] to cover the whole axial measurement range in parallel in one shot. However, the working distance (the distance between the specimen and the lenses) of microlenses can be extremely short. A slit aperture can also be used to create an array of multiple focal points in a lateral plane [46], though the confocal effect is lost in the direction along the slit.

As a consequence, a new motionless parallel-depth scanning scheme is proposed in this thesis, targeting for a simplified configuration and a cost-effective data processing. The novel approach is to incorporate a tilted plane technique in a confocal imaging system [12, 14, 15]. Figure 1.1 (b) then shows that multiple foci of monochromatic light are formed at the tilted focal plane. These help to eliminate the need to scan in the axial direction, neither optically nor mechanically. The system configuration is therefore greatly simplified compared to classical CMs. Nonetheless, this new measuring concept will be completed only when the specimen is scanned in the lateral direction through the in-line focal stack of Figure 1.1 (b). Consequently, particular algorithms for the data processing are developed to support this new measuring concept. The new sensor is then named as *Confocal Line Scanning Sensor* (CLSS), following the in-line scanning approach employed. The CLSS is attempted to measure a two-dimensional height or *depth* profile covering a long lateral scan range while maintaining the *depth discrimination* manifested in a confocal imaging system. Two-dimensional profiling of up to a few ten millimeters is initially addressed, corresponding to targeted applications. Moreover,

a three-dimensional profiler can further be developed based on this principle.

In this thesis, a novel parallel depth scanning scheme of the CLSS is thus proposed, developed and investigated.

1.2 Goals

The novelty of a parallel depth scanning scheme of the *Confocal Line Scanning Sensor* (CLSS) allows the sensor to be built as a robust and simplified configuration. Neither the moving parts in the optical setup nor the scan methods in axial direction are required. The goals of this thesis are to:

- minimize the complexity of a confocal imaging system. This is done by using a stack of stationary foci generated at different depths which help to create an array of fixed sampling points in the axial direction. Therefore, the scan in the axial direction are not necessary, making the configuration simple and robust.
- incorporate a tilted plane technique in a confocal imaging system. The new *concept* of a parallel depth scanning scheme established in this thesis is defined with the use of an inclined focal plane comprising of stationary foci projecting at different depths. Then, with the use of a monochromatic illumination a simple setup with high light budget efficiency per wavelength per sampling point is obtained.
- extend the knowledge and understanding of the confocal imaging applied with a tilted plane technique. The investigations in theory, in experiment and in simulation are performed to support new explanations.
- serve as a model for developing a low cost or a high speed instrument for surface inspection.

1.3 Organization of the thesis

Chapter 2 provides the basic principle of confocal microscopy. The Nipkow disk based confocal microscopes are discussed as the basic configurations, from which the CLSS is developed. The optical resolution and a targeted application of the CLSS employed for surface inspection are introduced at the end of this chapter.

Chapter 3 proposes the theoretical design of the CLSS. The working principle of the new parallel depth scanning scheme and essential theories needed to support the design are presented. A tilted plane technique following the Scheimpflug's rule and the pinhole mask design form the subject matter of this chapter. In addition, a new approach to predict and to correct for the variation of the magnification

inherent in a tilted plane imaging system is established. Finally, the imaging characteristics of the CLSS is discussed. Accordingly, the simulation studies are used to validate some of the discussions and explanations.

Chapter 4 contributes to discuss the system's construction and alignment of the CLSS. The design described in Chapter 3 is implemented in this chapter. Main contributions of the system's construction and alignment are to obtain uniform illumination and equally spaced foci. These ensure that the highest degree of depth discrimination and depth-sampling precision are obtained. In this chapter, the magnification in a tilted plane system, newly derived in Appendix D, is used to predict the errors caused by the system misalignment tolerances. Then, the hardware overview of the process control and data acquisition is presented. The speed enhancement of the data acquisition is also briefly discussed. At the end of the chapter, errors and noises inherent in the system are summarized to provide a background knowledge for the errors correction in the following chapter.

Chapter 5 deals particularly with the development of the data processing and calibrations. With the knowledge of the design and construction described in the previous chapters, the new parallel depth scanning scheme of the CLSS is completed in this chapter. Data processing and calibrations are explained in two parts. The first part describes the concept of the data processing, in which the errors are not yet taken into account. In the second part, including the errors the newly developed calibrations and data processing are discussed. The main target of the calibrations is to ensure the traceability of the sampling coordinates, x and z . Finally, the surface roughness of the 2D measured depth-profile is evaluated according to ISO 4287-1997 standard.

Chapter 6 presents the experimental results of the CLSS. The results demonstrate that the incorporation of a titled plane technique in a confocal imaging system is feasible. The new parallel depth scanning scheme of the CLSS provides comparable results to that of calibrated specimens and a commercial confocal imaging system. In addition, the effective resolution of the CLSS is evaluated. Then, significant aspects concerning the measurements are also observed and reported in this chapter.

Chapter 7 concludes the major results achieved in this thesis and outlines possible future research work in this field.

Chapter 2

Background of Confocal Microscopy

The development of the *Confocal Line Scanning Sensor* (CLSS) in this thesis is to incorporate a tilted plane technique in a confocal imaging system, such that no moving part is required in the optical configuration. In this development, the novelty of the CLSS also lies in its new parallel depth scanning scheme [12, 14, 15]. Accordingly, this chapter is aimed to provide significant background and notable properties of the confocal imaging technique. The advent of Confocal Microscopy (CM) and Nipkow disk based confocal microscopes form the subject matter of this chapter. Then, the optical resolution used to define the limit of an imaging system is presented, which will be useful for the optical design in Chapter 3. At the end of this chapter, the major interest of the CLSS on surface inspection is described.

2.1 The advent of Confocal Microscopy (CM)

Preceding the advent of Confocal Microscopy (CM), it was impossible for light microscopes to gain information in the depth direction. In 1957, Marvin Minsky described the first complete principle of a confocal point-sensor in his patent [55], in which technique the ability of the light microscopes to measure object's depth was manifested, as illustrated in Figure 2.1. He also made notable suggestions on several aspects of confocal microscopy. With a point source and a point detector, the confocal point sensor introduces a unique property of *optical sectioning* or *depth discrimination* to ensure that only in-focus object is imaged efficiently at a time. In order to image the object in three dimensions, the measuring point is scanned in 3D, by either scanning the beam or the specimen [49, 55, 114]. Therefore, a clear-cut hint made by Minsky on how to scan was to rather scan the specimen, which is simpler but slower than to scan the beam.

It is fascinating to point out that several key inventions in confocal microscopy were inspired by the eagerness to study live brain cells or neurons in the brain [49],

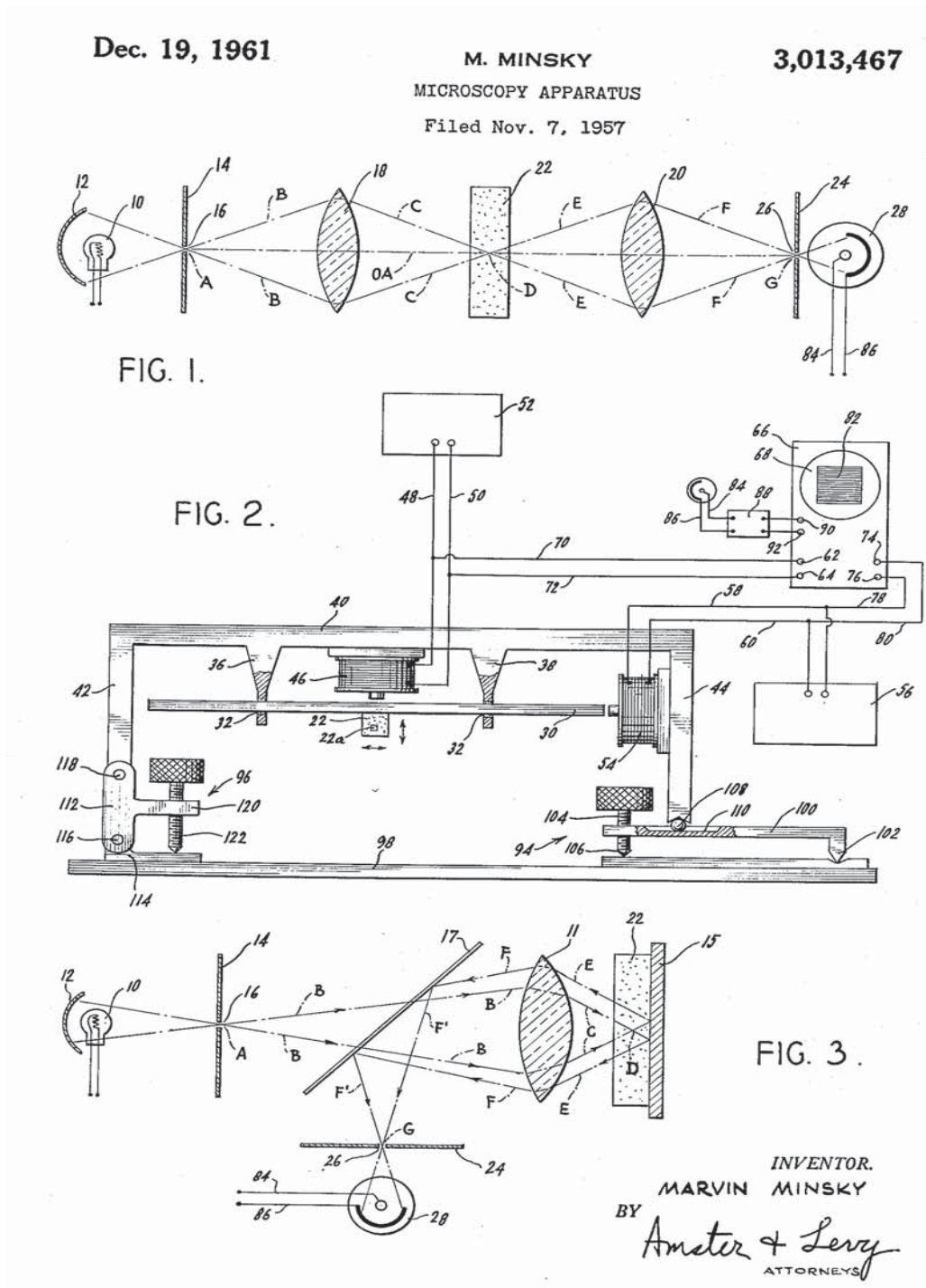


Figure 2.1: Confocal point-sensor described in Minsky's patent [55]. FIG.1 shows the transmission confocal point sensor. FIG.2 shows the stage-scanning system. FIG.3 shows the reflection confocal point sensor with one objective lens and a beam splitter.

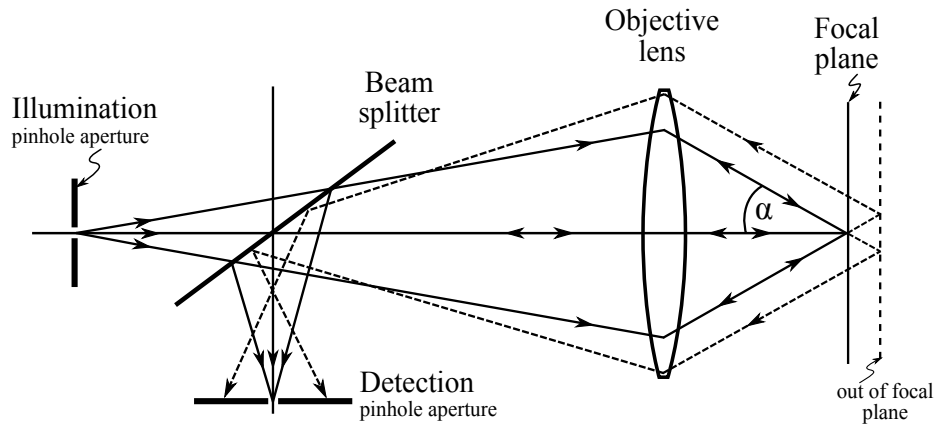


Figure 2.2: Schematic diagram showing the depth discrimination capability of a confocal imaging system and how the in-focus light discriminates against the out-of-focus light, where the numerical aperture (NA) of the objective lens is $NA = \sin \alpha$, and α is the half aperture angle of the objective lens.

including Minsky [56], Petrán and Hadravsky [64, 70], and Naora [59]. Although it may be less known than the Minsky's patent, earlier in 1951 Naora [59] succeeded in inventing and constructing the primal non-imaging confocal microscope in Japan, meanwhile in the same year of 1951 Young and Roberts [74, 123] succeeded in implementing the first confocal scanning optical microscope in UK.

2.1.1 Depth discrimination property and applications

The well-known property of *depth discrimination* in confocal microscopy offers a solution to eliminate blurred images attributed by out-of-focus planes, enabling a confocal microscope to optically cut through the specimen [114], as depicted in Figure 2.2. Depth discrimination can be realized by using a pinhole aperture to operate as a point source and a point detector. The pinhole aperture functions as a spatial filter to pass only in-focus light and eliminate out-of-focus light. When the pinhole is extremely small, the illumination becomes *spatially coherent illumination*¹ [27], regardless of the frequency bandwidth of light. In a confocal microscope, not only the capability of depth discrimination is manifested, but also

¹The confocal microscope uses *spatially coherent illumination*, while the conventional light microscope uses spatially incoherent illumination. This is because a point illumination in the confocal microscope substitutes a large-area illumination in the conventional light microscope. Light from either a broadband illumination source such as an arc lamp or a narrowband source like a laser when passes through an infinitesimal pinhole will behave as a spatially coherent illumination. In other words, the phase of all illuminated points vary uniformly, although the relative phases of these points are different, as stated by Goodman [27]. In this situation, the *temporally coherent* property of light is not changing. Generally, *coherent illumination* refers to the spatially coherent illumination.

the optical resolution and contrast are improved.

Due to the non-invasive measuring scheme of the optical technique with the improved contrast and the depth discrimination capability, confocal microscopes have seriously earned interests, especially, in the field of life science and three-dimensional imaging applications. Nonetheless, these microscopes are employed in widespread areas ranging from metallography, geology, semiconductor devices, biology to medicine [3, 19, 20, 26, 49, 51, 66]. However, the area of interest in this thesis work is related mainly to surface characterization.

2.2 The evolution of the Nipkow disk based confocal microscopes

A brief evolution of the Nipkow disk based confocal microscopes is presented in this section, which provide a vital knowledge of the optical configuration for the CLSS development. The Nipkow disk based confocal microscope is considered as the first real-time confocal imaging system in the reflection mode. Thousands of points are scanned in parallel by rotating the Nipkow disk, to enhance the speed of the measurement. In 1884, the Nipkow disk, patented by Nipkow [60], was first attempted to use in television technology. Then in 1966, Petráň and Hadravský [70, 69] notably incorporated the Nipkow disk in a confocal imaging system, namely a Tandem-Scanning Confocal Microscope (TSCM). Figure 2.3 shows that in this design one half of the disk is used for illumination, whereas the other half is used for detection. In consequence, mis-centering of the Nipkow disk contributes to the mis-alignment of the illumination pinholes and the detection pinholes, such that the confocal effect might not be realized. Thus, laborious alignment is required for the TSCM. In addition, the vibration of the Nipkow disk attributes to degrade the quality of the measurement [49, 114, 121].

To eliminate the drawbacks of the TSCM, a one-sided Nipkow disk based confocal microscope was developed by Kino, Corle and Xiao at Stanford University in 1988 [18, 42, 120, 121]. They received a patent later in 1990 according to the invention. In this system, the same set of the pinholes are used for both illumination and detection, resulting in a simplification of the alignment. The system is also less sensitive to the vibration of the Nipkow disk. In addition, Kino, Corle and Xiao proposed a method to eliminate back reflection of light, $\approx 98\%$ of the incident light, from the back side of the Nipkow disk to the detector, by tilting the Nipkow disk about $6-8^\circ$ with respect to the plane normal to the optical axis. This tilting technique is thus further developed in the CLSS. Prior to this elimination, light reflected from the back side of the Nipkow disk causes serious problems in the imaging quality. Not until the 1980s, the Nipkow disk based CM could be operated in real-time in connection with the presence of the desktop computers and software to display and render images.

Subsequently, a *pinhole disk* containing pinholes in quasi-uniform pattern was

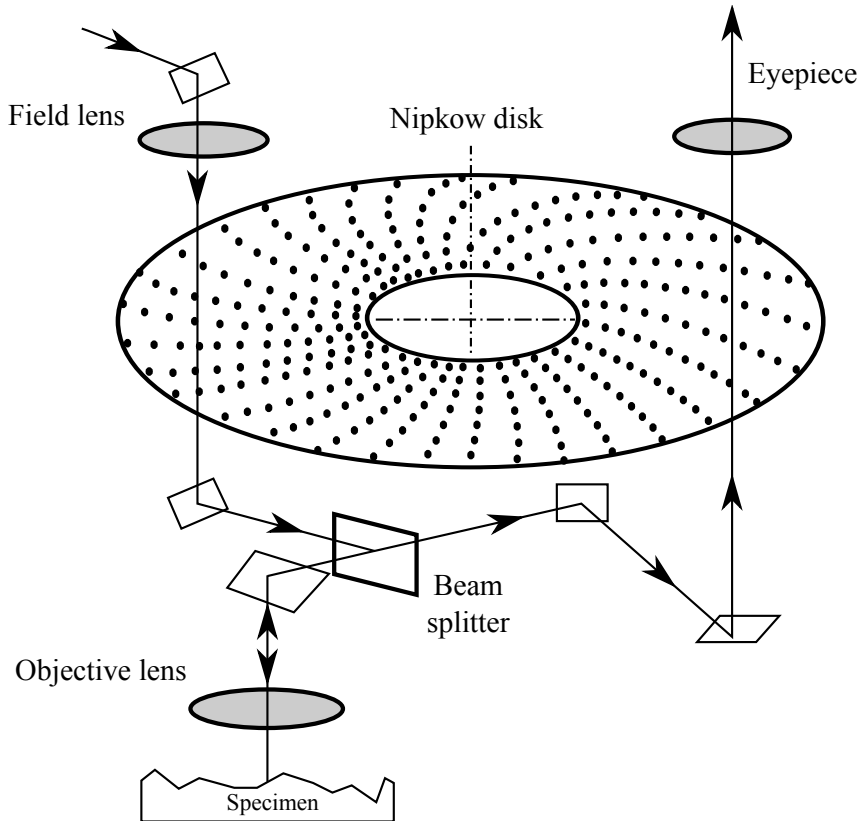


Figure 2.3: Schematic diagram of a Tandem-Scanning Confocal Microscope (TSCM) invented by Petráň and Hadravský [70, 69] in 1966.

designed and patented by Weber [110] in 2009, depicted Figure 2.4. The pinhole disk comprising of quasi-uniformly arranged pinholes then replaces the Nipkow disk which has the pinholes arranged in Archimedes spiral pattern. The major advantage of this quasi-uniform patterned pinhole disk is its compact size. As a result, unwanted vibration caused by the rotating disk is dramatically alleviated [110]. In addition, an extra slit window on the pinhole disk shown in Figure 2.4 allows the microscope to image in confocal mode and in conventional microscope mode using the same pinhole disk.

2.3 The *pinhole disk based* confocal microscope

The principle of the *pinhole-disk-based* confocal microscope is thus described in this section. Its optical configuration is the reference model to develop the CLSS'

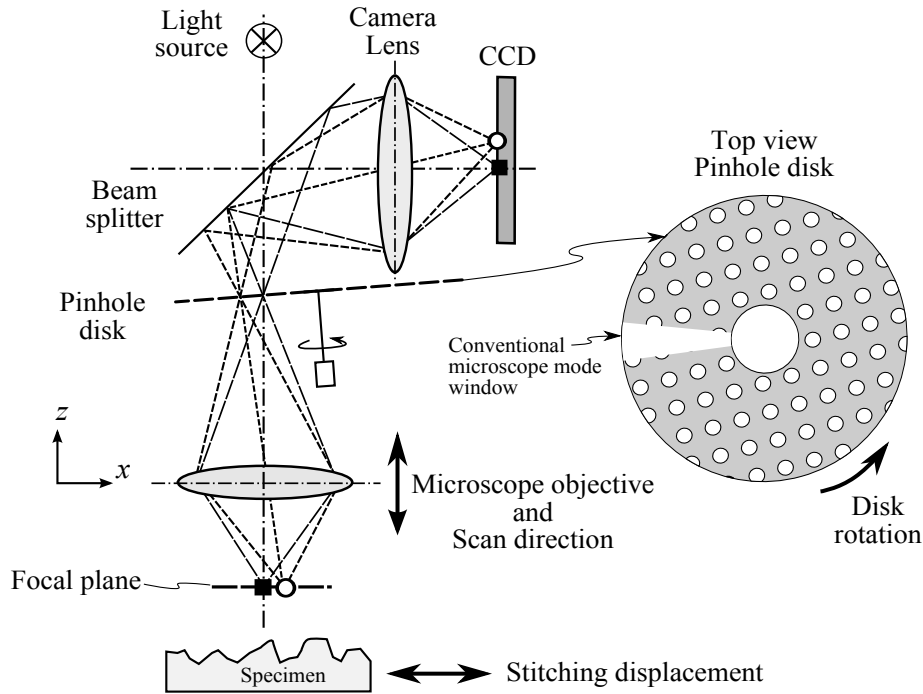


Figure 2.4: Schematic principle of the pinhole-disk based confocal microscope. The pinhole disk is rotated to initiate a raster scanning of the focal points on the specimen in the lateral plane, and the objective lens is scanned in the axial direction to extend the measurement in 3D.

configuration. Figure 2.4 schematically illustrates the pinhole-disk-based confocal imaging system. Multiple pinholes in the pinhole disk help to create parallel point-like illumination. Then, the multiple illumination-points are parallelly scanned on the specimen in a raster fashion by rotating the pinhole disk. Accordingly, light reflected from the specimen retraces the same path, and passes through the same set of pinholes to function as parallel point-like detectors. However, a raster scanning of the pinhole disk facilitates the parallel scanning merely in the lateral plane. To extend the measurement in the *axial* or *depth* direction, the objective lens is scanned in the axial direction, e.g. using a piezoelectric actuator [40, 58], as depicted in Figure 2.4. This way three-dimensional images can be obtained. For the detection of reflected light, a CCD is used to record the data as individual frames per field-of-view. In consequence, the data are stored layer by layer in the confocal data stack, and will be processed later to reveal the surface topography. This optical configuration in Figure 2.4 will then be mentioned again in Chapter 3.

Note that the main disadvantage of the pinhole-disk-based confocal imaging system is the low light transmission, $\approx 1\% - 2\%$ of the incident light [68]. Recently, the successful integration of microlenses in these confocal imaging systems allows the microlenses to improve the light transmission efficiency [103, 105, 122]. However,

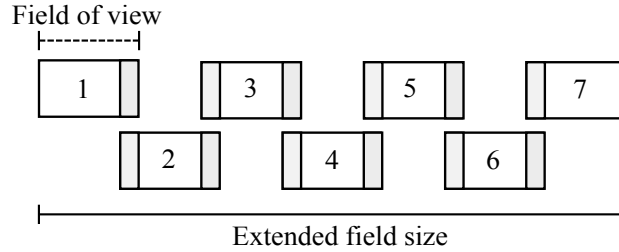


Figure 2.5: An extended field size obtained using image-stitching techniques, by correlating and merging the images of the successive field-of-views.

for high reflective surfaces in material science, the efficiency of light transmission $\approx 1\% - 2\%$ of the incident light is sufficient in most applications. For measuring very low reflective specimens, a slit aperture can be employed instead of a pinhole aperture. However, the confocal effect will be lost in the direction along the slit. Note that using the entire optical field-of-view in this system for measuring, the correction for aberrations is imperative to maintain good quality of the imaging across the field-of-view.

2.3.1 Stitching technique

The lateral field size of the measurement in the pinhole-disk-based confocal microscope is limited basically by the optical *field-of-view* (FOV), where the FOV is the maximum field size allowed by the optical configuration. To enlarge the lateral field size, the image per FOV is combined or stitched to each other using an image-stitching technique [48, 119]. The concept of the image-stitching is presented in Figure 2.5. However, this technique may degrade the final result, e.g. in the case of the specimens having periodic pattern. In Chapter 6, some improvements obtained with the new scanning scheme of the CLSS are presented and compared to that obtained with the traditional stitching technique.

2.4 Optical resolution

The optical resolution presented in this section is used to describe the resolving ability of an imaging system. This will be useful particularly when designing and optimizing the optical configuration discussed in the following chapter. However, the real resolution of the CLSS will be evaluated in Chapter 6. There are two main approaches for defining the optical resolution: *two-point resolution* [72, 96] and *single-point resolution*, known as *full width at half maximum* (FWHM). If the foci are formed far apart from each others, a single focal point can be considered at a time. This corresponds to the *single-point resolution*. On the other hand, if the foci influence each other, the optical resolution follows the *two-point resolution*.

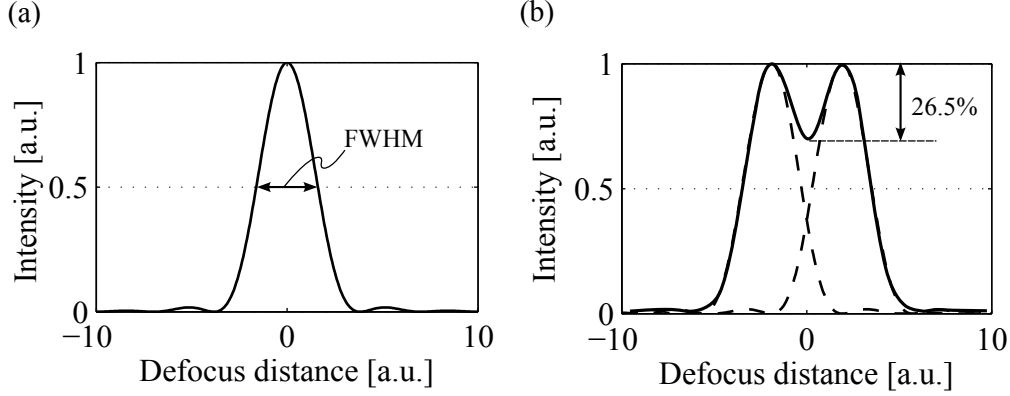


Figure 2.6: Illustration of the single-point and two-point resolution. (a) Single-point resolution or the FWHM approach. (b) Two-point resolution, conforming with the well-known Rayleigh criterion.

2.4.1 Single-point resolution

When a single illuminated point is considered at a time, the optical resolution is characterized by the geometry of the optical probe or the *intensity response*. In an ideal case, the intensity response is named the *point spread function*² (PSF). In analogy to the probing tip in a tactile profilometer, size of the optical probe imposes a limit on the resolution, in which the object smaller than the optical probe cannot be resolved. This way, the *single-point resolution* [17, 34, 66, 114] is defined using the half-power width of the main lobe of the intensity response, known as the *full width at half maximum*, shown in Figure 2.6 (a). The *single-point resolution* can be applied mutually in the lateral and axial directions.

Single-point lateral resolution

For a confocal microscope, the single-point resolution in the lateral direction is given by [17]

$$r_{xy,CONF}(3dB) = \frac{0.37\lambda}{NA}, \quad (2.1)$$

where NA is the Numerical Aperture. In this expression, r_{CONF} is 0.73 times smaller than the single-point resolution of a conventional light microscope, which takes the form

$$r_{xy,CONV}(3dB) = \frac{0.51\lambda}{NA}. \quad (2.2)$$

Eq.(2.2) is identical to the *Sparrow criterion* for an incoherent imaging system [33].

²The definition of *point spread function* is described in Appendix A.

Single-point axial resolution

The single-point axial resolution is the half-power width of the intensity response in the axial direction. In the confocal microscope, the axial resolution of a planar reflector is obtained as

$$r_{z,CONF}(3\text{dB})_{plane} = \frac{0.45\lambda}{n(1 - \cos \alpha)}, \quad (2.3)$$

where α is the maximum half angle subtended by the focused beam to the objective. For a point reflector, the single-point axial resolution becomes [17]

$$r_{z,CONF}(3\text{dB})_{point} = \frac{0.62\lambda}{n(1 - \cos \alpha)}. \quad (2.4)$$

It can be seen that the single-point axial resolution obtained with a planar reflector is 1.38 times smaller than that of a point reflector, meaning that the axial resolution in a planar reflector case is 1.38 times higher.

Note that eq.(2.1), eq.(2.2), and eq.(2.3) are commonly used in this thesis to calculate the theoretical optical resolution of the CLSS.

2.4.2 Two-point resolution

When two illuminated points are closely formed until they influence each other, the optical resolution is better defined by the *two-point resolution* based upon the well-known Rayleigh criterion. The *Rayleigh criterion* [33] suggests that two closely spaced illumination points are just distinguished from each other if the maximum of one response curve is located at the minimum of another response curve, depicted in Figure 2.6 (b). Basically, the Rayleigh criterion corresponds to the 26.5% dip in the intensity response between two illuminated points of the same brightness. In a confocal microscope, the *two-point resolution* is not applicable in the axial direction when only a single focal point is formed at a given depth, which rather corresponds to the *single-point resolution*.

Two-point lateral resolution

The distance between two illuminated points which can just be resolved is defined by [33]

$$r_{xy,CONV}(\text{Rayleigh}) = \frac{0.61\lambda}{\text{NA}}, \quad (2.5)$$

for a conventional light microscope, and

$$r_{xy,CONF}(\text{Rayleigh}) = \frac{0.56\lambda}{\text{NA}}, \quad (2.6)$$

for a confocal microscope [17]. Therefore, the two-point resolution in the confocal microscope is 8% higher than that in the conventional microscope.

2.5 Surface inspection application

In recent years, surface textures have been noted as a key parameter in many applications. The surface textures, particularly, the surface roughness play a significant role in the product performance, life time prediction, and wear rate of a workpiece [112]. For example, in tribology the micro-roughness on engine bores help to retain lubricant by which it can increase lubrication efficiency and life-time of the engine [71]. In automotive manufacturing, paint appearance of the auto body is significantly affected by the topography and roughness of the surface [81]. Even in tooling and machining the surface roughness can indicate stability of the machine tools or early failure in the process [99]. It seems explicit that surface texture is markedly important. Though, the challenge is in acquiring the information on the surface texture most effectively.

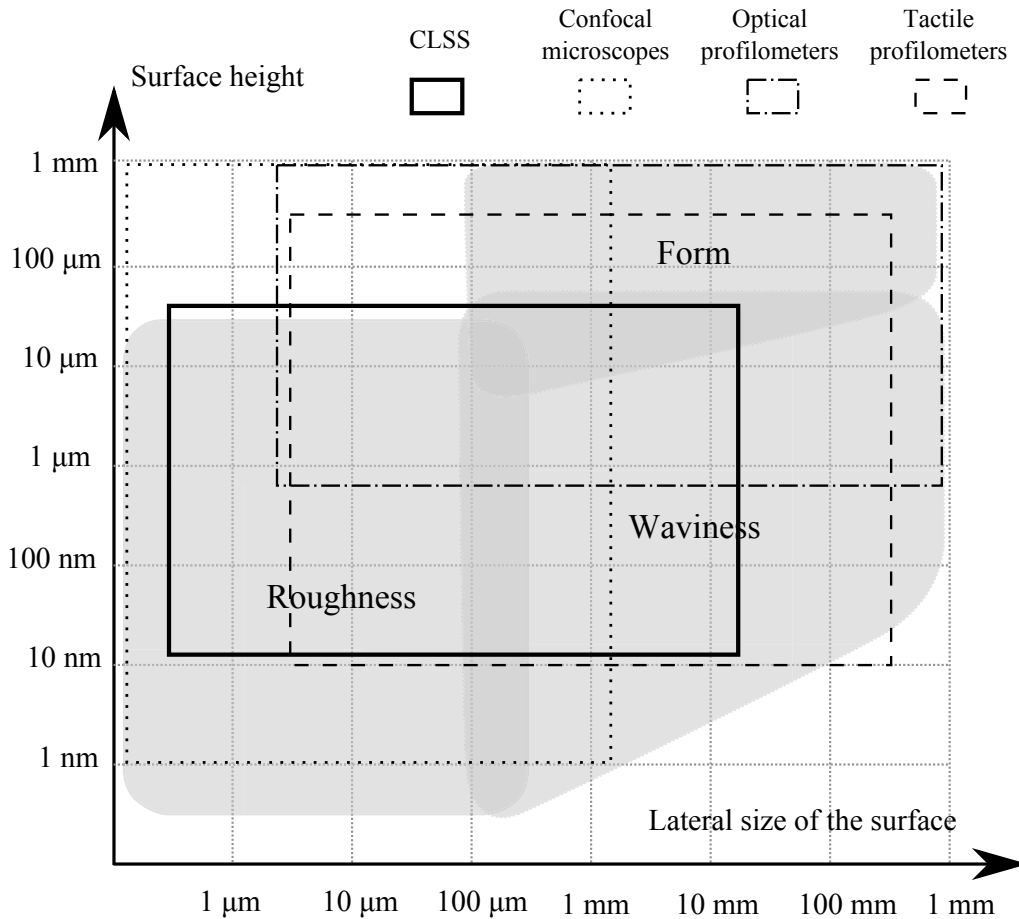


Figure 2.7: The range of the surface features which can be measured by several surface inspection techniques, i.e. CLSS, confocal microscopes, optical profilometers, and tactile profilometers [118]. In addition, the surface features can be categorized as *roughness*, *waviness* and *form*, depicted by gray areas.

In the early 1990s, the measurement of a single profile, providing a two-dimensional (2D) height profile was sufficient for many industrial applications. Not until recently three-dimensional (3D) surface characterization gained significant interests in order to provide additional information on the surface functionality [38, 98, 99, 111]. However, 2D height profiling still plays a strong part in quality assurance [84], such as in cutting tool industry [107], steel industry [21], or even in today's skin care industry [73].

Furthermore, this section provides an overview on the measurement range in which the CLSS can be used to inspect the size of surface features. Basically, surface features are categorized into *waviness* and *form* (the low-frequency components defining the overall shape) and *roughness* (the high frequency components) [112]. Figure 2.7 then depicts the ranges of surface heights and lateral structures measurable with several measuring techniques, including CLSS, confocal microscopes, optical profilometers and tactile profilometers (a contact method).

Nonetheless, the CLSS, first developed as a 2D optical profilometer, can be developed further as a 3D optical profilometer to cover a lateral scan range up to a few ten millimeters.

2.6 Conclusion

The basic knowledge of the confocal microscopy is given in this chapter to provide a significant background of a confocal imaging technique e.g. the CLSS. The tilting technique proposed by Kino, Corle, and Xiao [18, 42, 120, 121], to eliminate back reflection of light from the back side of the Nipkow disk, is then developed further in the CLSS to manifest the new parallel depth scanning scheme [12, 14, 15]. Then, the configuration and principle of a pinhole-disk based confocal microscope [110] is presented here, which serves as a model for developing the CLSS configuration. In addition, the stitching technique used to extend the measurement field-size used in the pinhole-disk based CM is briefly discussed. In Chapter 6, some improvements obtained with the new scanning scheme of the CLSS are presented and compared to that obtained with the traditional stitching technique. Moreover, the *single-point resolution* or the *full-width at half-maximum* (FWHM) approach is described mainly to define the optical resolving ability of the CLSS, which is useful when designing the optical configuration. Finally, the measurement ranges of several instruments for surface inspection are outlined. The CLSS as a 2D optical profiler can measure surface heights from a few ten nanometers up to 50 μm and the lateral structures from sub-micrometer to 15 mm. Nevertheless, the CLSS can be further developed as a 3D optical profiler. The suggestion on extending the CLSS measurement to 3D profiling is noted in Chapter 3.

Chapter 3

Theory of the Confocal Line Scanning Sensor (CLSS)

This chapter presents the theoretical design of the Confocal Line Scanning Sensor (CLSS). The pinhole mask design is a major subject of this chapter. The main target in designing the pinhole mask is to optimize the *depth discrimination* capability and the optical resolution of the CLSS' imaging system. The major challenge in developing the CLSS coping with in this chapter is to incorporate a tilted plane technique in a confocal imaging system. Thus, the chapter begins with the system overview, and follows by the theoretical explanation dealing with the tilted plane technique based on the Scheimpflug's rule. Moreover, the variation of the magnification inherent in a tilted plane system, known as *keystone distortion*, introduces more complexity in designing the pinhole pattern. As a consequence, a compact equation of the magnification in a tilted plane system is specifically derived and applied in this chapter to design the pinhole pattern. Then, a theoretical prediction of the keystone distortion and a newly discovered approach to correct for the keystone distortion are highlighted. The intensity responses of a point-like source and a finite-sized detector are thus described in this chapter in order to give a background knowledge for optimizing the pinhole size. Finally, the effects of a tilted pinhole mask on the imaging characteristics of the CLSS are investigated in theory and in simulation.

3.1 System overview

The *confocal line scanning sensor* (CLSS) is developed based on the pinhole-disk based confocal imaging system, described in the previous chapter. The novelty of the CLSS lies in the concept of a new parallel depth scanning scheme, which earned a patent in 2010 [12]. By using a tilted plane technique, a stack of stationary diffraction-limited foci or *diffraction foci* projected at different depths are created at a tilted focal plane, depicted in Figure 3.1. These *diffraction foci* are then

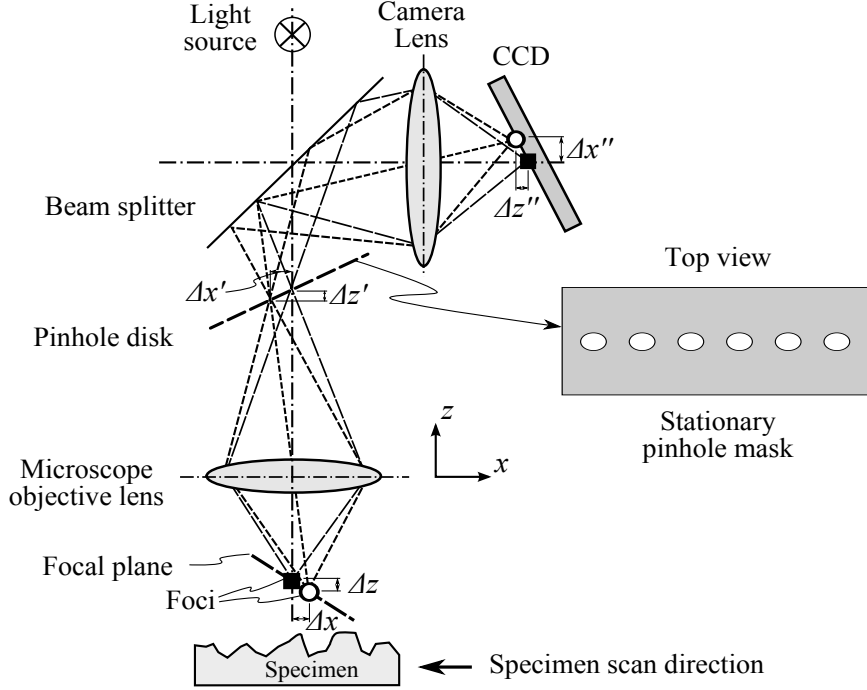


Figure 3.1: Schematic principle of the confocal line scanning sensor (CLSS). The tilted focal plane is formed from the tilted pinhole mask by an objective lens. To create a parallel depth scanning scheme, the specimen is scanned through the stationary stack of *diffraction foci* in a stepwise fashion or in a continuous approach, where Δx & Δz , $\Delta x'$ & $\Delta z'$, and $\Delta x''$ & $\Delta z''$ denote the spacing intervals between the foci, pinholes, and pinhole images, respectively.

used to inspect the specimen in parallel when the specimen is laterally scanned through the focal stack. The parallel scan of the in-line *diffraction foci*¹ thus gives the name *line scanning* to the CLSS. It should also be noted that a stationary tilted pinhole mask replaces the rotating pinhole disk and scanning piezoelectric actuator, which are required in the pinhole-disk based confocal imaging system, shown in Figure 2.4.

The notable advantage of the CLSS' configuration is its robustness and stability, in which no moving part is required in the optical setup. The CLSS was first developed as a 2D optical profiler, and its lateral measurement range can be theoretically extended to infinity. The CLSS is designed to operate mainly with a $20\times/0.45$ NA objective at 530 nm wavelength of light. There are 160 sampling points formed per shot, spacing with the focal intervals of $\Delta x = 5\mu\text{m}$ and $\Delta z = 0.3\mu\text{m}$, shown in Figure 3.2. Following eq.(2.1) and eq.(2.3), the optical resolutions are $0.44\mu\text{m}$ and $2.3\mu\text{m}$ in the lateral and in the axial directions.

¹Here, the diffraction focus means the unique point of maximum intensity when sufficiently small aberrations are present in the system, defined by Born and Wolf [6].

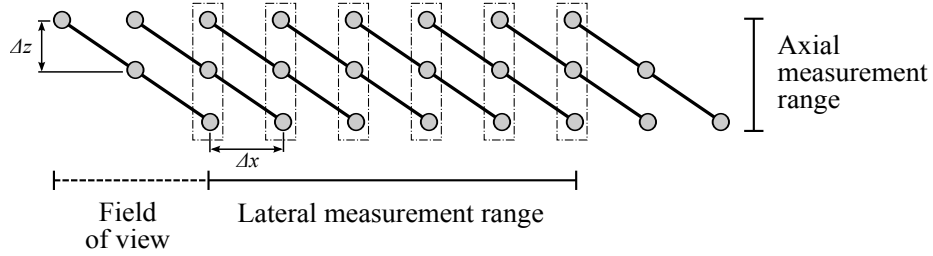


Figure 3.2: An illustration of the lateral and axial measurement ranges in the CLSS. The *lateral measurement range* is extended with the successive scans, whereas the *axial measurement range* is fixed and limited by the tilt angle of the focal plane and by the number of the sampling foci, where Δx and Δz are the focal intervals.

3.1.1 The principle of operation

The property of *optical sectioning* is maintained in the CLSS with the use of pinhole apertures. Figure 3.1 shows that the in-line pinhole apertures, when illuminated will function as multiple point-like sources, generate the inclined focal stack at the specimen. When the specimen is scanned through this inclined focal stack, light reflecting back from the specimen retraces the same path through the same set of the pinholes, where these pinholes now perform as point-like detectors. This way the *optical sectioning* is realized. Then, the light is deflected by the beam splitter to the CCD. In the detection part, the CCD is tilted to align with the tilted image plane, and the data are captured as a frame per shot of scan.

Figure 3.2 illustrates that the *lateral measurement range* is extended with the successive scans. This makes the parallel depth scanning scheme of the CLSS unique in that the data intensities are recorded in a non-sequential order in correspondence with the sampling coordinates. In consequence, the data sorting and related data processing are originally developed to support this unique data acquisition of the CLSS. The main target of the data processing is to reveal the axial intensity responses along the x coordinates; then the surface height evaluation can be implemented. Chapter 5 deals particularly with the data processing.

3.1.2 Speed and system's accuracy

The specimen is stepwise scanned in the lateral direction using a linear scanning stage, such that the parallel measurement can be executed simultaneously in the lateral and the axial directions. Thus, the speed and accuracy of the CLSS' measurement partly depend on the linear scanning stage's performance. Errors and noises in a low performance stage can cause the reduction in accuracy, whereas a high precision linear scanning stage can be costly. A linear scanning stage used in the CLSS is driven by a stepper motor at 5.8 frames per second (fps), up to 15 mm. With 160 sampling points per shot, the acquisition rate is obtained as $\approx 1,000$ points per second. However, the speed of the measurement can greatly be

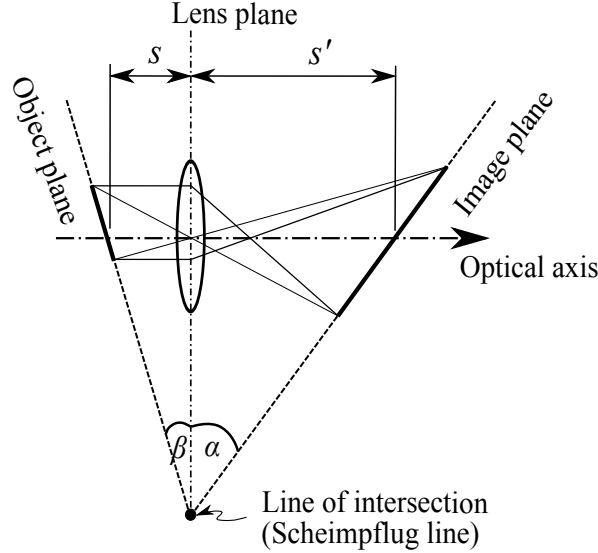


Figure 3.3: Schematic description of the Scheimpflug condition. The relation of the tilt angles is given by $m = \tan(\beta)/\tan(\alpha)$, where m is the on-axis magnification of the imaging lens, $m = s'/s$.

enhanced by increasing the acquisition rate and reducing the synchronization time between the hardwares. With the recent technology of high speed cameras, the data can be recorded up to a thousand frames per second, which will increase the acquisition rate up to 160,000 points per second.

To primarily increase the data density in the x direction, the measurement should be acquired with a finer lateral sampling interval, which in turn increases the measurement time. Only the data density in the axial direction is invariant, corresponding to a fixed sampling interval between the foci. Though, main disadvantage of the CLSS is the limit in the axial measurement range. A higher axial measurement range can be established, for instance, by using a higher tilt angle of the pinhole mask and a lower magnification of the imaging lens.

3.1.3 Tilted focal plane: Scheimpflug's rule

By applying a tilted plane technique in the CLSS, the tilt relation of the pinhole mask and the focal plane follows the Scheimpflug's rule [82]. The Scheimpflug principle, named after T. Scheimpflug [82, 83], was stated in 1904 that if a lens is tilted such that the lens plane intersects the object plane, the plane of the sharp image must also pass through the same line of intersection, shown in Figure 3.3. This principle was originally applied in view cameras, in which the magnification varied at the tilted image plane is obviously recognized [5].

Consequently, in the CLSS the tilted focal plane, formed by the imaging lens,

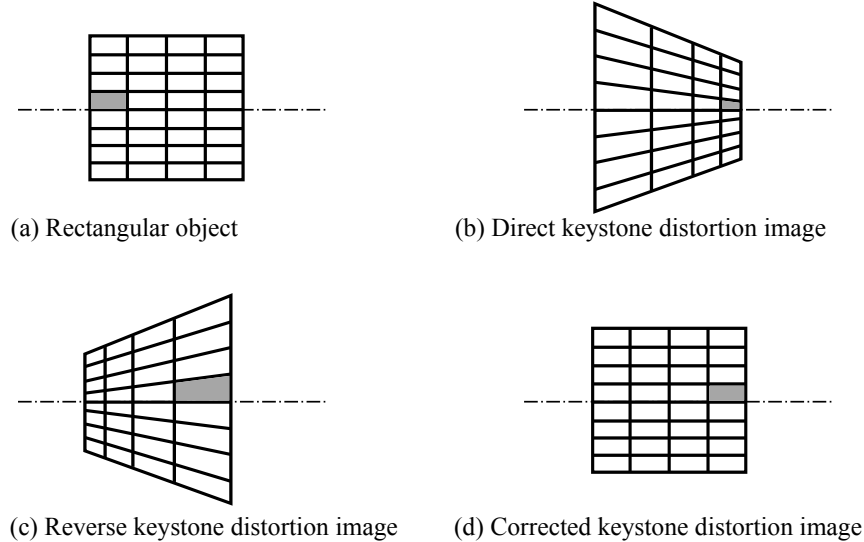


Figure 3.4: Illustration of the keystone distortion images of a rectangular object.

intersects the same line of intersection of the pinhole mask's plane and the lens' plane, denoted by the *Scheimpflug line* in Figure 3.3. This line, not a point, has its dimension extending in depth (into the paper plane). In consequence, the tilt of planes cause the object and image distances (s and s') vary along the tilted field-of-view. Therefore, the lateral magnification, $m = s'/s$, varies accordingly across the field-of-view. The full derivation of the magnification in this tilted plane system is found in Appendix D. The magnification is expressed as a function of four variables: *on-axis* and *off-axis lateral magnifications*, the *tilt angles* of the object and image planes. The derived magnification is then implicated in the pinhole design explained later in this chapter.

3.2 Keystone distortion

Note that the variation of the magnification in this tilted plane system is known as the *keystone distortion* [28], which creates a trapezoidal image from a rectangular object as can be seen in Figure 3.4. Mathematically, the keystone distortion was classified as quadratic distortion type II, using a power series expansion [78].

In this section, the effect of the keystone distortion, caused by the shifting of the *principal planes*², is highlighted. It is an interesting effect found only in a compound lens system. The pattern of the magnification is then modified as the positions of the principal planes are shifted. Consequently, three significant cases of the keystone distortion were discovered during the development of the CLSS.

²A plane normal to the principal axis of a lens, at which the focal length is referenced.

3.2.1 Shifting of the principal planes and patterns of the keystone distortion

The principal plane is a hypothetical plane which cannot directly be measured [33]. In a simple case of a single lens or a *singlet*, the first and the second principal planes are always fixed in places because the principal planes cannot deliberately be shifted. On the contrary, consider a compound lens system consisting of two thin lenses in Figure 3.5 (a). In this case, the positions of the principal planes can be shifted by changing the distance between these two lenses. Figure 3.5 shows that the same set of thin lenses can be rearranged to shift the positions of the principal planes, for example, by increasing the distance d by 40 cm from Figure 3.5 (a) to Figure 3.5 (b). Without any physical movement of the object referenced from the first lens, the object distance increases from 45 cm to 55 cm in connection with the shift of the principal planes. For brevity, the detailed calculation is demonstrated in Appendix B. This example illustrates that when the principal planes are shifted the object and image distances vary accordingly, and so does the magnification, which leads to a significant conclusion in this section.

In the CLSS system, a more complicated compound lens system is employed, so that the principal planes can possibly be shifted approaching infinity. Imagine that a compound lens system is represented by a black box, shown in Figure 3.6. The object and image distances, s_o and s_i , are then measured from the principal planes [33]. The *positive* sign convention of the object and image distances is depicted in Figure 3.6, whereas the *negative* sign convention is thus vice versa. According to that, a shifting of the principal planes can even cause the sign conversion of the

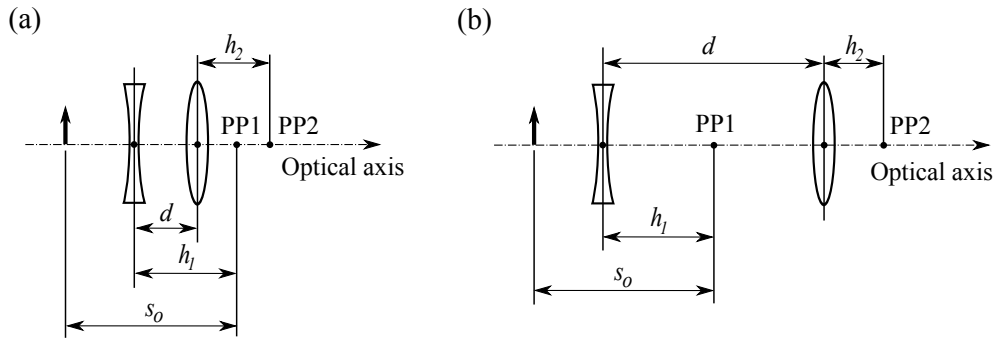


Figure 3.5: Schematic illustration of the principal planes shifting in a compound lens system by changing the distance between these two lenses. This simple compound lens system consists of two thin lenses. PP1 and PP2 represent the first and second principal planes. h_1 is the distances measured from the center of the first lens to the first principal plane, and h_2 is the distances measured from the center of the last lens to the second principal plane, respectively. d is the distance between two lenses, while s_o is the object distance measured from the first principal plane. (a) $d = 10$ cm, $h_1 = +15$ cm, $h_2 = +10$ cm, and $s_o = 25$ cm. (b) $d = 50$ cm, $h_1 = +25$ cm, $h_2 = +16.667$ cm, and $s_o = 35$ cm.

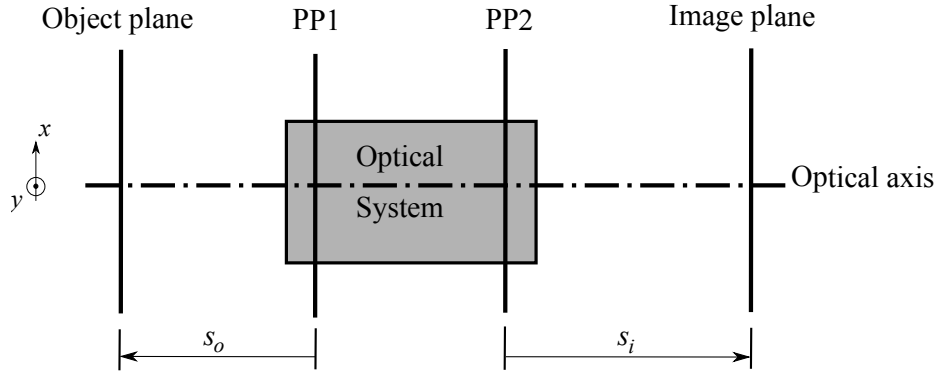


Figure 3.6: Schematic of a compound lens system represented in a black box, where PP1 is the first principal plane. PP2 is the second principal plane. s_o is the object distance measured from PP1. s_i is the image distance measured from PP2.

distances s_o and s_i to change from positive to negative.

Figure 3.4 depicts a simplified illustration of the keystone distortion. In the first case, the object and image distances are in positive values, where the keystone distortion is termed as *direct keystone distortion*, depicted in Figure 3.7 (a). In the second case, the pattern of the keystone distortion is reversed from the first case, caused by the sign conversion of the object and image distances from positive to negative values, depicted in Figure 3.7 (b). This reverse effect is termed as *reverse keystone distortion*, which is the case existing in the CLSS.

Although the keystone distortion changes its pattern according to the shifting of the principal planes, the Scheimpflug's rule is still valid. If there is no change in the physical positions of the object and image and no change in the magnification along the optical axis, the tilt angles of the object and image planes are preserved, so the Scheimpflug's condition. Figure 3.7 shows that the sign conversion of the object and image distances is equivalent to interchanging of the places between the object and the image, hypothetically. According to that, the object "1" is reversely magnified in Figure 3.7 (b) comparing to Figure 3.7 (a), when the principal planes are shifted from the positive to the negative coordinates. This can be illustrated as the reverse effect in magnifying the gray rectangle in Figure 3.4 (b) to (c).

3.2.2 The correction of the keystone distortion

It is noteworthy to point out that the link between the shifting of the principal planes and the keystone distortion pattern leads to a newly approach to correct for the keystone distortion. When the principal planes are shifted approaching infinity, the object and image distances become closer to infinity. Thus the magnification - *the ratio of the image distance to the object distance*, is corrected uniformly across the tilted image plane, depicted in Figure 3.4 (d). This property can be found in two optical configurations namely *telescopic* and *telecentric*. However the

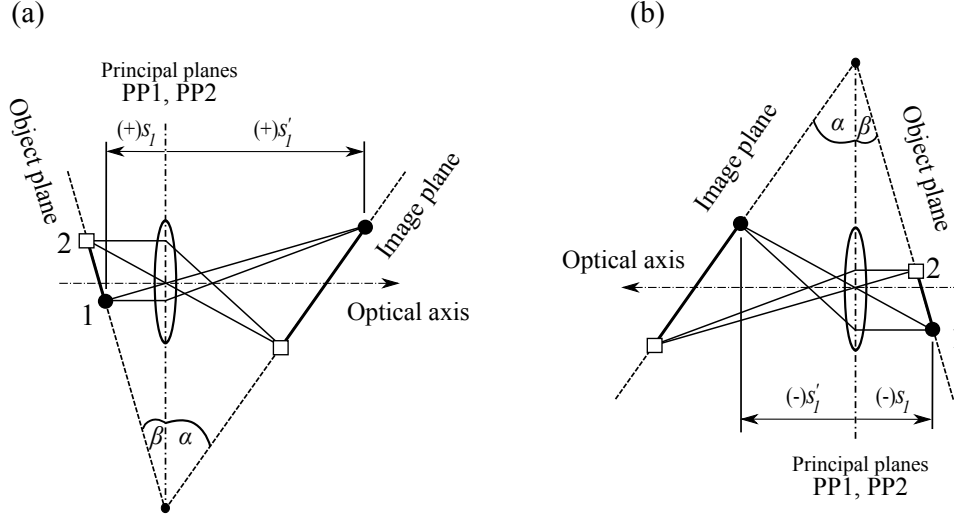


Figure 3.7: Direct and reverse keystone distortion. This illustrates the reverse effect in magnifying the object when the sign of the object and image distances changes from positive to negative. (a) Direct keystone distortion. (b) Reverse keystone distortion.

magnification is not necessarily being infinity. This contributes to the third case of the keystone distortion presented in this section, which is the most advantageous case namely *corrected keystone*. The uniform magnification across the tilted field-of-view allows parallel focal lines to be formed to inspect the surface topography in three-dimensions. The experimental investigation of the keystone distortion in all cases is then presented in Chapter 4.

3.3 Intensity responses and criteria to define the pinhole size

In this section, the role of the pinhole diameter on the intensity responses is taken into account. The intensity responses of a point source and a finite-sized detector is described to give a criteria to determine the pinhole size at best optical resolution and depth discrimination capability.

Following the study of Wilson and Carlini [116, 115], the intensity response of a point source and a finite-sized detector is given by

$$I(v, u) = |h_1(v, u)|^2 \cdot \left(|h_2(v, u)|^2 * D(v) \right), \quad (3.1)$$

where $h_1(v, u)$ and $h_2(v, u)$ are the *point spread functions*³ of the imaging and detecting lenses. Here, the symbol $*$ denotes the convolution operation and $D(v)$ rep-

³The definition of *point spread function* is described in Appendix A.

resents the sensitivity of a finite-sized detector. In a reflection confocal microscope, these two point spread functions are equal, where $h_1(v, u) = h_2(v, u) = h(v, u)$.

For simplicity, the intensity response is expressed in the optical coordinates (v, u) , where the optical coordinates are the physical-coordinates normalized by the wavelength of light (λ) and the half aperture angle of the objective lens (α). The normalized lateral optical coordinate (v) is written as [115]

$$v = \frac{2\pi}{\lambda} \cdot r \cdot \sin \alpha, \quad (3.2)$$

where r is the physical radial coordinate. In addition, the normalized axial optical coordinate (u) takes the expression [115]

$$u = \frac{8\pi}{\lambda} \cdot z \cdot \sin^2 \left(\frac{\alpha}{2} \right), \quad (3.3)$$

where z is the physical axial coordinate.

3.3.1 Lateral intensity response

Consider first the lateral intensity response of a point object at the focal plane. Substituting $D(v)$ by the circle function⁴, $circ(v/v_p)$, in the convolution term in eq.(3.1), eq.(3.1) can be rewritten as [116]

$$I_{\text{point}}(v, 0) = \begin{cases} |h(v)|^2 \left[2\pi \int_0^{v_p-v} |h(t)|^2 t dt \dots \right. \\ \quad \left. + 2 \int_{v_p-v}^{v+v_p} |h(t)|^2 \cdot \cos^{-1} \left(\frac{t^2+v^2-v_p}{2t \cdot v} \right)^2 t dt \right] & , v < v_p \\ \text{or} \\ 2 |h(v)|^2 \int_{v-v_p}^{v+v_p} |h(t)|^2 \cdot \cos^{-1} \left(\frac{t^2+v^2-v_p}{2t \cdot v} \right)^2 t dt & , v > v_p, \end{cases} \quad (3.4)$$

where v_p is the radius of the pinhole in the normalized optical unit; $u = 0$ is the reference of the focal plane in the axial coordinate, and t is a dummy variable.

Following eq.(3.4), the *half width at half maximum* (HWHM) intensity of the lateral response ($v_{1/2}$) is delineated as a function of the pinhole radius v_p in Figure 3.8. In this graph, the smaller the pinhole radius v_p , the narrower the lateral response curve ($v_{1/2}$). To obtain the narrowest $v_{1/2}$ then the highest optical lateral resolution, the pinhole radius should be $v_p \leq 0.5$. See the definition of the optical

⁴The *circle* function can be written as [27]

$$circ(\sqrt{x^2 + y^2}) = \begin{cases} 1 & , \sqrt{x^2 + y^2} \leq 1 \\ \frac{1}{2} & , \sqrt{x^2 + y^2} = 1 \\ 0 & , \text{otherwise.} \end{cases}$$

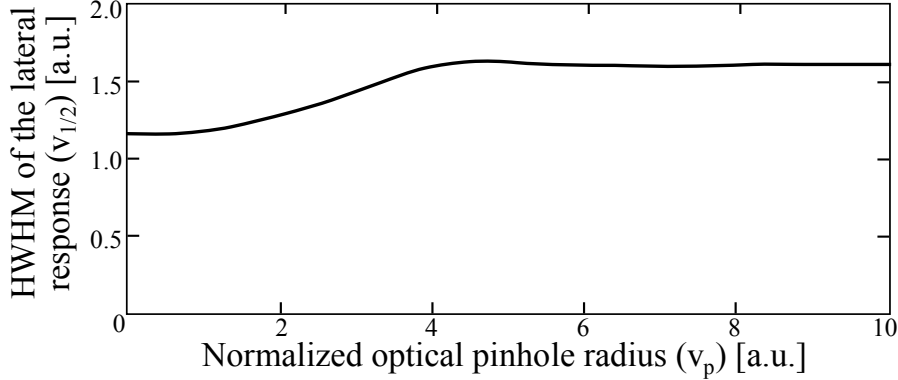


Figure 3.8: The half width of the lateral response ($v_{1/2}$) plotted corresponding to the pinhole radius (v_p) in the normalized optical unit, using eq.(3.4). [After Wilson and Carlini [116].]

resolution in the previous chapter. However, if $v_p = 0$ there will be nearly no light passing through the pinhole. *Therefore, at $v_p = 0.5$ the HWHM ($v_{1/2}$) of the lateral response is just optimized, which leads to the first criterion to determine the pinhole diameter.* Moreover, when the value of v_p is around 4.0 in the normalized unit, the optical lateral resolution will be worse than that in the conventional microscopes [116].

3.3.2 Axial intensity response

Wilson and Carlini [116] also pointed out a significant role of a finite-sized pinhole on the depth-discrimination property. Following their derivations, when a planar reflector being moved axially through focus, the axial response takes the form

$$I_{\text{plane}}(u) = \int_0^{v_p} |h(2u, v)|^2 v \, dv. \quad (3.5)$$

Using eq.(3.5), the axial intensity response can be obtained as a function of the pinhole radius, v_p . The results are depicted in Figure 3.9. The axial response curves are widened as the pinhole radius v_p increases from 0 to 15, shown in Figure 3.9 (a). Then, the HWHM of the axial responses are plotted in Figure 3.9 (b). It can be seen in Figure 3.9 (b) that the optimal HWHM of u is where $v_p \leq 2.5$ to realize best depth discrimination. In theory, if $v_p = 0$, eq.(3.5) reduces to $[\sin(u/2)/(u/2)]^2$ [116], resulting in the highest degree of depth discrimination. However, in practice when the pinhole radius is smaller than 2.5 in the normalized optical unit, the depth-discrimination will not be improved further. Only light passing through the pinhole is reduced. On the contrary, the degree of depth-discrimination is deteriorated when the pinhole radius is higher than 2.5 in the normalized optical unit, resulting in a larger HWHM of u as shown in Figure 3.9 (b).

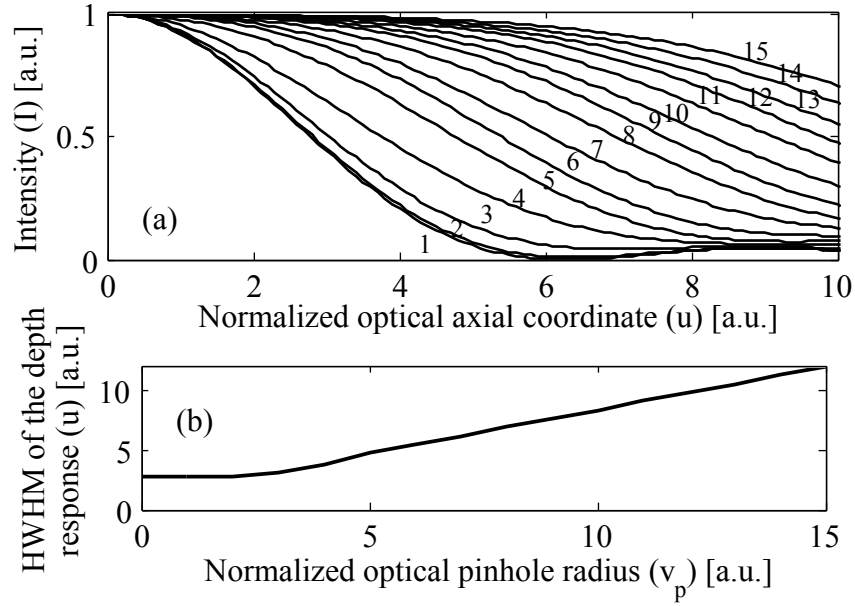


Figure 3.9: The axial responses, or depth responses, with respect to different pinhole radii, obtained using eq.(3.5). (a) The intensity responses plotted against u with various values of the pinhole radii, $v_p = 1, 2, \dots, 15$. (b) The HWHM of the axial responses plotted corresponding to v_p . [After Wilson and Carlini [116].]

In conclusion, the lateral intensity response suggests that the optimal confocal operation can be best obtained when $v_p = 0.5$. However, to gain the optimal *depth discrimination* a recommended value of the pinhole radius is $v_p = 2.5$. In the case of $v_p = 2.5$, there will be no improvement in the optical lateral resolution, but the best optical sectioning can be obtained with 50% more light efficiency [17]. In consequence, this criterion is selected to determine the pinhole diameter in the following section. Note also that the optimized axial-intensity response is the main target in developing the data processing in Chapter 5, and in investigating the system performance in Chapter 6.

3.4 Pinhole mask design

In the CLSS, the geometry of the pinhole aperture and its pattern are designed in order to facilitate the working principle of the CLSS and to achieve the highest degree of depth discrimination.

The equally spaced diffraction foci necessitated for the parallel depth scanning scheme of the CLSS are manifested with the pinhole pattern design in connection with the keystone distortion. Here, the pinholes pattern means an in-line arrangement of the pinholes. Therefore, the newly derived magnification in a tilted plane system, obtained in Appendix D, is applied in this section to facilitate the pin-

hole pattern design. Typically, the pinhole is designed in circular shape having an optimum pinhole diameter. The smaller the pinhole, the optical resolution and depth discrimination are enhanced but that have to be traded off with low light transmission efficiency. Thus, to retain the highest degree of *depth-discrimination* in the CLSS, the pinhole size and shape are optimized as follows.

3.4.1 Pinhole shape

The pinhole can be made in a variety of shapes. As far as they are smaller than the central lobe of the diffraction image at the pinhole mask, the exact shape is not important [53]. Square, hexagonal or octagonal pinholes can be employed [23, 53, 67]. Alternative to the pinhole is a slit aperture. When a higher light transmission is required, a slit is used to replace the pinhole. However, the confocal effect is lost in the directions along the slit [41, 43, 50, 88, 115].

For symmetry reasons, elliptical pinhole apertures are employed in the CLSS to compensate for the tilting effects. The elliptical pinhole at the tilted pinhole mask are designed to have their perspective in circular shape at the normal plane. In consequence, the confocal effect is symmetric about the optical axis. For circular objects such as a point object, the symmetry of the confocal effect about the optical axis is important to resolve a point object evenly in all directions [115].

If the pinhole mask is tilted by Θ degree, an elliptical pinhole is expressed by $b = R$ and $a = R/\cos\Theta$, where R is the radius of the perspective circular-pinhole, depicted in Figure 3.10. a and b are the semi-major and the semi-minor axes of an ellipse, respectively. The ratio of b to a is defined as the eccentricity (e). When the pinhole mask has a higher tilt angle, the eccentricity is increased. The elliptical geometry of the pinhole can then be expressed as a function of the tilt angle of the pinhole mask (Θ) by $b/a = \sqrt{1 - e^2} = \cos\Theta$.

The equation of an ellipse is written as

$$\frac{x^2}{a^2} + \frac{y^2}{b^2} = 1. \quad (3.6)$$

By substituting the semi-major axis, $a = R/\cos\Theta$, and the semi-minor axis, $b = R$, into eq.(3.6), the formula then takes the form: $x^2 \cos^2(\Theta) + y^2 = R^2$.

Proof of the symmetrical confocal effect using an elliptical pinhole

This section verifies using a simulation study that an elliptical pinhole helps to maintain the symmetry of the confocal effect in all directions. In this study, the fast Fourier transform (FFT)⁵ algorithm, which is relatively fast and effective, is used to observe a plane wave propagating through a pinhole aperture at a tilted plane. The diffraction patterns formed by a tilted pinhole aperture are observed

⁵The fast Fourier transform (FFT) is a discrete Fourier transform algorithm which reduces the number of computations needed for N points from $2N^2$ to $2N \cdot \log_2 N$.

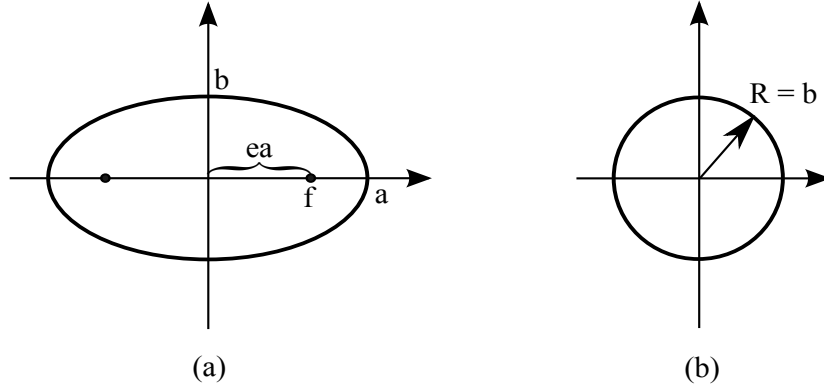


Figure 3.10: Elliptical pinhole aperture and its perspective in circular shape. a is the semi-major axis. b is the semi-minor axis. e is the eccentricity of the ellipse. R is the radius of the perspective circular-pinhole at the plane perpendicular to the optical axis, where Θ is the tilt angle of the pinhole mask and $R = a \cdot \cos(\Theta) = b$.

at a far field image plane normal to the optical axis. Figure 3.11 (a) and (b) show that a circular pinhole worsens the confocal effect in the direction perpendicular to the rotation axis, when tilting the pinhole mask. In contrary, Figure 3.11 (c) and (d) validate that an elliptical pinhole in a tilted plane helps produce symmetry diffraction patterns at the far field image plane. If the far field image plane is the aperture plane of the objective lens, the symmetrical confocal effect is maintained in correspondence to a symmetry diffraction focal point formed by the objective lens. Note that this can be achieved when designing the elliptical pinhole following the previous section.

In order to propagate a tilted plane wave using the FFT technique, the tilted coordinates should initially be transformed into the coordinate of the plane normal to the propagation axis. The tilted plane wave is thus first rotationally transformed in the frequency domain [15]. Then, the diffraction pattern of the tilted input plane wave is observed using diffraction formulas, including *Rayleigh–Sommerfeld diffraction equation* and *Fresnel diffraction equation*. Referring to Figure 3.12, the simulation is implemented as follows.

- The amplitude $U(x, y)$ right behind the plane II is calculated by [106]

$$U(x, y) = T(x, y) \cdot \exp [2\pi j \cdot x \cdot (\cos \theta / \lambda)],$$

where θ is the angle of rotation around the y axis (normal to the paper plane). $T(x, y)$ is a transmittance of the aperture.

- Apply the FFT to the input plane wave $U(x, y)$ which is perpendicular to the optical axis z , by expressing $U(f_x, f_y) = FFT \{U(x, y)\}$. This process is to convert the input plane wave from the spatial domain (x, y) to the frequency domain (f_x, f_y) .

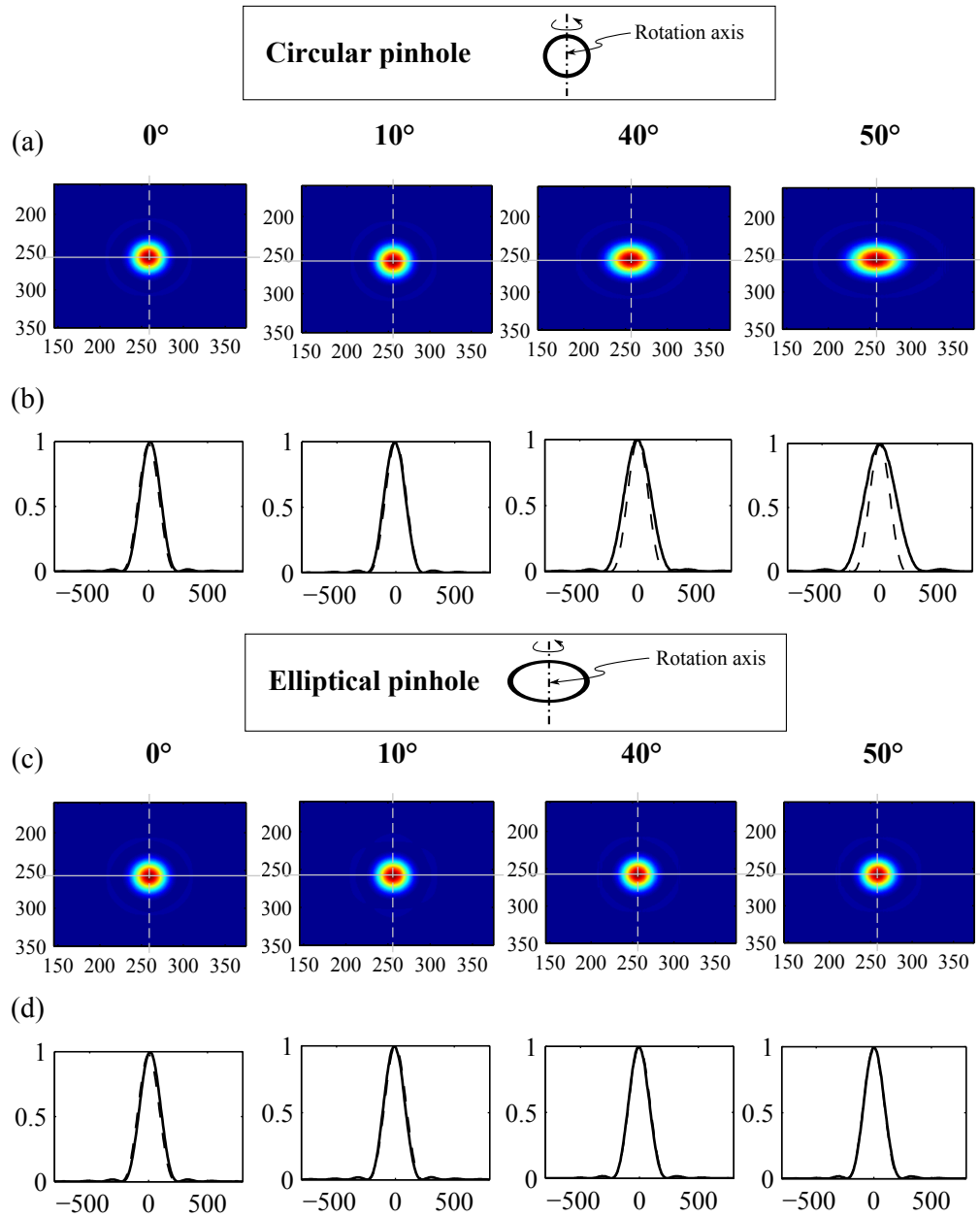


Figure 3.11: The simulation results of a diffraction pattern formed by a pinhole aperture at a far field image plane normal to the optical axis. The diffraction patterns are observed using the fast Fourier transform (FFT) algorithm. This shows that a tilted elliptical pinhole helps maintaining the symmetry of the diffraction pattern when the pinhole mask is tilted up to 50° . In contrary, a tilted circular pinhole results in a worsen confocal effect in the direction perpendicular to the rotation axis, in this particular case. (a) Intensity output and (b) two dimensional diffraction patterns formed by a tilted circular pinhole. (c) Intensity output and (d) two dimensional diffraction patterns formed by a tilted elliptical pinhole.

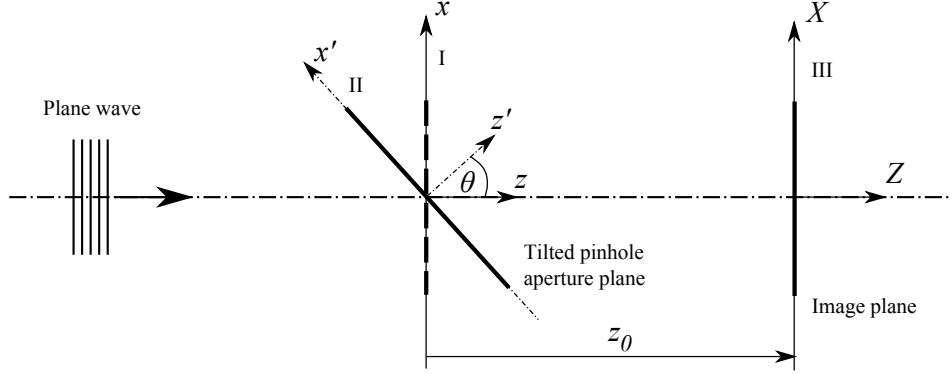


Figure 3.12: A simplified illustration of a tilted plane wave propagation using the FFT technique. The input plane wave is tilted according to the tilted pinhole aperture. Then, it is propagated along the z axis using an interpolation technique and a diffraction equation.

- Perform a rotation transformation. The discrete index of the transformed frequency spectrum is then interpolated using eq.(3.8) in order to sample the frequency spectrum of the plane II to match the spatial sampling interval of the plane I. Here, a linear interpolation is sufficient. When the frequency spectrum is sampled with a constant step equally both in x and y , the FFT algorithm can be used to propagate the transformed plane wave [106]. The frequency shift can also be applied here to center the diffraction pattern [52].
- Apply the inverse FFT to the interpolated plane wave to convert it back from the frequency domain to the spatial domain.
- The interpolated plane wave is then propagated along the z axis using Fresnel diffraction equation in eq.(3.9). Then, a final result of the amplitude and intensity output of the diffraction pattern in the far field is obtained.

Suppose that R is a matrix used to transform the coordinates (x, y, z) into (x', y', z') , where $(x, y, z)^t = R(x', y', z')^t$ and $(f_{x'}, f_{y'}, f_{z'})^t = R(f_x, f_y, f_z)^t$ in the spatial and the frequency domains, respectively. The superscript t denotes the transpose operation. Accordingly, $f_z = (\lambda^{-2} - f_x^2 - f_y^2)^{1/2}$ [27].

In consequence, the transformation matrix used to rotate the coordinates about the y axis at the angle of θ is given by

$$R = \begin{bmatrix} \cos \theta & 0 & \sin \theta \\ 0 & 1 & 0 \\ -\sin \theta & 0 & \cos \theta \end{bmatrix}. \quad (3.7)$$

As a result, a rotation formula in the frequency domain is obtained as $f_{x'} = f_x \cdot \cos \theta + f_z \cdot \sin \theta$.

Following Tommasi and Bianco [106], the index (i) of the frequency spectrum in the x axis is interpolated as a function of the indices of the frequency spectrum

in the x' and y' axes (ii and jj) by

$$i = \cos \theta \cdot ii + \sin \theta \left(\frac{D^2}{\lambda^2} - ii^2 - jj^2 \right)^{1/2}, \quad (3.8)$$

where i, ii , and $jj = [N/2, -N/2]$ and a matrix $N \times N$ is considered. D is the actual size (in a length unit) of a square transmittance window. In the case that the pinhole mask is rotated about the y axis, merely the index in the x coordinate needs be interpolated.

The *Fresnel diffraction equation* is then expressed by [33]

$$U(X, Y) = FFT \left\{ U(x, y) \cdot \exp \left(\frac{jk}{2z_0} (x^2 + y^2) \right) \right\}. \quad (3.9)$$

3.4.2 Pinhole size

The size of the pinhole plays a significant role in determining the optical resolution and depth-discrimination property, namely *confocality*, in a confocal imaging system. From a theoretical point of view, the smaller the pinhole, the higher the confocality is. Though a larger pinhole can transmit more light, it will degrade the optical resolution and depth-discrimination. Additionally, when the pinhole is smaller than a certain limit, the optical resolution and depth-discrimination will not be further enhanced; only the transmission of light is reduced.

Wilson and Carlini [116, 114] had suggested that the pinhole should be designed at $v = 2.5$, where v represents the normalized lateral optical coordinate, described in the previous section. If $v = 2.5$, the highest degree of depth-discrimination is obtained as the HWHM of the axial response curve becomes the narrowest. By substituting $v = 2.5$ and $NA = \sin \alpha$ in eq.(3.2), the suggested pinhole radius at the pinhole mask plane is

$$R \approx (0.4\lambda/NA) \cdot M, \quad (3.10)$$

where M is the magnification ratio from the focal plane to the pinhole mask plane.

As an alternative approach, the size of the pinhole can be defined using the *full width at half maximum* of the *Airy disk* pattern [33]. The Airy disk is the diffraction pattern formed by a perfect circular lens with an ideal point source.

In the CLSS, the wavelength of the illumination light (λ) is 530 nm, the numerical aperture of the objective lens (NA) is 0.45, and the magnification ratio from the focal plane to the pinhole mask plane (M) is $12\times$. Since the pinhole aperture in the tilted pinhole mask is designed to project an effective circular pinhole to the plane normal to the optical axis, the radius of the effective circular pinhole (R) is then defined based on the Airy disk radius and the FWHM:

Definition	Formula	Pinhole Radius (μm)
Airy disk radius	$R = (0.61\lambda/NA) \cdot M$	8.125
FWHM conventional microscopy	$R = (0.514\lambda/NA) \cdot M$	6.846
FWHM confocal microscopy	$R = (0.37\lambda/NA) \cdot M$	4.928

The expression of the FWHM in confocal microscopy approach provides similar result to eq.(3.10). If the pinhole is designed using this formula, depth discrimination will be best obtained. Nevertheless, the pinholes were fabricated in various sizes following all definitions above, to be investigated in experiments. It was found that a pinhole of $R = (0.37\lambda/\text{NA}) \cdot M$ is the best candidate. *In conclusion, the effective pinhole radius should be designed at thirty three percent less than the Airy disk radius imaged at the pinhole mask.*

3.4.3 Pinholes pattern

As already mentioned, the main purpose for designing the pinhole pattern is to obtain equally spaced foci (Δx and Δz) at the tilted focal plane in order to manifest the new parallel depth scanning scheme of the CLSS, as illustrated in Figure 3.1 and Figure 3.2. In the presence of the keystone distortion, the in-line pinholes are non-uniformly spaced with advancing interval ($\Delta x'_p$ and $\Delta z'_p$) to form equally spaced foci. In addition, the pinhole images at the detector are also non-uniformly spaced ($\Delta x''_p$ and $\Delta z''_p$), due to the keystone distortion. Generally, the space between the pinholes is optimally defined by 10 times the pinhole diameter [114], to avoid the crosstalk between the neighboring pinholes.

Here, two approaches are derived to outline the pinhole pattern: *Geometry approach* and *Gaussian lens equation approach*. The Geometry approach is relatively direct but the calculation is laborious, as presented in Appendix C. This approach has no analytical solution, so its applicability is limited to some extent. Alternative to the Geometry approach, the Gaussian lens equation approach is more versatile and compact, having an analytical solution. To facilitate the calculation of the pinhole coordinate, the magnification is particularly derived in terms of the tilted plane coordinates, demonstrated in Appendix D.

In this section, the coordinates of the in-line pinholes are calculated using the derived magnification.

Axial measurement range and the field-of-view

First, the relation of the *axial measurement range* (AMR) and the *field of view* (FOV) is presented, referring to Figure 3.13. Following the law of trigonometry, the relation of the tilt angles of the focal plane (Φ) and the pinhole mask plane (Θ) is given by

$$\tan(\Phi) = \frac{\tan(\Theta)}{m_0}. \quad (3.11)$$

The AMR and FOV then take the form:

$$\text{AMR} = L \cdot \sin(\Phi), \quad (3.12)$$

and

$$\text{FOV} = L \cdot \cos(\Phi), \quad (3.13)$$

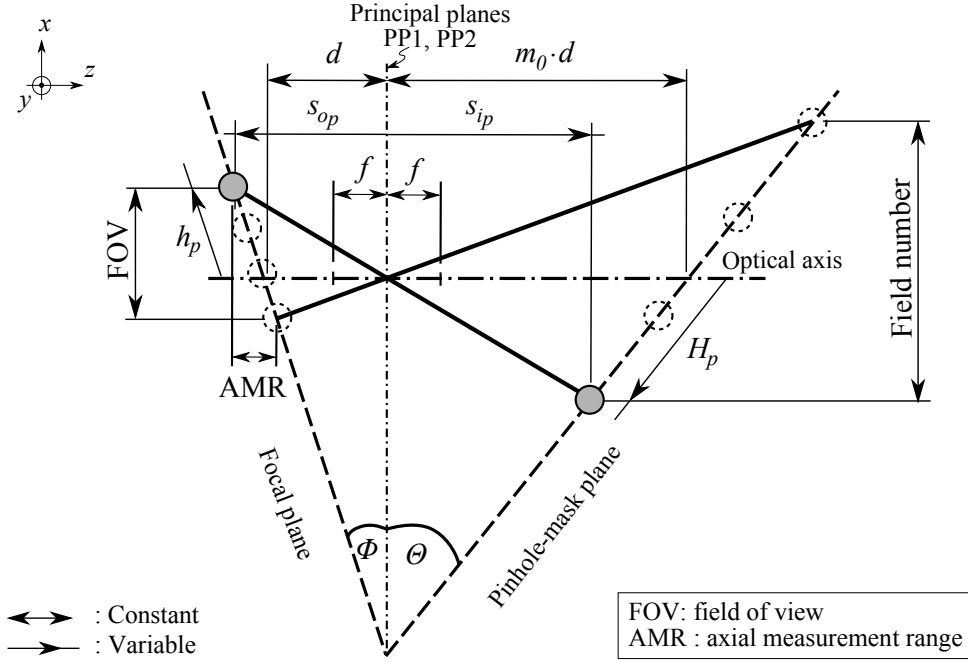


Figure 3.13: Schematic illustration of the Gaussian lens equation approach to calculate the pinhole coordinate. Φ is the tilt angle of the focal plane. Θ denotes the tilt angle of the pinhole-mask plane. d is the focal length of the microscope objective. m_0 represents the lateral magnification on the optical axis. f is the effective focal length of the optical system. s_{op} is the object distance with respect to the first principal plane (PP1). s_{ip} is the image distance with respect to the second principal plane (PP2). h_p is the focal coordinate along the tilted focal line. H_p is the pinhole coordinate, where $p = 1, 2, \dots, n$ are the indices of the pinhole-focus pairs.

where L is the length of the focal line per FOV at the tilted focal plane.

In the CLSS, the AMR is constrained mainly by the tilt angle of the focal plane (Φ) and the magnification of the imaging lens, whereas the FOV is limited by the field number of the optical system, shown in Figure 3.13. In this case, the field number is 22 mm in diameter. The length of the focal line (L) is then calculated as a function of the field number. In consequence, the AMR and the FOV can be obtained.

The AMR calculated with various values of the magnification and the tilt angle of the pinhole mask is presented in Figure 3.14. It can be seen that the AMR can be extended by increasing the tilt angle of the pinhole mask (Θ) thereby increasing the tilt angle of the focal plane (Φ), or by reducing the magnification (m_0). When the magnification is higher than $12\times$, it is difficult to realize a higher AMR, as illustrated in Figure 3.14. Moreover, with a magnification higher than $20\times$, the focal plane formed at a high tilt angle cannot easily be achieved by just increasing the tilt angle of the pinhole mask, illustrated in Figure 3.15.

As a result, $12\times$ magnification is applied in the CLSS setup to gain an ac-

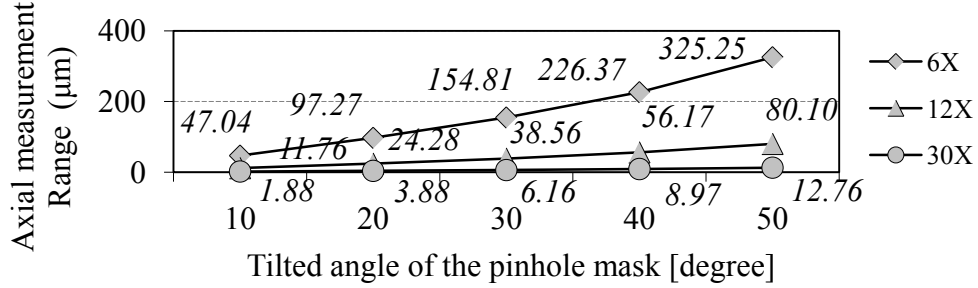


Figure 3.14: Distribution of the axial measurement range (AMR) calculated as a function of the tilt angle of the pinhole mask (Θ) and the magnification ratio from the focal plane to the pinhole mask, including 1:6, 1:12, and 1:30.

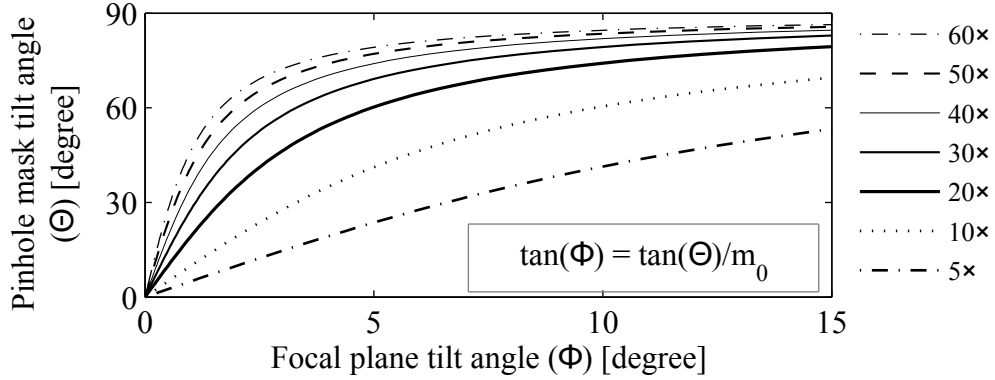


Figure 3.15: Distribution of the tilt angle of the pinhole mask (Θ) as a function of the tilt angle of the focal plane (Φ) and the imaging magnification (m_0), where $m_0 = 5\times, 10\times, \dots, 60\times$.

ceptable AMR at the highest possible tilt angle of the pinhole mask. However, a $12\times$ objective lens is not available as a standard product; therefore, the $12\times$ magnification is accomplished using a $20\times$ objective lens. Thus, $20\times$ infinity-corrected microscope objectives with 0.45 NA and 0.6 NA are used to magnify or demagnify at $12\times$. For this reason, the axial measurement range obtained in the CLSS is $50\ \mu\text{m}$. A higher magnifying objective lens can be employed as well, but that leads to a drastic reduction in the axial measurement range. On the contrary, a lower magnifying objective lens usually designed at lower NA leads to the optical resolution worse than that of 0.45 NA or higher NA objectives. Therefore, if a higher NA objective lens designed at low magnification is available, it will be a preferable choice. In addition, by tilting the pinhole mask too high to extend the axial measurement range, the light output will be reduced non-uniformly across the focal line. In general, the AMR targeting from a hundred micrometers to a few millimeters can cover a wide field of applications for the surface inspection.

Pinhole coordinate

Now, the coordinates of the in-line pinholes are calculated using the derived magnification based on the Gaussian lens equation approach, demonstrated in Appendix D. The schematic illustration of the calculation is depicted in Figure 3.13. Following the derivation in Appendix D, the lateral magnification (m_{x_p}) at the tilted pinhole mask plane is expressed as a function of the x coordinate by

$$m_{x_p} = m_{y_p} = \frac{s_{i_p}}{s_{o_p} - h_p (1 + m_0) \sin(\Phi)}. \quad (3.14)$$

In this expression, s_{i_p} is the image distance with respect to the second principal plane (PP2), and s_{o_p} is the object distance with respect to the first principal plane (PP1). The axial magnification (m_{z_p}) in terms of m_{x_p} is obtained as

$$m_{z_p} = -m_{x_p}^2. \quad (3.15)$$

Finally, the pinhole coordinate (H_p) as a function of h_p , m_{x_p} , m_0 , and Φ is given by

$$H_p = h_p \cdot m_{x_p} \sqrt{\cos^2(\Phi) + m_0^2 \sin^2(\Phi)}. \quad (3.16)$$

This formula is relatively compact and feasible. It provides a direct expression of the pinhole coordinate (H_p) as a function of the sampling-focal coordinate (h_p), and the tilt angle of the pinhole mask (Φ). Note that the keystone distortion is already accounted for in terms of the lateral magnification (m_{x_p}).

Moreover, based on both theoretical and experimental results of Fewer *et al.* [23], it is possible to reduce the pinhole space from ten times to five times the pinhole diameter. However, the crosstalk between pinholes can be drastically increased. In confocal microscopy, crosstalk means the overlapping of the sidelobes of the diffraction patterns from the neighboring pinholes. Nevertheless, only two neighboring pinholes in the CLSS can contribute to the crosstalk. Thus, it is reasonable to define the pinhole space eight times the pinhole diameter. The experiments proved that this pinhole space is sufficient. In consequence, 160 sampling points per full line of scan are formed in the CLSS. The pattern of an in-line pinholes is then depicted in Figure 3.16.

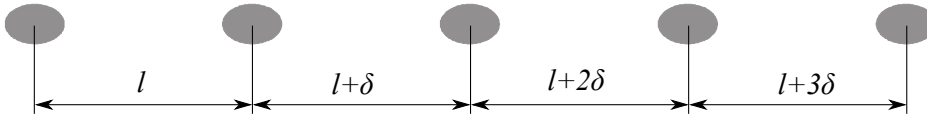


Figure 3.16: The pattern of an in-line elliptical pinholes. The pinholes are linearly spaced with advancing interval, where $\Delta H_p \approx l + n\delta$ and $n = 1, 2, \dots, n$.

3.5 Imaging characteristics of the CLSS

This section attempts to investigate the imaging characteristics of the CLSS. Apart from the tilting effects, the imaging characteristics of the CLSS is similar to that of a confocal imaging system. In a tilted plane system, the *keystone distortion* is basically introduced at the tilted image plane, where the magnification varies across the image field. However, the keystone distortion supposes to cause no effect either on the imaging quality or on the optical lateral resolution. The theoretical explanation and the simulation study are given here to explore the effect of the keystone distortion on the imaging quality of the CLSS.

Therefore, this section begins with the theoretical explanation of the aberrations in connection with the axial response. Then, the effect of the optical aberrations mainly the keystone distortion on the imaging quality is described. Finally, the simulation study is presented. The simulation is divided into two parts: *the imaging part* and *the detecting part*, in order to point out where the thickness of the tilted quartz substrate of the pinhole mask plays an important role.

3.5.1 The effect of aberrations on the axial response

To account for the aberrations in theory, the pupil function⁶ is given by [17]

$$P(r, \phi) = \exp 2j\pi (a \cdot r^4 + b \cdot r^3 \cos \phi + c \cdot r^2 \cos^2 \phi), \quad (3.17)$$

where r is the radial distance at the pupil plane referenced from the optical axis, a , b , and c are the *Seidel coefficients* of spherical aberration, primary coma, and primary astigmatism, respectively [7, 117]. Moreover, ϕ denotes the angle of rotation around the optical axis. The spherical aberration term essentially affects the symmetry of the axial response curve, whereas the other terms can affect its width [17]. For an aberration-free system, the pupil function $P(r, \phi)$ is constant, in which case the axial response can be derived analytically [114]. Following Maréchal, a well corrected optical system should have the wave-front error less than one fourteenth of the wavelength of light ($\lambda/14$) in the *root-mean-square* value [8].

The axial response of a perfect reflector in a confocal imaging system satisfying the sine condition can be expressed as [86]

$$I(z) = \left| \int_0^\alpha R(\theta) P^2(\theta) \exp(-j2k \cdot z \cos \theta) \sin \theta \cos \theta \, d\theta \right|^2, \quad (3.18)$$

where θ is the angle of convergence of a ray, and α and $P(\theta)$ are the maximum half-angular aperture and the pupil function of the lens, respectively. Then, $R(\theta)$ is the reflection coefficient of the object, which is equal to unity when the object is a perfect reflector. Here $k = 2\pi/\lambda$, where λ is the wavelength of the illumination light.

⁶The pupil function contributes to the physical extent of the lens and its transmissivity [114], in which the aberrations and defocus effect can be added as a complex function here.

In addition, Corle et al. [16] had suggested a convenient way to model spherical aberration, using a trial apodization function of the form

$$\begin{aligned} P(\theta) &= \exp(A \sin^2 \theta) \exp(-jB \sin^4 \theta) & (\theta < \alpha), \\ P(\theta) &= 0 & (\theta > \alpha), \end{aligned} \quad (3.19)$$

where A is an amplitude coefficient, and B is related to the Seidel coefficient of spherical aberration with respect to the defocus distance (z). Different values of A and B can be specified, and the results of the axial response are depicted in Figure 3.17. This demonstrates that the term $\sin^2(\theta)$ yields a broader axial response while the term $\sin^4(\theta)$ introduces asymmetry and shift to the response. Unwanted effects caused by the aberrations will mainly reduce the accuracy of depth discrimination and surface height evaluation of the CLSS later on.

Although spherical aberration⁷ in a tilted plane system of the CLSS should be less significant as compared to keystone distortion, spherical aberration is basically introduced by the tube length mismatch between the objective and the tube lens and the refractive index mismatch between the sample and the medium.

3.5.2 Keystone distortion and the imaging quality

It was concluded by Born and Wolf [8] that two of the five Seidel aberrations, *field curvature* and *distortion*, do not affect the structure of the three-dimensional diffraction pattern. Only the position of the diffraction pattern shifts from the ideal case, such that merely the position and form of the image is distorted. This means that the sharpness of the image, or the *imaging quality*, is not deteriorated by these two aberrations.

Theoretically, the wave-front deformation represents the aberrations of the form

$$\Phi = A' \cdot r^n \cdot \cos^m \phi, \quad (3.20)$$

where r is the radial distance referenced from the optical axis, and ϕ denotes the angle of rotation at the pupil plane around the optical axis. In eq.(3.20), A' is the coefficients expressed in the power series representation as a function of the Zernike's circle polynomials [8].

In particular, the distortion is written as

$$\Phi_{distortion} = A'_{111} \cdot r \cdot \cos \phi, \quad (3.21)$$

where A'_{111} is the coefficient in the wavelength unit as a function of the displacement coordinate and the Seidel coefficient of distortion. As concluded by Born and

⁷The spherical aberration arises from light from different zones focusing at different axial positions. With spherical aberration, an asymmetry of the axial response is introduced resulting in strong sidelobes on one side of the origin and weak ones on the other [91]. Sheppard et al. [92] also noted that the spherical aberration increases with the higher radius of the aperture of the imaging lens, so that the effect of the aberration can become less strong if the aperture of the lenses is slightly reduced.

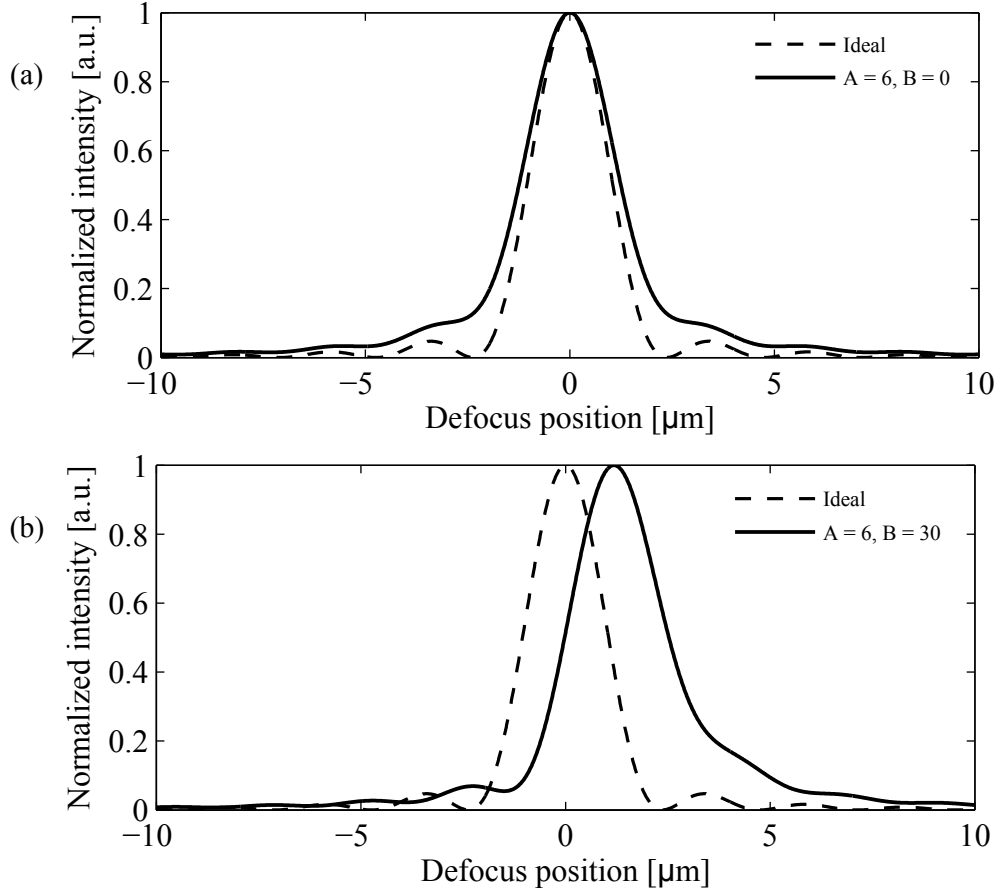


Figure 3.17: Unwanted effects of the aberrations in the axial responses, theoretically obtained using the weighted $P(\theta)$ in eq.(3.19) and eq.(3.18). A $20\times/0.45\text{NA}$ objective is applied in this case at $\lambda = 530$ nm. (a) $A = 6$ and $B = 0$. (b) $A = 6$ and $B = 30$.

Wolf [8], the first degree of r in this formula causes only the shift in the diffraction pattern, not the change in its quality. Moreover, the keystone distortion⁸ is given as a function of the first degree of r by [79]

$$\Phi_{keystone} = A_{keystone} \cdot r \cdot \cos \varphi \cdot \cos \gamma, \quad (3.22)$$

where φ is the angle between the wave field and pupil vector, and γ is the angle between the symmetry unit vector and the pupil vector. Following the same conclusion, the first degree of r in the keystone distortion expression will not affect the imaging quality of the CLSS.

⁸In eq.(3.22), $A_{keystone} = W_{21110}H^2$ is the keystone distortion coefficient as a function of the wave field coordinate (H). This representation was developed by Sasian [79] to represent the aberration function of the tilt in terms of the wavefront deformation across the field of view and across the exit pupil of the optical system.

3.5.3 The effect of the tilted pinhole mask on the imaging part

To prove that the imaging quality of the CLSS is not affected by the *keystone distortion*, the simulation results are presented in this section. Only the imaging part is investigated in this section. The imaging part is the optical part in which light is illuminated from the pinhole mask to the specimen. The illustration of the optical layout is shown in Figure 3.18, which includes a field lens, a tube lens, and an objective lens.

The quartz thickness can be excluded here, since the pinholes function as multiple point-like sources after light passing through the quartz substrate. Note that the pinhole apertures are fabricated on a chrome film laminated on one side of the quartz substrate. In this simulation, perfect lenses are employed in order to eliminate the aberrations caused by the lens. Therefore, only the aberrations introduced by the tilted pinhole mask is realized. A widely used optical design software Zemax is employed to obtain the simulation results.

The simulation results are then depicted in Figure 3.19. It can be concluded from these results that the diffraction pattern formed at the tilted focal plane is not degraded by the tilt of the pinhole mask, even up to 50° of tilt angle. Figure 3.19 (b) shows that the FWHM of the lateral intensity response is widened by only 2% when the pinhole mask tilts from 10° to 50° , in which case the numerical aperture of the imaging lens is 0.45. The strehl ratio of the intensity is about unity in all cases, showing negligible aberrations in the imaging part. By definition, the strehl ratio, ranging from zero (for a system having significant aberration) to one (for a perfect system), is the ratio of the maximum intensity of an aberrated pattern to the maximum intensity of an unaberrated pattern [33].

Nevertheless, Figure 3.19 (a) illustrates that the tilted pinhole mask introduces distortion, corresponding to various numerical apertures and off-axis pinhole positions at 5 mm and 10 mm from the optical axis. The distortion increases when the pinhole mask is tilted by a higher tilt angle. As a result, only the keystone distortion is seen at the tilted focal plane.

3.5.4 The effect of tilted quartz on the detection part

In the CLSS setup, a 0.25 NA camera lens is used to focus light to the detector. Therefore, a 0.25 NA lens is then modeled. The detection part is the part in which light passes through the pinhole mask to the detector. Figure 3.20 illustrates the optical layout of the detection part. In this simulation, the reflected light returns the same path from the specimen through the same set of pinholes and passes to the detector, at which point the tilted glass introduces aberrations. Then, the changing of the image quality can be observed at the tilted detector plane.

Theoretically, astigmatism is always introduced when light focuses through a tilted glass [24]. The quartz substrate of the pinhole mask will definitely affect

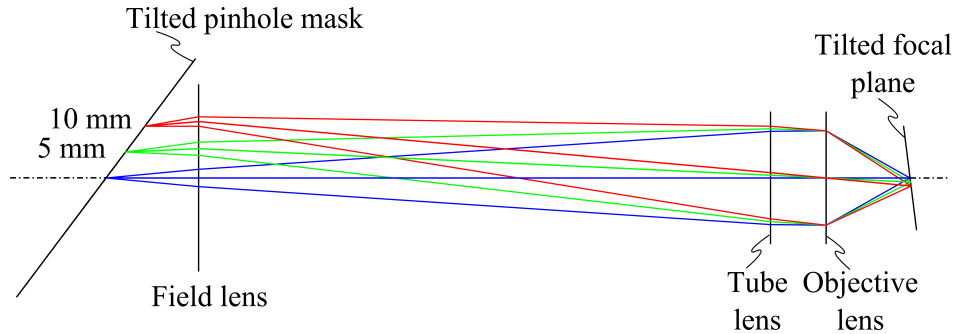


Figure 3.18: Simulation layout of the imaging part in the CLSS, including a field lens, a tube lens and an objective lens but excluding the quartz thickness. The simulation was implemented using Zemax.

the image quality at the detector. Therefore, this section contributes mainly to investigate the aberrations caused by the tilted quartz on the image at the detector.

Table 3.1 summarizes the simulation results. The wavefront errors in accordance with the tilt angle of the quartz substrate of the pinhole mask are presented. The RMS wavefront errors increase with a higher tilt angle of the tilted quartz. Accordingly, the Strehl ratio is severely degraded. The changes of the modulation transfer function (MTF) and the Strehl ratio of the lateral intensity responses are manifested in Figure 3.21. It shows that the intensity signal is almost lost at a higher than 40° tilt angle, as indicated by extremely low Strehl ratio.

As a consequence, the pinhole images at the tilted detector plane are degraded and enlarged with respect to a higher tilt angle of the pinhole mask, illustrated by the spot diagram in Figure 3.22 (a). In addition, the Ray fan pattern in Figure 3.22 (b) shows that the aberrations introduced by the tilted quartz substrate are dominated by astigmatism and coma. Black circles in Figure 3.22 (a) represent the Airy pattern of $2.6 \mu\text{m}$ in diameter. However, the total intensity captured by the CCD is more meaningful than the shape of the pinhole images. When the pixel size of the detector is about $6 - 8 \mu\text{m}$, the worst case of the pinhole image is then covered by 1 – 2 pixels.

In conclusion, the simulation shows that the tilted quartz substrate introduces primarily the keystone distortion, astigmatism, coma, and a lower degree of the field curvature and spherical aberration. The variation of the field curvature and distortion as a function of the tilt angle of the pinhole mask is depicted in Figure 3.23. Although the image quality at the tilted detector is seriously degraded at a high tilt angle of the pinhole mask, the imaging quality at the tilted focal plane is not affected. In consequence, in the following section the experimental results of the axial response are used to confirm that the tilted quartz substrate causes insignificant effect on the measuring quality of the CLSS, when applying with a $20\times/0.45$ NA objective. This allows the CLSS to operate using the pinhole mask tilted up to 40° .

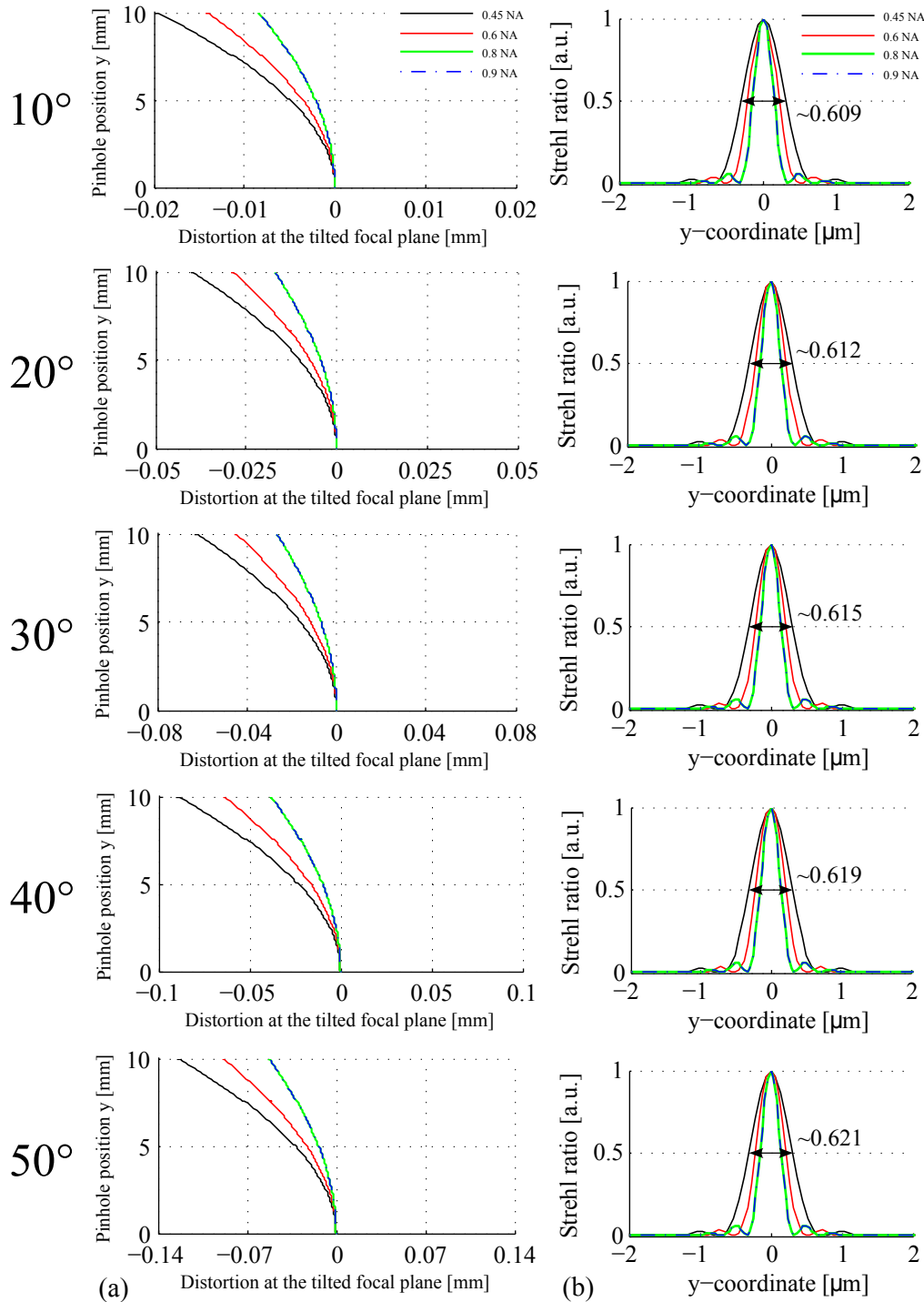


Figure 3.19: (a) Distortion, and (b) Huygens PSF strehl as a function of the tilt angle of the pinhole mask, simulated using ZEMAX.

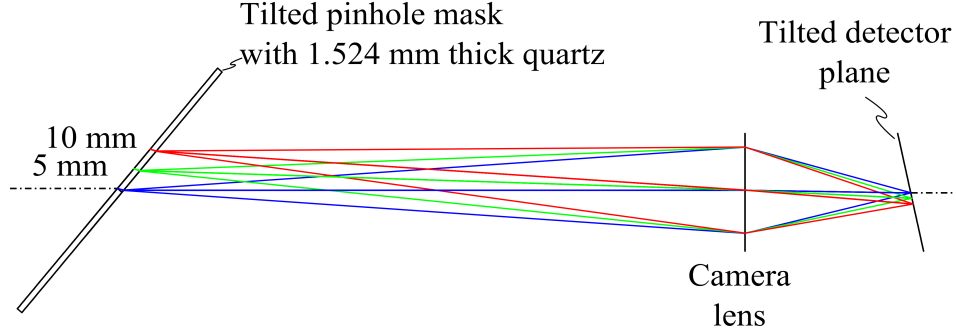


Figure 3.20: Simulation layout of the detection part in the CLSS. The effect of the quartz substrate with 1.524 mm thickness is investigated using Zemax.

Table 3.1: Wavefront error caused by the tilted quartz substrate of the pinhole mask. The RMS* represents the wavefront error in terms of the *root mean square* of the optical path difference after subtracting out the piston distortion. The Strehl ratio** is calculated from the wavefront variance.

Tilt angle of the pinhole mask (degree)	Wavefront error RMS* (wavelength)	Strehl ratio**
0	0.00719781	0.99846975
10	0.01133883	0.99654907
20	0.04890870	0.91994841
30	0.12212375	0.57141428
40	0.24915165	0.00000000
50	0.43815624	0.00000000

3.5.5 Axial response in the CLSS

As stated above, the aberrations can degrade the axial intensity response and then the imaging quality of the CLSS i.e. by widening the axial intensity-response curve and introducing sidelobes and asymmetry to the curve. Figure 3.24 then delineates the axial intensity responses obtained with the CLSS, using a planar reflector. It can be seen that the axial responses are rather symmetric having low sidelobes with a few degree of noise floor, as compared to the ideal case.

The FWHM of the measured axial responses varies from $3.5 \mu\text{m}$ to $3.7 \mu\text{m}$, which obtain on the optical axis and off the optical axis, respectively. The axial responses across the focal line are rather uniform, having approximately 10% reduction in the normalized intensity. Though the FWHM in the ideal case is $2.3 \mu\text{m}$, where $\text{NA} = 0.45$ and $\lambda = 530 \text{ nm}$, these symmetry axial intensity responses having exceptionally low sidelobes conclude that the aberrations introduced by

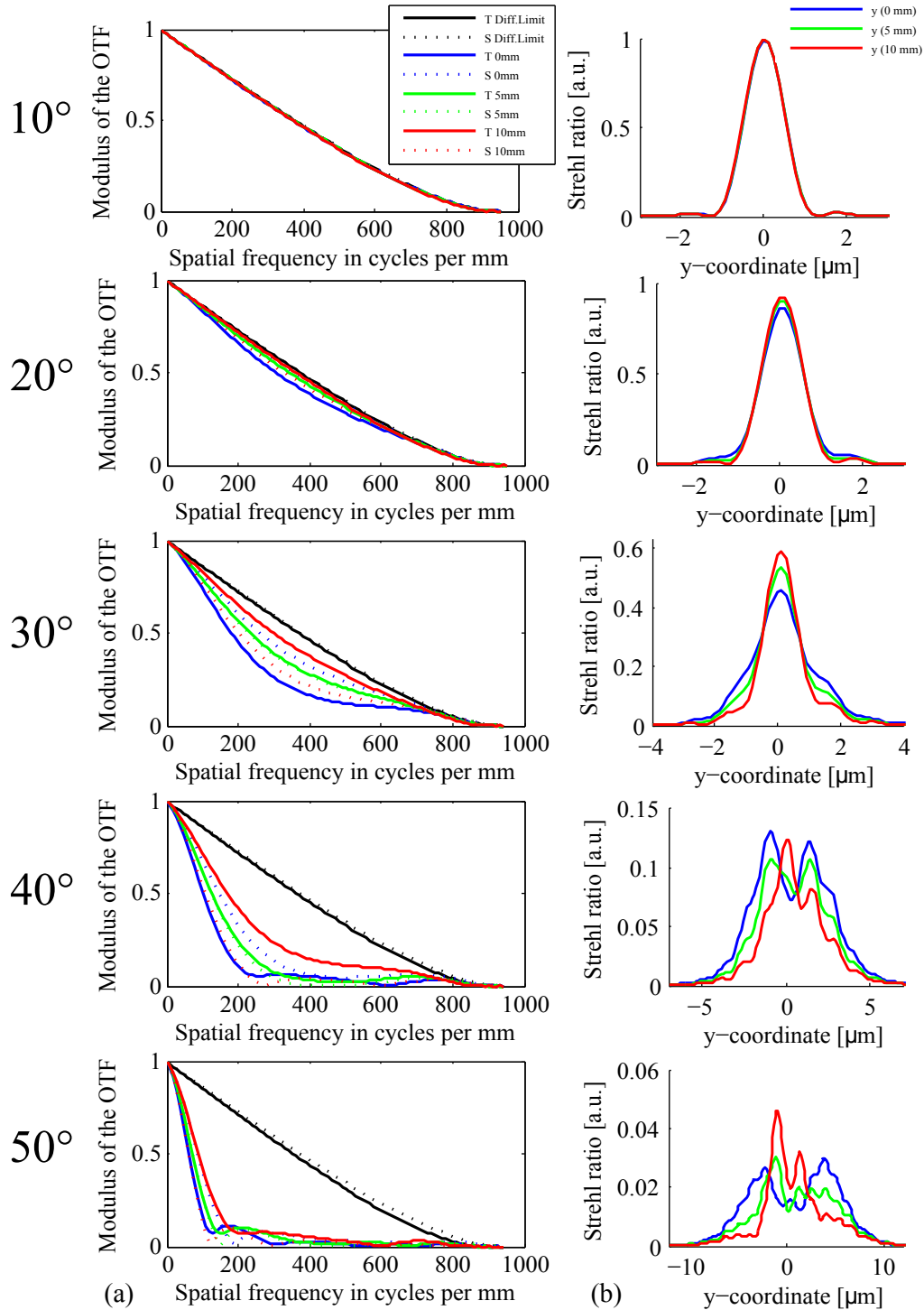


Figure 3.21: (a) MTF, (b) Strehl ratio of the PSF at the detector as a function of the tilt angle of the quartz substrate having 1.524 mm thickness, simulated using ZEMAX.

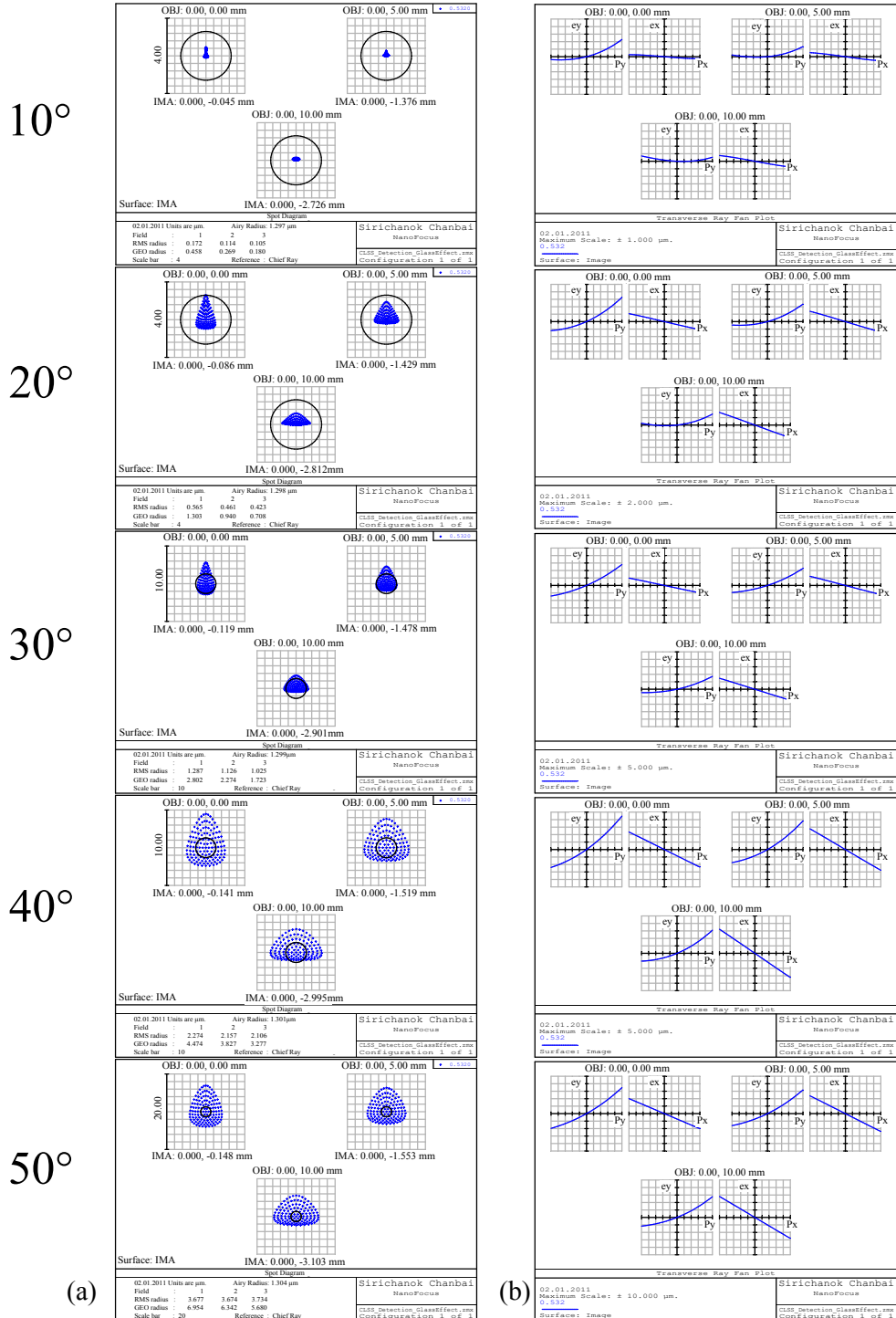


Figure 3.22: (a) Spot diagram, and (b) Ray fan at the detector as a function of the tilt angle of the quartz substrate having 1.524 mm thickness, simulated using ZEMAX.

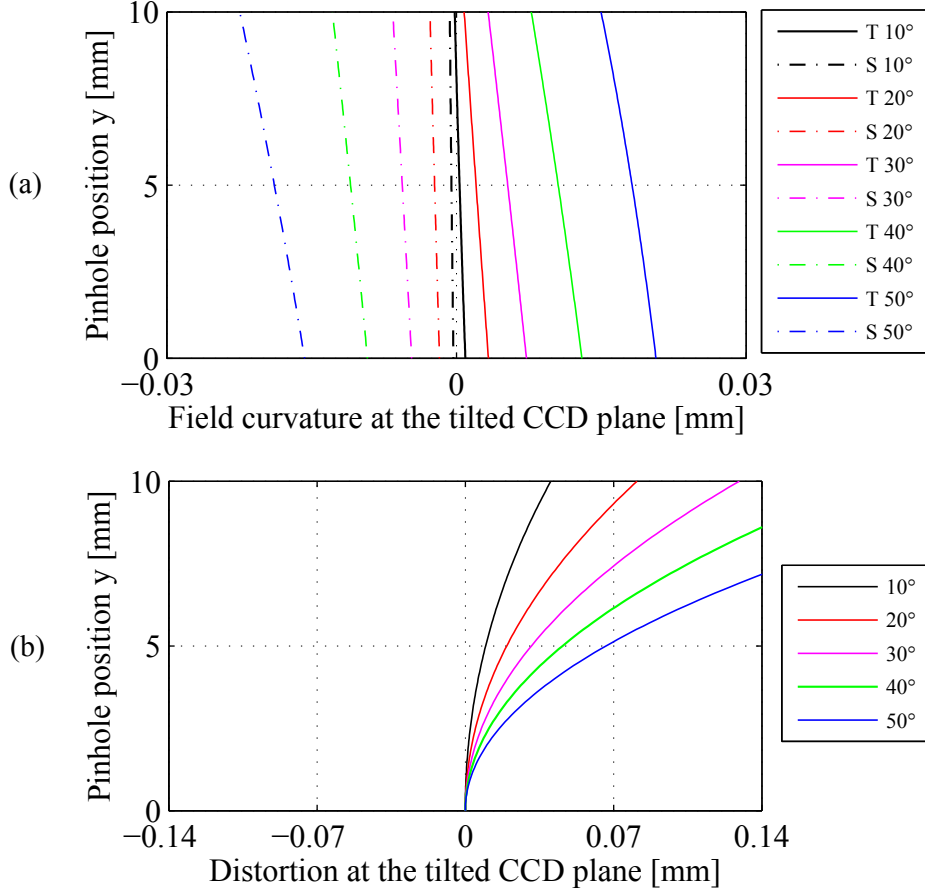


Figure 3.23: (a) Field curvature, (b) Distortion at the tilted detector plane or CCD, as a function of the tilt angle of the quartz substrate having 1.524 mm thickness, simulated using ZEMAX.

the tilted quartz substrate play insignificant role in the measuring quality of the CLSS. As the pinhole aperture is optimally designed to reach the axial intensity response in the ideal case, the widening of the axial response curves is not caused by the finite-sized pinhole, however, rather by the residual aberrations such as spherical, astigmatism and coma. This issue can further be investigated using eq.(3.17) and eq.(3.18) and some notes on the measured axial intensity responses given in Chapter 6.

As far as the axial intensity responses deliver true information of the surface heights, the CCD is used merely to record the intensity of the pinhole images not to image the specimen. The residual aberrations including that introduced by the tilted quartz substrate will just reduce the power of the light output at the detector, and so the sensitivity of the measurement. Therefore, the correction of

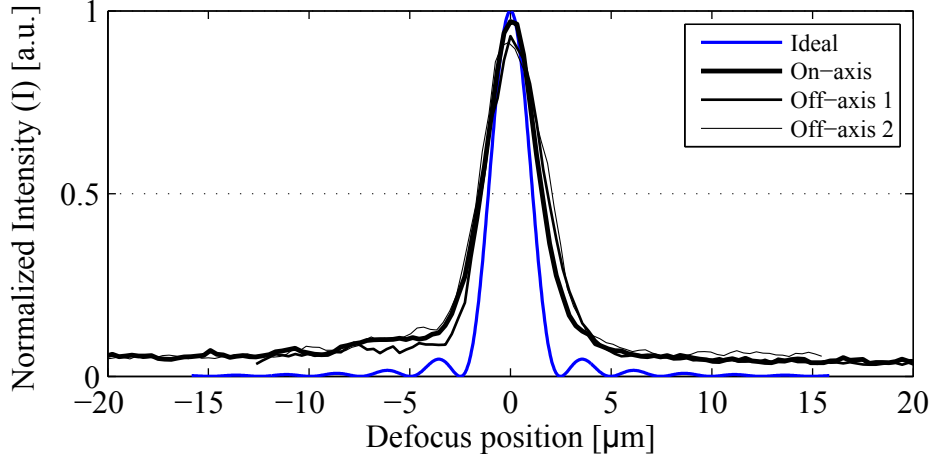


Figure 3.24: Axial responses experimentally obtained with a plane reflector using the CLSS. The responses obtained on the optical axis and off the optical axis across the focal line are in good agreement. As compared to the ideal case of the axial response, these measured axial responses with minimum aberrations show that the tilted quartz substrate should not affect the measuring quality of the CLSS.

the residual aberrations will then improve the sensitivity of the measurement.

3.6 Conclusion

A stationary tilted pinhole-mask used in the CLSS is a key component to help manifesting the new parallel depth scanning scheme [12, 14, 15], and to preserve the property of the *depth-discrimination*. A stack of equally spaced foci projected at different depths on the specimen is vital to create a parallel depth scan without the need to mechanically or optically scan the sampling points in the axial direction. A major advantage of the CLSS, developed as a 2D optical profiler, is a simplified and robust configuration, in which case no moving part is required. A $20\times/0.45$ NA objective used in the CLSS at the wavelength of 530 nm provides the lateral optical resolution of $0.44\ \mu\text{m}$ and the axial optical resolution of $2.3\ \mu\text{m}$.

In the CLSS, an optimal operating condition is when the pinhole mask is tilted by 40° from the plane normal to the optical axis, where the focal sampling intervals of $\Delta x = 5\ \mu\text{m}$ and $\Delta z = 0.3\ \mu\text{m}$ are established. The disadvantage of the CLSS is the limit in the axial measurement range of $50\ \mu\text{m}$, whereas the lateral measurement range can be implemented covering up to 15 mm. On the other hand, the CLSS configuration provides a good start for further developments of a low cost or a high speed instrument for surface inspection. Moreover, a unique working principle of the CLSS allows the data to be recorded in non-sequential order in respect to the sampling coordinates to extend the lateral measurement

range, theoretically, up to infinity. Accordingly, the data sorting and the additional data processing are developed in Chapter 5 to support the new concept.

The CLSS is developed by incorporating a tilted plane technique in a confocal imaging system, where the Scheimpflug's rule is applied with a confocal imaging system. The variation of the magnification inherent in a tilted plane system, known as the *keystone distortion*, is theoretically explained in this chapter. In consequence, a newly discovered approach for predicting and correcting for the keystone distortion is established. It was found that the shifting of the principal planes in a compound lens system can modify the pattern of the keystone distortion or even correct for it. Three significant cases of the keystone distortion are classified as *direct keystone distortion*, *reverse keystone distortion*, and *corrected keystone distortion*. The reverse keystone distortion is employed in the CLSS, whereas the corrected keystone distortion is noted as a useful case in extending the surface inspection technique to three-dimensions by using parallel tilted focal lines instead of a tilted focal line.

The pinhole shape and size are optimized for depth discrimination. It was concluded by McCarthy et al. [53] that the pinhole shape can be in any form, as long as the pinhole is smaller than the central lobe of the diffraction image. In addition, Wilson and Carlini [116, 115] had suggested that the pinhole radius should be designed at 33 % less than the radius of the Airy disk imaged at the pinhole mask. Following this suggestion, the pinholes used in the CLSS are also designed in elliptical shape to compensate for the tilting effects having their perspective at the normal plane in circular shape, such that the confocal effect is uniformly maintained in all directions. Then, the pinhole pattern is designed using the newly derived expression of the magnification in a tilted plane system, detailed in Appendix D. The pinholes are linearly spaced in line with advancing interval to create equally spaced foci, resulting in 160 sampling points per full line of scan in the CLSS. Therefore, a simple line camera is sufficient for the application of the CLSS. In addition, the derived magnification is also useful for investigating the effect of the tolerance limits in adjusting the system, discussed in Chapter 4.

Finally, the effect of the tilted pinhole mask on the imaging characteristic of the CLSS is investigated in theory and in simulation. Using a simulation technique, it was found that the tilted pinhole mask caused no effect on the imaging quality and on the diffraction foci at the tilted focal plane. On the contrary, the residual aberrations including that caused by the tilted quartz substrate of the pinhole mask contribute to reducing the light output at the tilted detector, but not always the measuring quality of the CLSS. Since the CCD is mainly used to record the sampling intensity detected by each pinhole and not to image the specimen, the pixel size of the detector does not pose a limit on the lateral resolution.

Chapter 4

System Design Description

The main target in constructing the CLSS' system is to gain the highest possible degree of the *depth discrimination* according to the design. The pinhole mask designed in the previous chapter is a key component to initially achieve the target. Therefore, the system's construction and alignment are detailed in this chapter. The design of equally spaced foci plays an important role in realizing the new parallel depth scanning scheme of the CLSS, such that the system misalignment is then responsible for unequally spaced foci and a poorer quality of the depth discrimination. In consequence, the system construction and alignment are optimized for best axial intensity response. In this chapter, the new derivation of the magnification in a tilted plane system, illustrated in Appendix D, is also used to explore the errors of the focal spacing corresponding to the system misalignment tolerances. The equally spaced foci are significant for simplifying the data processing in Chapter 5. The process control of the hardwares and the data acquisition are also discussed in this chapter. Furthermore, suggestions on how to improve the acquisition rate of the CLSS are then provided. Finally, the errors and noises inherent in the system are investigated. These provide necessary knowledge for the error correction, discussed in the next chapter.

4.1 CLSS' configuration

To carry out the experimental work presented in this thesis, a prototype of the CLSS was built on a breadboard to function as a test-bed. The CLSS' setup and its photograph are schematically depicted in Figure 4.1 and in Figure 4.2, respectively.

Figure 4.1 represents key components used in this configuration. A light-emitting diode (LED) is employed as a light source in this configuration due to its high stability, inexpensive and incoherent light source, whereas a laser is a poor choice. It is due to the fact that a laser can generate *speckle pattern* - an interference pattern of the coherent light, which significantly reduces the image

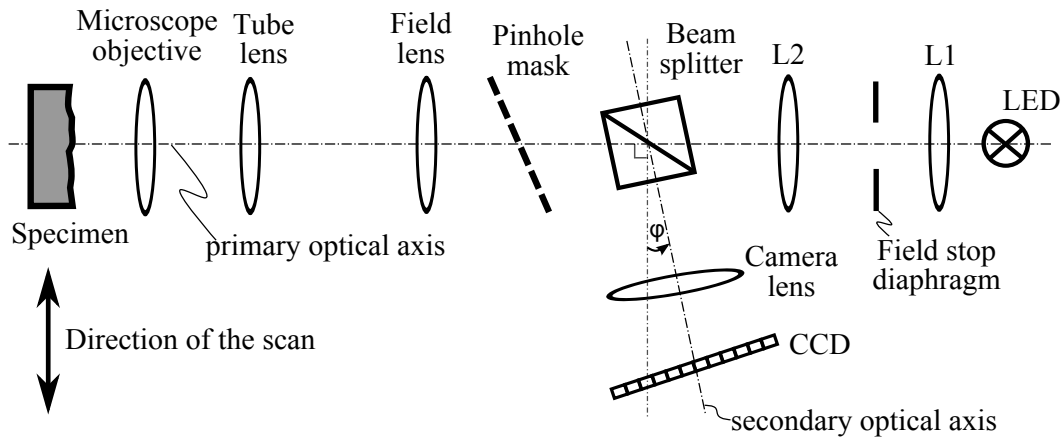


Figure 4.1: Schematic diagram of the CLSS system, where L1 and L2 represent a condenser lens and a collector lens, respectively. φ is the tilt angle of the secondary optical axis or the *detection arm* with respect to the normal arm.

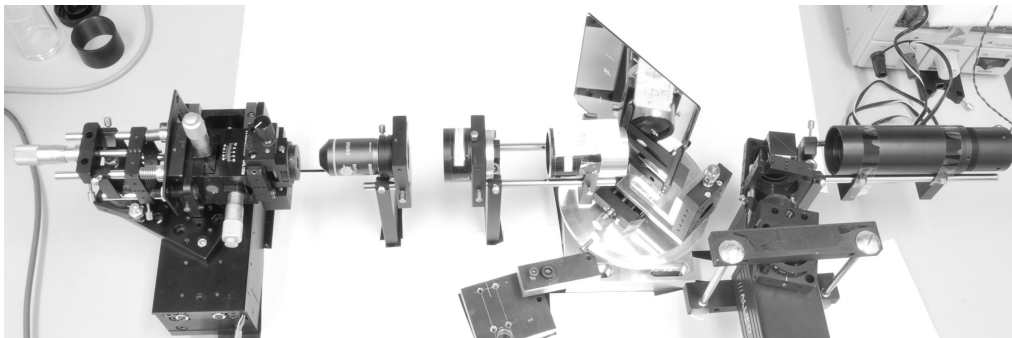


Figure 4.2: Photograph of the CLSS setup.

quality. In addition, LEDs are generally more stable than lasers as their output do not vary considerably over a certain range of temperature and lifetime. A white-light LED¹ (Luxeon, III star), emitting green light at $\lambda = 530$ nm wavelength, is selected as a light source, corresponding to the optimum performing region of the detector. In the detection part, a matrix charge-coupled-device (CCD) camera (AVT Dolphin, F145B) is utilized as a detector. It allows the complete image field to be observed, though a few lines of detection is sufficient in the CLSS. Nevertheless, in the current setup, visualization of the entire field of view is of vital importance for the system alignment and investigation. Furthermore, a stepper motor (Haydon 35000 Series, E35H4N-05) is employed here as a driver of the linear

¹White-light LEDs produce white light from devices that are fundamentally monochromatic. LEDs, having a narrow bandwidth of $\Delta\lambda = 12 - 40$ nm, are considered as monochromatic light sources. Due to their short coherence length (of a few wavelengths [33]), these light sources, however, are classified as white light sources.

scanning stage to scan the specimen in the lateral direction, while the optical head is fixed in place. In the case that to scan the specimen is difficult, the optical head can be scanned instead.

Microscope objectives² used in the CLSS are 20× infinity-corrected objectives from Olympus. Basically, an infinity-corrected objective lens requires a matching tube lens ($f = 180$ mm, Olympus) to produce a collimated beam, or an optical infinity space, to the objective lens. The microscope objective and the matching tube lens are typically employed together to minimize the five Seidel aberrations. However, it differs from producer to producer on how to design the objective lens and the tube lens to correct for the aberrations. For example, Olympus has designed the objective lens to minimize chromatic, spherical, wavefront aberrations, and field curvature, while the tube lens to correct for coma, astigmatism, and distortions [97].

Consequently, main targets in designing and constructing the CLSS are:

- to gain the highest degree of *depth discrimination*,
- to create uniform illumination based on Köhler illumination,
- to incorporate keystone distortion into the optical system to form equally spaced foci at the tilted focal plane,
- to minimize stray light and ghost effects.

4.1.1 Image formation in the CLSS

To develop an imaging system, the image formation is of major interest. In the CLSS, the image formation of four *conjugate field planes*, or the images of the field stop, is depicted in Figure 4.3. Essentially, light is focused from the LED by the condenser lens (L1) to the field stop diaphragm, forming the first conjugate field plane. The field stop is then imaged by the collector lens (L2) to the pinhole mask, forming the second conjugate field plane perpendicular to the primary optical axis. From the tilted pinhole mask, light emerges as parallel point-like sources, and is focused to infinity by the field lens and the tube lens, at which point the exit pupil of the objective lens is filled by the emitter image. Then, the microscope objective creates a tilted focal plane at the specimen, forming the third conjugate field plane. In the detection path, light reflected from the specimen returns via the same route and is deflected by a 50/50 beam splitter cube to the CCD. On the return path, the same set of pinholes function as parallel point-like detectors, creating the confocal effect. The pinholes are thus imaged by a camera lens to the tilted CCD, forming the fourth conjugate field plane.

Among the four conjugate field planes, the focal plane is the most important one, at which plane the *diffraction-limited focal points* are formed by the objective

²Throughout this thesis, a *microscope objective lens*, a *microscope objective*, an *objective lens*, or an *objective* is used interchangeably.

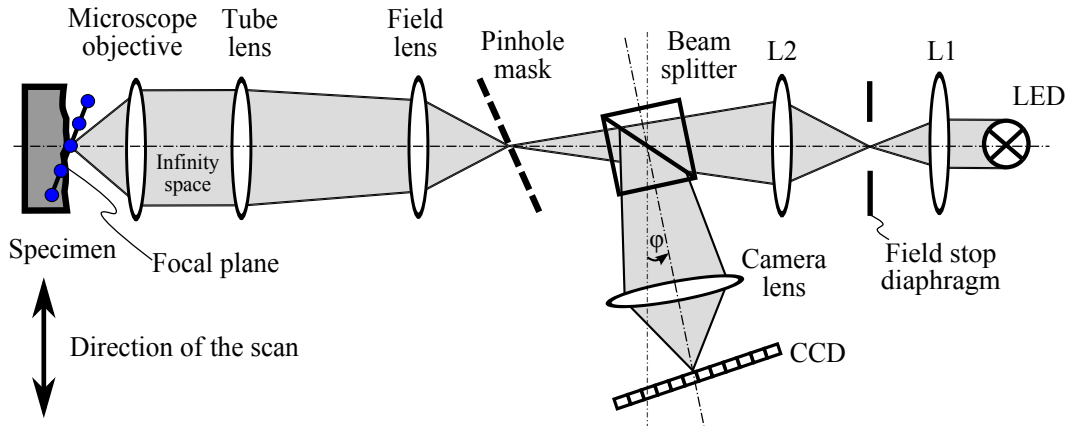


Figure 4.3: Schematic diagram of four conjugate field planes forming in the CLSS' system. L1 and L2 denote a condenser lens and a collector lens, respectively, and φ is the tilt angle of the secondary optical axis, or the detection arm, with respect to the normal arm.

lens. If the optical system consists of negligible wavefront aberrations, the term *diffraction foci* coined by Born and Wolf [6] is used instead of the *diffraction-limited focal points*. Henceforth, the *diffraction foci* are employed throughout this thesis. At the tilted focal plane, the equally spaced diffraction foci function as multiple optical probes to facilitate the new parallel depth scanning scheme of the CLSS.

4.1.2 Pinhole mask

Note that size of the stationary pinhole mask used in the CLSS is relatively small as compared to the rotating pinhole disk of the confocal imaging system presented in Chapter 2. See the preceding chapter for the pinhole design. In the CLSS, the pinhole patterns were fabricated on anti-reflective chrome on a quartz substrate using electron beam lithography. This technology allows elliptical pinholes to be manufactured with a minimum feature size of $0.5 \mu\text{m}$, a placement tolerance of $\pm 0.3 \mu\text{m}$, and a reference-grid fidelity of 100 nm. Since the anti-reflective chrome film is extremely thin $\approx 100 \text{ nm}$, its thickness will not introduce any notable aberration in the system [18].

4.1.3 Confocal effect and degradation

As discussed in the preceding chapter, the optimal *depth-discrimination* capability is achieved mainly by the pinhole design, in connection with the pinhole size and numerical aperture of the objective lens, *not the magnification*. The higher the numerical aperture, the superior the depth discrimination is. However, depth discrimination can be degraded by the presence of aberrations in the optical system

and the reduction in the effective numerical aperture³ (NA) of the objective lens.

The effects of aberrations on depth discrimination are already discussed in the previous chapter. Thus, this section will briefly discuss the effects of the effective NA on *depth discrimination*. Following Wilson [115], a non-uniform pupil function and pupil shading are responsible for the reduction of the effective NA. The pupil shading, known as *vignetting* [23, 115], is the falling-off in transmissivity toward the edge of the objective lens. The study by Fewer *et al.* [23] also confirmed that the pupil shading can reduce the effective NA of the objective lens. Accordingly, depth discrimination as a function of NA is degraded. Mathematically, the pupil shading function (P) is not represented by a constant but is a function of a radius unit (ρ), which takes the form [115]

$$P(\rho) = \begin{cases} f(\rho) & \text{if } \rho \leq 1 \\ 0 & \text{otherwise.} \end{cases}$$

This leads to the conclusion that uniform illumination at the exit pupil of the objective lens can ensure the highest degree of depth discrimination. Based on this knowledge, the confocal effect and contrast can be optimized by modifying the pupil function [31].

4.1.4 Uniform illumination: Köhler illumination

A uniform illumination across the field-of-view at the specimen plane is of vital significance for homogeneous sensitivity of the measurement. In this section, the Köhler based illumination is therefore described. Accordingly, the effective NA is optimized by filling the exit pupil of the objective lens with the emitter image.

Before the advent of the Köhler Illumination⁴, the filament of the light bulb used in a light microscope is visible in the specimen plane, such that the illumination across the field-of-view is not uniform. The filament image appearing on the specimen can confuse the data interpretation. As a result, the images seen under a microscope can be problematic, uneven, vague, and to some extent conveying incorrect information.

Köhler solved this problem in 1893 [44]. He introduced a solution which provides a uniform and bright illumination over the entire field-of-view. Basically,

³The numerical aperture (NA) of a lens is a dimensionless number that characterizes the range of light angles over which the lens can receive light. An exceedingly important role of the numerical aperture was first pointed out by Ernst Abbe in 1873 [1]. Abbe had observed the significance of the aperture-angle corresponding to the resolving power of an objective lens. He defined that the imaging resolution is based on the necessity for the diffracted light rays from the specimen to be collected by the objective lens. If these diffracted rays at high angle are excluded, fine details of the object cannot be resolved [33, 61].

⁴The Köhler Illumination has revolutionized the design of light microscopes, and is widely used in traditional as well as modern digital imaging techniques today.

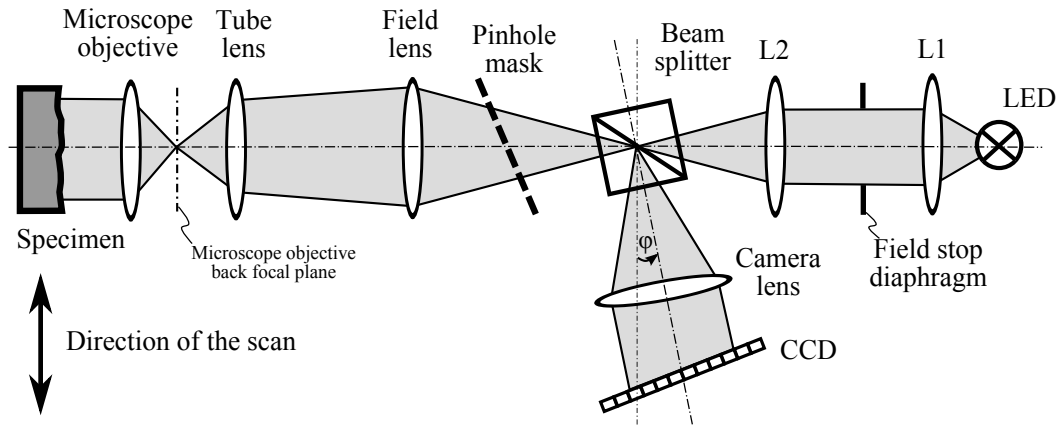


Figure 4.4: Schematic diagram of three conjugate aperture planes, or *emitter images*, forming in the CLSS' system, based on Köhler Illumination. L1 and L2 denote a condenser lens and a collector lens, respectively.

Köhler Illumination eliminates the emitter image from the observing plane by separating those of the conjugate field images from the conjugate emitter images, shown in Figure 4.3 and Figure 4.4, respectively. This setup allows the microscope objective to project light at full cone (full angle) at the specimen to evenly illuminate the field-of-view, such that the resolution and contrast are optimized.

In the CLSS configuration, a patented Köhler based illumination tube [109] is incorporated. Figure 4.4 shows that uniform illumination at the specimen can be achieved when the emitter image is formed at infinity. In other words, the emitter image should be brought into focus to fill the microscope objective back focal plane. This in turn maintains the optimum effective NA of the objective lens.

Figure 4.4 shows that a compound lens of the collector lens (L1) illuminates the field stop diaphragm evenly, and also initiates the separation between the emitter images light-path and the field images light-path. Though the illustration of the dissection between these two light-paths is not a true representation, it is suited for visualization and intuitive understanding [2]. In consequence, the condenser lens (L2) forms the conjugate emitter images at the back focal plane of the field lens and next at the back focal plane of the microscope objective, depicted in Figure 4.4. In addition, the field lens is used to collect dispersed light, so that the vignetting effect at the field-of-view is mitigated. In the detection arm, if the camera lens forms a uniform image across the tilted CCD, the sensitivity of the CLSS measurement should be best attained. However, certain vignetting at the detector is acceptable, such that the system alignment and the optical configuration are greatly simplified. Subsequently, the detection sensitivity of the measurement can be normalized later in the data processing.

4.1.5 Incorporation of the keystone distortion in the CLSS

The variation of the magnification inherent in a tilted plane system is known as the *keystone distortion* [28]. As explained in Chapter 3, the principal planes' positions play a key role in changing the pattern of the keystone distortion: *direct keystone*, *reverse keystone*, and *corrected keystone*. The principal planes are hypothetical planes in which their positions can be calculated or indirectly measured. These planes can be adjusted or shifted by the optical arrangement. From this point of view, it should be noted that when the positions of the principal planes are shifted, the object and image distances referenced from the principal planes vary accordingly. The lateral magnification, as the ratio of the object distance to the image distance with respect to the first and the second principal planes, is then modified. Note that the reverse keystone distortion is applied in the CLSS case.

This section then presents the simulation and the experimental studies to validate the connection between the principal planes' positions and the keystone distortion patterns, as explained in Chapter 3. In the CLSS, three lenses involved in shifting the principal planes are the microscope objective lens, the tube lens and the field lens. Moreover, Olympus infinity-corrected microscope objectives are exploited in the CLSS. In the imaging part, the tube lens is employed to collimate the beam to the microscope objective, whereas the field lens facilitates the collection of dispersed light to the microscope objective. Typically, the collimated beam, depicted in Figure 4.5, allows the microscope objective to move forward to and away from the tube lens without varying the magnification. However, in the tilted plane system of the CLSS, sliding the microscope objective in the same manner will result in a shift of the principal planes.

Simulation study discovers that by sliding the microscope objective lens with respect to the tube lens results in a shift of the principal planes from the positive coordinate to infinity and back to the negative coordinate. The notation of the direction is shown in Figure 4.5. In the simulation, only the simplified version of the imaging part is simulated in OSLO (an optical design software), since the specification of a complex optical element such as the microscope objective is not known. There are two simplified cases presenting here.

1. **Case 1:** three perfect lenses ⁵, having the focal length of 36 mm, 180 mm and 67 mm are used to perform as the microscope objective, the tube lens and the field lens, respectively, as depicted in Figure 4.5.
2. **Case 2:** replace the lens having the focal length of 36 mm by another one having a focal length of 9 mm, which represents the microscope objective.

The simulation and experimental results indicate that sliding the objective lens in Case 1 can shift the principal planes from the positive ($d < 21.6$ mm) to infinity

⁵A perfect lens means that the lens focuses light onto a single point, free of aberration.

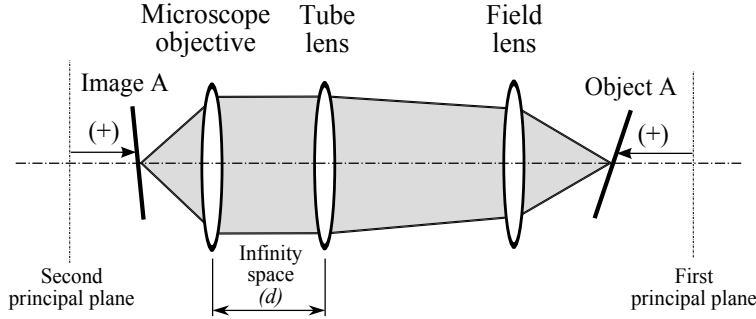


Figure 4.5: Three lenses involving in shifting the principal planes: the microscope objective, the tube lens, and the field lens. The positive direction of the object and image distances measured from the first and the second principal planes are presented; the negative direction is hence vice versa.

($d = 21.6$ mm), and reverse back to the negative direction ($d > 21.6$ mm), where d is the infinity space shown in Figure 4.5. Note that these values of d are obtained from the simulation; slightly different values are needed in the experiment. In Case 2, the principal planes are already located in the negative coordinate, representing the case of the CLSS' setup. Thus, shifting the principal planes to infinity or positive coordinate is not possible, when d should be reduced less than zero which is impossible. Figure 4.6 then depicts the image of the keystone distortion obtained in this case. It shows that the parallel lines in the tilted pinhole mask are imaged as diverging lines at the tilted image plane.

As described in Chapter 3, the case in which the principal planes are located in the negative coordinate is coined as the *reverse keystone distortion*; vice versa is the *direct keystone distortion*. When the principal planes approach infinity, the magnification is made uniformly across the tilted image plane, in which case is referred as the *corrected keystone*. In the *corrected keystone* case, the optical system becomes a *telescopic optical system* [95], when the principal planes approach infinity.

4.1.6 Minimization of the stray light and ghost images

Stray light and ghost images are unwanted light induced by the reflection or scattering of light, which appear in the field of view. In the CLSS, *ghost images*⁶ are eliminated from the image field of view by tilting the beam splitter. Figure 4.3 shows that the beam splitter is tilted $\varphi \approx 5\text{-}10^\circ$ with respect to the normal axis, so that the reflection of the ghost images are directed out of the image field of view in the detection part. In this case, ghost images are mainly the reflection from the back side of the pinhole mask and from the internal beam splitter. Since the

⁶Ghost images are induced by the inter-reflection of light from optical component surfaces [63]

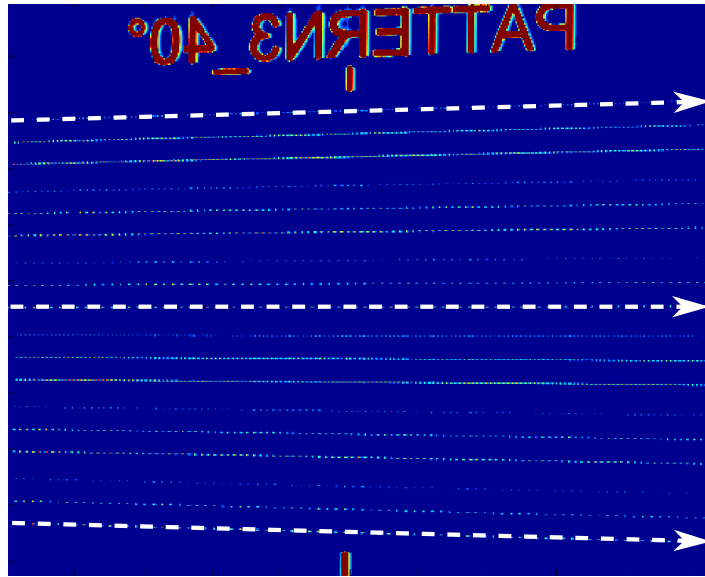


Figure 4.6: The keystone distortion pattern of parallel lines object. The image is captured at the tilted image plane and displayed by MATLAB (a technical computing software). The bold dash lines are marked as lines of sight.

beam splitter is tilted, the detection arm is thus aligned accordingly.

The CLSS is build on an optical test-bed and operated in the optical laboratory, such that a housing of the optics is not necessary. However, in a real product, a housing of the device is of essential significance, such that it will significantly introduce scattered light or *stray light* [63]. In such the case, more complicated methods should be implemented to eliminate the stray light and ghost images, for example, by employing polarizer, analyzer, and quarter wave plate [18, 42].

4.2 System alignment

The CLSS is built on a breadboard of the Microbench set provided by Linos. The Microbench set places a limit on the alignment flexibility, but offers maximal ease to align the optical elements along the optical axis in a concentric manner. Once the optical system is aligned it tends to remain so for weeks. The only component needed to be checked on a daily basis is the CCD. The CCD usually drifts approximately 1 to 2 pixels within a week.

Most of the optical components in the CLSS are aligned perpendicular and concentric to the optical axis, whereas the pinhole mask and the CCD are not. The pinhole mask and the CCD are tilted with respect to the optical axis. The intention to tilt the pinhole mask is to create the titled focal plane, in which equally spaced diffraction foci are formed. In addition, the CCD is aligned to the tilted image plane.

This section then presents the pinhole mask and the CCD alignment. The errors of the focal spacing corresponding to the system misalignment-tolerances are theoretically investigated, following the derivation in Appendix D. System misalignment include the pinhole mask off-centering, incorrect tilt angle of the pinhole mask, and improper adjustment of the magnification in the optical system.

4.2.1 Pinhole mask alignment

The pinhole mask is aligned in the optical system using an in-house designed rotation stage, depicted in Figure 4.7. Three linear stages assembled on the rotation stage facilitate the translation of the pinhole mask in three dimensions. The goal to align the pinhole mask is to center the pinhole pattern to the optical axis and to tilt the pinhole mask to a desired angle. Thus, the diffraction foci can be formed with equal spacing when the pinhole mask is aligned correctly. Otherwise, misalignment of the pinhole mask will cause errors in the focal sampling interval. Accordingly, the depth discrimination and accuracy of the measurement is degraded.

The theoretical analysis is accomplished using the derivation in Appendix D, in which case the pinhole mask is considered as a tilted object plane, whereas the tilted focal plane is a tilted image plane. In order to monitor the error of the focal interval, the effects of the pinhole misalignment are added by substituting $H_p \pm \delta$ and $\Theta \pm \delta$ in eq.(4.1). Consequently, the focal coordinate (h_p) can be calculated. In this expression, H_p is the pinhole coordinate, Θ denotes the tilt angle of the pinhole mask, and δ is a dummy error.

$$h_p = H_p \cdot m_{x_p} \sqrt{\cos^2(\Theta) + m_0^2 \sin^2(\Theta)}. \quad (4.1)$$

The mechanics to align the pinhole mask allow for a ± 1 mm tolerance in centering the pinhole mask, and a $\pm 1^\circ$ tolerance in tilting the pinhole mask. The centering tolerance is limited not only by the sensitivity of the linear stages (Micos, APT-65 and APT-38), but also by the precision of the method for centering the pinhole pattern to the optical axis. With the different values of positional tolerances, the error of the focal interval can be theoretically calculated, as summarized in Figure 4.8 and Figure 4.9. It is rather unfortunate that the predicted errors of the focal interval cannot be cross-checked with the experimental results, since the instruments at hand do not provide enough resolution to directly measure the focal interval at the tilted focal plane. From the theoretical analysis, the centering tolerance of the pinhole mask of ± 1 mm results in the focal interval of $\Delta x = 5 \pm 0.065 \mu\text{m}$ and $\Delta z = 0.35 \pm 0.00485 \mu\text{m}$. In the same manner, the tilting tolerance of the pinhole mask of $\pm 1^\circ$ yields the focal interval of $\Delta x = 5 \pm 0.073 \mu\text{m}$ and $\Delta z = 0.35 \pm 0.0008 \mu\text{m}$. Note that the nominal values of the focal intervals are $\Delta x = 5 \mu\text{m}$ and $\Delta z = 0.35 \mu\text{m}$, and the nominal value of the tilt angle of the pinhole mask is 40° with respect to the plane normal to the optical axis.

Though the pinhole mask is correctly centered and tilted, an incorrect imaging magnification can cause unequally spaced diffraction foci. In the CLSS, the imag-

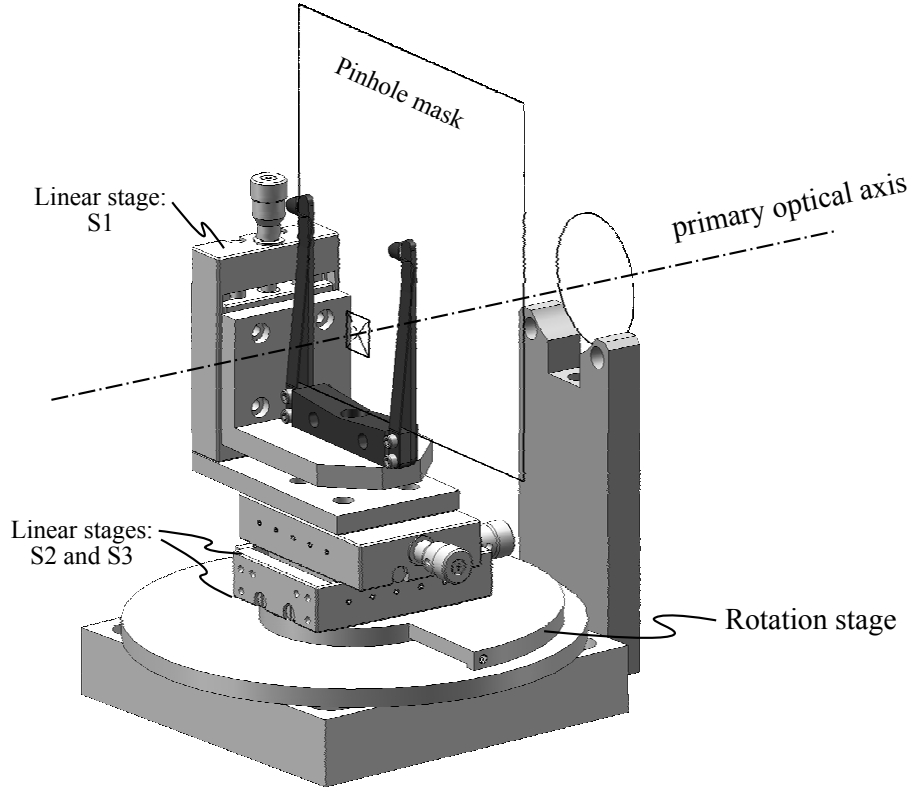


Figure 4.7: An in-house designed rotation stage. The linear stages S1 (Micos, APT-65) and S2 & S3 (Micos, APT-38) are assembled on the rotation stage to offer translation movement. These linear stages have travel ranges of 25 mm and 5 mm with $5\mu\text{m}$ sensitivity, respectively.

ing magnification is adjusted with an objective lens, a tube lens, and a field lens. When the objective lens is moved towards or away from the tube lens within the collimated beam space, the magnification is varied in connection with the shifting of the principal planes. Nonetheless, the magnification at the tilted focal plane can be measured using a supported CCD. The effect of the error caused by incorrect magnification is then theoretically analyzed. Note that the nominal value of the imaging magnification is $12\times$. By substituting $m_0 \pm \delta$ in eq.(4.1), the variation of h_p is obtained. The results are depicted in Figure 4.10. It shows that the magnification tolerance of $\pm 1\times$ results in the focal intervals of $\Delta x = 5 \pm 0.1 \mu\text{m}$ and $\Delta z = 0.35 \pm 0.011 \mu\text{m}$.

Therefore, it can be concluded that the magnification in the imaging part is the most sensitive parameter for the adjustment to realize equally spaced diffraction foci, as compared to the pinhole mask centering and tilting. However, if the *corrected keystone* is incorporated in the optical system, the pinhole mask centering can be eliminated. This helps to simplify the pinhole mask alignment. Only the

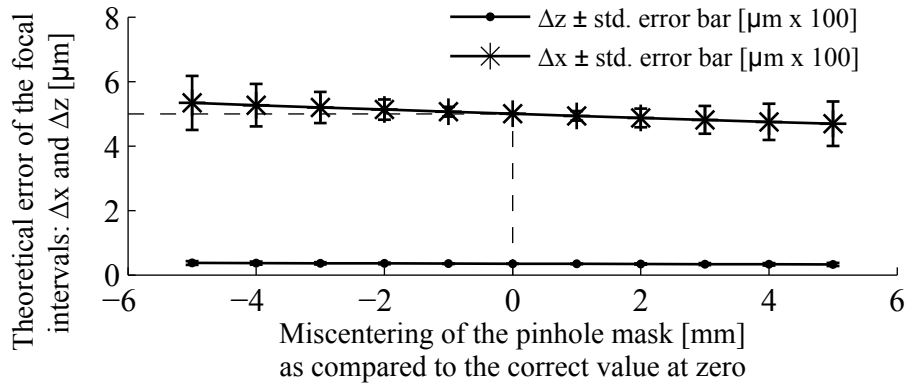


Figure 4.8: Theoretical errors of the focal intervals (Δx and Δz) in regard of mis-centering of the pinhole mask. The nominal value of Δx is 5 μm and Δz is 0.35 μm .

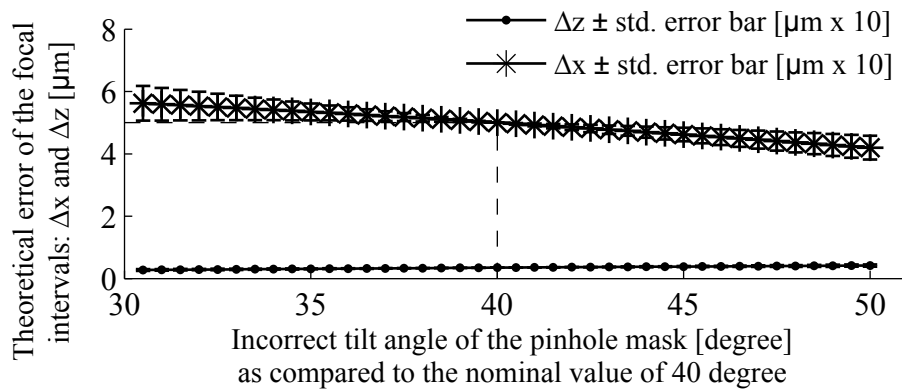


Figure 4.9: Theoretical errors of the focal intervals (Δx and Δz) in regard of mis-tilting of the pinhole mask. The nominal value of Δx is 5 μm and Δz is 0.35 μm .

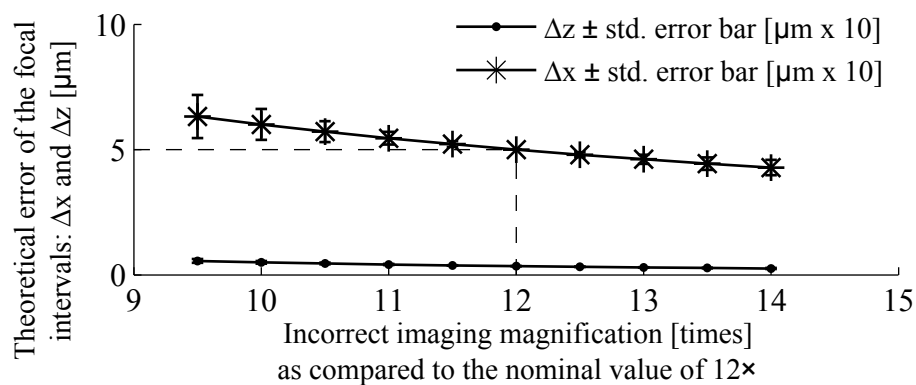


Figure 4.10: Theoretical errors of the focal intervals (Δx and Δz) in regard of incorrect adjustment of the imaging magnification. The nominal value of Δx is 5 μm and Δz is 0.35 μm , whereas the nominal value of the magnification is 12 \times .

pinhole mask tilting and the magnification adjustment need be implemented.

4.2.2 CCD alignment

The CCD alignment is less critical than the pinhole mask alignment. The target of alignment is to ensure that the CCD will capture sharp pinhole images across the tilted image plane. Nonetheless, the CCD is aligned in order to adjust the in-line pinhole images to a line of the CCD's pixels. This will substantially simplify the data processing afterward. The CCD is then mounted on a breadboard using an in-house constructed holder, shown in Figure 4.11. Since the holder is not optimized for stability, it can cause a slight shift of the CCD after setting up the system. Therefore, the CCD needs to be checked on a daily basis or before performing the measurement.

Since the CCD is used for recording the intensity output rather than imaging, the size and shape of the pinhole images formed at the CCD are not of significant importance. Only the total intensity of each pinhole image is meaningful, which contributes to the quality of the axial response and depth discrimination. Thus, the Nyquist-Shannon sampling theorem is not applied here. This also means that the lateral resolution is not connected with the pixel sampling. As a result, the optimal condition for the pixel sampling is when each pinhole is imaged by a single pixel of the CCD.

Figure 4.12 shows different sampling conditions of a pinhole image at the CCD. The best solution would be Figure 4.12 (a), when the image is formed as a square to symmetrically correspond with a square pixel. However, this solution is not practical, since the images of the pinholes applied in the CLSS are formed in an elliptical shape at the CCD. In this case, an acceptable condition is shown in Figure 4.12 (b), where a pinhole is imaged onto a square pixel. In contrast to Figure 4.12 (a) and (b), Figure 4.12 (c) represents several sampling conditions in which case higher noise level may be introduced by a larger unprofitable area of the pixels.

4.3 Process control and data acquisition

This section describes the process control and data acquisition used in the CLSS. The process control involves running movable parts, such as the linear scanning stage, and synchronizing the moving parts with the data acquisition mechanism. All of the optical components are solidly held in place throughout the process, which makes the system relatively robust.

In order to operate the system, the process control and data acquisition are handled by the following hardware: a linear scanning stage driven by a stepper motor, a CCD, a computer, a motion control unit and a power supply, depicted in Figure 4.13.

The linear scanning stage used to scan the specimen is Haydon 35000 Series, E35H4N-05, with high resolution step angle, Bipolar, Chopper drive, and a linear

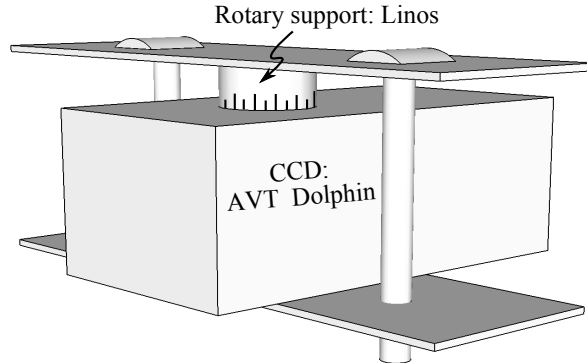


Figure 4.11: An in-house constructed CCD holder. The holder helps align the CCD in the detection arm, using the rotary support from Linos with 5° increment on the angular scale.

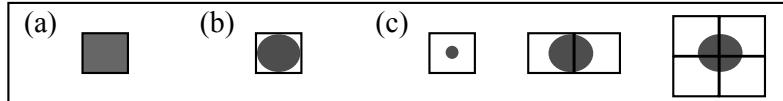


Figure 4.12: Schematic demonstration of the pixel sampling. The squares denote pixels of the CCD, whereas the gray areas represent the pinhole images formed at the CCD. (a) optimal condition (b) acceptable condition (c) SNR degradation conditions.

travel of $610 \mu\text{m}$ per one rotation. The linear movement along the axis of the stepper motor can traverse with a step resolution of $3.05 \mu\text{m}$ in the full-step mode and of 190 nm in the micro-step mode. It was observed that the linear scanning stage travels with high precision in the relative coordinate, but fails to accomplish that in the global coordinate. The stage can repeat its path precisely within a given range, but will provide different global coordinate after the range is reset. In general, this drawback can be overcome by using a closed loop controlled stage, or a high precision stage such as a piezoelectric actuator stage.

The employed CCD is an AVT Dolphin F145B, SXGA+ 1392×1040 pixel progressive, with 8-bit output in gray scale ranging within $0 - 255$. The CCD communicates with the computer via a high speed communication interface, IEEE 1394 (Firewire) connection bus standard. The computer, used to control the process and store the measurement data, is the Genuine Intel CPU T2250@ 1.73GHz, with 797 MHz 1.99 GB Ram. For the light source, a stable illumination source is a definite requirement. Therefore, an LED from Luxeon, III star, 64 mW Radiometric Power is used as a light source. The motor control unit is an in-house developed motor controller for a stepper motor, NFusbMotor V0.3 and -SUB V0.4, and the power supply is a DC power supply, 0-15 V, max. 2 A.

In the CLSS, the intensity output is recorded by the CCD, while the specimen is stepwise scanned in the x direction through the stack of the diffraction foci using a linear scanning stage. In consequence, the CCD is triggered by a hypothetical

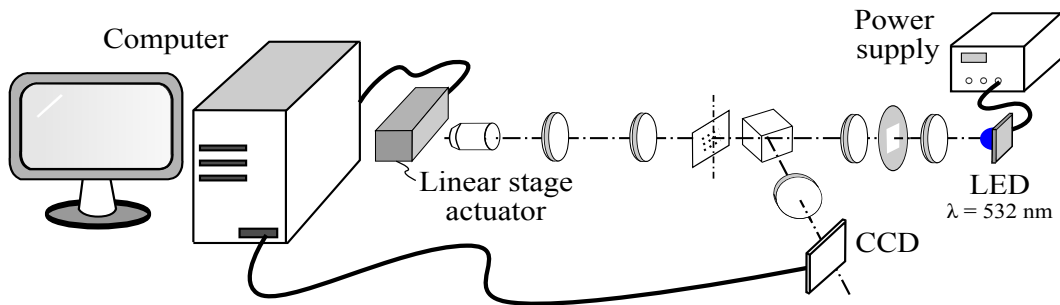


Figure 4.13: Schematic diagram of the hardware for data acquisition and process control of the CLSS.

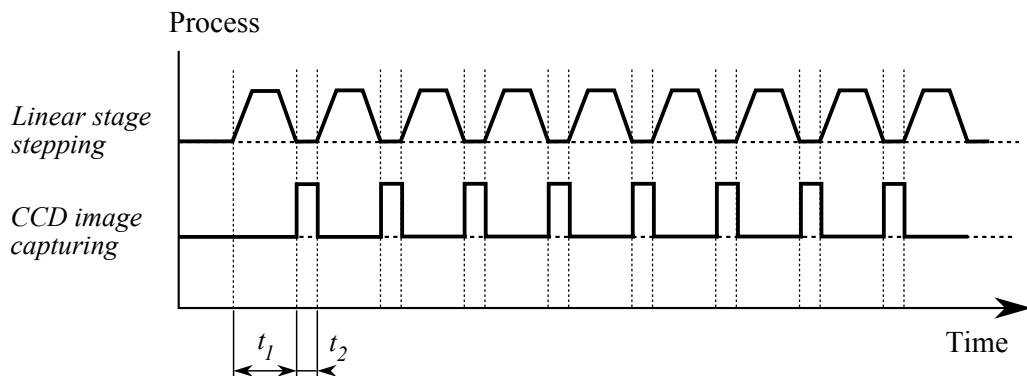


Figure 4.14: Timing diagram for the process control in *trigger-mode*. The CCD starts capturing each frame when it is triggered by the end state of the linear scanning stage after t_1 , and takes t_2 as the CCD exposure time.

stop of the linear scanning stage to record the data. The read-out data is thus the intensity output of the light reflected from the specimen. The timing diagram for the process control is schematically shown in Figure 4.14, namely *trigger-mode*.

In the *trigger-mode*, the data is acquired at 5.80 frames per second (fps). The acquisition time (t_a) includes the exposure time (t_e) of the CCD, the scanning time (t_s) of the linear stage, and the remaining delay time (t_r), i.e., from synchronization, software algorithm and electronic delay. In the case of a 5.80 fps acquisition time, 173 ms is taken per frame. For each frame, 34 ms is consumed approximately by the CCD for the exposure time, 1 - 2 ms is taken by the linear stage for the scanning time, whereas the rest of 137 ms is consumed by several sources of delay time and synchronization. Therefore, the formula to calculate the acquisition time (t_a) can be obtained as

$$t_a = t_e + t_s + t_r.$$

To reduce the acquisition time, the stage should be driven continuously, while the CCD is triggered automatically to read out the data, as shown in Figure 4.15,

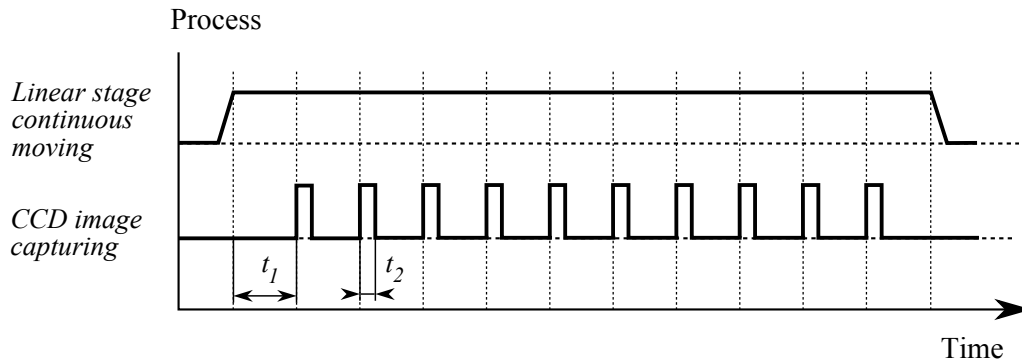


Figure 4.15: Timing diagram for the process control in *continuous-mode*. The CCD starts capturing each frame every t_1 , when it is triggered automatically, i.e. by internal clock, and takes t_2 as the CCD exposure time.

namely *continuous-mode*. In this case, the acquisition time will be dramatically reduced, as the synchronization and communication time is shortened, so does the delay time. However, acquiring the intensity output while the specimen is in motion, especially at high speed, the effect of a short exposure time resulting in a dark looking image should be taken into account. In this thesis, the acquisition rate of 5.80 fps is, however, sufficient to validate the proof-of-concept of the CLSS and to investigate the system in a number of aspects. Nonetheless, a high speed system can be developed later, based upon the results of this thesis. For example, a faster scanning mechanism can be implemented with the process control in *continuous-mode*. If the scan speed of the linear stage meets the frame rate of the recent developed CCD cameras, at least a thousand frames per second can be achieved, contributing to 1 ms per frame.

4.4 Errors and noises in the CLSS

The errors and noises inherent in the CLSS system are briefly explored here, which are classified into two groups: *systematic errors* and *statistical errors*. Since statistical errors or random noises in the system cannot be corrected or compensated in general, these attributes worsen the precision of the measurement. However, systematic errors can be corrected to some extent. It is of vital significance to manifest the systematic errors introduced in the CLSS system for developing the error correction procedures. The following chapter deals particular with the error correction and calibrations. Consequently, the accuracy of the measurement will be improved after applying the error correction and calibrations to the system.

Notable sources of errors and noises inherent in the CLSS system are:

- the error and noise of the linear scanning stage,
- misalignment of the optical system,

- the aberrations inherent in the optical system,
- noises of the CCD.

The systematic error of the linear scanning stage is mainly corrected. However, the statistical errors from the other sources cannot be corrected, resulting in a lower precision of the measurement, and worsened signal-to-noise ratio and depth discrimination.

4.4.1 Systematic errors

This section presents the systematic errors caused by the linear scanning stage and imperfections of the optical system. However, only two dominant systematic errors will be corrected, concerning *flatness of the linear scanning stage* and *detection sensitivity*.

Flatness of the linear scanning stage

Instead of a flat-like movement, the linear scanning stage used in the CLSS traverses with a wave-like movement having a flatness tolerance in the axial direction (z) of $\pm 0.75 \mu\text{m}$. The wave-like systematic error is shown in Figure 4.16 (a), which can be observed using a flat mirror specimen. The wave-like systematic error has an amplitude of $\approx 1.5 \mu\text{m}$ and a period of $\approx 610 \mu\text{m}$. The motor-driven lead screw of the linear scanning stage is found to be the source of the systematic error, showing the matching period between the sinusoidal wave-like error and the period of the lead screw of $610 \mu\text{m}$ in Figure 4.16. In consequence, this systematic

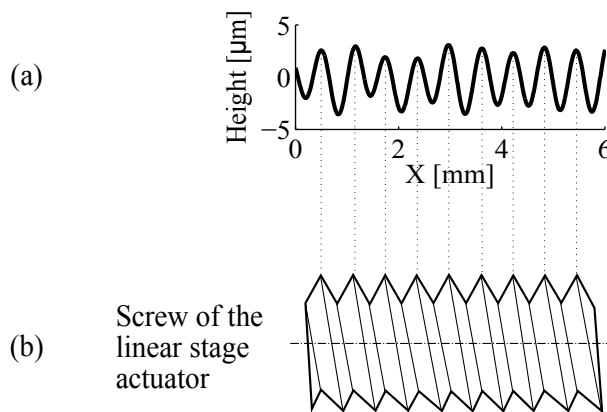


Figure 4.16: Simplified schematic of the systematic error caused by the motor-driven lead screw of the linear scanning stage. The wave-like systematic error has an amplitude of $\approx 1.5 \mu\text{m}$ and a period of $\approx 610 \mu\text{m}$, which is matched with the period of the motor-driven lead screw of $610 \mu\text{m}$.

error can be eliminated by subtracting the error out of the measurement data, which will be discussed later in the following chapter.

Vignetting and detection sensitivity

In the detection part, non-uniform light signal at the CCD is another systematic error to be corrected. When a flat mirror is aligned to the tilted focal plane, light reflected from the mirror to the CCD is supposed to be uniform, but it is not, as shown in Figure 4.17. This is caused mainly by the vignetting, pixel sampling, and dust particles on the pinhole aperture. The center part of the focal line has a higher maximum than that at the edges, so does the sensitivity of the pinhole detection. However, the signal can be modulated to meet the same maximum level, by normalizing the signal with the local maximum. The normalized sensitivity for each pinhole across the focal line is essential to improve the accuracy of the surface height evaluation. As the data will be sorted out in order to rearrange the signal mixing from different pinholes, a non-uniform detection sensitivity across the focal line will thus worsen the axial response as well as the depth discrimination. The sensitivity normalization is therefore described in the following chapter.

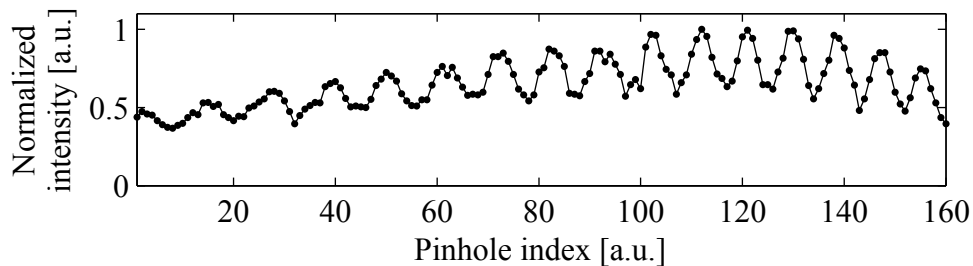


Figure 4.17: Vignetting and detection sensitivity effect across the focal line at the CCD.

Thermal noise: dark current and hot pixels

The temperature-generated charge is known as *dark current*. It generates signal even if the chip is completely in the dark. Following the technology of the CCD and chip architecture, the electrons can be generated in the pixels of the CCD not only by the incoming light but also by the chip temperature. Dark current is usually expressed in electrons per second per pixel at a defined temperature or at a defined exposure time, for instance $1e^-/s$ per pixel at 0°C .

In the case of the CLSS, dark current depends on the variation of the exposure time after the warm-up time and then the temperature remains constant. Typically, dark current always produces a fixed pattern frame or a dark frame at a given exposure time, and it can simply be eliminated by subtracting the dark frame from the original image. A dark frame of the CCD used in the CLSS can be

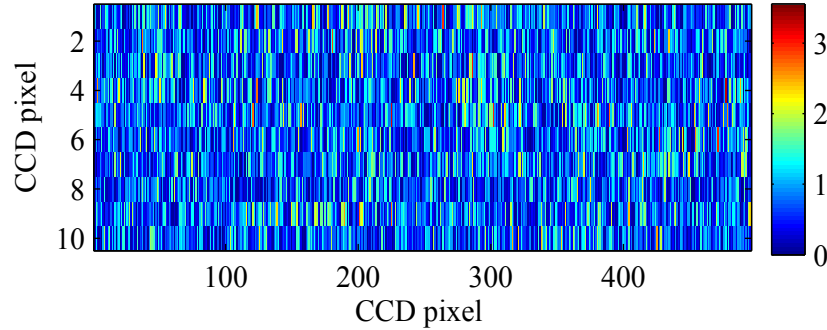


Figure 4.18: Dark frame acquired with the CCD camera (AVT Dolphin, F145B).

measured in root mean square (RMS) unit, shown in Figure 4.18. However, this systematic error of about 2 gray scale per second per pixel is relatively trivial.

Nonetheless, if the dark current linearly depends on temperature or exposure time, a dark frame can be calculated from other dark frames taken at different temperatures and/or different exposure times. Frequently, several dark frames taken at different exposure times are sufficient. Then, a dark frame at a given exposure time can be interpolated based upon these results [37].

Flat field image

Due to imperfections in the manufacturing process the sensitivity of the CCD pixels may vary slightly across the grid, usually by a few percent [35]. In addition, dust particles on the filter and the CCD chip can create ring-like shades, shown in Figure 4.19. This image is obtained when a bare CCD is evenly illuminated. All these effects result in the degradation of the detection sensitivity. However, in the CLSS the detection sensitivity of the used CCD pixels is corrected in the *sensitivity normalization* described earlier. Nonetheless, the field of a matrix CCD can typically be corrected, for example, by applying flat field division [113]. In order to apply the flat field division, the measured result of all pixels should be multiplied first by the flat field average before performing the division.

4.4.2 Statistical errors

Noise is defined as a stochastic phenomenon that can neither be compensated nor eliminated [108]. Thus, noises inherent in the CLSS system contribute to deteriorate the precision of the measurement.

Noise of the motor stepping

The linear scanning stage used in the CLSS is driven by a stepper motor. The stepper motor traverses with a step-like movement, having 3200 micro steps per

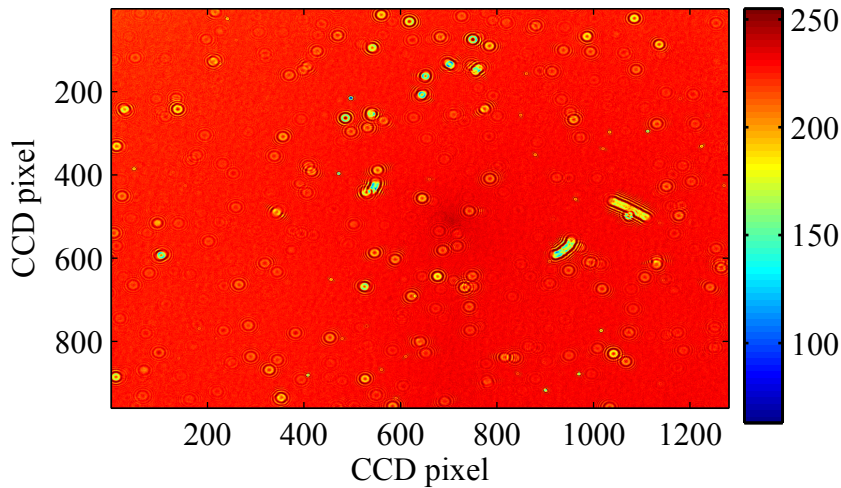


Figure 4.19: Flat field image acquired with the CCD camera (AVT Dolphin F145B). These ring-like spots come from dust particles on the CCD chip.

one rotation of the motor-driven lead screw. Basically, the precision of a micro step will be degraded, if the relation between the twisting angle of the rotor for an exact micro step and the current control to raise the torque is not sufficiently linear and precise [80]. This is caused mainly by non-homogeneous magnetic field between the rotor and stator.

The step error of the linear scanning stage is shown in Figure 4.20. The results are concluded from 20 data set, in which case the linear scanning stage steps by one full step comprising of 16 micro steps, and repeats the traversing length of $60 \mu\text{m}$ for each data set. An interferometric distance measurement is used to verify the distance traveled. It can be seen that the step error is randomly accumulated in the distance traveled by the linear scanning stage. As a result, the step error is considered as a statistical error, resulting in the error of $\pm 5 \mu\text{m}$ from a traversing distance of $60 \mu\text{m}$. At a longer traversing distance, the effect of a statistical error of the motor step will be investigated in Chapter 6.

CCD read noise and A/D conversion

The noise sources that play a role in scientific CCD cameras are: photon noise, thermal noise (dark current and hot pixels), readout noise (amplifier noise, on-chip electronic noise and noise associated with the gate capacitor of a field effect transistor of a CCD chip [47]) and quantization noise [35]. As already mentioned, thermal noise can be considered as a systematic error. The other noises are classified as statistical errors which cannot be eliminated.

Several of these noise sources can be negligible, by using a proper electronic design and cautious operating conditions. However, the photon noise can never be eliminated, which essentially poses a marginal limit to the CCD if the other noise

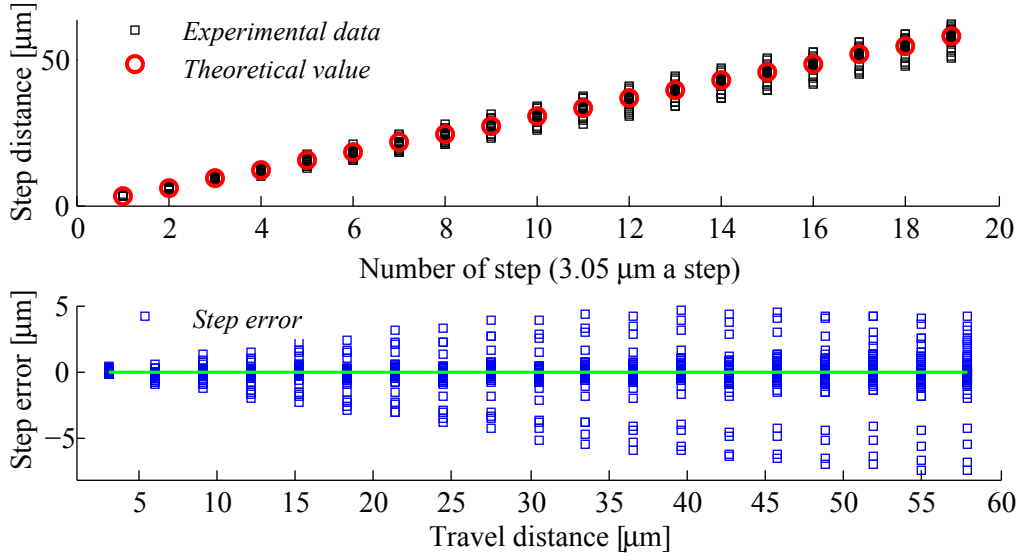


Figure 4.20: Step error in the linear scanning stage. The traveled distance is verified by an interferometric distance measurement.

sources are trivial as compared to this one. The photon noise is caused by a fundamental law of nature, or the quantum nature of light. It is a statistical property, i.e., Poisson distribution, that involves the number of photoelectrons generated by the incident photons. However, the photon noise is rather insignificant noise in the CLSS, as the CLSS is not designed to operate at extremely low light condition.

In addition, the read out mechanism of a CCD can generate an extra noise. A pixel value is read out of a CCD as a voltage signal, where the read out mechanism engages in the conversion of the electric charges to the voltage signals. During this process, the voltage output is digitized by external electronics, analog-to-digital (A/D) conversion, which also introduces certain noises. The CCD read noise is often expressed in electrons, e.g., 15 e⁻ RMS, which means that a CCD cannot read the image with a precision higher than 15 e⁻ RMS, regardless of the chip temperature. However, well designed electronics can reduce the CCD read noise to an insignificant level, as considered in the CLSS case.

4.5 Conclusion

This chapter presents the methods for constructing and aligning the CLSS' system. The main target is to obtain the highest degree possible of the depth discrimination, reflecting in a good quality of the axial intensity response. Therefore, correct aligning the pinhole mask and knowing which keystone distortion pattern is formed are of major concerns for obtaining the equally spaced foci. Moreover, a Köhler based illumination tube is incorporated in the CLSS system to maximize the effec-

tive numerical aperture (NA) of the imaging system, then to enhance the detection sensitivity and the quality of the axial intensity response. In consequence, the optical resolution and depth discrimination as a function of the effective NA are optimized accordingly. After applying the data processing, described in Chapter 5, the optimal axial intensity responses will finally be obtained.

The experimental exploration also shows that the keystone distortion pattern can be manipulated, for example, by arranging the optical components in the imaging part consisting of an objective lens, a tube lens and a field lens. Therefore, by sliding the objective within the collimated beam space with respect to the tube lens, the shifting of the principal planes can be manifested, resulting in three different cases of the keystone distortion. However, the CLSS system is operated with the *reverse keystone* case. If the optical system is designed with the *corrected keystone*, the pinhole mask design and alignment will greatly be simplified.

The effects of the pinhole mask misalignment on the focal interval are theoretically investigated, by following the derivation in Appendix D. The pinhole mask misalignment is mainly caused by the pinhole mask centering, the pinhole mask tilting, and the adjustment of the imaging magnification. It was found that the adjustment of the imaging magnification is the most sensitive one. Note that the design nominal values of the focal intervals in the CLSS are $\Delta x = 5 \mu\text{m}$ and $\Delta z = 0.35 \mu\text{m}$, and the nominal value of the tilt angle of the pinhole mask is 40° . With the tolerance of the magnification adjustment of $\pm 1\%$, the spacing error between the foci become $\Delta x = 5 \pm 0.1 \mu\text{m}$ and $\Delta z = 0.35 \pm 0.011 \mu\text{m}$. In addition, the tolerance of the pinhole mask centering of $\pm 1 \text{ mm}$ results in the focal spacing error of $\Delta x = 5 \pm 0.065 \mu\text{m}$ and $\Delta z = 0.35 \pm 0.00485 \mu\text{m}$, whereas the tolerance of the pinhole mask tilting of $\pm 1^\circ$ yields the focal spacing error of $\Delta x = 5 \pm 0.073 \mu\text{m}$ and $\Delta z = 0.35 \pm 0.0008 \mu\text{m}$.

It is noteworthy to point out that size of the stationary pinhole mask used in the CLSS is greatly reduced as compared to the rotating pinhole disk used in the pinhole-disk based confocal microscope, contributing to increasing the robustness of the system. To carry out the measurement with the CLSS, the specimen is scanned using a linear scanning stage in the lateral direction with the sampling rate of 5.8 frames per second (fps), or $\approx 1,000$ points per second. Nonetheless, the sampling rate can be enhanced, for instance, by applying a faster linear scanning stage. If the traversing speed of the linear stage meets the recent frame rate of the CCD cameras, the sampling rate, or *acquisition rate*, of a thousand fps or 160,000 points per second will be obtained. However, with an extremely short exposure time applied at high sampling rate, low light reflection of a dark looking image is of major concern.

It was also found that the dominant systematic errors to be corrected in the CLSS system are the wave-like motion of the linear scanning stage and the non-uniform detection sensitivity. In addition, the stepping of the motor introduces a statistical error which will be examined in Chapter 6.

Chapter 5

Data Processing and Calibrations

This chapter deals particularly with the development of the data processing and calibrations. The final target is to precisely reconstruct a 2D height profile. Following the design and construction of the CLSS discussed in the preceding chapters, the data processing and calibrations are applied in the last step to manifest the new parallel depth scanning scheme of the CLSS. In order to reconstruct a 2D height profile, the axial responses are obtained first. At this point, the data processing plays a vital role in sorting out the raw data to reveal the axial responses. In this chapter, the concept of the developed data processing is initially described, in which case the errors and imperfections inherent in the system are excluded. Thereafter, the newly developed algorithms for the error corrections and calibrations are presented, where the systematic errors are taken into account. The calibrations are basically used to assure the traceability of the CLSS. Here, the explanations of the data processing and calibrations are then supported by the experimental results. Finally, a 2D surface height profile can be reconstructed. The calculation of the profile roughness is thus described at the end of the chapter.

5.1 Conceptual data processing

The parallel depth scanning scheme of the CLSS requires equally spaced foci to sample the specimen in a way that a sampling focal point can repeat the adjacent sampling point along the x coordinate. In contrary, with non-equally spaced foci the parallel depth scanning scheme needs more sophisticated data processing and calibrations to complete the concept. According to that, equally spaced foci are designed and constructed in the CLSS. The concept of the data processing is then first described in this section. To make it more intuitive, Figure 5.1 presents a flowchart showing the procedures of the data processing. However, in this chart only the conceptual data processing is highlighted. The procedures depicted in

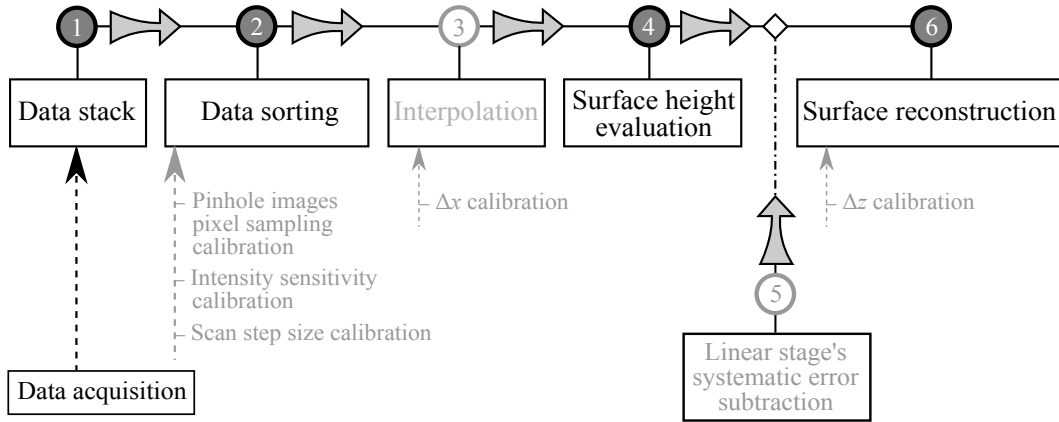


Figure 5.1: Flowchart of the conceptual data processing and calibrations in the CLSS.

pale color are for the systematic error correction and calibrations, which will be discussed later in this chapter.

In the CLSS, the data are acquired and stored layer by layer in the data stack, denoted by the process number 1 in Figure 5.1. The data in each layer contain intensity output reflected from the specimen, sampled by an in-line foci. Consequently, the data stack is processed by the *data sorting* in process number 2. At this point, the data are sorted out to meet the same x sampling coordinates and to cover the whole axial-sampling range. The distribution of the intensity output obtained from different heights, at a given x coordinate, then forms the *axial intensity response*. An axial intensity response enables the surface height evaluation to be executed in process number 4. The surface height evaluation is to find the maximum peak of the axial response, which corresponds to the real surface height of the specimen at a given x sampling coordinate. After the surface height evaluation is completed, a precise 2D height profile along the x sampling coordinates can be reconstructed in process number 6. Finally, the roughness of the reconstructed 2D profile is then evaluated.

The data processing and data analysis in the CLSS are implemented in MATLAB, as off-line processes. The processes include data sorting, surface reconstruction, calibrations, systematic errors subtraction and 2D profile analysis.

5.1.1 Data acquisition

When the focal intervals (Δx and Δz) are constant across the focal line, a repetitive sampling method required in the parallel depth scanning scheme of the CLSS can be realized. Figure 5.2 thus illustrates the sampling coordinate in connection with the coordinates of the specimen and the focal points. The specimen is traversed by stepwise scanning using a linear scanning stage, such that the lateral sampling interval can simply be traversed by a distance Δx per step. However, in practice

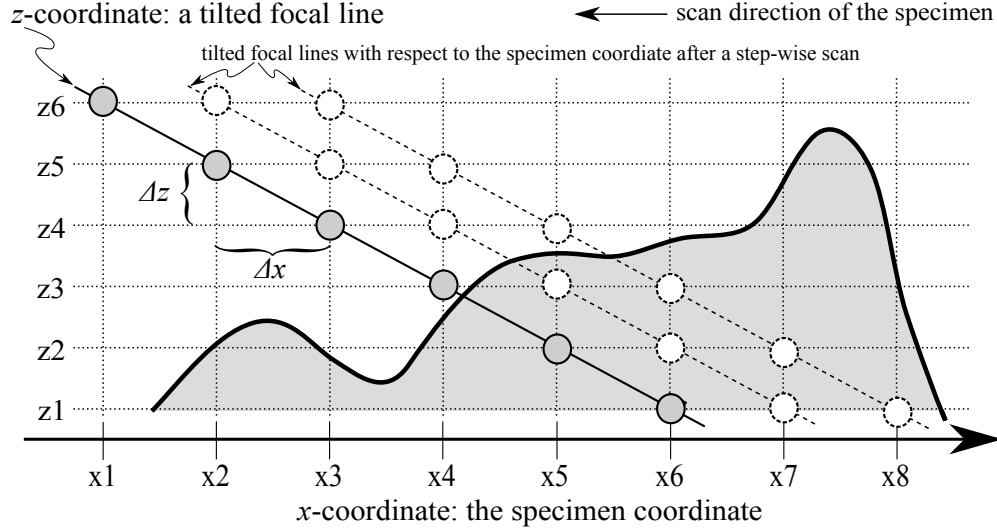


Figure 5.2: The concept of repetitive data sampling in the parallel depth scanning scheme of the CLSS, where Δx and Δz are the focal sampling intervals.

the scan step size can be differed from the lateral focal interval (Δx) to optimize the sampling rate and the lateral resolution by compromising time of the measurement. In this section, the errors inherent in the CLSS system are not taken into account yet, in which both the systematic and statistical errors are responsible for the uneven focal interval and non-uniform scan step size. The error correction and calibrations will then be discussed later, step by step.

An in-house developed software is used to acquire and store the data measured with the CLSS. Thus, the data are saved in the data stack, also called the *raw stack*, shown in Figure 5.3. The black dots denote the intensity output reflected from the specimen at given sampling points, x_i and z_p . It can be seen in Figure 5.3 that the data sampled at a given x coordinate are mixed in different order, therefore the raw stack needs be processed to rearrange the data of the same x -sampling coordinate and then to reveal the axial intensity response.

Consequently, the parallel depth scanning scheme of the CLSS means that the specimen is sampled at different depths in parallel using the stationary focal stack, which help to discard any mean to scan in the axial direction. This scheme will be completed only if the specimen is laterally scanned through the focal stack. For that matter, the axial sampling interval is fixed by the space between foci in the axial direction (Δz), while the lateral sampling interval can be adjusted with the scan step size (ΔF) with respect to the lateral focal-interval (Δx).

5.1.2 Data sorting

When the specimen is stepwise scanned with a step size of $\Delta F = \Delta x$, the data sorting is the simplest case. Each data frame in Figure 5.3 contains intensity out-

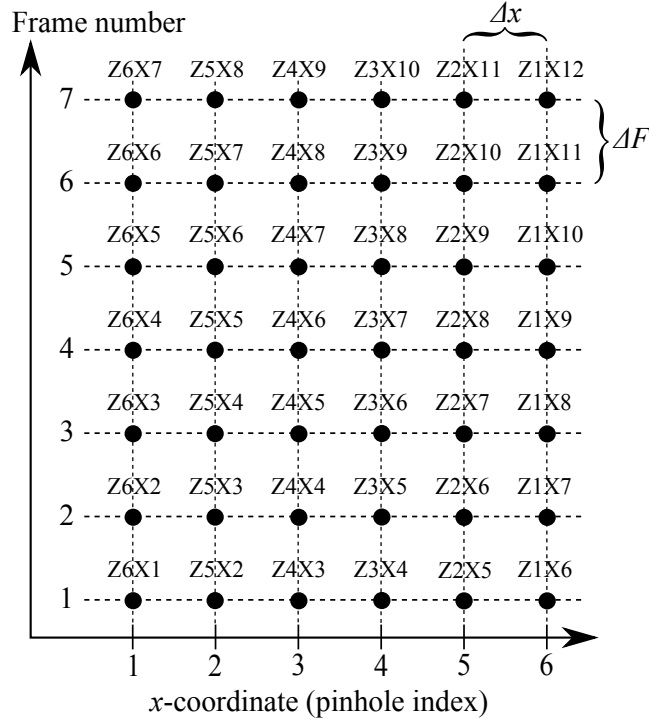


Figure 5.3: Data stack or *raw stack*, where x_i and z_p are the sampling coordinate, $i = 1, 2, \dots, m$ denote the lateral sampling points, and $p = 1, 2, \dots, n$ represent the axial sampling points which are equivalent to the number of the pinholes and the diffraction foci. In addition, Δx is the lateral focal-interval, and ΔF denotes the scan step size.

put reflected from the specimen per field-of-view, where the sampling coordinates follow Figure 5.2. However, it can be seen that in Figure 5.3 Δz is hidden in the raw stack. To reveal Δz information, the raw stack is sorted out to meet the same x sampling coordinate, as shown in Figure 5.4.

In the raw stack, each frame is separated by the step size (ΔF). After applying the sorting process, the axial focal-interval (Δz) is revealed in the pinhole index unit, in terms of the frame number. The z -height coordinate becomes more obvious after the data in each column are cropped within the axial sampling range (z_1 to z_n), depicted in Figure 5.5. In this process, the x axis in the raw stack is initially in the *pinhole index* unit. Then, it becomes an uncalibrated length unit along the x axis after the sorting process.

In the case that $\Delta F \neq \Delta x$, sorting out the data to meet the same x sampling coordinate might not be possible. Therefore, interpolation of the raw data along the x coordinate is vital to enable the CLSS measurement scheme. The interpolation will be discussed later in the calibration section.

A raw stack and a sorted stack obtained from the experiments are shown in Figure 5.6. The specimen is a so-called groove standard comprising three different

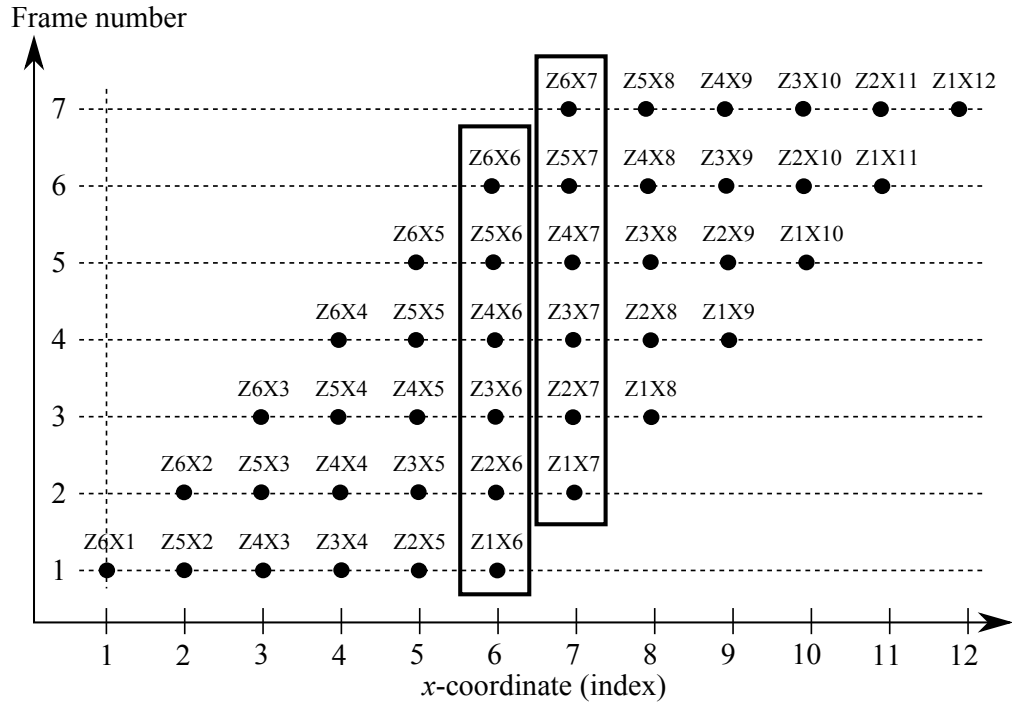


Figure 5.4: Sorted stack. The data stack is sorted to meet the same x sampling coordinate.

z -height (pinhole index)

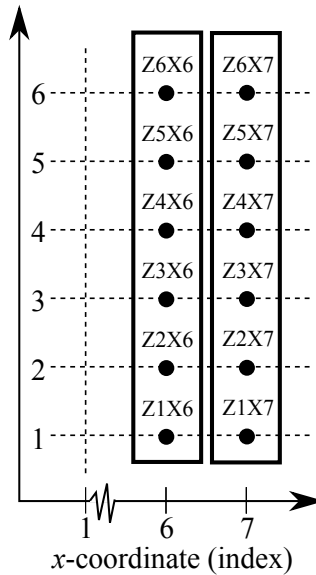


Figure 5.5: Cropped sorted stack. Each column is cropped within the axial measurement range (z_1 to z_n), where the axial sampling points ($1, 2, 3, \dots, n$) are the index of diffraction foci and corresponding pinholes.

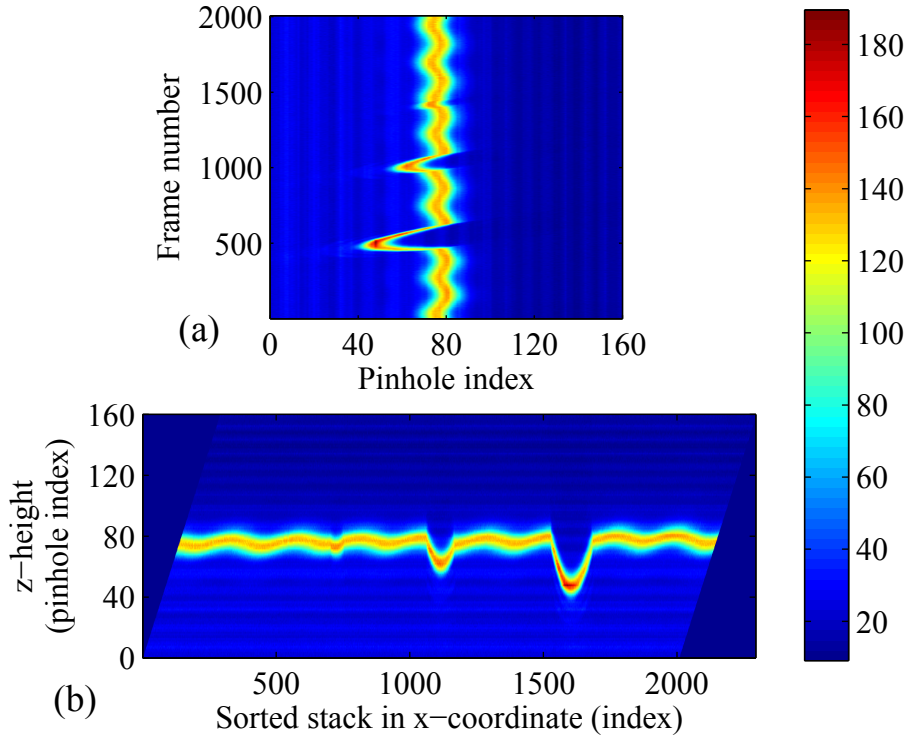


Figure 5.6: Raw stack and sorted stack of the measurement result obtained with a groove standard. (a) Raw stack (b) Cropped sorted stack.

groove depths. Figure 5.6 (a) presents the measured raw stack, whereas the frame numbers are now the number of the steps scanned in the lateral direction. After applying the sorting process, an axial response is obtained in the form of the intensity distribution along the z -height coordinate at a given x . The color in Figure 5.6 represents the intensity output in 8 bit gray scale.

5.1.3 Surface profile reconstruction

The surface profile reconstruction is carried out by evaluating the axial intensity response. This section thus presents the surface height evaluation, which relates to the *maximum peak finding* methods, and the algorithm and mathematical tools required for the surface profile reconstruction.

Axial response and depth-discrimination

In confocal microscopy, the axial response is the intensity distributed along the axial coordinate (z), and its maximum peak is related to the real surface height of the specimen. The intensity-to-height relation contributes to the depth-discrimination capability found in a confocal microscope [20]. Figure 5.7 shows that the intensity

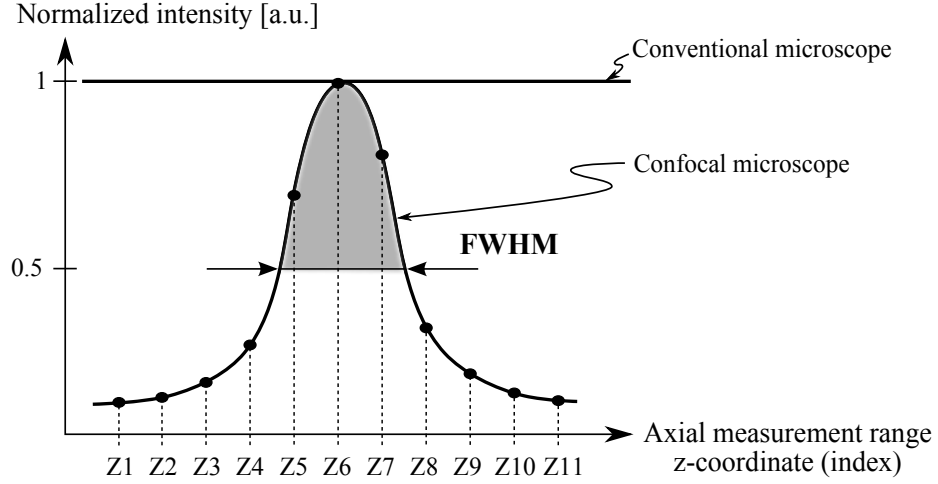


Figure 5.7: Axial response and depth-discrimination property. The depth discrimination property is realized through the intensity-to-height relation in a confocal microscope, but not in a conventional microscope.

is a function of the axial coordinate in the confocal microscopes. However, the intensity response is always constant in the conventional microscopes.

Note that the axial response is the object dependent response, which means that a plane object provides an axial response different from that of a point object. For example in a useful case of a point source and a point detector, the theoretical axial response obtained with a plane specimen is given by [114]

$$I(u) = \text{sinc}^2(u/2),$$

where I is the intensity, $\text{sinc}(x) = \sin(x)/x$ is the sinc function, and u denotes a normalized axial optical coordinate, $u = \frac{8\pi}{\lambda} \cdot z \cdot \sin^2(\alpha/2)$ [114]. In this equation, z is the axial coordinate, λ is the wavelength of light, and $\sin(\alpha)$ is the numerical aperture of the lens.

Maximum peak finding algorithm and surface height evaluation

As stated above, the maximum peak of the axial response corresponds to the real surface height of the specimen at a given x coordinate. In consequence, a highly robust and fast algorithm for the maximum peak finding method [25, 75], known as the *center of gravity* algorithm, is applied in the CLSS. To obtain an accurate result when evaluating with the center of gravity, sufficient sampling points of the axial response are required, of at least 16 points within the *full-width at half-maximum* of the response curve [77], or $\text{FWHM}/16$. However, the center of gravity is sensitive to the asymmetry of the axial response, which may result in a slight shift of the evaluated surface height from the exact value. Note that the asymmetry of the axial response in a confocal microscope is basically caused by

the optical aberrations inherent in the system. Additionally, poor quality of the focal intervals and an imprecise scan step size in the CLSS can attribute to worsen the axial response.

The center of gravity is implemented using the weighted approach. The real surface height, $h(x)$, is calculated by dividing the distance-weighted intensity by the summation of the intensity, which takes the expression

$$h(x) = \frac{\sum_{z_p \in \text{FWHM}} I(x, z_p) \cdot z_p}{\sum_{z_p \in \text{FWHM}} I(x, z_p)}, \quad (5.1)$$

where x is the lateral sampling coordinate on the specimen. $I(x, z_p)$ is the intensity reflected from the coordinate (x, z_p) of the specimen, and z_p represents the axial sampling coordinate, or so-called *defocus distance*, within the range of a FWHM, where $p = 1, 2, \dots, n$ are the number of the pinholes.

Noise integrated in the axial response may introduce uncertainty to the maximum peak finding position, $h(x)$. If the cause of the integrated noise is unknown, uncertainty can be determined as the standard deviation [13], or *root mean square* (RMS), from a set of repeated measurements. Taylor and Kuyatt [100] suggested that at least ten data set of the repeated measurement are required. In the CLSS, an uncertainty of the maximum peak finding of 11.7 nm is obtained by measuring with a flat mirror.

As an alternative to the *center of gravity*, several other algorithms can also be applied. Basically, the other algorithms, such as deconvolution, least squares fit of a parabola, and Savitzky-Golay fit are rather precise but fairly slow and require high computing power for calculation [75]. For a Savitzky-Golay fit, a notably accurate result can be achieved even from an asymmetrical curve of the axial response, which usually creates problems for the center of gravity algorithm, as reported by Hao¹ [32].

Surface reconstruction

A 2D height profile can now be reconstructed after the surface height is evaluated along the x sampling coordinates, shown in Figure 5.8, where the maximum peak of the axial intensity response provides the information of the surface height at a given x . Note that a 2D profile is now denoted in the index unit. Therefore, calibrations are required mainly to convert the index unit into the physical length unit and to assure the traceability of the CLSS. The calibration of the focal intervals (Δx and Δz) then helps to convert the index unit to the physical length unit.

¹This result was presented in an internal WEMESURF network meeting, where **WEMESURF** stands for “Characterization of **WE**ar **ME**chanisms and **SURF**ace functionalities with regard to life time prediction and quality criteria - from micro to the nano range”. This thesis was supported by WEMESURF network in the EC Sixth Framework Programme and Marie Curie Action under contract number MRTN CT 2006 035589.

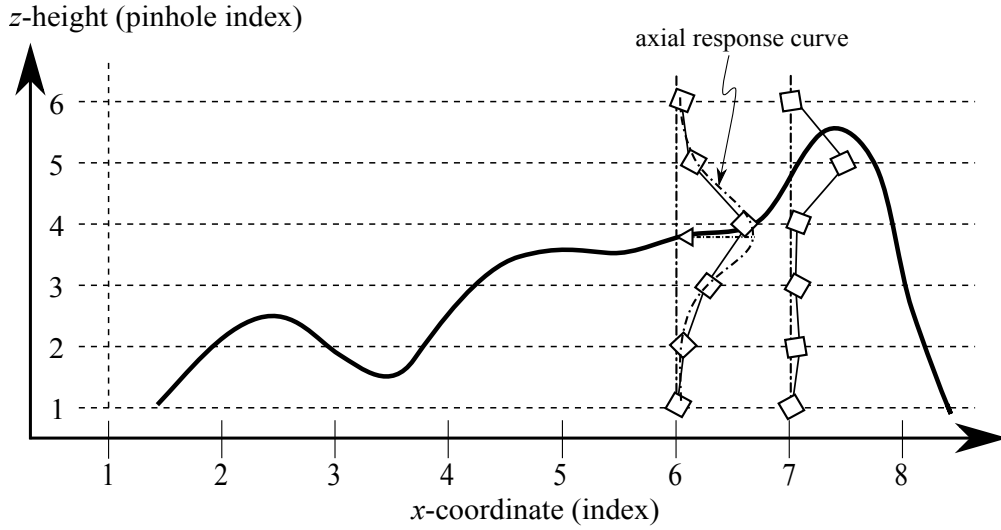


Figure 5.8: Reconstructed 2D height profile. This illustration shows that a 2D profile is revealed after the surface height was evaluated for all the x sampling coordinates.

It should be pointed out again that when a scan step size (ΔF) differs from the lateral focal-interval (Δx), a supplementary interpolation is required to add interpolated data into the raw stack. This introduces an extra pre-process to the surface reconstruction. On the other hand, it gives more flexibility in acquiring the data with variable lateral sampling intervals, and compromising the data density and the lateral resolution with the measurement time.

5.2 Calibrations

Calibration and systematic error correction are of vital importance in any measurement device, including the CLSS, which helps to improve the measurement accuracy. The accuracy of the profile measurement using the CLSS depends primarily on the quality of the focal intervals (Δx and Δz), where the quality means evenness of the focal spacing and its absolute value. Several errors can contribute to the degradation of the quality of the focal intervals. Therefore, this section is mainly devoted to explaining the systematic error corrections and calibrations applied in the CLSS. Three calibrations, two systematic error corrections, one data processing operation, and one interpolation are described in consecutive order following the practical implementation, illustrated in Figure 5.9. Nevertheless, the focal-interval calibrations can only be implemented on a mean basis, in which approach the errors of the focal intervals are averaged throughout the focal line.

The images of the pinholes sampled by the CCD pixels are first processed. As the pinhole mask is not moving, stationary pinhole images formed at the CCD are captured and sampled by certain pixels at all times. Therefore, the amount of

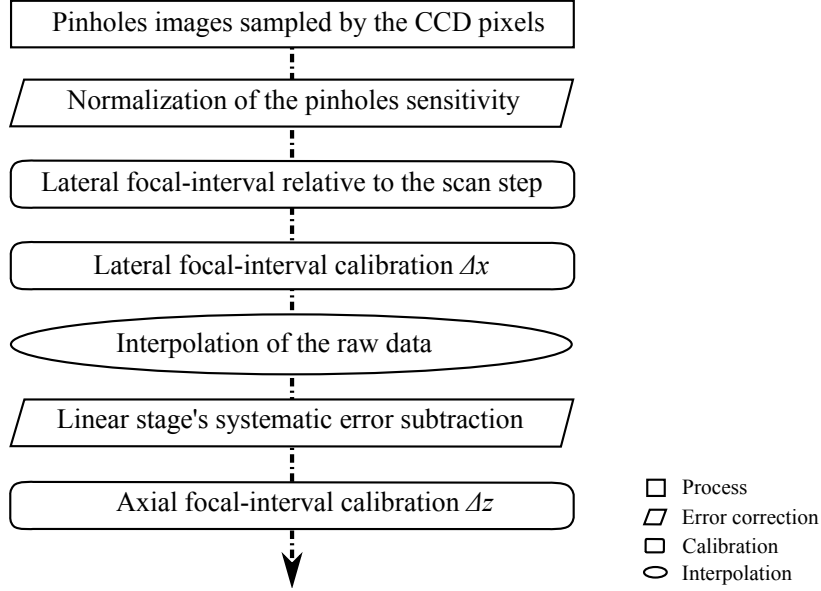


Figure 5.9: Flowchart of the error corrections and calibrations applied in the CLSS, following the practical implementation order.

light passing through the pinholes may be reduced, for instance, by dust particles on the pinhole apertures, thereby decreasing the pinhole sensitivity. The second step in Figure 5.9 is the normalization of the pinhole sensitivity, which helps to eliminate non-uniform detection sensitivity of a pinhole across the focal line. This step attributes to a systematic error correction. After the pinhole sensitivity is normalized, the lateral focal-interval (Δx) can be calibrated relative to the scan step (ΔF) in the third step, which also means that both distances need be calibrated further in the absolute length unit in the fourth step. As previously mentioned, a scan step (ΔF) differed from the lateral focal-interval (Δx) can result in a finer lateral sampling interval (Δs), so some of the data in the sorted stack are missed out of every Δs sampling interval. In consequence, an interpolation is required to interpolate raw data to fill the missing gaps in the fifth step, so to improve the data density in the lateral direction. In the sixth step, systematic errors caused by the linear scanning stage is corrected. Finally, after the axial focal-interval (Δz) is calibrated, an accurate 2D profile is obtained.

5.2.1 Images of the pinholes sampled by the CCD

Figure 5.10 (a) shows that an in-line images of the pinholes formed at the CCD can be adjusted to be in line with the CCD's pixels. Accordingly, the sampling condition is greatly simplified. Only the CCD pixels which can detect the intensity of light passing through the pinholes are then selected. The rest of uninformative

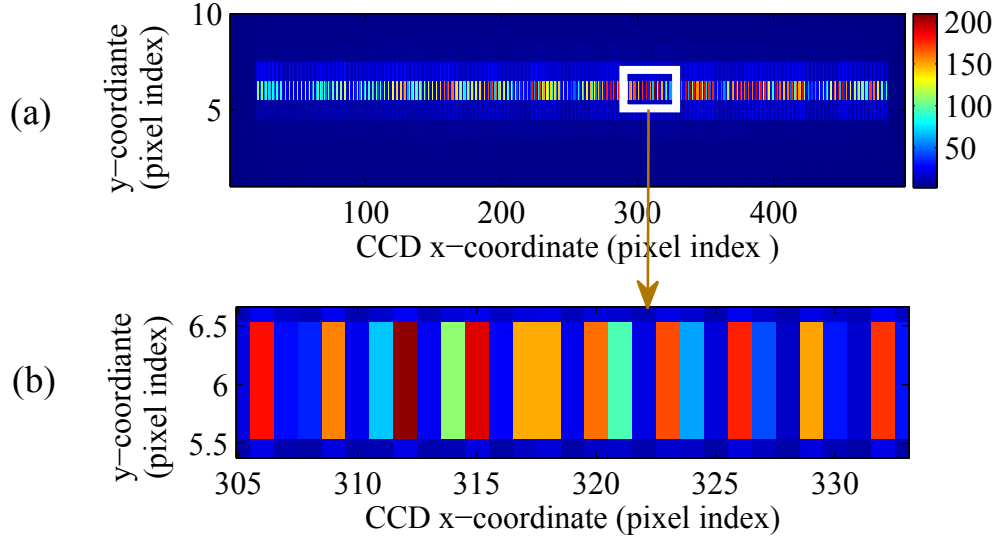


Figure 5.10: Images of the pinholes sampled by the CCD pixels. (a) the pinhole images are in line with the CCD pixels (b) a close-up view of the pixel sampling.

pixels are then excluded. Though the images of the pinholes containing information of light reflected from the specimen will not be resolved by the CCD, the total intensity per pinhole should be captured with minimal loss. This means that a sampling condition that follows the Nyquist theorem is not applied here. In this situation, the optimal sampling condition would be when a pinhole image is sampled by one CCD pixel. This follows the fact that the total intensity per pinhole can be captured by the full area of a pixel, such that any noise is limited to only one pixel.

The CCD used in the CLSS is a black and white CCD camera from AVT Dolphin, F145B, having the pixel size of $6.45 \times 6.45 \mu\text{m}^2$. Basically, the size of the CCD pixel is set by manufacturing limitations. A large-scale integrated circuit of preferable quality and a small capacitor demanding at near perfect operational condition place a limit on the size of the CCD pixel. Nowadays, megapixel CCD cameras having 2 – 10 micrometers width per pixel can successfully be produced [35]. However, a small pixel size is not necessary in the case of the CLSS. Thus, the optical system of the CLSS is designed in a way that the image of a pinhole is formed onto a single CCD pixel.

Nevertheless, Figure 5.10 (b) shows that the image of a pinhole can be sampled by a couple of the CCD pixels. In demonstrating a sampling by more than one pixel the noise level is increased accordingly. The *signal-to-noise ratio* (SNR) is then calculated in respect to three different sampling conditions as case studies:

- one pinhole image sampled by one pixel,
- one pinhole image sampled by two pixels,

- one pinhole image sampled by three pixels.

Consider that the intensity output acquired by a CCD pixel is measured in the form of the intensity signal plus additive noise, as expressed by

$$\begin{aligned} y_1 &= s_1 + n_1 \\ y_2 &= s_2 + n_2 \\ &\vdots \\ &\vdots \\ y_i &= s_i + n_i \end{aligned}$$

where y represents the total intensity output per pixel, s denotes the signal level per pixel, and n is the noise level per pixel, where i denotes the number of pixels.

In addition, the most complete equation to calculate SNR of a CCD was proposed by Merline and Howell [54, 35], which takes the expression

$$SNR = \frac{N_*}{\sqrt{N_* + n_{pix}(1 + \frac{n_{pix}}{n_B})(N_s + N_D + N_R^2 + G^2\sigma_f^2)}}, \quad (5.2)$$

where N_* is the total number of photons signal collected from the object of interest per pixel. n_{pix} represents the number of pixels. The term, $(1 + \frac{n_{pix}}{n_B})$, provides a measure of the noise of the background level on the CCD image. N_s is the total number of photons per pixel from the background. N_D is the total number of dark current electrons per pixel. N_R^2 is the total number of electrons per pixel resulting from the read noise. Note that this noise source is not a Poisson noise source but rather a shot noise; as a result it enters into the noise calculation as the value itself, not the square root of the value, as Poisson noise sources do. In the last term $(G^2\sigma_f^2)$, G is the gain of the CCD in electrons/analog-to-digital unit, where σ_f is an estimate of 1 sigma error introduced by the analog-to-digital conversion.

When only a single pixel is considered, noise per pixel can be obtained as

$$N = N_* + (1 + \frac{1}{n_B})(N_s + N_D + N_R^2 + G^2\sigma_f^2). \quad (5.3)$$

Based upon these rigorous equations to calculate the SNR as a function of the CCD noises, the SNR in regard of three different cases of the pixel sampling conditions are evaluated as follows. For simplicity, it is presumed that there is no defective pixel comprising in the CCD.

Case 1: the image of a pinhole is sampled by a CCD pixel. Therefore, $s_1 = N_*$ represents the total number of the photons collected per pixel. $N_1 = N$ is the total number of photons representing total noise per pixel, expressed by eq.(5.3). Therefore, the intensity output is obtained as $y_1 = N_* + N$. In consequence, the signal-to-noise ratio calculated using eq.(5.2) becomes

$$SNR = \frac{N_*}{\sqrt{N_* + N}}.$$

Case 2: the image of a pinhole is sampled by two CCD pixels. Assume that the total number of the photons collected is now split equally into two pixels, so that $s_1 = s_2 = \frac{1}{2}N_*$. The total number of the photons representing total noise per pixel is the same for each pixel, where $N_1 = N_2 = N$ following eq.(5.3). The intensity output is then obtained as $y_1 + y_2 = N_* + 2N$. The signal-to-noise calculated using eq.(5.2) finally takes the form

$$SNR = \frac{N_*}{\sqrt{N_* + 2N}}.$$

Case 3: the image of a pinhole is sampled by three CCD pixels. Now, assume that the total number of the photons collected is split equally into three pixels, such that $s_1 = s_2 = s_3 = \frac{1}{3}N_*$. The total number of the photons representing total noise per pixel is considered to be the same for each pixel, where $N_1 = N_2 = N_3 = N$ following eq.(5.3). The intensity output is thus determined by $y_1 + y_2 + y_3 = N_* + 3N$. Following eq.(5.2), the signal-to-noise is obtained as

$$SNR = \frac{N_*}{\sqrt{N_* + 3N}}.$$

It can be seen that the best sampling condition is when the image of an individual pinhole is sampled by a single CCD pixel, resulting in the highest SNR. When the image of a pinhole at the CCD is larger than one pixel or imaged by several pixels, the SNR is reduced due to higher additive noise accumulating by more pixels, as illustrated in the second and third cases. Nevertheless, it was suggested by Howell [35] that the SNR can be improved by using a pixel binning mode.

5.2.2 Normalization of the pinholes sensitivity

After processing with the pixel sampling of the pinhole images, detection sensitivity of the pinholes across the focal line should be normalized. Non-uniform detection sensitivity of the pinholes across the focal line can lead to the degradation of the axial response, since the data from different pinhole channels will be sorted out in a mixing order to reveal an axial response. Accordingly, vignetting effect and imperfections of the pinhole apertures can degrade the detection sensitivity of the pinholes at the detector. The vignetting effect means that the image is dimmer at the borders compared to the center region. For an 8-bit CCD camera, gray-scale sensitivity ranges between 0 - 255. However, the gray-scale sensitivity is attenuated if the local maximum of the detected intensity is much lower than 255.

Figure 5.11 (a) shows that the local maximum of the intensity detected at the CCD across the focal line is not uniform. To mitigate this effect, the detection sensitivity is normalized by the local maximum intensity of each pinhole. In the CLSS, 160 pinholes are used to produce 160 sampling points per full line of scan. After the normalization, the maximum gray scale value is made uniformly across the focal line regardless of the pinhole positions, depicted in Figure 5.11 (b).

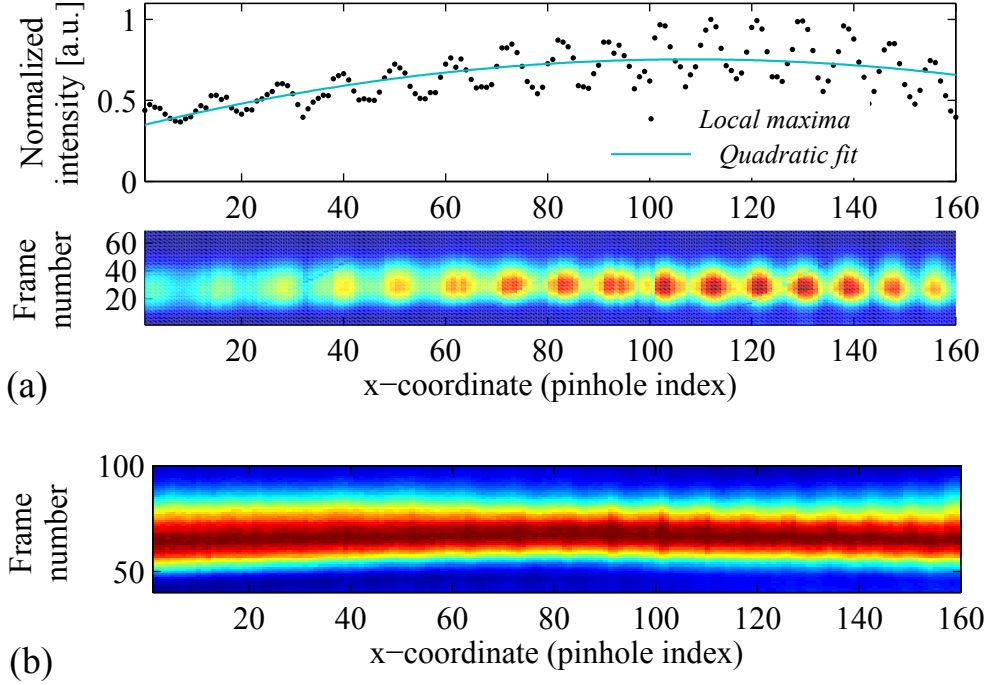


Figure 5.11: Normalization of the pinholes sensitivity. (a) Non-uniform pinholes sensitivity across the focal line. (b) Normalized pinholes sensitivity across the focal line.

5.2.3 Lateral focal-interval relative to the scan step size

The focal intervals, along the tilted focal line (Δx and Δz), should be calibrated before the surface profile can be accurately reconstructed. The calibration of the lateral focal-interval is more complicated than that of the axial focal-interval, and must be carried out in the preceding step. However, in the CLSS, the focal intervals can only be calibrated on a mean basis, which means that the errors of the focal intervals are averaged across the focal line. In this section, two calibration steps of the lateral focal-interval are presented; whereas the calibration of the axial focal-interval will be illustrated in the next step.

The developed algorithm for the lateral focal-interval calibration is effective, albeit relatively simple and robust. Since the calibration cannot be realized in one process, it is divided into two steps. In the first step, the lateral focal-interval is determined relative to the scan step size in an uncalibrated length unit, denoted by Δx_{rel} and ΔF_{idx} , respectively. Note that the scan step size can be seen as the distance separated between the data frames, so that it is represented by ΔF . In the second step, Δx_{rel} and ΔF_{idx} are then calibrated using a certified length of a standard specimen, such that the relative distances are now converted into an absolute length unit (μm).



Figure 5.12: Ultra high resolution target for use in the lateral focal-interval calibration. The black area represents the glass plate, whereas the white area depicts the chrome layer of periodic patterns.

An ultra high resolution target, shown in Figure 5.12, is used as a certified standard for the lateral focal-interval calibration. The periodic patterns are created on a thin layer of chrome on a glass plate. The periodic chrome pattern on a glass substrate, when measuring with the CLSS, creates parallel inclined strips in the raw stack, depicted in Figure 5.13 (a). With a certified period of an ultra high resolution target, a constant inclination of parallel strips is used to linearly relate the scan step size (ΔF_{idx}) to the lateral focal-interval (Δx_{rel}), using eq.(5.4). In consequence, the Hough transform for edge detection [36] is applied to roughly fit lines to the edges of parallel inclined strips. Then, a line-fitting optimization technique is additionally implemented to optimize the line fitting, where the result is shown in Figure 5.13 (b).

$$\text{slope} = \tan(\vartheta) = \frac{\Delta F_{idx}}{\Delta x_{rel}}, \quad (5.4)$$

The mean value of the inclined angle of parallel strips is $0^\circ < \vartheta < 90^\circ$. Then, Δx_{rel} and ΔF_{idx} in the index unit or an uncalibrated length unit can subsequently be calibrated with the known period of an ultra high resolution target.

The Hough transform can be best executed in MATLAB by setting parameters as follows: “RhoResolution = 1 – 2” and “ThetaResolution = 0.3 – 0.6” in the *Hough* function, and “FillGap= 5 – 7” and “MinLength= 7 – 9” in the *Houghlines* function. The *Hough* function is used to detect lines, and the *Houghlines* function is employed to extract line segments for the Hough transformation. However, the Sobel operator should be first applied to mark points at the edges before carrying

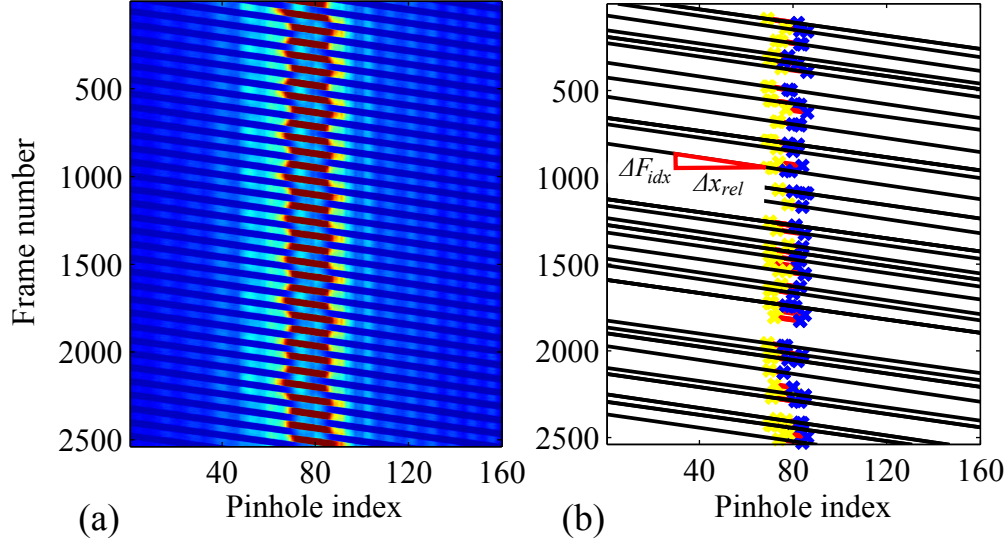


Figure 5.13: Lateral focal-interval (Δx_{rel}) relative to a scan step size (ΔF_{idx}). (a) Parallel inclined strips obtained using an ultra high resolution target. (b) Lines fitting to the edges of parallel inclined strips, giving the linear relation between Δx_{rel} and ΔF_{idx} in index unit.

out the edge detection using the Hough transform. Nonetheless, a Scharr filter is employed instead, since it is as fast as but more accurate than the Sobel filter [9, 39]. The coefficients of the Scharr filter include

$$\begin{bmatrix} 3 & 10 & 3 \\ 0 & 0 & 0 \\ -3 & -10 & -3 \end{bmatrix}, \text{ for filtering horizontal edges}$$

and

$$\begin{bmatrix} 3 & 0 & -3 \\ 10 & 0 & -10 \\ 3 & 0 & -3 \end{bmatrix}, \text{ for filtering vertical edges.}$$

Here, the filter coefficient for filtering vertical edges is proven to be more effective in most cases.

After applying the Hough transform, lines are not yet optimally fitted to the data set. As a result, introducing an extra step to optimize the line-fitting can help to improve the accuracy of the calibration. An optimization algorithm based upon minimizing the vertical-offset is developed particularly for use in this case. In consequence, the optimization is performed by windowing along the edges of the parallel inclined strips shown in Figure 5.13 (b). A line is then optimally fitted to one of the edges by minimizing the vertical offset between the previously fitted line and the data inside the windowing area.

5.2.4 Lateral focal-interval calibration

The reflectivity difference between the chrome layer and the glass substrate of the ultra high resolution target allows the relative scan step size (ΔF_{idx}) and the lateral focal-interval (Δx_{rel}) to be calibrated with the known length. Thus, this section presents the final step of the lateral focal-interval (Δx) calibration. It is worth noting that the data stack can only be sorted out in an uncalibrated length unit using the knowledge of the obtained Δx_{rel} . Subsequently, (Δx_{rel}) is calibrated by the known period of an ultra high resolution target, in connection with the period of the reflection result shown in Figure 5.14. After the reflectivity is plotted in an uncalibrated length unit, the measured period of the ultra high resolution target (Γ) can be extracted by applying the *autocorrelation* technique. The expression of the autocorrelation is given by

$$c(x) = f(x) \odot f(x) = \int_{-\infty}^{+\infty} f(x')f(x' - x) dx',$$

where $c(x)$ is the autocorrelation result, and $f(x)$ represents the reflectivity as a function of x . The symbol \odot denotes the autocorrelation operation.

In consequence, the autocorrelation of the reflection result is obtained in Figure 5.15. The rectangular-like silhouette of the maxima and minima in Figure 5.15 is resultant from the autocorrelation of a rectangular-like pattern in Figure 5.14 [10]. The measured period (Γ) is then calculated by averaging the period of the autocorrelation maxima and minima. Thereupon, a correction factor (ζ) can be obtained by dividing the certified period of the ultra high resolution target (P) by the measured period (Γ), using eq.(5.5). With this correction factor, the lateral focal-interval (Δx) and the scan step size (ΔF) are finally converted into an

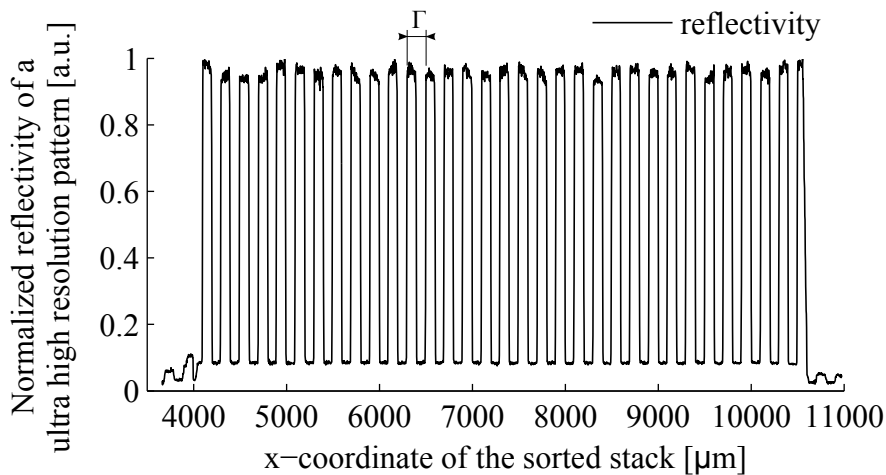


Figure 5.14: The reflection result obtained with an ultra high resolution target, where Γ is the measured period of the reflection-result in an uncalibrated length unit.

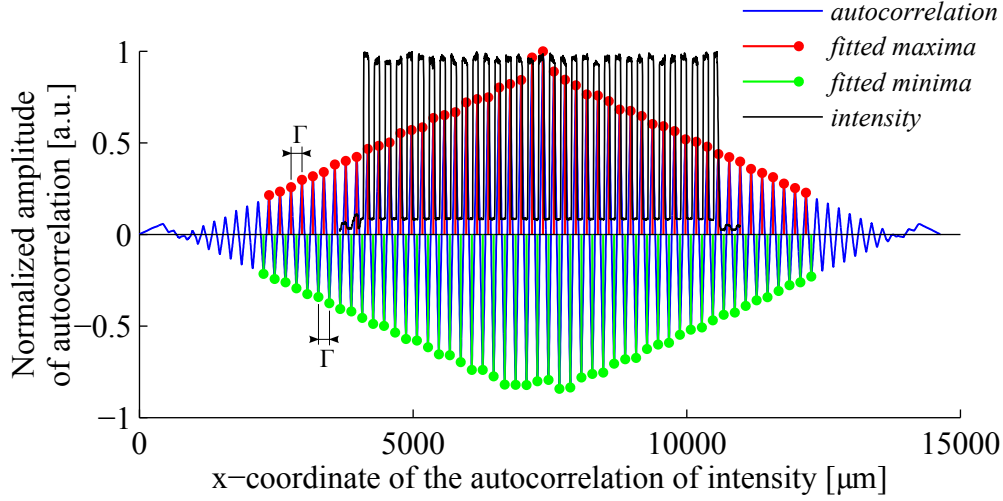


Figure 5.15: Autocorrelation of the reflection result of an ultra high resolution target. The black line represents the intensity of the reflection result, whereas the blue line is its autocorrelation result, having a period between the maxima and the minima equivalent to Γ . This measured period of the reflection result is in the uncalibrated length unit.

absolute length unit, where $\Delta x = \zeta \cdot \Delta x_{rel}$ and $\Delta F = \zeta \cdot \Delta F_{idx}$.

$$\text{correction factor} = \zeta = \frac{P}{\Gamma}. \quad (5.5)$$

The lateral focal-interval (Δx) of $5.05 \mu\text{m}$ is obtained with standard deviation of $0.0343 \mu\text{m}$, from twenty data sets. The calibrated Δx is found to be 1.0097 times higher than the designed value of $5 \mu\text{m}$.

5.2.5 Interpolation of the raw data

The lateral sampling interval (Δs) in the CLSS can be varied by adjusting the scan step size (ΔF), where Δs is at least equal to ΔF . If the specimen is scanned with $\Delta F = 1/3\Delta x$, the sorted stack will look like Figure 5.16. In consequence, the interpolation of the raw data to fill in the missing gaps will improve the data density in the lateral direction, in this example, up to 3 times the non-interpolated density. The missing points are denoted by the cross symbols. If the scan step size is fine enough, the lateral resolution is improved to meet the limit of the optical lateral resolution. On the contrary, the measurement time is drastically increased.

If the number of the missing points are much higher than the actual sampling points in the raw data, the interpolation will add up uncertainty to the measurement result. Oversampling by interpolating the raw data will then attribute to the degradation of the accuracy of the profile measurement. This is obvious when sampling with a fraction of Δx . However, the interpolation strategy is extremely

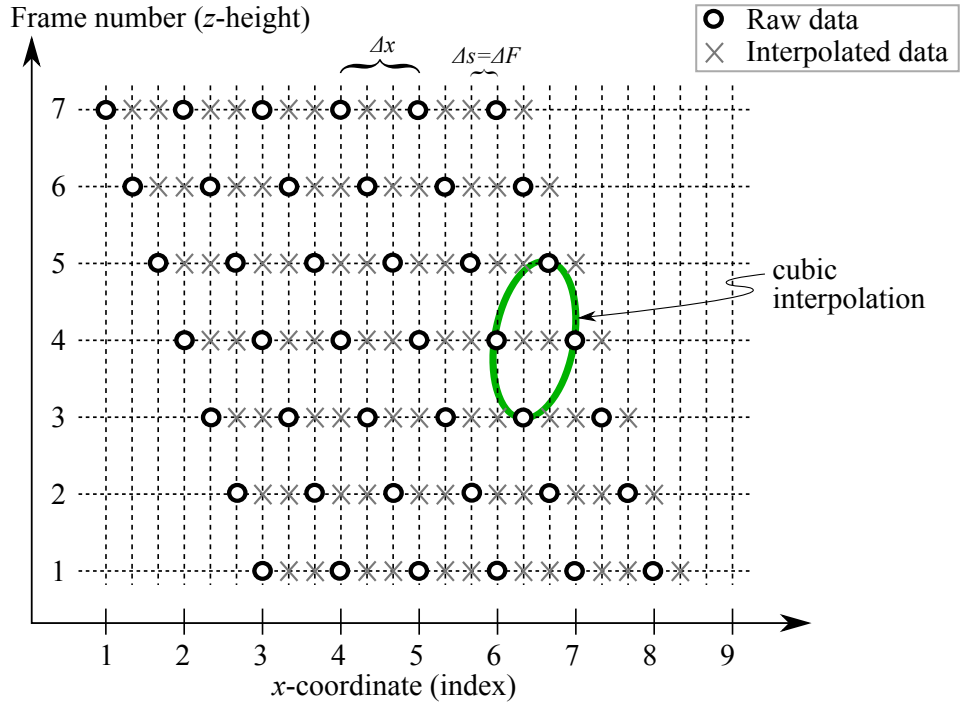


Figure 5.16: Interpolation of the raw data. This schematic shows an example case when the specimen is scanned with $\Delta F = 1/3\Delta x$. The data density along the x axis is triply increased, since the scan step size is reduced by a fraction of three.

useful in real applications, when the distance errors between the focal interval and the scan step size can be compensated. In consequence, the interpolation of the raw data along the vertical dash lines at a given x sampling coordinate in Figure 5.16 is of vital importance, to preserve the axial sampling density and to maintain the quality of the axial intensity response.

The interpolation is implemented by a triangle-based cubic interpolation technique, using the “GRIDDATA” function provided in MATLAB. As compared to the linear interpolation of 2 points, the cubic interpolation of 4 points can be achieved with much better results [65].

5.2.6 Linear stage’s systematic error subtraction

A wave-like systematic error of the linear scanning stage is basically caused by the motor-driven lead screw, once discussed in Chapter 4. Nonetheless, the systematic error can directly be subtracted out of the measured profile. With a plane mirror and a step mirror, the obtained systematic errors are shown in Figure 5.17.

It can be seen that phase of the wave-like systematic error is shifted in connection with the feature of the specimen. With a step mirror, a height difference introduces phase shifting to the wave-like systematic error, where the height dif-

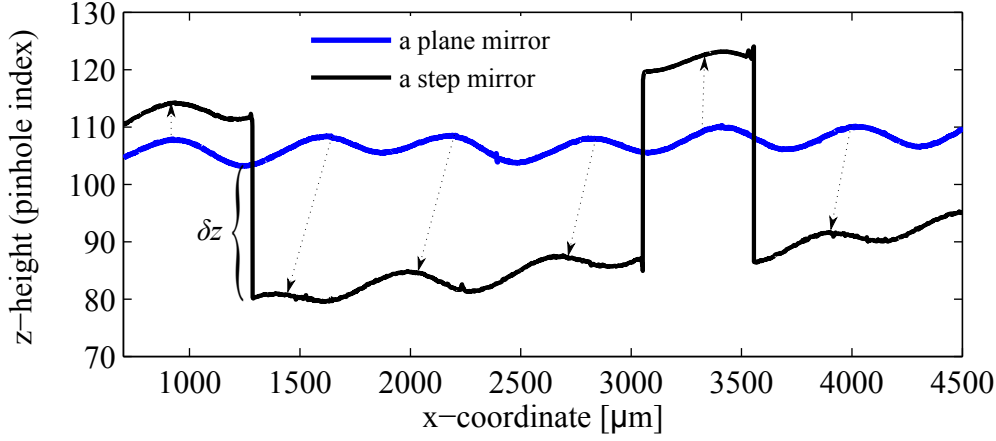


Figure 5.17: Systematic errors of the linear scanning stage obtained with a plane silicon-mirror and a step silicon-mirror. In the case of a step mirror, the systematic error varies in phase with δx increment, which is converted from the height difference of δz using eq.(5.6).

ference (δz) is related to the phase shift increment (δx) as

$$\delta x = \frac{\delta z}{\tan \Phi}, \quad (5.6)$$

where Φ is the tilt angle of the focal line. In consequence, the systematic error (E_{sys}) can be expressed in terms of the phase shift (δx) by

$$E_{sys} = \sum_{j=1}^n A \cdot e^{i(kx_j - \delta x_j)},$$

where $j = 1, \dots, n$ are the lateral sampling points. A is the amplitude of the wave-like error and $k = 2\pi/\Lambda$, where Λ is the wavelength of the wave-like error.

The developed algorithm for the systematic error subtraction initially requires a reference of the systematic error before implementing the subtraction. A reference of the systematic error is obtained by measuring a plane mirror. Thereafter, phase of the systematic-error reference will be corrected and shifted in connection with the surface features, which have the heights differ from the reference mirror. With the knowledge of the height differences, the phase correction along the sampling x coordinates can then be implemented by applying the cubic spline interpolation. In consequence, Figure 5.18 and Figure 5.19 depict the results of the interpolated systematic-errors and the subtractions of a sinusoidal standard (PTB 5381 with $R_a = 0.951 \mu\text{m}$) and a roughness standard (PTB 5602 with $R_a = 1.63 \mu\text{m}$), respectively. The systematic-error correction presented in this section is relatively robust, and can be executed in MATLAB as an off-line process.

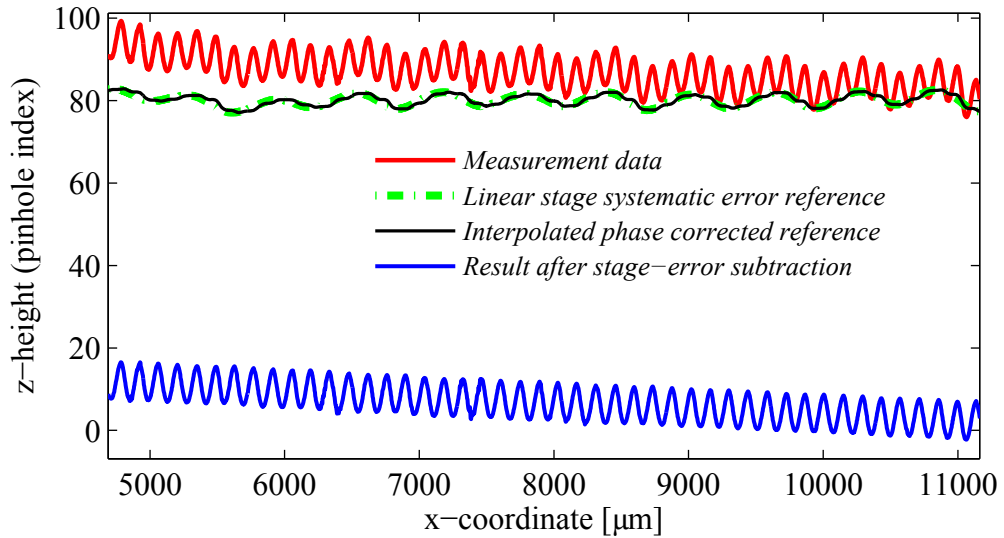


Figure 5.18: Two-dimensional profile of a sinusoidal standard PTB 5381 with $R_a = 0.951 \mu\text{m}$, a systematic error of the linear stage, and the corresponding phase-corrected reference. The 2D height profile after the systematic error subtraction can be seen at the bottom.

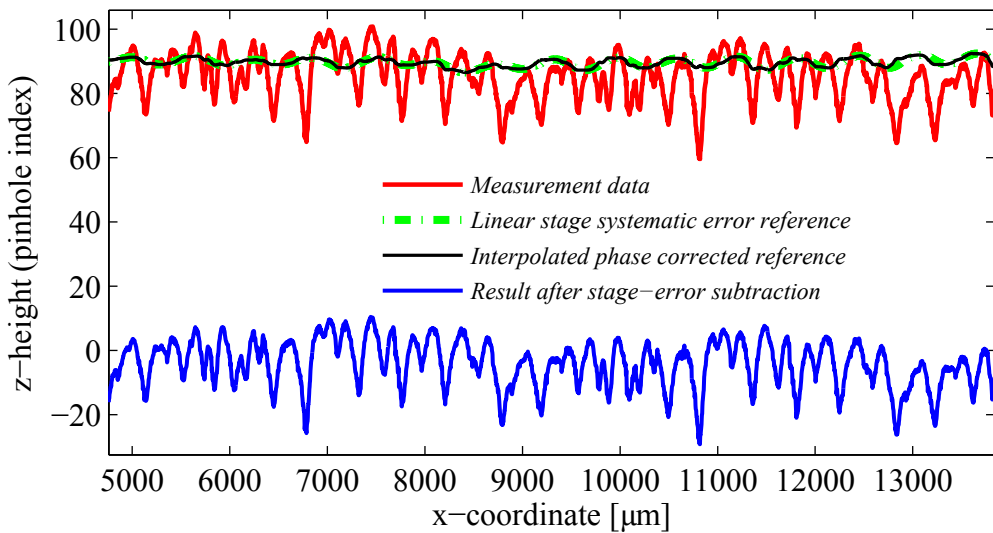


Figure 5.19: Two-dimensional profile of a roughness standard PTB 5602 with $R_a = 1.63 \mu\text{m}$, a systematic error of the linear stage, and the corresponding phase-corrected reference. The 2D height profile after the systematic error subtraction can be seen at the bottom.

5.2.7 Axial focal-interval calibration

In the last step of the calibration process, the axial focal-interval (Δz) is calibrated with a certified depth-standard. This process is to convert the measured profile height in the pinhole-index unit into a physical length unit, normally in μm . A depth standard used for this task is a groove standard, certified according to A2(ISO 5436-1) standard by Physikalisch Technische Bundesanstalt Braunschweig (PTB). The height evaluation and the calibration can be executed only after the groove profile is reconstructed in the pinhole-index unit and the systematic error of the linear scanning stage is subtracted from the data, shown in Figure 5.20 (a). Accordingly, Δz is calibrated by

$$\Delta z = n \cdot h_{groove}, \quad (5.7)$$

where n is a non-integer number of the pinhole-indices covering the z -height of the groove depth, and where h_{groove} is a certified groove depth. Note that the groove depth profile is evaluated following DIN EN ISO² 5436-1 standard. The evaluation is carried out in a windowing area of about three times the groove width. Then, the groove base is fitted with a polynomial second order preceding the groove depth evaluation.

This method of calibration is used to calibrate the axial focal-interval on a mean basis, such that the error of the axial focal-interval is averaged across a certain range of the foci covering one groove. A selected groove of $9 \mu\text{m}$ in Figure 5.20 (b) is roughly covered by 28 pinhole-indices. In consequence, Δz of $0.324 \mu\text{m}$ is obtained with standard deviation of $0.05 \mu\text{m}$ calculated from ten data sets, where Δz is designed at $0.35 \mu\text{m}$.

5.3 One-dimensional roughness parameters

One-dimensional roughness parameters of a reconstructed 2D height profile can now be evaluated. One-dimensional texture is basically split into *waviness* and *form* (the low-frequency components defining the overall shape) and *roughness* (the high-frequency components) at the cut-off frequency following the standards, i.e., ASME B46.1-1985 and ISO 4287-1997. In general, there is no concrete rule setting for defining the frequency of roughness, waviness and form. It depends on the nature of surfaces³ and machining processes [112]. However, the standards provide general information on the cut-off frequency, the evaluation of roughness

²DIN stands for “Deutsches Institut für Normung” (German Institute for Standardization). EN represents “Ergonomics of human-system interaction”, and ISO denotes “International Organization for Standardization”.

³The surface is defined as a boundary of the erosion, in the mechanical scheme [112]. Most of the engineering components’ failures are caused by the surface initiation [22, 112]. This means that the surface characteristics can give an in depth intuition into further subjects such as the prediction and prevention of the failure and product lifetime.

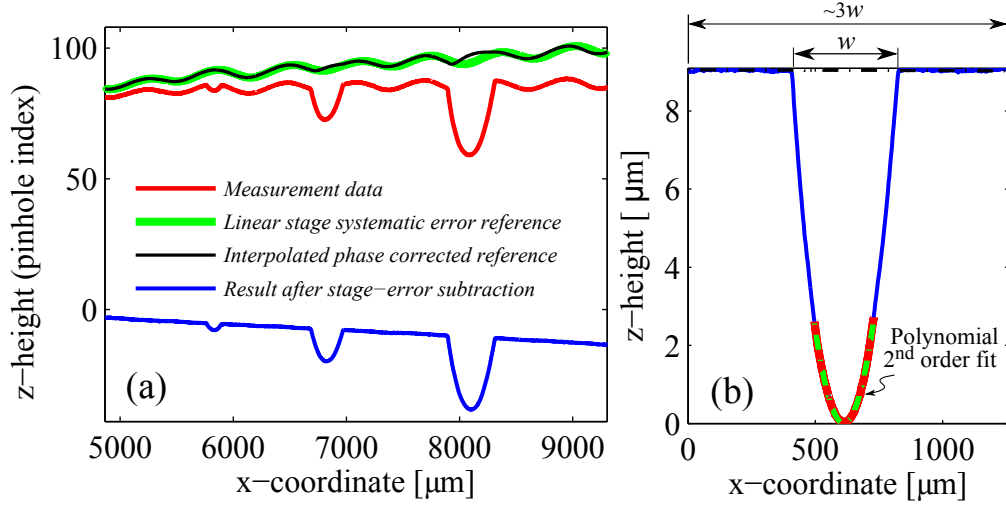


Figure 5.20: Axial focal-interval calibration using a certified groove standard. (a) Reconstructed groove profile before and after the systematic error subtraction in the pinhole-index unit. (b) A selected groove of 9 μm for depth evaluation following DIN EN ISO 5436-1 standard.

parameters, and the filtering techniques. The most common filter applied is the Gaussian filter [98].

One-dimensional roughness parameters are essentially classified into different groups, including amplitude or height, spacing, and hybrid parameters. However, these roughness parameters mainly provide statistical information not functional information [98]. The amplitude parameters are sufficient for the analysis of the CLSS. Therefore, notably six of one-dimensional roughness parameters are briefly presented here, illustrated in Table 5.1. Further information on additional roughness parameters can be seen in ASME B46.1-1985 and ISO 4287-1997.

The expressions of these six roughness parameters are given below [98]. Arithmetic mean, R_a , is expressed by

$$R_a = \frac{1}{N} \sum_{n=1}^N (z_n - \bar{z}). \quad (5.8)$$

It is commonly used to indicate the smoothness of the surface in general, and is measured in term of the average height as the mean value.

Root mean square (RMS), R_q , takes the form

$$R_q = \sqrt{\frac{1}{N} \sum_{n=1}^N (z_n - \bar{z})^2}. \quad (5.9)$$

It represents the dispersion statistics of the height values with respect to the mean value, in the form of the RMS or standard deviation.

Maximum peak to valley, R_t , can be formulated as

$$R_t = (|R_{pi}| + |R_{vi}|)_{max}, \quad \text{for } 1 \leq i \leq M, \quad (5.10)$$

where $M = 5$. $R_{pi_{max}}$ is the highest peak and $R_{vi_{max}}$ is the deepest valley, within each of the five subsections.

Ten points average height difference, R_z , can be obtained as

$$R_z = \frac{1}{M} \sum_{i=1}^M (|R_{pi}| + |R_{vi}|), \quad \text{for } 1 \leq i \leq M, \quad (5.11)$$

where $M = 5$. It is the average of the maximum distance from peak to valley, within each of the five subsections.

Skewness, R_{sk} , is formulated as

$$R_{sk} = \frac{1}{N \cdot R_q^3} \sum_{n=1}^N (z_n - \bar{z})^3. \quad (5.12)$$

It gives a measure of the symmetry of the profile height distribution with respect to the mean value, depicted in Table 5.1. R_{sk} equaling to zero represents a symmetry Gaussian curve, while the positive and negative values of R_{sk} indicate asymmetry of the distribution curve. Therefore, when $R_{sk} > 0$ it physically interprets a spiky-like 2D profile, whereas when $R_{sk} < 0$ it suggests a *flat top-* or *deep valley-* like 2D profile.

Kurtosis, R_{ku} , is given by

$$R_{ku} = \frac{1}{N \cdot R_q^4} \sum_{n=1}^N (z_n - \bar{z})^4 - 3. \quad (5.13)$$

It gives a measure of the sharpness of the profile height distribution, depicted in Table 5.1. R_{ku} is zero in the case of the Gaussian curve. The positive of R_{sk} indicates a wider but flat top curve, while the negative of R_{sk} points out a narrower and sharper curve of the profile height distribution. However, R_{sk} has no physical meaning. In addition, -3 can be omitted from the calculation in certain cases, which make $R_{ku} = 3$ *not zero*, in the case of a Gaussian curve.

5.4 Conclusion

The developed data processing and calibrations for the CLSS are thoroughly described in this chapter. The equally spaced foci facilitate the simplification of the data processing and calibrations. In addition, the focal points formed in a tilted line are used to repeat the sampling points step after step in both the vertical and lateral directions. According to the new approach of the CLSS, a scan step size of

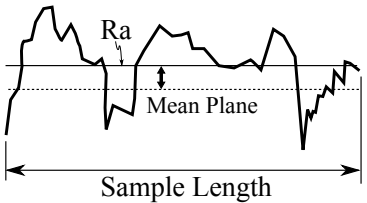
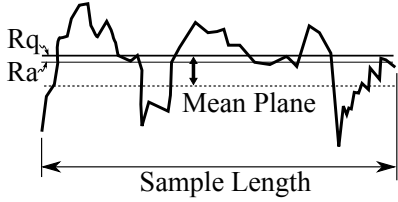
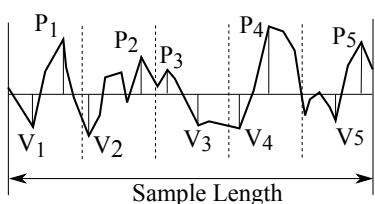
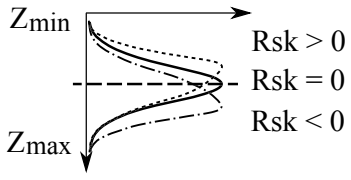
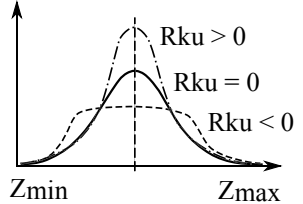
the specimen is adjustable to optimize the data sampling density and the lateral resolution. However, this will compromise the measurement time. If the lateral sampling interval is fine enough, e.g. approaching size of the focal point, the lateral resolution can then be defined by the lateral optical resolution. However, the real axial resolution of 11.7 nm obtained in the CLSS is determined based on the noise limited approach.

When the systematic and statistical errors inherent in the CLSS system are taken into account, additional data processing, calibrations and interpolation are necessitated. Therefore, the proposed techniques in this chapter are summarized as follows:

- The CCD detection sensitivity is normalized by the local maximum intensity detected by each pinhole. This helps to optimize the axial intensity response after applying the data sorting process.
- In the case that a scan step size (ΔF) is made different from the lateral focal interval (Δx), a triangle-based cubic interpolation technique is applied to interpolate the raw data. In consequence, the axial sampling density at a given x coordinate is maintained at the highest possible value as allowed by the actual sampling points along the axial direction.
- The lateral focal interval is then calibrated relatively to the scan step size using a developed techniques, based on Hough transformation for edge detection and line fitting optimization.
- In consequence, the lateral focal interval is calibrated with a known length of a periodic standard, where the x -coordinate in an uncalibrated length unit resulted from the previous step is converted into an absolute length unit, i.e. μm .
- Next, a wave-like error of the linear scanning stage is corrected by directly subtracting it from the measurement data. A reference of the wave-like error is first acquired using a plane mirror. Then, the phase shifting of the wave-like error, caused mainly by the height differences between the specimen surface and the reference mirror, is corrected using a cubic spline interpolation technique.
- Finally, the axial sampling interval (Δz), or the *axial focal interval*, is calibrated with a known depth standard, following the calibration procedure provided in DIN EN ISO 5436-1 standard.

Accordingly, a series of the axial responses along the x coordinate is evaluated using the *center of gravity* algorithm, to find the maximum peak of the response curve, which corresponds to the real surface height at a given x coordinate. A 2D height profile is thus reconstructed as the final result.

Table 5.1: Illustration of one-dimensional roughness parameters, according to ISO 4287-1997 standard.

Symbol	Parameter	Formula
R_a	Arithmetic mean	
R_q	Root mean square (RMS)	
R_z R_t	Ten points average height difference Maximum peak to valley	
R_{sk}	Skewness	
R_{ku}	Kurtosis	

Chapter 6

Experimental Results and Discussions

This chapter is devoted to investigate the performance of the CLSS in many aspects. As a results, a series of experiments is conducted. First, the measurements of calibrated standard specimens are used to validate the *new concept* of the CLSS, where the measurement results are compared to those of a commercial Confocal Microscope (CM). Next, the effective resolution of the CLSS is investigated. Finally, the accuracy and precision of the CLSS are examined, in corresponding to prominent errors, such as the error of the scanned length in the lateral direction, residual aberrations inherent in the optical system, and the errors introduced by the tilting of the specimen.

6.1 Calibrated standards

In this section, the *new concept* of the CLSS is verified using calibrated standard specimens. The calibrated standards, including a sinusoidal standard and a roughness standard, calibrated by Physikalisch-Technische Bundesanstalt (PTB)¹ are used in this measurement. Thereafter, the measurement results are compared to those of a commercial Confocal Microscope (CM), showing comparable results.

6.1.1 PTB sinusoidal standard

The PTB sinusoidal standard with a periodic structure exploited in this experiment is shown in Figure 6.1. In this experiment, the measurement results of the CLSS correspond to the calibrated values and are in good agreement with that of a commercial CM, seen in Table 6.1 and Table 6.2. In consequence, it shows

¹The Physikalisch-Technische Bundesanstalt (PTB) is based in Braunschweig and Berlin. It is the national institute for natural and engineering sciences and the highest technical authority for metrology and physical safety engineering in Germany.

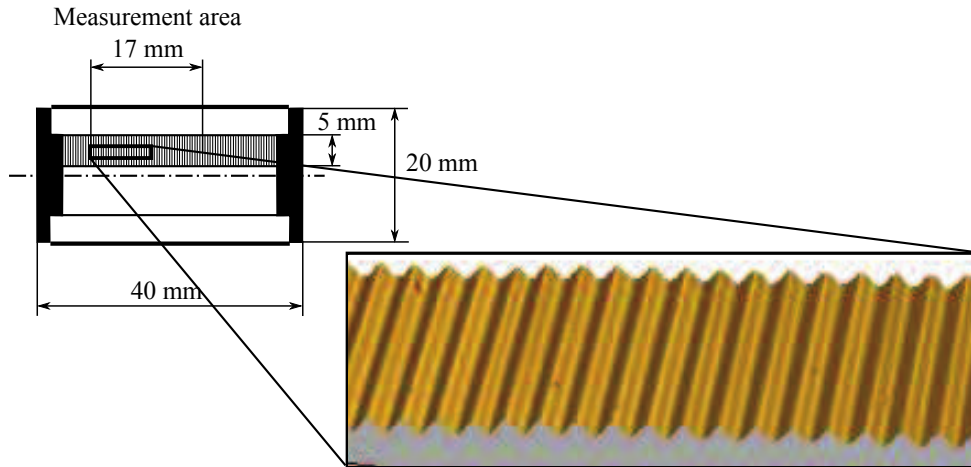


Figure 6.1: Illustration of a PTB sinusoidal standard with $R_a = 0.951 \mu\text{m}$.

Table 6.1: The calibrated results of a PTB sinusoidal standard, obtained with a tactile profilometer using a stylus radius of $\approx 5 \mu\text{m}$. The roughness parameters are calculated from twelve measurements according to DIN EN ISO 4287 (1998), after applying the filtering technique according to DIN EN ISO 11562 (1998).

Parameter	Mean	Maximum	Minimum	Standard deviation
R_a	$0.951 \mu\text{m}$	$0.953 \mu\text{m}$	$0.948 \mu\text{m}$	$0.001 \mu\text{m}$
R_z	$3.02 \mu\text{m}$	$3.03 \mu\text{m}$	$3.01 \mu\text{m}$	$0.01 \mu\text{m}$
R_t	$3.03 \mu\text{m}$	$3.05 \mu\text{m}$	$3.02 \mu\text{m}$	$0.01 \mu\text{m}$

that the incorporation of a tilted plane technique in a confocal imaging system is feasible. The measured profiles are carried out at three main locations on the sinusoidal standard: *at the left edge*, *in the middle*, and *at the right edge*, depicted in Figure 6.2, Figure 6.3 and Figure 6.4, respectively. The roughness parameters, shown in Table 6.2, are then calculated according to DIN EN ISO 4287 (1998), after applying the filtering to the measured profile with the cut-off wavelength of 0.8 mm , according to DIN EN ISO 11562 (1998).

A PTB sinusoidal standard used in this case was calibrated with a tactile profilometer using a stylus tip radius of $5 \mu\text{m}$ and 1 mN contact force. Twelve measurements were obtained across the entire measurement area. The total evaluation profile length of 4.0 mm was obtained after applying the cut-off wavelength of 0.8 mm . The roughness parameters calibrated by the PTB standard are thus summarized in Table 6.1.

A $20\times/0.45 \text{ NA}$ objective is used as a default objective in this measurement for both the CLSS and a commercial CM. Even though the sampling intervals in

Table 6.2: The measurement results of a PTB sinusoidal standard, measured with the CLSS and a commercial confocal microscope. The measurement results are carried out across the measurement area: *at the left edge, in the middle, and at the right edge*. The roughness parameters are calculated from three measurements according to DIN EN ISO 4287 (1998), after applying the filtering technique according to DIN EN ISO 11562 (1998).

CLSS				
Parameter	Mean	Maximum	Minimum	Range: Max - Min
R_a	0.953 μm	0.966 μm	0.940 μm	0.026 μm
R_q	1.057 μm	1.069 μm	1.044 μm	0.025 μm
R_z	3.143 μm	3.166 μm	3.114 μm	0.052 μm
R_t	3.262 μm	3.340 μm	3.169 μm	0.171 μm
R_{sk}	0.119	0.146	0.092	0.077
R_{ku}	-1.492	-1.480	-1.508	0.028
A commercial confocal microscope				
Parameter	Mean	Maximum	Minimum	Range: Max - Min
R_a	0.985 μm	0.987 μm	0.982 μm	0.0005 μm
R_q	1.097 μm	1.100 μm	1.090 μm	0.01 μm
R_z	3.357 μm	3.370 μm	3.340 μm	0.03 μm
R_t	3.507 μm	3.550 μm	3.480 μm	0.070 μm
R_{sk}	0.036	0.056	0.022	0.034
R_{ku}	-1.477	-1.470	-1.480	0.01

the CLSS case are coarser than in a commercial CM, the measurement results are in good agreement. This means that the lateral sampling interval of 2.5 μm is sufficient for inspecting the PTB sinusoidal standard having micro-lateral features larger than $\approx 5 \mu\text{m}$, following the Nyquist sampling theorem [62]. In the CLSS, the lateral sampling interval is 2.5 μm and the axial sampling interval is 0.324 μm , whereas the lateral sampling interval in a commercial CM is 0.8 μm and the axial sampling interval is 0.28 μm .

The roughness parameters obtained with the CLSS are more accurate with respect to the calibrated values. This demonstrates that the accuracy of the CLSS is relatively good, showing that the developed calibrations applied in the CLSS provide a good result. However, a higher range of the maximum to the minimum means that the precision of the CLSS is, to some degree, lower than the commercial CM. The causes of uncertainties in the CLSS are responsible for the degraded precision, which include the stepping error of the linear scanning stage and the mounting method of the specimen. The effects of these uncertainties will be investigated further in this chapter.

Note that irregular waviness of the profiles obtained with a commercial CM,

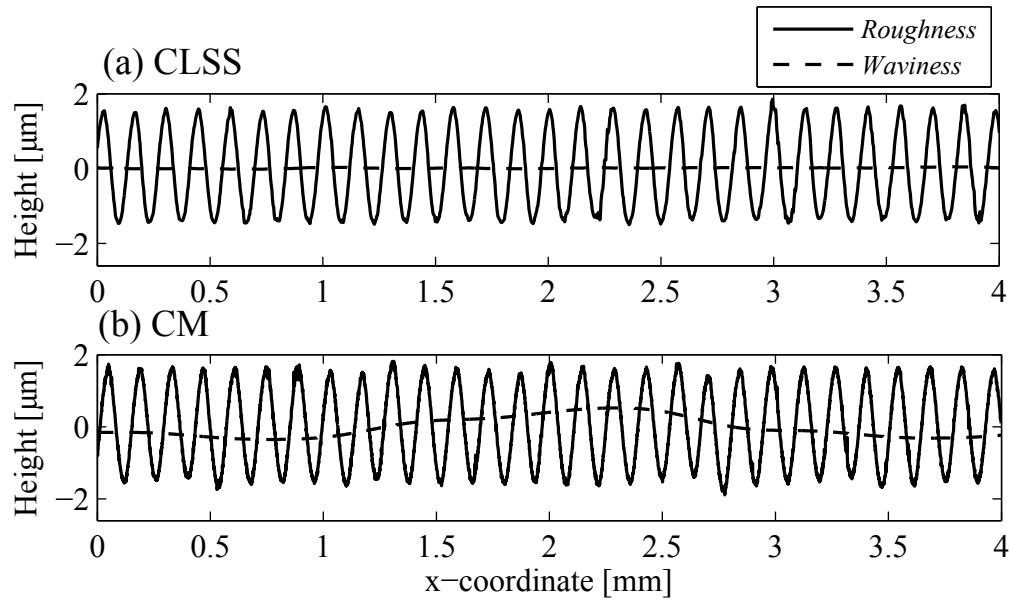


Figure 6.2: Comparison of the measurement results of a PTB sinusoidal standard having $R_a = 0.951 \mu\text{m}$, obtained with the CLSS and with a commercial confocal microscope (CM), *at the left edge* of the standard.

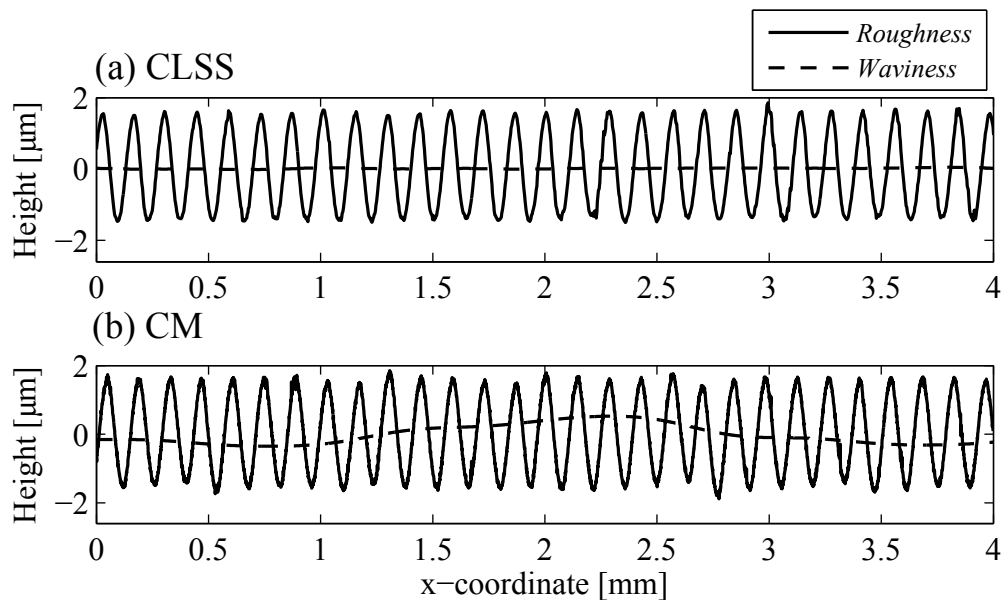


Figure 6.3: Comparison of the measurement results of a PTB sinusoidal standard having $R_a = 0.951 \mu\text{m}$, obtained with the CLSS and with a commercial confocal microscope (CM), *in the middle* of the standard.

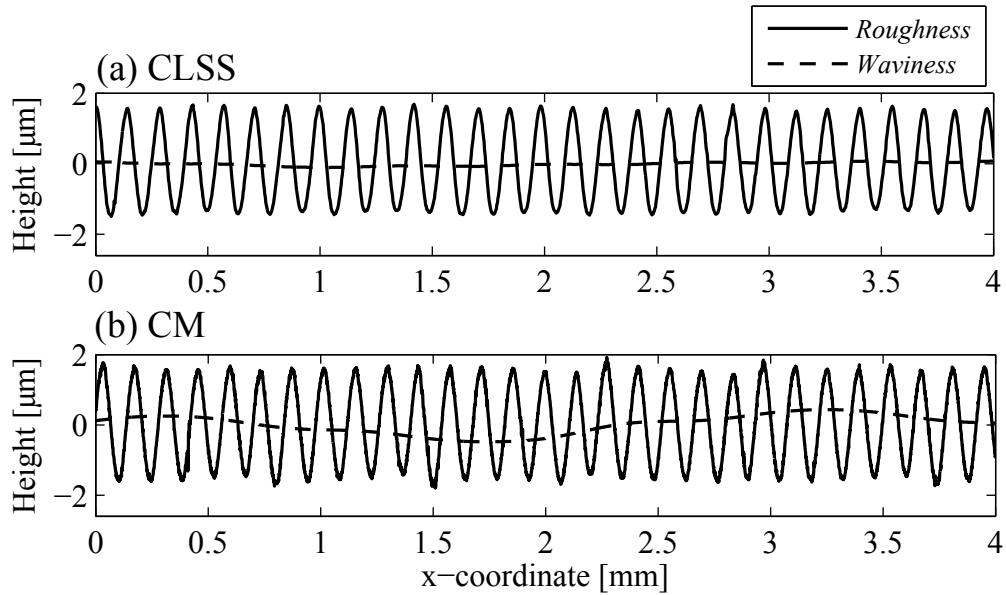


Figure 6.4: Comparison of the measurement results of a PTB sinusoidal standard having $R_a = 0.951 \mu\text{m}$, obtained with the CLSS and with a commercial confocal microscope (CM), *at the right edge* of the standard.

seen in Figure 6.2, Figure 6.3, and Figure 6.4, are caused by a correlation based stitching technique, which is not required in the CLSS. This effect is obvious, especially when measuring a periodic structure such as this sinusoidal standard.

6.1.2 PTB roughness standard

A PTB roughness standard having a non-periodic structure, shown in Figure 6.5, is also used to validate the *new concept* of the CLSS. The results of the CLSS, comparable to that of a commercial CM and the calibrated values, confirm that the CLSS and its new concept of a parallel depth scanning scheme are feasible. The measurements are carried out at two main locations on the roughness standard: *at the left edge* and *at the right edge*, where the measured data summarizing in Table 6.4 correspond to the calibrated values in Table 6.3. In addition, Figure 6.6 and Figure 6.7 demonstrate that the results obtained with the CLSS and a commercial CM are in good agreement.

The PTB roughness standard was calibrated with a tactile profilometer using a stylus tip radius of $5 \mu\text{m}$, a contact force of 0.6 mN , and a lateral sampling interval of $0.2 \mu\text{m}$. Twelve measurements were obtained across the entire measurement area and filtered with the cut-off wavelength of 0.8 mm , resulting in the total evaluation length of 4.0 mm . The roughness parameters calibrated by the PTB standard are then summarized in Table 6.3.

Similar conclusions on the CLSS performance can be drawn from the measure-

Table 6.3: The calibrated results of a PTB roughness standard, obtained with a tactile profilometer using a stylus radius of $\approx 5 \mu\text{m}$, a contact force of 0.6 mN, and a lateral sampling interval of $0.2 \mu\text{m}$. The roughness parameters are calculated from twelve measurements according to DIN EN ISO 4287 (1998), after applying the filtering technique according to DIN EN ISO 11562 (1998).

Parameter	Mean	Maximum	Minimum	Standard deviation
R_a	$1.63 \mu\text{m}$	$1.66 \mu\text{m}$	$1.59 \mu\text{m}$	$0.02 \mu\text{m}$
R_z	$7.84 \mu\text{m}$	$7.96 \mu\text{m}$	$7.68 \mu\text{m}$	$0.10 \mu\text{m}$
R_t	$9.87 \mu\text{m}$	$10.19 \mu\text{m}$	$9.62 \mu\text{m}$	$0.24 \mu\text{m}$

Table 6.4: The measurement results of a PTB roughness standard, measured with the CLSS and a commercial CM. The measurement results were carried out *at the left edge* and *at the right edge*. The roughness parameters are calculated from two measurements according to DIN EN ISO 4287 (1998), after applying the filtering technique according to DIN EN ISO 11562 (1998).

CLSS				
Parameter	Mean	Maximum	Minimum	Range: Max - Min
R_a	$1.655 \mu\text{m}$	$1.655 \mu\text{m}$	$1.654 \mu\text{m}$	$0.0001 \mu\text{m}$
R_q	$2.021 \mu\text{m}$	$2.021 \mu\text{m}$	$2.020 \mu\text{m}$	$0.0001 \mu\text{m}$
R_z	$7.929 \mu\text{m}$	$8.084 \mu\text{m}$	$7.774 \mu\text{m}$	$0.310 \mu\text{m}$
R_t	$10.029 \mu\text{m}$	$10.324 \mu\text{m}$	$9.734 \mu\text{m}$	$0.590 \mu\text{m}$
R_{sk}	-0.791	-0.779	-0.802	0.023
R_{ku}	0.094	0.139	0.049	0.090
A commercial confocal microscope				
Parameter	Mean	Maximum	Minimum	Range: Max - Min
R_a	$1.650 \mu\text{m}$	$1.650 \mu\text{m}$	$1.650 \mu\text{m}$	$0.0000 \mu\text{m}$
R_q	$1.995 \mu\text{m}$	$2.000 \mu\text{m}$	$1.990 \mu\text{m}$	$0.0100 \mu\text{m}$
R_z	$8.370 \mu\text{m}$	$8.510 \mu\text{m}$	$8.230 \mu\text{m}$	$0.280 \mu\text{m}$
R_t	$10.900 \mu\text{m}$	$11.100 \mu\text{m}$	$10.700 \mu\text{m}$	$0.400 \mu\text{m}$
R_{sk}	-0.807	-0.791	-0.822	0.031
R_{ku}	0.230	0.290	0.170	0.120

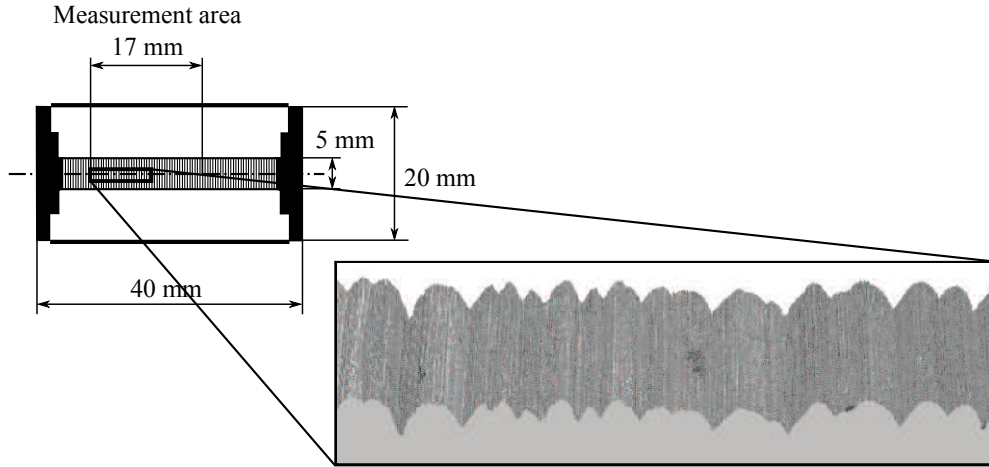


Figure 6.5: Illustration of a PTB roughness standard having $R_a = 1.63 \mu\text{m}$.

ment results of a PTB roughness standard. The CLSS seems to be more accurate than a commercial CM, when comparing the measured data to the calibrated values, but less precise, as the maximum and minimum are more diverged from the mean value in the CLSS case. The degraded precision of the CLSS will be investigated in connection with prominent *statistical errors* later in this chapter. The lateral sampling interval of $2.5 \mu\text{m}$ used in the CLSS allows the lateral structure of at least $5 \mu\text{m}$ to be resolved, following the Nyquist sampling theorem [62], which in this case is sufficient for measuring the PTB roughness standard. Therefore, a finer lateral sampling interval of $0.8 \mu\text{m}$ applied in a commercial CM might gain a bit more information on the micro-lateral structures down to $1.6 \mu\text{m}$. The axial sampling interval is rather the same in the CLSS case and a commercial CM case, which are $0.324 \mu\text{m}$ and $0.28 \mu\text{m}$, respectively.

Nonetheless, the correlation based stitching technique required in a commercial CM, not in the CLSS, works practically well when applying with a non-periodic structure of the PTB roughness standard, showing a good agreement of the roughness and the waviness in Figure 6.6 and Figure 6.7.

6.2 Axial resolution beyond the FWHM

This section investigates whether the axial resolution of the CLSS is beyond the diffraction limit [11], based on the *full-width at half-maximum* (FWHM) approach. Imagine that when an opaque surface is observed, the intensity of the axial response is distributed with a single maximum peak corresponding to the real surface height. The ability to resolve the surface height then depends on the technique used to find the maximum peak. Therefore, the real axial resolution of the CLSS is instead limited by the noise inherent in the axial response, as explained in the preceding chapter. In theory, the FWHM of the axial response is $2.3 \mu\text{m}$ when

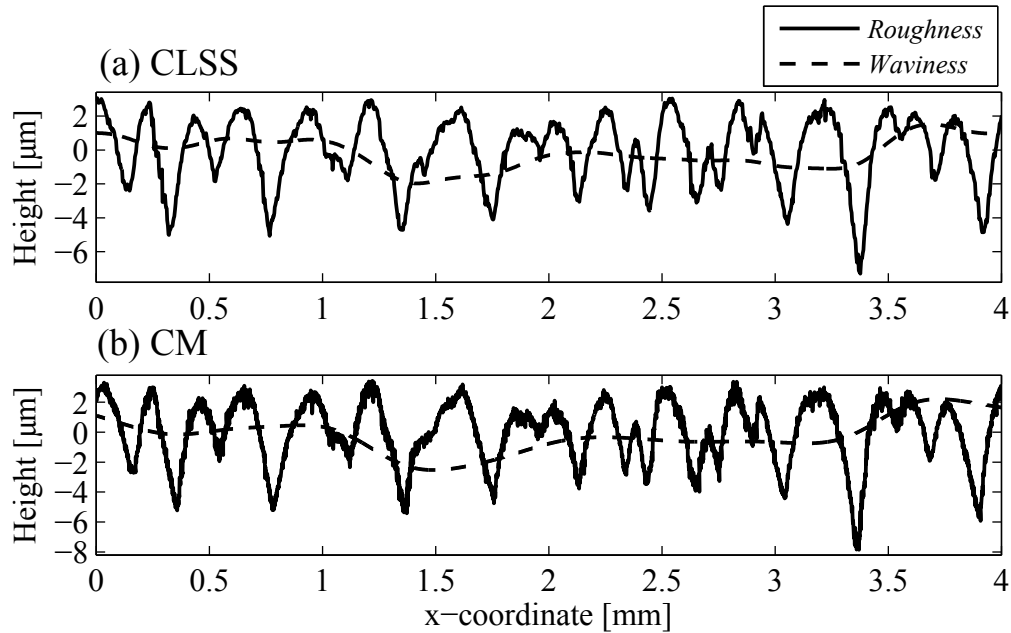


Figure 6.6: Comparison of the measurement results of a PTB roughness standard having $R_a = 1.63 \mu\text{m}$, measured with the CLSS and with a commercial confocal microscope (CM), at the right edge of the standard.

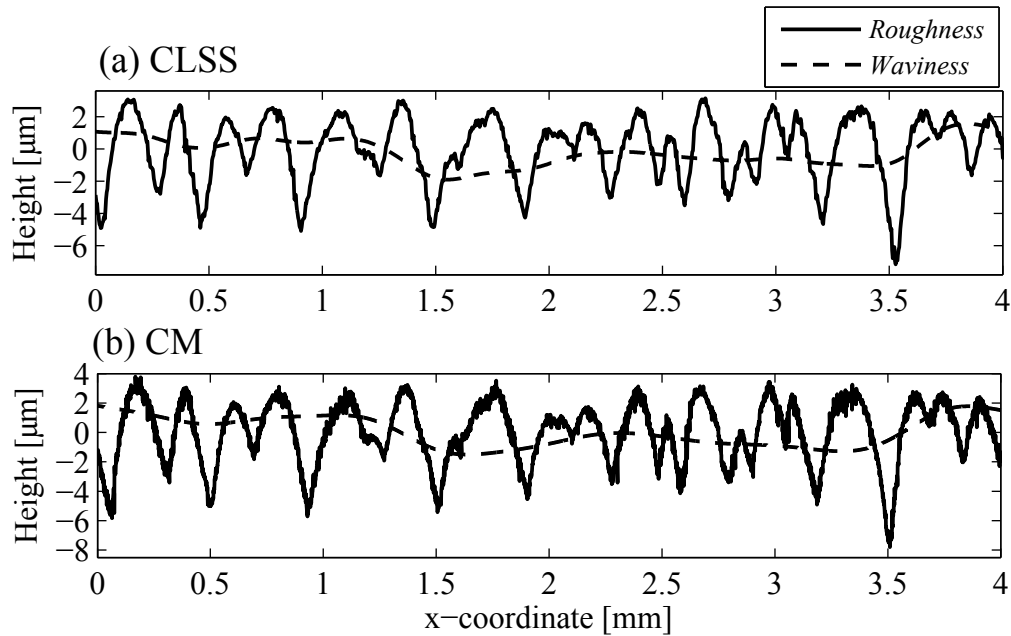


Figure 6.7: Comparison of the measurement results of a PTB roughness standard having $R_a = 1.63 \mu\text{m}$, measured with the CLSS and with a commercial confocal microscope (CM), at the left edge of the standard.

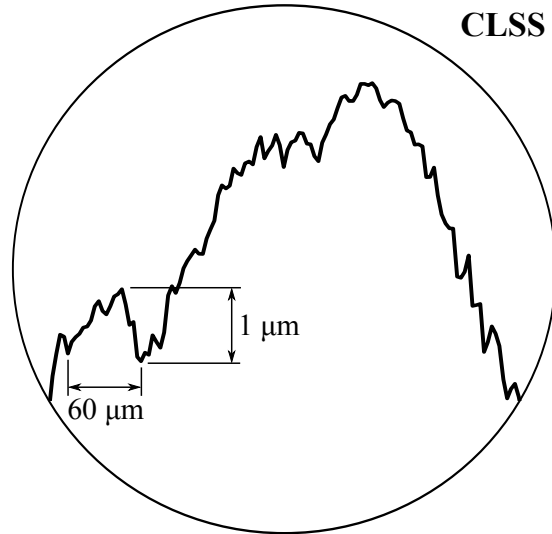


Figure 6.8: Enlarged image of a PTB roughness standard obtained by the CLSS.

using a $20\times/0.45$ NA objective applied at $\lambda = 530$ nm. The FWHM of the axial intensity response is $3.5 \mu\text{m}$ when observed with the CLSS, as previously discussed in Chapter 3. However, a micro-height feature of $1 \mu\text{m}$ which is smaller than the FWHM of $3.5 \mu\text{m}$ can be resolved using the CLSS, as seen in Figure 6.8.

In the CLSS, the *center of gravity* technique is used to evaluate the maximum peak of the axial response, by which mean the real axial resolution is greatly improved down to the nanometer scale beyond that defined by the FWHM. Noise adhered to the axial intensity response is the cause of the uncertainty when evaluating with the *center of gravity* technique. In consequence, the uncertainty is used to define the smallest height which can just be resolved by the CLSS.

The uncertainty of the *center of gravity* technique can be measured with a calibrated flat mirror. Since the mirror represents a highly flat surface having a single height level, the *root-mean-square* roughness parameter (R_q) of the measured profile is then used to express the uncertainty of the surface height finding technique. From ten measurements, R_q is obtained as 11.7 nm with standard deviation of 0.48 nm, where R_q is calculated according to DIN EN ISO 4287 (1998) after applying the filtering according to DIN EN ISO 11562 (1998). This value becomes a real limit of the axial resolution which is achieved by the CLSS. In contrary, the lateral features on the specimen of about the optical probe size might be responsible for the reduction in accuracy of the measured profile heights, as reported also by other measuring techniques [4].

As a consequence, the measurement results of a fine PTB roughness standard with $R_a = 0.186 \mu\text{m}$ shown in Figure 6.9 are examined. There are two significant effects to be clarified here. First, it is the effect of the sampling density, or the *lateral sampling interval*. By following the Nyquist sampling theorem [62], the

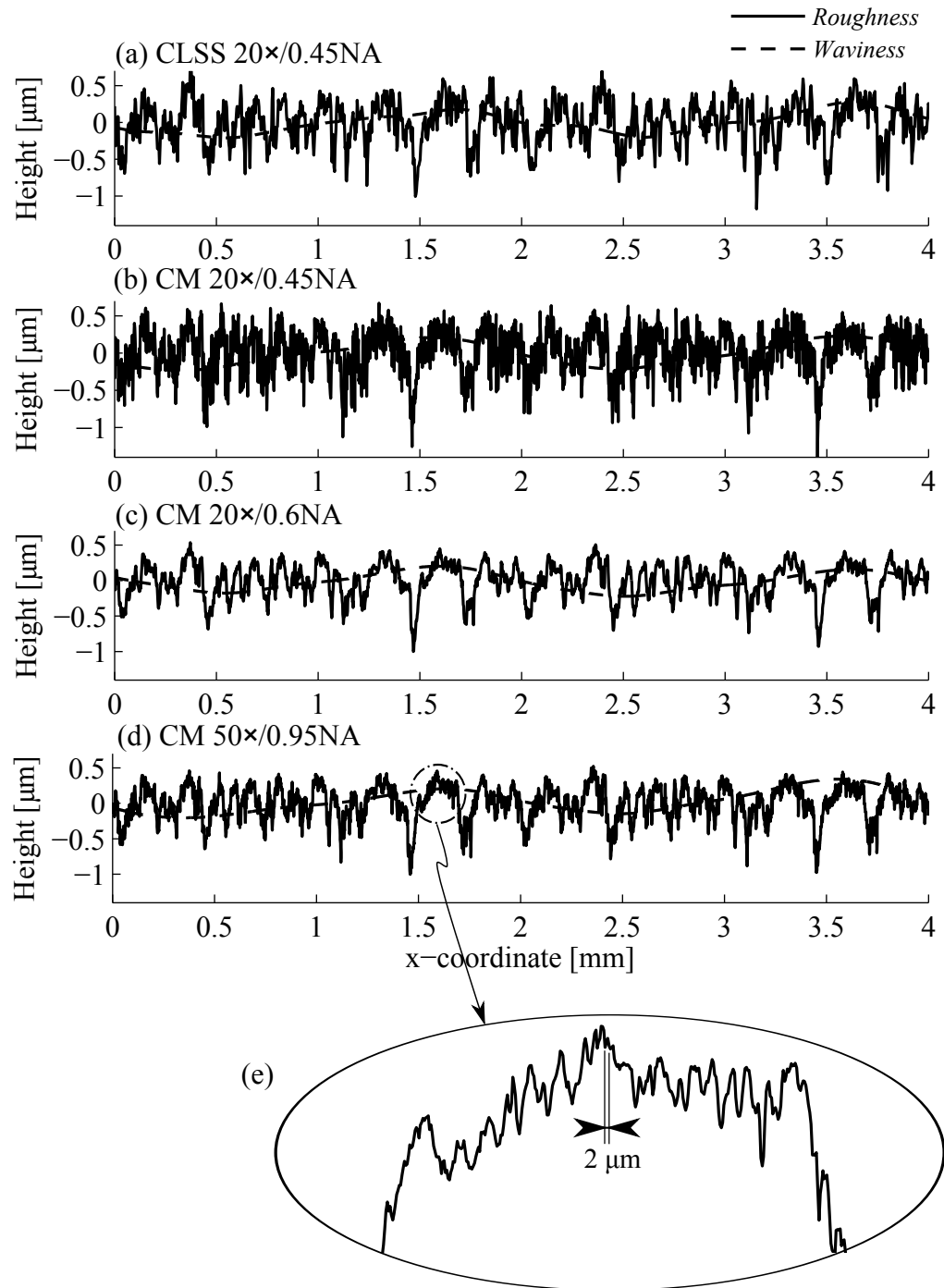


Figure 6.9: Comparison of the profile measurement of a PTB roughness standard having $R_a = 0.186 \mu\text{m}$, obtained with (a) CLSS using 20 \times /0.45 NA objective, (b) a commercial CM using 20 \times /0.45 NA objective, (c) a commercial CM using 20 \times /0.6 NA objective, and (d) a commercial CM using 50 \times /0.95 NA objective. (e) An enlarged profile of (d).

Table 6.5: The measurement results of a PTB roughness standard having $R_a = 0.186 \mu\text{m}$. The standard was calibrated with a Tactile Profilometer (TP). Thereafter, the measurement results are obtained with the CLSS and a commercial confocal microscope (CM). The roughness parameter are then calculated according to DIN EN ISO 4287 (1998), after applying the filter according to DIN EN ISO 11562 (1998).

	TP	CLSS	CM		
Parameter (mean)	Tip radius	(2.59 μm)	Lateral sampling interval		
	3 μm	(1.5625 μm)	(2.59 μm)	(1.5625 μm)	(0.625 μm)
		0.45 NA	0.45 NA	0.6 NA	0.95 NA
R_a	0.186 μm	0.232 μm	0.213 μm	0.185 μm	0.194 μm
R_q	-	0.291 μm	0.261 μm	0.231 μm	0.243 μm
R_z	1.333 μm	1.524 μm	1.445 μm	1.180 μm	1.305 μm
R_t	1.446 μm	1.724 μm	1.710 μm	1.380 μm	1.495 μm

lateral features of the surface which are smaller than two times the lateral sampling interval cannot be resolved. Figure 6.9 (b) shows that a finer lateral sampling interval of 1.5625 μm helps to resolve more details of the profile as compared to Figure 6.9 (a), which is sampled with a coarser lateral sampling interval of 2.59 μm .

Note that Figure 6.9 (a) and (b) are measured using the same NA objective. When different NA objectives are applied, the second effect should be pointed out. Table 6.5 shows that a higher NA objective provides more accurate result, when comparing the profile in Figure 6.9 (c) to Figure 6.9 (b). This phenomenon can be explained with the relation of the *numerical aperture* (NA) of the objective and the optical probe size, or the size of the diffraction-limited focal point. The higher the NA, the smaller the optical probe is and the more light is captured by the objective lens. If a 0.6 NA and a 0.95 NA are used instead of a 0.45 NA objective, the FWHM of the optical probe is reduced by 1.36 times and 2.15 times, respectively. Though the same lateral sampling interval of 1.5625 μm is applied in Figure 6.9 (b) and (c), the higher NA objective lens obtains the profile with lower noise, which might be caused by the micro-lateral features on the specimen.

The PTB roughness standard used in this case comprises of micro-lateral features of at least 1-2 μm , seen in Figure 6.9 (e). Therefore, when probing with a 0.45 NA objective having the FWHM of 3.5 μm , inaccurate results as depicted in Figure 6.9 (b) are obtained, showing a spiky-like profile. The origin of this discrepancy is not yet clear. Though, it can be assumed that the micro-lateral features on the specimen is the main cause of the error, when inspecting the specimen having the micro-lateral features about the same size as the optical probe the signal reflected from different heights within the optical probe might induce more noise to the axial intensity response, as illustrated in Figure 6.10 (a) and (b).

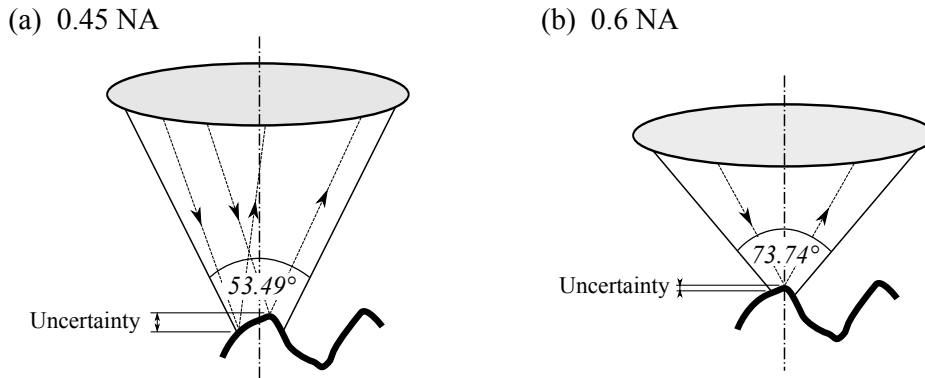


Figure 6.10: A simplified illustration showing that the lateral features of the surface relative to the optical probe size might induce uncertainty to the measured signal. A 0.6 NA objective having a higher accepting angle with respect to light reflected from the specimen can generate a smaller optical probe, where $NA = n \cdot \sin \alpha$. Thus, the receiving intensity as a function of the surface height is more accurate.

Therefore, higher uncertainty inherent in finding the maximum peak of the axial intensity response is responsible for the degradation in accuracy of the measured profiles.

Figure 6.9 (d) is the most accurate profile of all, as the specimen is sampled with a high NA objective and a finest lateral sampling interval of $0.625 \mu\text{m}$. Though the result obtained with the CLSS in Figure 6.9 (a) has better appearance than that in Figure 6.9 (b), notable errors of the measured profile height can be observed in the roughness parameters, listed in Table 6.5. This shows that 0.45 NA objectives provide consistent results.

It can be concluded that measuring with the CLSS the smallest height feature of 11.7 nm can be resolved, as limited by noise inherent in the axial intensity response. However, the micro-lateral features on the specimen of about the same size as the FWHM of the lateral response may degrade the accuracy of the measured profile heights and then lower the real axial resolution. Moreover, the smallest lateral feature of the specimen resolved by the CLSS, is limited by two times the lateral sampling interval, following the well-known Nyquist sampling theorem [62].

6.3 Lateral resolution improved with a finer sampling interval

As stated above, the lateral resolution of the CLSS can be enhanced by reducing the lateral sampling interval. Figure 6.11 suggests that the finer the lateral sampling interval, the higher the lateral resolution of the edge responses. Note that the edge response is another useful definition of resolution [87]. Following Corle and Kino [17], the 20%-80% edge response of a Confocal Scanning Optical Microscope

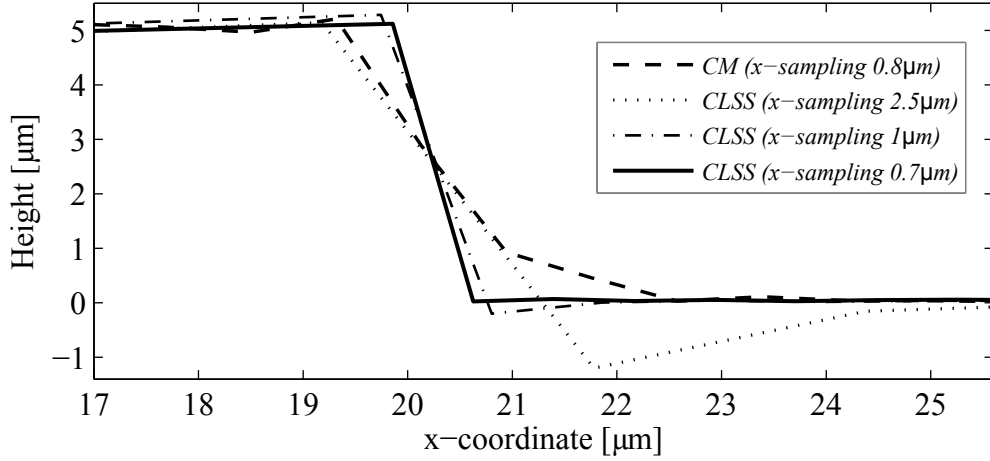


Figure 6.11: Comparison of the edge responses obtained with the CLSS and a commercial CM at various sampling intervals.

(CSOM) is given by

$$d_c(\text{Edge}) = \frac{0.33\lambda}{\text{NA}}. \quad (6.1)$$

As a consequence, d_c is $0.389 \mu\text{m}$, when λ is 530 nm and NA is 0.45 . In Figure 6.11, the edge response of the CLSS is improved when the lateral sampling interval is reduced from 2.5 to 1 and to $0.7 \mu\text{m}$, resulting in the 20%-80% edge responses of 1.8 , 0.6 , $0.5 \mu\text{m}$, respectively. Moreover, this experiment confirms that the lateral resolution of the CLSS is not confined by the pixel size of the CCD. An edge response smaller than the pixel sampling interval of $1.7 \mu\text{m}$ at the focal plane can nevertheless be realized.

However, the *lateral sampling interval* is limited by the *diffraction-limit* of the focal point. It is due to the fact that the sampling point is not an infinitesimal point, so that sampling with a lateral sampling interval finer than the diffraction-limited focal point will not gain any further information. This leads to the conclusion that the *ultimate lateral resolution* of the CLSS is two times the FWHM of the lateral intensity response. In contrary, the *real lateral resolution* of the CLSS is the two times the *lateral sampling interval*. Note that the definition of the lateral resolution is of significance for defining the smallest lateral feature resolvable by the CLSS, which differs from the *lateral optical resolution* explained in Chapter 2.

To demonstrate that a finer lateral sampling interval helps to improve the lateral resolution, the measurement results in Figure 6.12 are presented. A lateral standard with a period of $6 \mu\text{m}$ is measured with the CLSS and a commercial CM. The lateral resolution of the CLSS is enhanced when the lateral sampling interval reduces from 2.5 to 1 and $0.5 \mu\text{m}$, resulting in more accurate profiles. However, the presence of the trenches, consisting of two closely spaced edges, in the lateral standard and a statistical error of the linear scanning stage when stepping with a

step size smaller than $\approx 2 \mu\text{m}$ are responsible for more noise induced in the axial intensity response. This results in spike-like profiles. Since the data in the CLSS are sorted in a mixing order before the profile height evaluation, the combination of these two errors is relatively strong. A more accurate and precise linear scanning stage will help to improve the result in this case.

6.4 Sampling focal-line in the CLSS

Figure 6.13 shows that the tilted focal line is slightly curved due to the field curvature inherent in the optical system. The residual of the curve from the linear fitted line is about $1 \mu\text{m}$ across the focal line. The experiment in this case was carried out in a special manner by scanning a flat mirror, which is tilted to the titled focal line, in the axial direction. In this experiment, the mean value of the focal interval in the axial direction is $0.36 \mu\text{m}$ with standard deviation of $0.12 \mu\text{m}$. Accordingly, the error in the lateral intervals between the foci is related to this $0.12 \mu\text{m}$ standard deviation.

The evenness and the exact value of the focal intervals strongly affect the accuracy and precision of the CLSS measurement. Uneven spaced foci across the focal line can be defined as a systematic error. If this error cannot be corrected properly, it will become a statistical error in the lateral direction, after the sorting process applied. However, it can be considered as a systematic error in the axial direction.

The aberrations, e.g. spherical aberration, coma, and astigmatism can contribute additionally to unevenly spacing of the foci. In general, to realize a uniform focal interval according to the design the aberrations should be minimized. In another approach, the positions of the foci can be designed to incorporate the aberrations, for example, distortion and field curvature. These are two of the five Seidel aberrations which will not degrade the optical resolution, as discussed in Chapter 3. However, the second approach might be difficult to realize in practice. The optical elements, even manufactured in the same lot, may perform differently, so does the characteristics of the distortion and field curvature.

6.5 Uncertainty in the lateral scan direction

In the CLSS, accuracy and precision of the profile length scanned in the lateral direction highly depend on the performance of the linear scanning stage. The linear scanning stage with an open-loop control used in the CLSS performs a bit worse than that of a close-loop control employed in a chromatic confocal point sensor. Figure 6.14 and Figure 6.15 show that the accuracy and precision of the CLSS is the worst case, when measuring a lateral standard having a periodic structure of $100 \mu\text{m}$ period and the total length of $2499.83 \mu\text{m}$. The largest errors and the most deviated scan lengths are obtained with the CLSS, varied from -0.49%

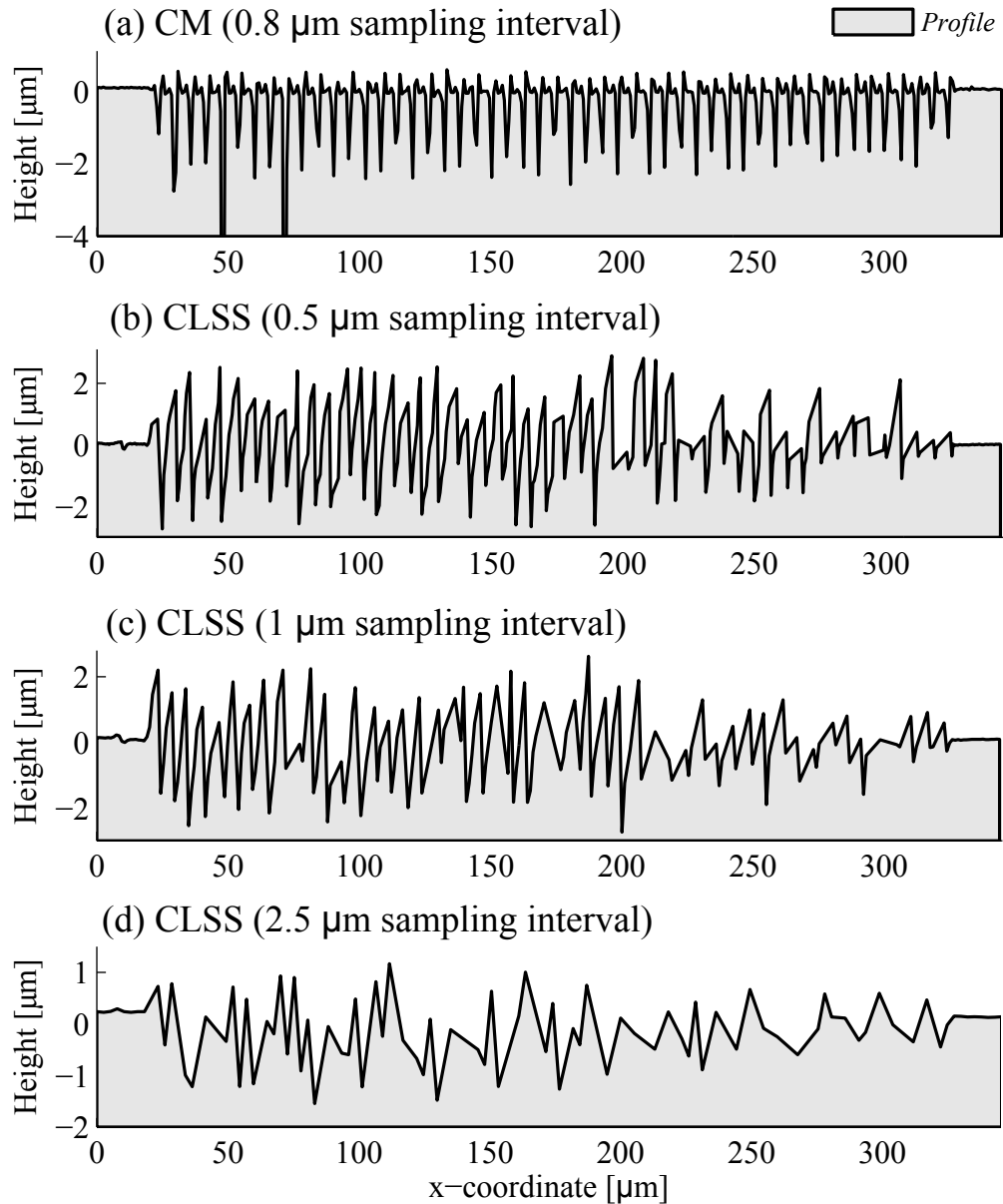


Figure 6.12: Comparison of the measured profiles of a lateral standard with a period of 6 μm , obtained with (a) a commercial CM, using $20\times/0.45$ NA objective and the lateral sampling interval of 0.8 μm , (b) CLSS using $20\times/0.6$ NA objective and the lateral sampling interval of 0.5 μm , (c) CLSS using $20\times/0.6$ NA objective and the lateral sampling interval of 1 μm , and (d) CLSS using $20\times/0.6$ NA objective and the lateral sampling interval of 2.5 μm .

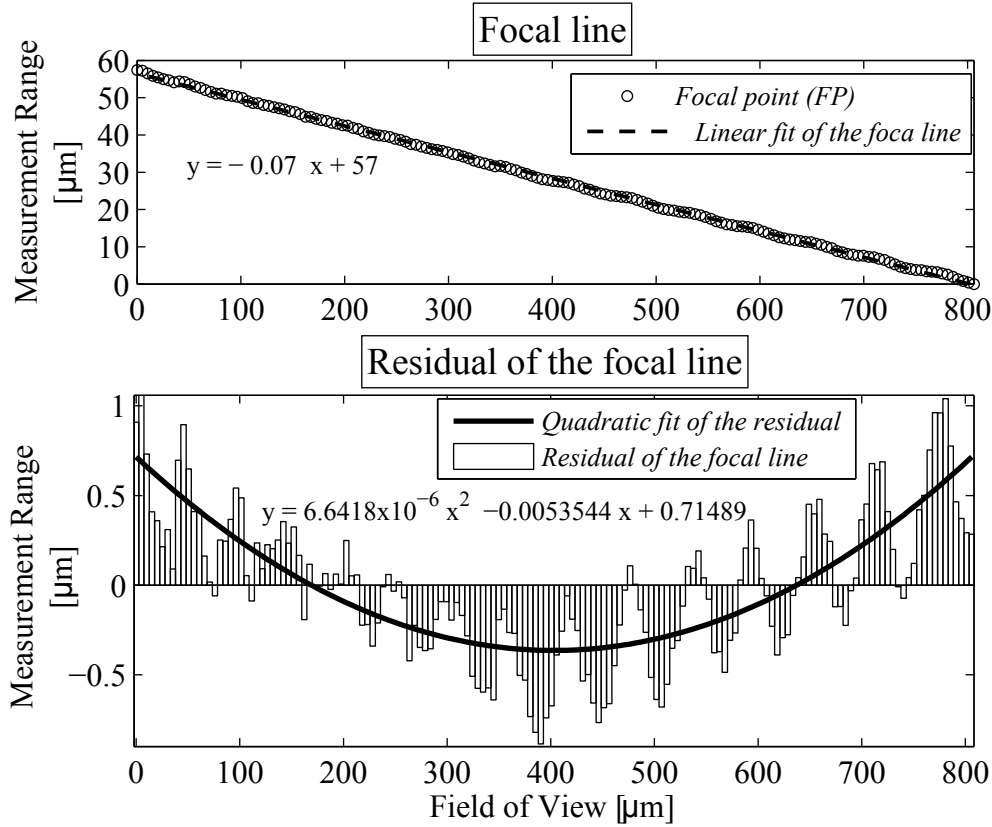


Figure 6.13: Experimental measurement of the focal line in the CLSS. The focal line is curved slightly by the field curvature inherent in the optical system.

to +1.04%. The uncertainty of the linear scanning stage is the main cause of this error, previously discussed in Chapter 4. In addition, Figure 6.15 (b) shows that the correlation based image stitching technique used in a commercial CM can introduce certain error, when measuring a periodic structure. An artificial structure having a 100 μm period was therefore added to the real structure.

6.6 Aberrations in the CLSS

In the CLSS, a 20 \times /0.45 NA is used to operate at 12 \times , such that the applied tube length is 108 mm instead of 180 mm. The change of the tube length induces residual aberrations in the optical system, mainly spherical aberration [17, 28, 29]. In theory, the higher the NA, the more pronounced aberration is [29]. However, a high NA objective is necessary for obtaining high resolution. Because a wider angle of scattered rays from the sample can be accepted by a high NA objective. The effect of spherical aberration on the axial response can be theoretically manifested using eq.(3.19), corresponding to various values of the amplitude apodization, A

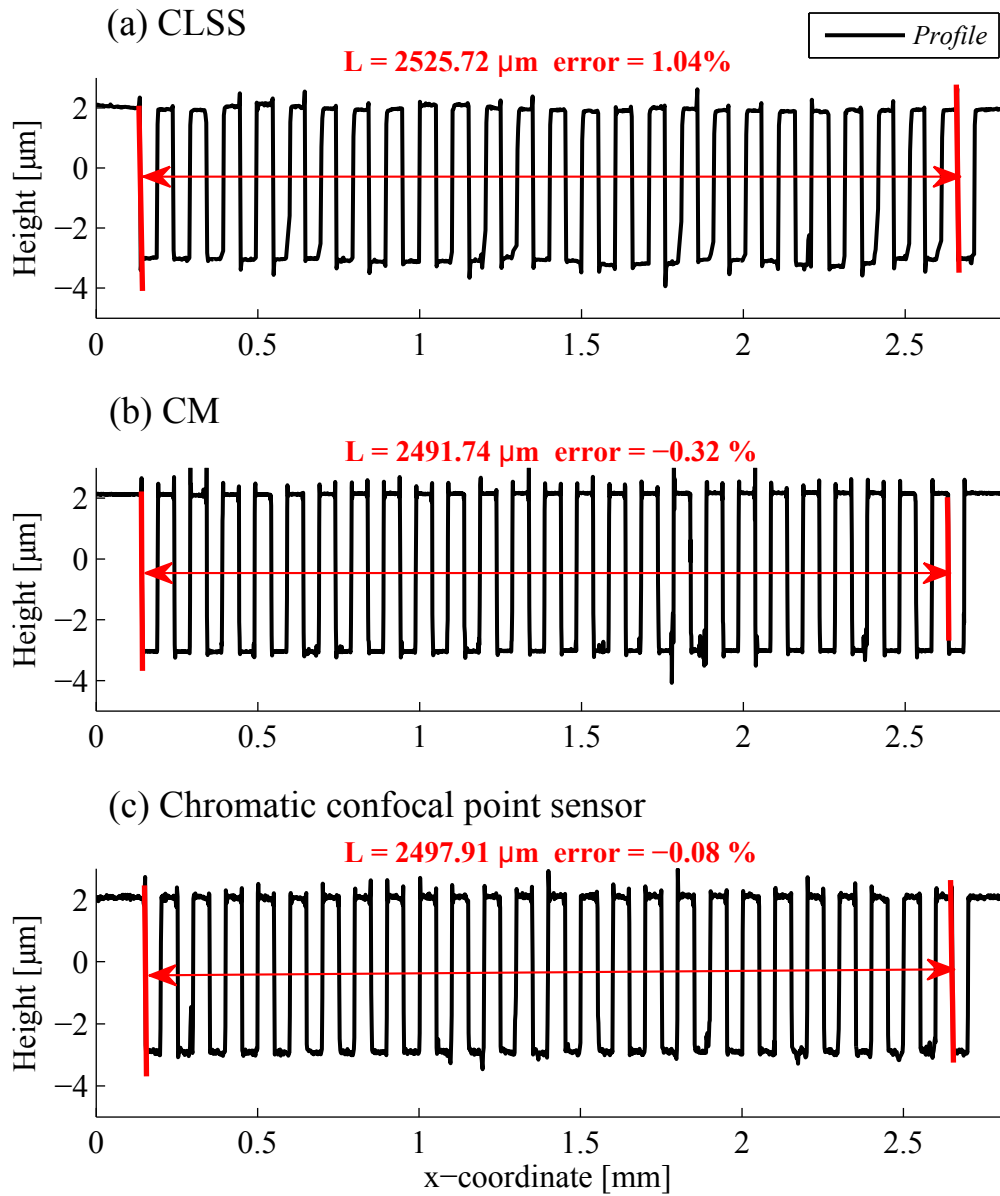


Figure 6.14: Comparison of the measured profiles of a lateral standard with a period of $100 \mu\text{m}$ having the total length of $2499.83 \mu\text{m}$, obtained with (a) CLSS, using $20\times/0.45$ NA objective, (b) a commercial CM, using $20\times/0.45$ NA objective, (c) a chromatic confocal point sensor, using $20\times/0.6$ NA objective. The error in total length are presented in each case.

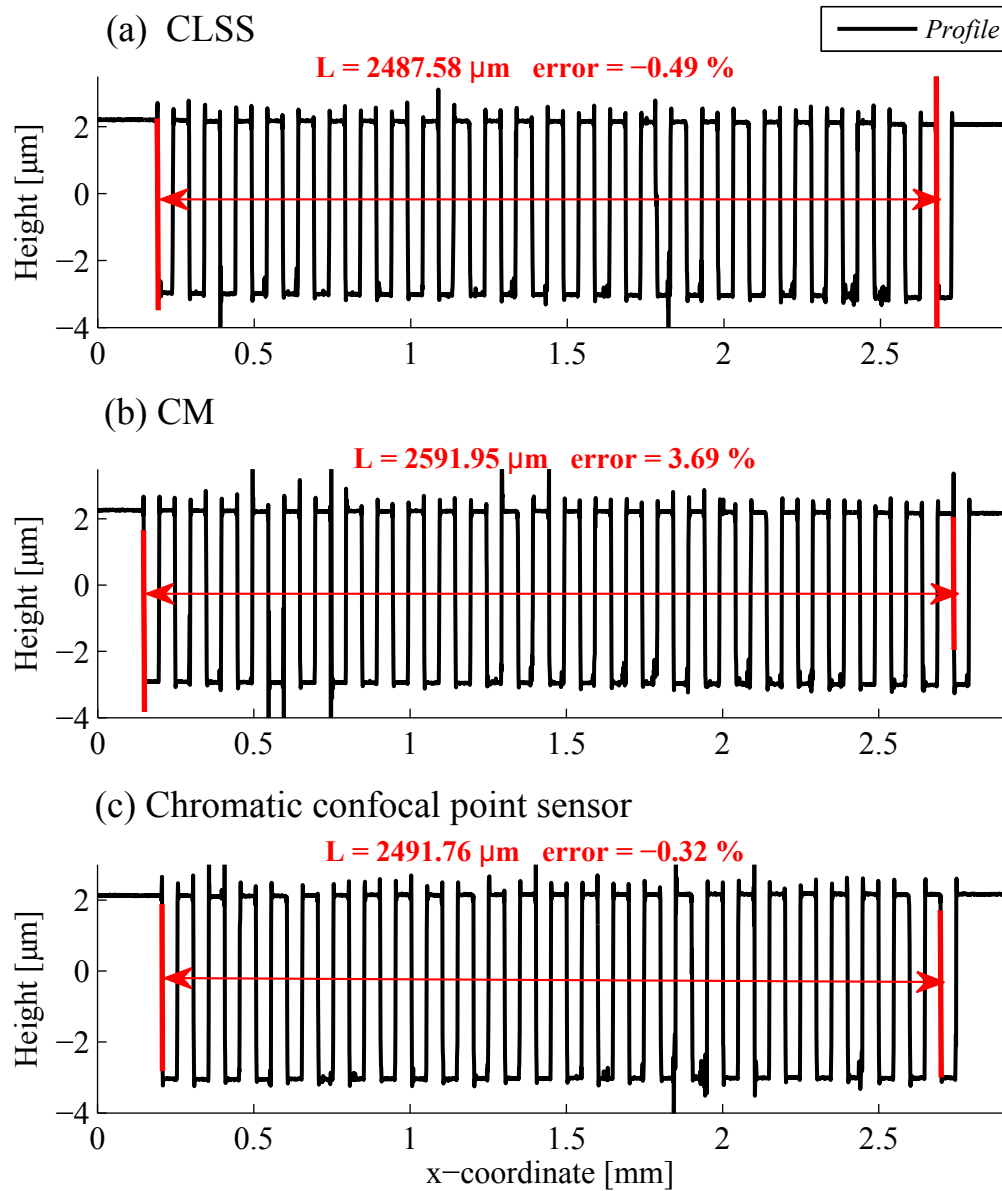


Figure 6.15: Comparison of the measured profiles of a lateral standard with a period of $100 \mu\text{m}$ having the total length of $2499.83 \mu\text{m}$, obtained with (a) CLSS, using $20\times/0.45$ NA objective, (b) a commercial CM, using $20\times/0.45$ NA objective, (c) a chromatic confocal point sensor, using $20\times/0.6$ NA objective. The error in total length are also presented in each case. Note that the error caused by the stitching technique applied in a commercial CM can introduce an artificial period to the real structure.

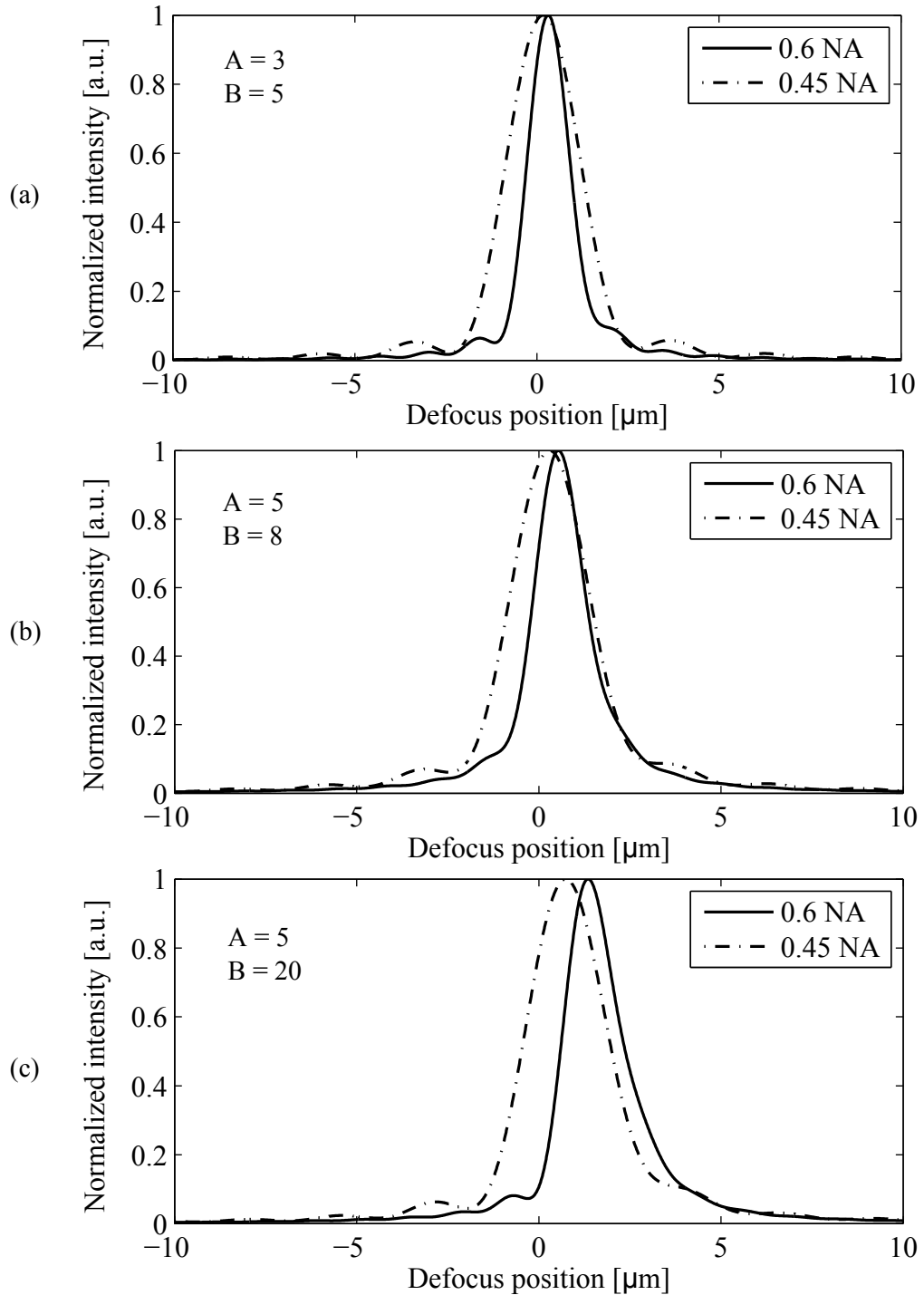


Figure 6.16: Axial responses theoretically modified with aberrations. Following the simplified expression of eq.(3.19), the axial responses are manifested, corresponding to different values of the amplitude apodization, A and B.

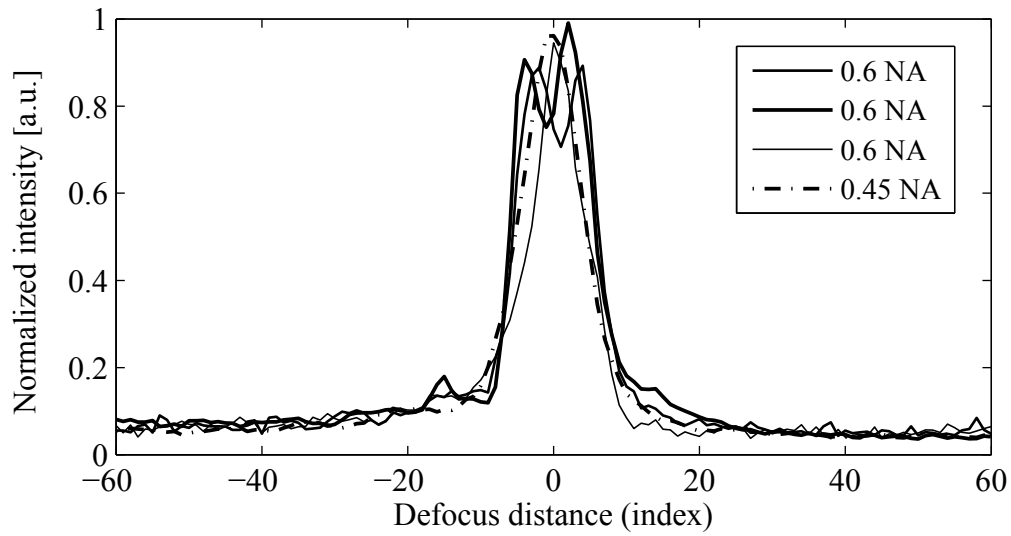


Figure 6.17: Axial responses experimentally obtained with different numerical aperture (NA) objectives ranging from 0.45 to 0.6 NA.

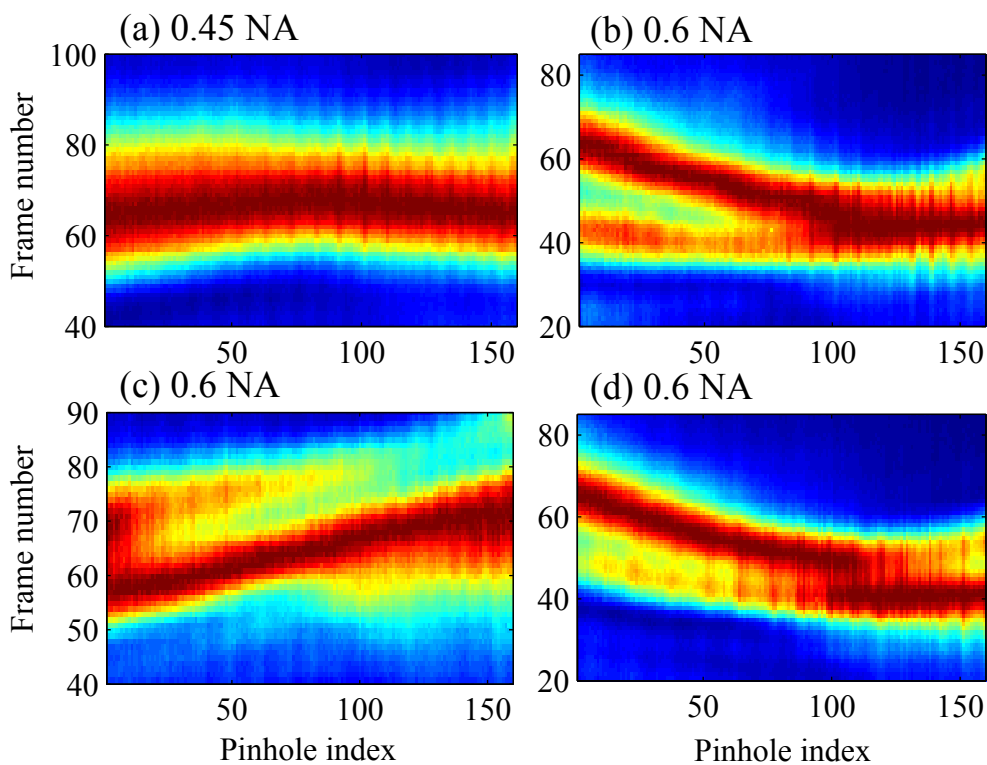


Figure 6.18: Raw data stacks obtained with different numerical aperture (NA) objectives. (a) 0.45 NA objective. (b) to (d) identical 0.6 NA objectives.

and B. Figure 6.16 demonstrates that the axial response obtained with a low NA objective is less affected by the same amount of aberration.

In order to examine the residual aberrations in the CLSS, three $20\times/0.6$ NA objective lenses from Olympus are applied instead of a $20\times/0.45$ NA. Figure 6.17 shows that the axial responses obtained with the $20\times/0.6$ NA objectives are broadened and distorted having double peaks. These distorted axial responses lead to a serious degradation in accuracy of the evaluated profile heights. However, the $20\times/0.45$ NA objective provides the axial intensity response comparable to the theory. This suggests that the residual aberrations are negligible when using a $20\times/0.45$ NA objective, but more prominent in higher NA objectives. The residual aberrations can also be observed in the raw data stacks, depicted in Figure 6.18 (b) to (d). In this measurement, a uniform pattern of the raw data stack shown in Figure 6.18 (a) is expected when measuring a flat mirror.

It can be implied that the spherical aberration caused by the mismatch tube length in the CLSS is more prominent than first expected. The spherical aberration can then be minimized by applying the objective lens at a designed tube length, though the axial measurement range will be reduced. To gain a reasonable axial measurement range, a low magnification and high NA objective is preferred.

6.7 The effect of tilted specimens on the axial response

In this section, the effect of the tilted specimen on the axial response is discussed. When measuring a tilted flat surface, the light captured by the objective lens may vary in intensity, depending on which part of the focal line is used to sample the specimen. A simplified schematic of this phenomenon is illustrated in Figure 6.19. Though the specimen is a flat surface, the micro-roughness of the surface generates a diffused reflection. It can be seen in Figure 6.19 that the objective can capture the scattered light differently across the focal line, with respect to the angle of the diffused beam and the NA of the objective. In this illustration, light reflected at the far left edge is partially captured by the objective and partially lost. Therefore, the detection sensitivity at this end is lower comparing to the other end. In consequence, the detection sensitivity is termed as the *pinhole sensitivity*, as it is directly connected with the position of the pinholes.

A series of the axial responses obtained with a flat surface perpendicular to the optical axis is shown in Figure 6.20. When the surface traverses in the lateral direction, the surface will cover only a given range of the foci at all times. Therefore, the maximum peak of the axial responses is almost at the same height. The slightly curved ridge of the axial responses along the x -coordinate is caused by the systematic error of the linear scanning stage, explained in the previous chapters. Otherwise, the ridge should be straight. When a tilted surface is measured, a series of axial responses, as shown in Figure 6.21, is obtained. This illustrates that the

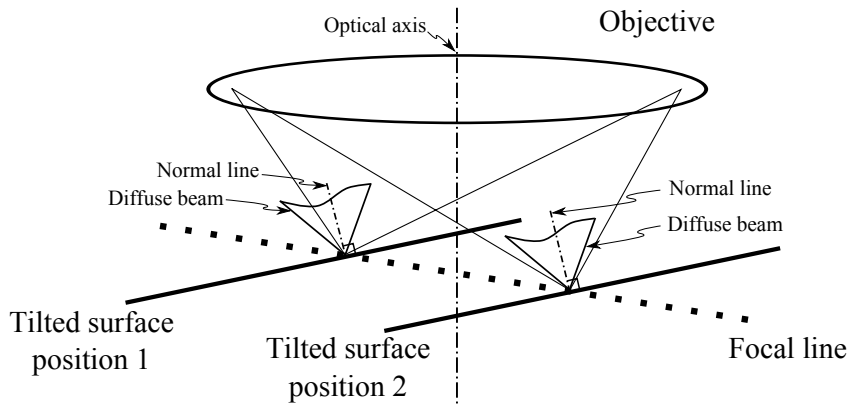


Figure 6.19: A simplified schematic showing the effect of a tilted flat surface on the detection sensitivity. The reflected light can be captured more at one end comparing to the other end across the focal line, when the surface is tilted with respect to the optical axis.

axial response at one end is seriously degraded more than the other end across the focal line. Though, the axial intensity responses of a normal flat surface obtained across the focal line are relatively similar. The axial intensity responses of a tilted flat surface are degraded by undercorrected aberrations when the objective lens is not used at full aperture [85, 94], as depicted in Figure 6.19.

Then, the influence of various tilt angles of a flat surface is investigated. Figure 6.22 summaries the obtained axial responses affected by undercorrected aberration of the objective lens due to the tilted surface. Figure 6.22 (a) to (d) present the results obtained when a flat surface is tilted counterclockwise from the plane normal to the optical axis. This gives the positive sign convention to the tilt angle, whereas the negative is vice versa. Then, Figure 6.22 (e) to (h) show the axial responses obtained from a negatively tilted flat surface. In this experiment, the axial responses in Figure 6.22 (e) to (h) are less distorted, since the measurements cover an extremely short measurement range when the specimen is tilted approaching the tilt angle of the focal line.

Finally, it can be concluded that tilted specimens play a significant role on the quality of the axial intensity response. The accuracy of the measurement might be degraded by the residual aberrations introduced by the tilt of the specimen.

6.8 Conclusion

This chapter verifies that the new concept of a parallel depth scanning scheme applied in the Confocal Line Scanning Sensor (CLSS) is feasible. The measurement of the PTB standards proves that a tilted plane technique is successfully incorporated in a confocal imaging system of the CLSS. In addition, the performance of

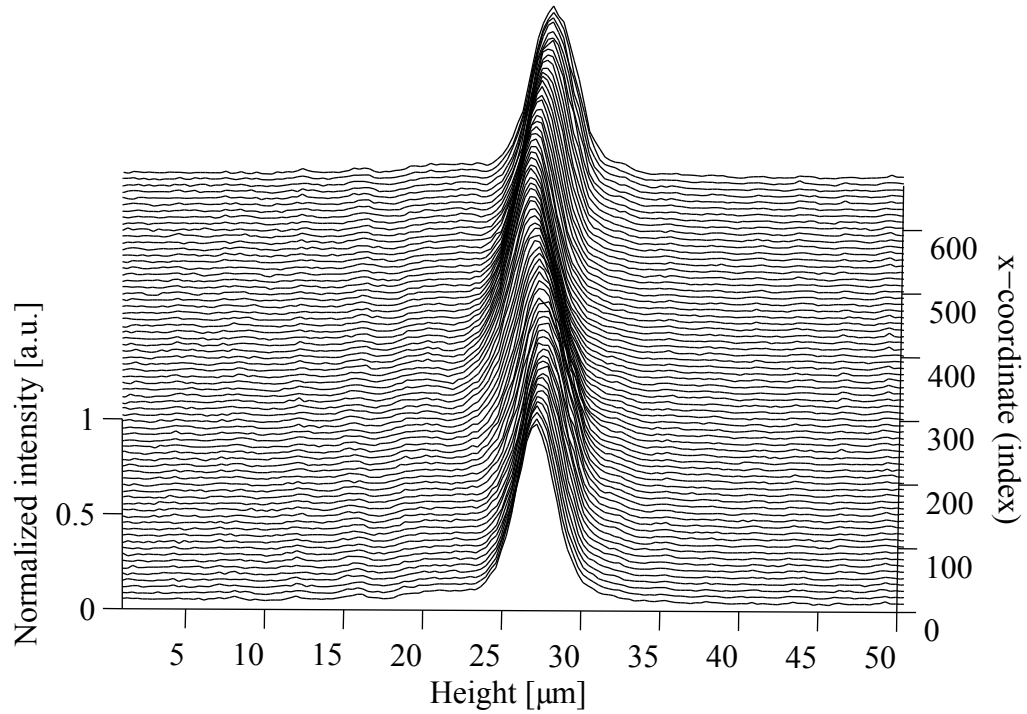


Figure 6.20: A series of the axial intensity responses of a flat surface normal to the optical axis, plotted along the x -coordinate.

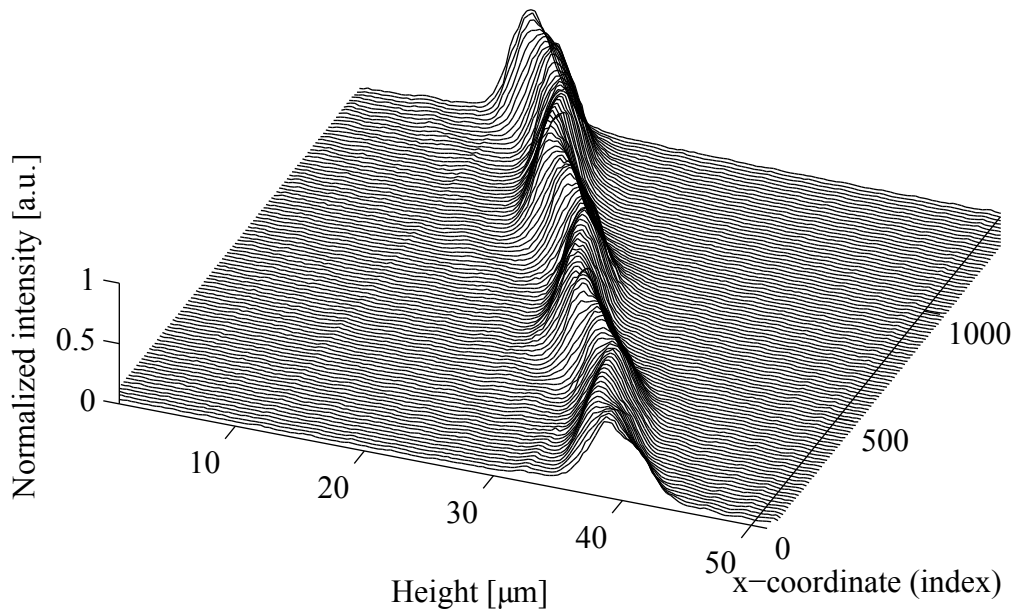


Figure 6.21: A series of the axial intensity responses of a tilted flat surface, plotted along the x -coordinate.

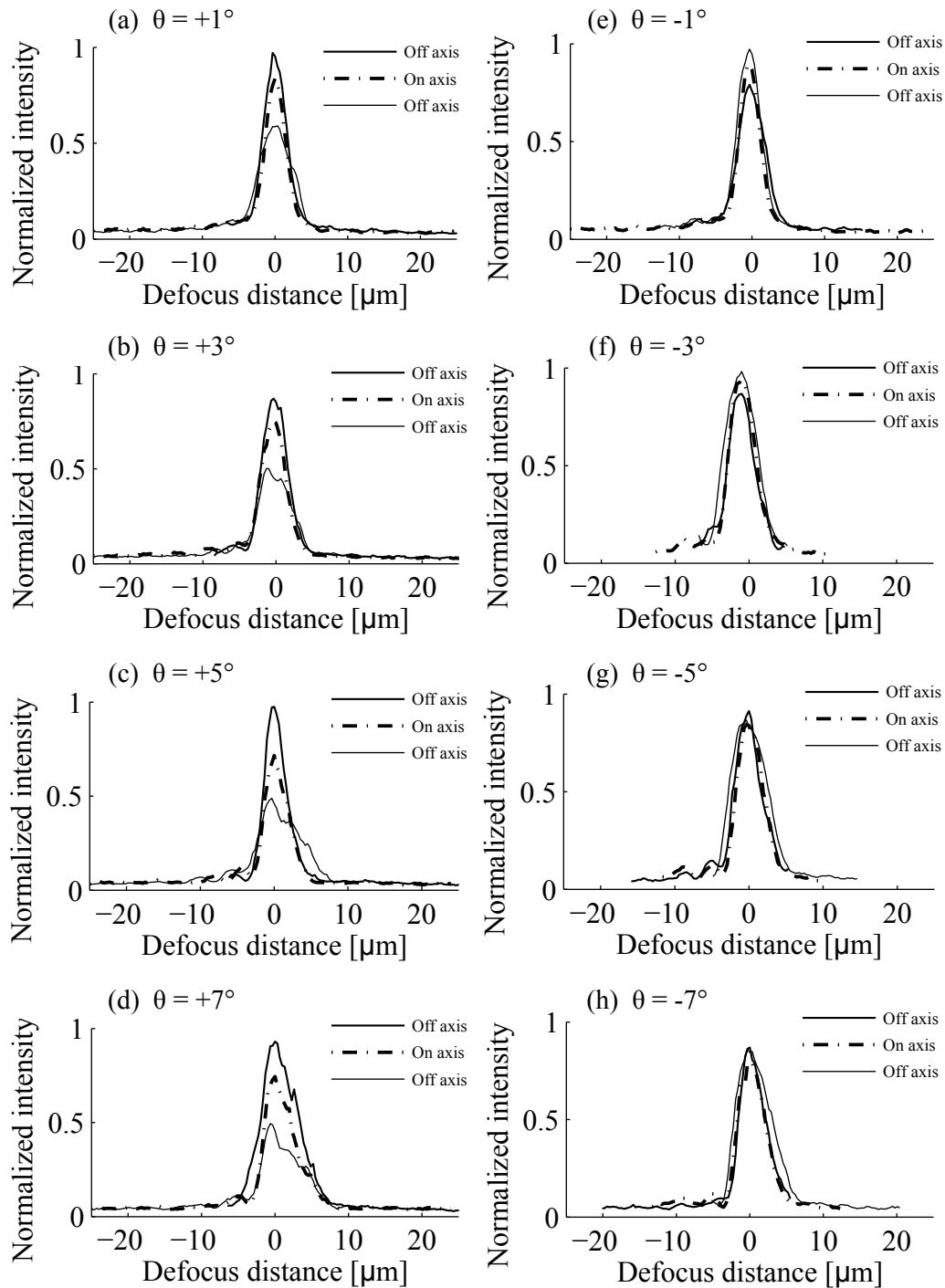


Figure 6.22: Comparison of the axial intensity responses of a tilted flat surface obtained at various tilt angles, $\theta = -7, -5, \dots, +7^\circ$.

the CLSS is comparable to that of a commercial Confocal Microscope (CM).

The real *axial resolution* of the CLSS is basically limited by the noise inherent in the axial response. According to that the axial resolution is beyond the diffraction limit, down to the nanometer scale. From the experiments, uncertainty in the surface height evaluation is found to be 11.7 nm. Therefore, this value is used to define the smallest height of which the CLSS can resolve. However, in practice micro-lateral structures on the specimen might be the cause of additional noise adhered to the axial response. Under this circumstance, the axial resolution of 11.7 nm cannot be reached.

Moreover, the *real lateral resolution* is the two times the *lateral sampling interval*. However, the lateral sampling interval is essentially limited by the diffraction limit, because the sampling point is not an infinitesimal point but rather a diffraction-limited focal point. In consequence, reducing the lateral sampling interval finer than the diffraction-limited focal point will not gain additional information. Accordingly, the *limited lateral resolution* is the two times the *full-width at half-maximum* (FWHM) of the lateral response. Nonetheless, the linear scanning stage with an open-loop control that is used in the CLSS induces a statistical error when stepping, which corresponds to the degradation in accuracy and precision of the scan length in the lateral direction.

A 20 \times /0.45 NA objective is the default objective used in the CLSS, which is designed to operate at 12 \times . Therefore, the change of the tube length between the objective lens and the tube lens from a designed value generates undercorrected spherical aberration. The residual aberrations in the CLSS can be observed with a higher NA objective, such as a 20 \times /0.6 NA objective. However, the experiments show that the residual aberrations can be negligible when measuring with a 20 \times /0.45 NA objective. In addition, it is found that tilted specimens strongly affect the quality of the axial response; the higher the tilt, the more prominent the degradation. When inspecting a tilted specimen, the objective lens is not used at full aperture. Consequently, undercorrected aberrations are induced in the system, which corresponds to degrade the quality of the axial intensity responses.

Chapter 7

Conclusions and Future Work

7.1 Conclusions

This thesis concludes that the novel concept of incorporating a titled plane technique in a confocal imaging system is feasible. The developed sensor introduces a new parallel and motionless depth scanning scheme [12, 14, 15], named *Confocal Line Scanning Sensor* (CLSS). The notable strength of this design is a simplified and robust setup. In this thesis, several well-known theories are used to support the design and to evaluate the CLSS system and its performance. However, new knowledge to apply a titled plane technique in a confocal imaging system is originally explained. The main contributions of the thesis can be summarized as follows, where notable specifications of the CLSS include:

- Lateral measurement range of up to 15 mm,
- Axial measurement range of 50 μm ,
- Sampling rate of 928 points per second or 5.8 frames per second,
- Optical lateral resolution of $\approx 0.5 \mu\text{m}$, based on 0.45 NA objective and $\lambda = 530 \text{ nm}$,
- Noise-limited axial resolution of 11.7 nm.

The pinhole mask design is presented in Chapter 3. The design target is to form equally spaced foci at the titled focal plane. As a consequence, the variation of the magnification, known as *keystone distortion*, inherent in a titled plane system is theoretically examined. Following the Scheimpflug's rule, a newly discovered approach for predicting and correcting the keystone distortion is established. It is found that the shifting of the principal planes in a compound lens system can modify the pattern of the keystone distortion and even correct for it. The newly derived expression of the magnification in a tilted plane system is then used to design the pinhole pattern. In the CLSS, the so-called *reverse keystone distortion*

is established. On the other hand, the *corrected keystone distortion* is the most useful case, where the keystone distortion is corrected across the *field of view*. The pinholes used in the CLSS are designed in an elliptical shape to maintain the confocal effect in all directions. Following Wilson and Carlini [116, 115], the pinhole radius should be designed at 33 % of the radius of the Airy disk image. In addition, a stationary and tilted pinhole mask much smaller than the rotating pinhole disk, used in the pinhole disk based confocal microscopes, is exploited in the CLSS. This contributes to enhance the CLSS robustness and simplification. In this chapter, the imaging characteristic of the CLSS is also investigated. The study shows that the tilted pinhole mask causes no effect on the imaging quality and the diffraction foci in the tilted focal plane. However, aberrations caused by the tilted quartz substrate of the pinhole mask are responsible for the reduction of intensity output, but not the measuring quality of the CLSS, based on a $20\times/0.45$ NA objective.

The construction and alignment of the CLSS system are discussed in Chapter 4. The main target is to obtain equally spaced foci with the highest degree of *depth discrimination*, as well as to optimize axial response. Correct alignment of the pinhole mask and a known keystone distortion pattern corresponding to the design plays a significant role in achieving the target. In this chapter, the newly derived expression of the magnification in a tilted plane system is used to investigate the effects of the pinhole mask misalignment. Furthermore, a Köhler based illumination tube is incorporated in the CLSS to maximize the effective numerical aperture (NA) of the imaging system. Accordingly, the detection sensitivity and the quality of the axial response are then optimized. When carrying out a measurement with the CLSS, the specimen is scanned in the lateral direction using a linear scanning stage. In consequence, dominant systematic errors in the CLSS to be corrected include the wave-like motion of the linear scanning stage and the non-uniform detection sensitivity of the CCD.

Chapter 5 explains the newly developed data processing and calibration for the CLSS, to support a novel parallel and motionless depth scanning scheme. The key procedure of the data processing is the data sorting process. As the measured data are recorded in a mixed order, these data should be rearranged in a corresponding manner to the same sampling coordinates. Next, the calibrations are applied to eliminate the systematic errors inherent in the system and to assure the CLSS' traceability. After applying the data sorting process, the detection sensitivity of each pinhole is normalized using the local maximum technique. This step helps to optimize the axial response and *depth discrimination* property. In addition, a triangle-based cubic interpolation technique is applied to interpolate the raw data when a scan step size (ΔF) is made different from the lateral focal interval (ΔX). Then, the lateral focal interval is calibrated relative to the scan step size, using the techniques developed based on Hough transform for edge detection and line fitting optimization. In consequence, the lateral focal interval is calibrated with a known length of a lateral standard to convert an uncalibrated length unit

into an absolute length unit, i.e. μm . Then, the wave-like error of the linear scanning stage is corrected by subtracting the error from the measurement data. In this procedure, an extra step is required. The height differences between the specimen surface and the reference surface generate phase shifting in the wave-like error caused by the linear scanning stage. The cubic spline interpolation technique is used to compensate for the phase shift. In the final step, the axial sampling interval between foci (Δz) is calibrated using a known depth standard. This process is implemented following the calibration procedure in the DIN EN ISO 5436-1 standard. To reveal the surface height at a given x coordinate, the most robust algorithm of the *center of gravity* is applied to find the maximum peak of the axial intensity response. A reconstructed two-dimensional height profile is obtained as the final result.

Chapter 6 verifies the feasibility of this new concept of a parallel depth scanning scheme. The measurements of the PTB standards prove that a tilted plane technique is successfully incorporated in the confocal imaging system of the CLSS. This chapter shows that the performance of the CLSS is comparable to that of a commercial Confocal Microscope (CM). Moreover, the *real lateral resolution* is found to be the two times the *lateral sampling interval*. However, reducing the lateral sampling interval finer than the diffraction-limited focal point will not gain additional information. Therefore, the *limited lateral resolution* is the two times the *full-width at half-maximum* (FWHM) of the lateral response. Nonetheless, the linear scanning stage with an open-loop control used in the CLSS induces a statistical error when stepping. This corresponds to the degradation in accuracy and precision of the scan length in the lateral direction. However, the real axial resolution is defined based on noise-limited approach. Accordingly, the real axial resolution of 11.7 nm is obtained by the CLSS. A $20\times/0.45$ NA objective is used as a default objective, and operated at $12\times$ to gain a reasonable axial measurement range. Under this condition, a change in tube length of the objective from a designed value generates spherical aberration. The residual aberrations in the CLSS can be observed using a higher NA objective, such as a $20\times/0.6$ NA objective. However, when measuring with a $20\times/0.45$ NA objective the experiments show that the residual aberrations are negligible. Furthermore, it is found that tilted specimens strongly affect the quality of the axial response; the higher the tilt, the more prominent the degradation. When inspecting a tilted specimen, the objective lens is not used at full aperture. Consequently, undercorrected aberrations are induced in the system, corresponding to degrade the axial response.

7.2 Future Work

In this thesis, the *Confocal Line Scanning Sensor* (CLSS) is designed and developed to validate the *new concept* of incorporating a tilted plane technique in a confocal imaging system. A few possible methods of the design and calibration are proposed in this thesis. More work can be done on improving and evaluating

the performance of the CLSS. Further measurements on real specimens should be examined. As a consequence, possible work based upon the results of this thesis may be extended to:

- investigate the effect of the residual aberrations, inherent in a tilted plane system such as astigmatism, on the axial response. The imaging and measuring quality of the system can be optimized accordingly.
- increase the data acquisition rate. When traversing speed of the linear scanning stage meets the recent frame rate of the CCD cameras, the sampling rate, or *acquisition rate*, of a thousand frames per second may be obtained. However, low light reflection of a dark looking image should be taken into account when an extremely short exposure time is applied at a high sampling rate;
- increase the axial measurement range using a high numerical aperture objective with low magnification. Only the numerical aperture is used to define the optical resolution not the magnification. Nonetheless, aberrations should be optimally minimized when exploiting a high numerical aperture objective;
- develop a compact and low cost instrument for surface inspection in two dimensions and three dimensions. This might be done using micro-system technology. In the future, the optical head might be scanned instead of the specimen. A three-dimensional surface topography inspection system can then be developed by incorporating a tilted plane technique. The *corrected keystone* distortion design clarified in this thesis is necessary in this case;
- minimize and optimize the optical system. Optical design software can be used to design and minimize the system, aberrations, and stray light;
- develop different techniques for the focal sampling interval calibration. The recent methods are implemented based upon the mean basis. Therefore, the techniques such as maximum likelihood calibration algorithm, Cramér-Rao bound, and various types of the Kalman filter might be useful for locally calibrating the focal interval. This will help to increase the accuracy and precision of the measurement.

Anyhow, it has been exciting to be involved in the growing field of confocal microscopy and surface characterization. New ideas will always emerge for developing systems to serve niche markets, especially from the manufacturers of scientific instruments who are active in industrial fields.

Appendix A

Point Spread Function

A.1 Amplitude point spread function

The amplitude *point spread function* (PSF), $h(x, y)$ or the *impulse response*, is presented here. Following Goodman [27, 114], the amplitude point spread function or the response of an imaging lens of a point source and point object, depicted in Figure A.1, is expressed by

$$h(x_3, y_3) = \int_{-\infty}^{\infty} \int_{-\infty}^{\infty} P(x_2, y_2) \exp \left[\frac{2\pi j}{\lambda} (x_2 \cdot x + y_2 \cdot y) \right] dx_2 dy_2, \quad (\text{A.1})$$

where $P(x, y)$ is the pupil function of the lens, and λ is the wavelength of light in free space. The pupil function contributes to the physical extent of the lens and its transmissivity [114], in which aberrations and the defocus effect can be added as a complex function here.

To derive the amplitude point spread function in terms of a dimensionless radial coordinate (ρ), ρ is defined by $\rho = r_2/a$ at the plane (x_2, y_2) , where a represents the radius of the imaging lens. The radial coordinate is thus $r_2 = \sqrt{x_2^2 + y_2^2}$. In most cases of a circular lens, using a dimensionless radial coordinate in the calculation is relatively convenient, such that the equation is greatly simplified. Eq.(A.1) then reduces to [114]

$$h(v) = 2 \int_0^1 P(\rho) J_0(v\rho) \rho d\rho, \quad (\text{A.2})$$

and

$$P(\rho) = \begin{cases} 1 & \text{if } \rho \leq 1 \\ 0 & \text{otherwise,} \end{cases} \quad (\text{A.3})$$

where J_0 is the zero order Bessel function of the first kind, and v is the normalized lateral optical coordinate as a function of the physical radial coordinate (r), written by

$$v = \frac{2\pi}{\lambda} \cdot r \cdot \sin \alpha. \quad (\text{A.4})$$

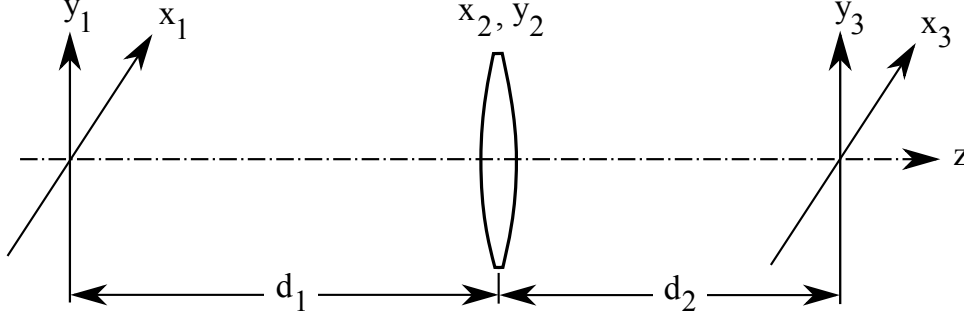


Figure A.1: Schematic illustration of the image formation geometry of a simple lens.

The numerical aperture (NA) of the lens is thus $NA = n \sin \alpha = a/d_2$, and n represents the refractive index of the medium ($n_{\text{air}} = 1$).

Additionally, the defocus effect can be added to yield a three-dimensional amplitude PSF. A quadratic phase factor, $\exp(1/2j \cdot u \cdot \rho^2)$, is used to account for the defocus distance. By substituting the quadratic phase factor into eq.(A.2), three dimensional amplitude PSF takes the form [114]

$$h(v, u) = 2 \int_0^1 P(\rho) \exp\left[\frac{1}{2}ju\rho^2\right] J_0(v\rho)\rho \, d\rho. \quad (\text{A.5})$$

In this formula, the normalized axial optical coordinate (u) is given as a function of the physical axial coordinate (z) by [115]

$$u = \frac{8\pi}{\lambda} z \sin^2\left(\frac{\alpha}{2}\right). \quad (\text{A.6})$$

The normalized axial optical coordinate (u), introduced by Wilson and Shepard [90, 115], provides accurate results particularly in the calculation with high numerical aperture. In addition, the normalized optical coordinates normalized by the light wavelength and the half aperture angle of the objective (α) are more general to use than the real physical coordinates.

Nonetheless, three-dimensional amplitude PSF in terms of the real physical coordinates (r, z) can be written by [7, 29, 30]

$$h(r, z) = \int_0^\alpha P(\theta) \exp(jkz \cos \theta) J_0(kr \sin \theta) \sin \theta \, d\theta, \quad (\text{A.7})$$

where $k = 2\pi/\lambda$, and α denotes the maximum half aperture angle of the imaging lens. Note that $P(\theta)$ is the apodization function of the objective lens [7, 29], and θ represents the angle of a ray of convergence in the medium.

Finally, the *intensity* PSF is calculated by taking the square of the *amplitude* PSF. In general, phase information is usually lost in the confocal microscopes; only the intensity is recorded.

A.2 Intensity point spread function

In a reflection confocal microscope, the objective lens is used twice as an imaging lens and a collecting lens, the amplitude PSF of these two lenses, h_1 and h_2 , are thus equal. Assume that the amplitude PSF is even in the radial coordinate, so $h_1 = h_2 = h(v, u)$. Therefore, the *intensity* PSF or the intensity impulse response, used to characterize the image formation of the optical system, becomes

$$I(v, u) = |h^2(v, u) * r(v, u)|^2, \quad (\text{A.8})$$

where $*$ denotes the convolution operation.

The amplitude reflectance of a point object is given by $r(u, v) = \delta(u, v)$, where a point source or a point detector is represented mathematically by a Dirac delta function¹. The intensity PSF then reduces to [114]

$$I(v, u) = |h(v, u)|^4. \quad (\text{A.9})$$

Accordingly, the intensity PSF can be plotted as a function of the normalized optical coordinates, v and u , using eq.(A.5) and eq.(A.9), resulting in a three-dimensional curve depicted in Figure A.2. In this curve, the lateral response along the v axis is narrower than the axial response along the u axis, which means that the optical lateral resolution is higher than the optical axial resolution (see Chapter 2 for the definition of the optical resolution).

It is worth noting that the lateral and axial intensity responses are objects-dependent. Therefore, the intensity responses obtained with simple objects, such as a point object and a plane object, are then summarized as follows.

A.2.1 Lateral intensity response

Following the formulae of Wilson [114, 115], the lateral response of a point object using a point detector in the confocal microscopes can be written as

$$I_{CONF}(v) = \left[\frac{2J_1(v)}{v} \right]^4, \quad (\text{A.10})$$

whereas the lateral response in the conventional microscopes is formulated by

$$I_{CONV}(v) = \left[\frac{2J_1(v)}{v} \right]^2. \quad (\text{A.11})$$

J_1 is the Bessel function of the first order of the first kind. The subscripts *CONF* and *CONV* denote the confocal and the conventional microscopes, respectively.

¹The Dirac delta function is useful for representing point sources, point charges, etc, which is defined as $\delta(x \neq 0) = 0$. Nonetheless, $\delta(x)$ is not a function in the ordinary mathematical sense, since the function is zero everywhere except at one point; though the integral of this function exists, as $\int_{-\infty}^{\infty} \delta(x) dx = 1$. Therefore, it is more appropriate to regard δx as a quantity with a certain symbolic meaning [7].

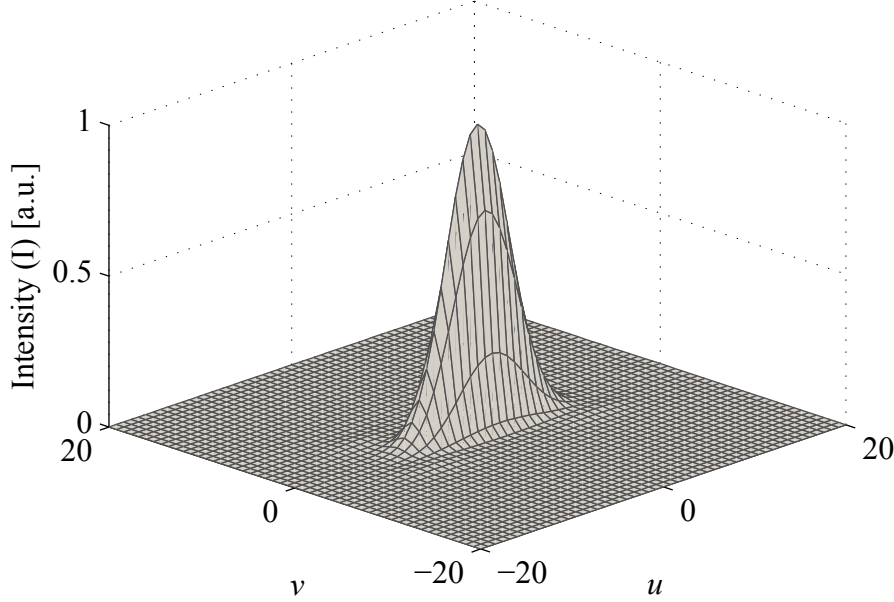


Figure A.2: 3D plot of the intensity PSF of the confocal microscopes, using eq.(A.5) and eq.(A.9), where u and v are the normalized axial and lateral optical coordinates, respectively

The *jinc* function, $J_1(x)/x$, in these expressions facilitates the calculation of the circular shape of the objective lens. In these formulas, v is the normalized lateral optical coordinate, where $v = (2\pi/\lambda) \cdot r \cdot \sin \alpha$.

Thus, the lateral responses plotted as a function of v are depicted in Figure A.3. The *half width at half maximum* (HWHM) of the lateral response in the confocal case is about 37% narrower than that in the conventional case. It can be concluded that with a point object the optical lateral resolution is enhanced more in the confocal case.

A.2.2 Axial intensity response

Following the expressions of Wilson [115], the axial response of a planar reflector using a point detector in the confocal microscopes is given by

$$I_{CONF}(u) = \left[\frac{\sin(u/2)}{u/2} \right]^2, \quad (\text{A.12})$$

whereas the axial intensity response in the conventional microscopes is constant throughout the whole range of u [115], delineated in Figure A.4 (a). In this formula, u is the normalized axial optical coordinate, $u = 8/(\pi\lambda) \cdot (z \sin^2(\alpha/2))$. For a point

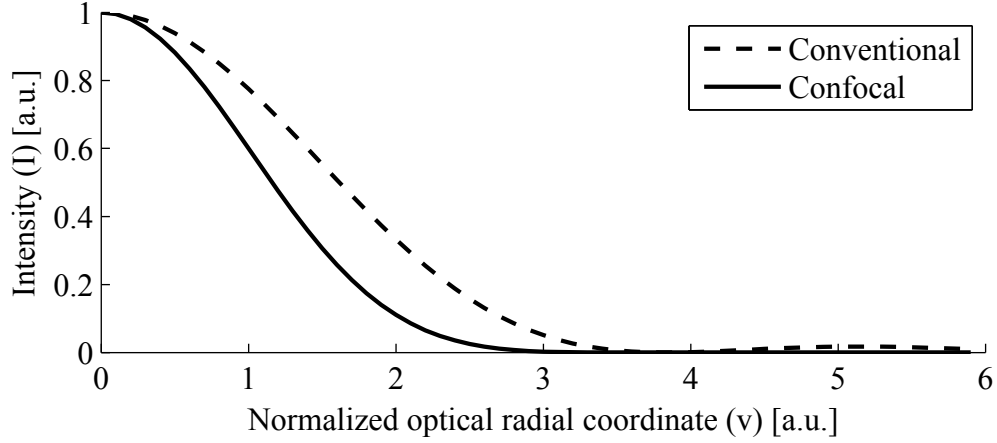


Figure A.3: Comparison of the lateral responses obtained with a point object in confocal and conventional microscopes. The graphs are plotted using eq.(A.10) and eq.(A.11).

object using a point detector, the axial response is expressed by [115]

$$I_{CONF}(u) = \left[\frac{\sin(u/4)}{u/4} \right]^4, \quad (\text{A.13})$$

in the confocal microscopes, and

$$I_{CONV}(u) = \left[\frac{\sin(u/4)}{u/4} \right]^2, \quad (\text{A.14})$$

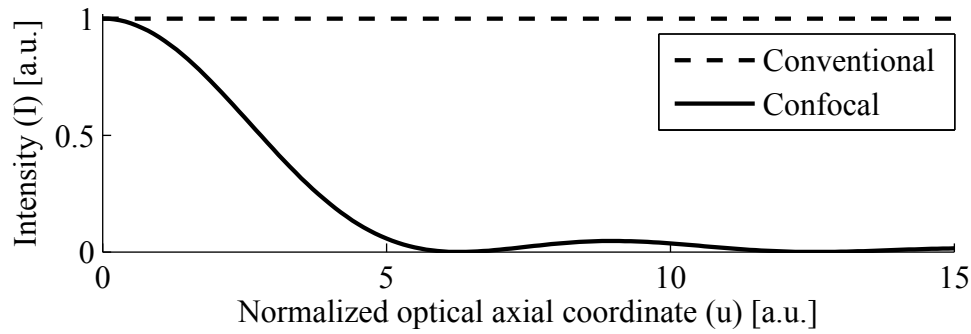
in the conventional microscopes. The responses are then plotted in Figure A.4 (b).

Figure A.4 (a) shows that the *depth-discrimination* property can be found only in the confocal case but not in the conventional case, because there is no connection between the intensity and the depth information in the conventional case. In the confocal microscopes, the axial intensity response of a planar reflector is narrower than that of a point object, so the depth-discrimination becomes more prominent when measuring with a planar reflector. The results in Figure A.4 (b) show that the conventional case seems to gain some degree of the depth-discrimination when measuring a point object. However, the curve in the confocal case is sharpened up more. This also points out that with a point object the depth-discrimination in a confocal microscope is stronger than in a conventional microscope.

A.2.3 Depth discrimination

As an alternative approach, the depth-discrimination property can be manifested using the *integrated intensity* approach or the *total power* calculation, described by Sheppard and Wilson [89, 114]. The calculated results are provided in the forms of the integrated intensity, as a function of the defocus distance. It should be noted

(a) Plane object



(b) Point object

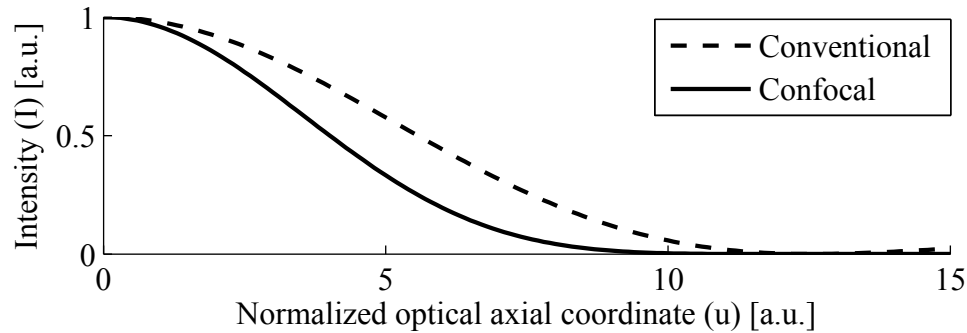


Figure A.4: Comparison of the axial responses in confocal and conventional microscopes, (a) obtained with a planar object, and (b) obtained with a point object. The graphs are developed using eq.(A.12), eq.(A.13) and eq.(A.14), respectively.

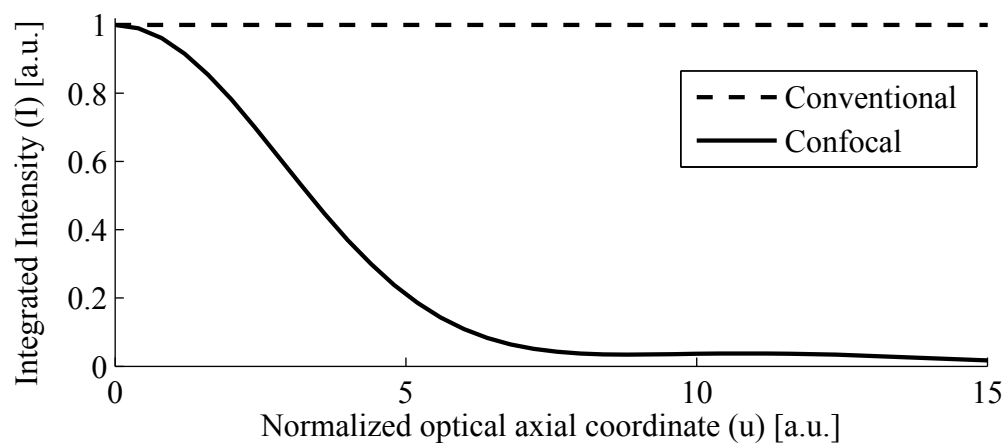


Figure A.5: The integrated intensity, an alternative approach to manifest the *depth-discrimination* property in the confocal microscopes, which cannot be realized with the constant intensity response in the conventional microscopes.

that this approach derives based upon point-source illumination. The integrated intensity is thus given by

$$I_{int}(u) = \int_0^{\infty} I(u, v)v \, dv. \quad (\text{A.15})$$

The plots of the integrated intensity distribution are delineated in Figure A.5. This graph shows that the integrated intensity in a conventional microscope is constant throughout the defocus range [114], which means that the property of depth-discrimination is not developed in a conventional microscope. In contrary, the intensity varied as a function of the defocus distance allows a confocal microscope or a confocal imaging system to obtain height information of the surface under inspection.

Appendix B

Principal planes shifting in a simple compound lens system

The calculation of the shifting of the principal planes using a simple case of two thin lenses is presented here. This appendix demonstrates that the principal planes can be shifted by varying the separation distance between the lenses in a compound lens system.

Figure B.1 illustrates a study case of two thin lenses, where $f_1 = -30$ cm and $f_2 = 20$ cm. These two lenses are separated by the distance d . Figure B.1 (a) and (b) demonstrate that the first principal plane is shifted dramatically when the separation distance between these two lenses increases by 40 cm, from $d = 10$ cm to $d = 50$ cm.

In order to calculate the related distances, the effective focal length of a compound lens system is first calculated. Note that the effective focal length is always measured from the principal planes, so it is used to calculate the positions of the principal planes.

The effective focal length (f) of the compound lens system is given by [33]

$$\frac{1}{f} = \frac{1}{f_1} + \frac{1}{f_2} - \frac{d}{f_1 f_2}, \quad (\text{B.1})$$

where f_1 and f_2 are the focal lengths of the first and the second lenses, respectively.

Furthermore, the distances measured from the principal planes to the center of the thin lenses can be written as

$$\overline{\text{PP1 H}_1} = \frac{f \cdot d}{f_2}, \quad (\text{B.2})$$

and

$$\overline{\text{PP2 H}_2} = \frac{f \cdot d}{f_1}, \quad (\text{B.3})$$

where $\overline{\text{PP1 H}_1}$ denotes the distance measured from the first principal plane to the center of the first lens. $\overline{\text{PP2 H}_2}$ is the distance measured from the second principal

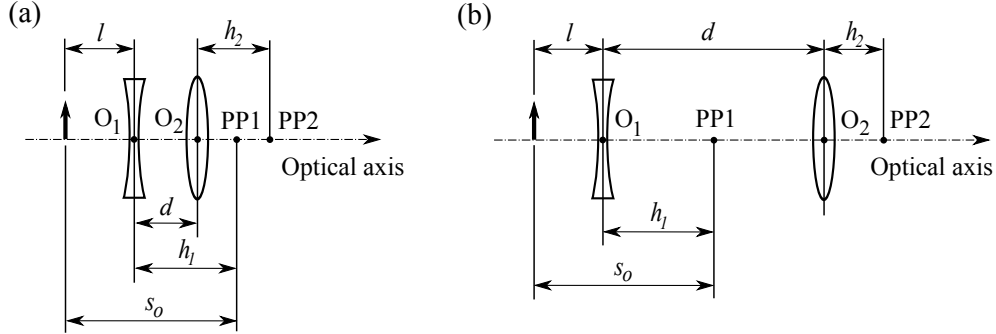


Figure B.1: Schematic illustration of the principal planes shifting in a compound lens system consisting of two thin lenses, by changing the distance between these two lenses. PP1 and PP2 represent the first and the second principal planes. h_1 is the distance measured from the first principal plane to the center of the first lens, and h_2 denotes the distance measured from the second principal plane to the center of the second lens. d is the separation distance between these two lenses, and s_o is the object distance measured from the first principal plane. l is the object distance measured from the center of the first lens, as an example $l = 10$ cm. (a) $d = 10$ cm, $h_1 = +15$ cm, $h_2 = +10$ cm, and $s_o = 25$ cm. (b) $d = 50$ cm, $h_1 = +25$ cm, $h_2 = +16.667$ cm, and $s_o = 35$ cm.

plane to the center of the second lens. Here, the positive sign convention of the distance is when the distances of h_1 , h_2 and s_o are measured to the left side of the principal planes, whereas the negative sign convention is vice versa.

Now, consider two cases of interest, depicted in Figure B.1 (a) and (b).

Case (a): $d = 10$ cm.

The effective focal length can be obtained using eq.(B.1)

$$\frac{1}{f} = \frac{1}{-30} + \frac{1}{20} - \frac{10}{(-30)(20)} = +\frac{1}{30}. \quad (\text{B.4})$$

As a result, the effective focal length is $f = 30$ cm. By substituting the focal lengths in eq.(B.2) and eq.(B.3), the distance referenced from the first principal plane to the center of the first lens is

$$\overline{\text{PP1 H}_1} = \frac{30(10)}{20} = +15 \text{ cm}, \quad (\text{B.5})$$

and the distance measured from the second principal plane to the center of the second lens is

$$\overline{\text{PP2 H}_2} = \frac{(-30)(10)}{-30} = +10 \text{ cm}. \quad (\text{B.6})$$

Consequently, the object distance referenced from the first principal plane becomes

$$s_o = 10 + 15 = 25 \text{ cm}. \quad (\text{B.7})$$

Case (b): $d = 50$ cm.

The same procedure of calculation is applied to case (b). The effective focal length is obtained using eq.(B.1)

$$\frac{1}{f} = \frac{1}{-30} + \frac{1}{20} - \frac{50}{(-30)(20)} = +\frac{1}{10}. \quad (\text{B.8})$$

Thus, the effective focal length yields $f = 10$ cm. By substituting the focal lengths in eq.(B.2) and eq.(B.3), the distance referenced from the first principal plane to the center of the first lens is expressed as

$$\overline{\text{PP1 H}_1} = \frac{10(50)}{20} = +25 \text{ cm}, \quad (\text{B.9})$$

and the distance measured from the second principal plane to the center of the second lens is

$$\overline{\text{PP2 H}_2} = -\frac{10(50)}{-30} = +16.667 \text{ cm}. \quad (\text{B.10})$$

In consequence, the object distance referenced from the first principal plane becomes

$$s_o = 10 + 25 = 35 \text{ cm}. \quad (\text{B.11})$$

This example demonstrates that the positions of the principal planes are shifted in accordance with the arrangement of the lenses in a compound lens system, such that the object and image distances measured from the principal planes are varied accordingly. By this mean, when the principal planes are shifted approaching infinity the object and image distances are increased to nearly infinity, even though the physical distances of the object and image referenced from the first lens and the last lens of a compound lens system are finite distances.

Appendix C

Geometry Approach for Pinhole Design

In Geometry approach, the pinhole coordinate is determined following the law of trigonometry. Consequently, the pinhole coordinate (H_p) is calculated as a function of the focal coordinate (h_p), the tilt angle of the pinhole mask (Θ), the magnification on the optical axis (m_0), and the focal length of the objective lens (d), where these variables are depicted in Figure C.1. Then, the Scheimpflug's rule is also expressed by the law of trigonometry.

Since there are two set of the similar triangles, the calculation is separated into two, where $H_p = H_i + H_j$ represents the pinhole coordinate in connection with the focal coordinate ($h_p = h_i + h_j$).

In the first case of the similar triangles, the local tilt angle of a focus-pinhole pair (γ_i), presented in Figure C.2, is written as a function of h_i by

$$\sin(\gamma_i) = \frac{h_i}{d} \cdot \sin\left(\frac{\pi}{2} - \Phi - \gamma_i\right), \quad (\text{C.1})$$

Then, H_i can be expressed as

$$H_i = m_0 \cdot d \cdot \frac{\sin(\gamma_i)}{\sin\left(\frac{\pi}{2} + \Theta - \gamma_i\right)}. \quad (\text{C.2})$$

In the second case of the similar triangles, by applying the same process to Figure C.3, the local tilt angle of a focus-pinhole pair (θ_j) as a function of h_j has the form

$$\sin(\theta_j) = \frac{h_j}{d} \cdot \sin\left(\frac{\pi}{2} + \Phi - \theta_j\right), \quad (\text{C.3})$$

consequently, the H_j can be obtained as

$$H_j = m_0 \cdot d \cdot \frac{\sin(\theta_j)}{\sin\left(\frac{\pi}{2} - \Theta - \theta_j\right)}. \quad (\text{C.4})$$

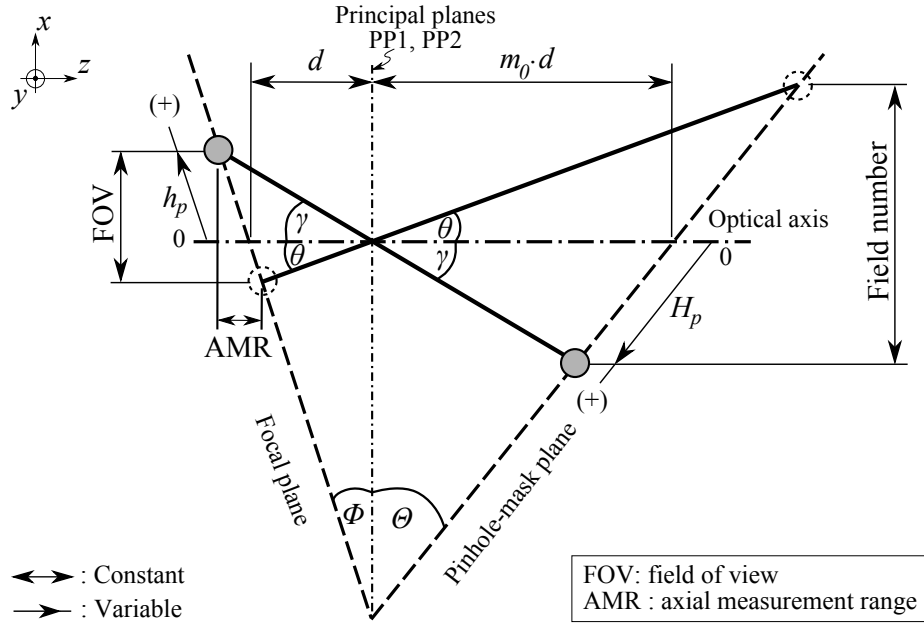


Figure C.1: Schematic of the Geometry approach to calculate the pinhole coordinate. Φ is the tilt angle of the focal plane. Θ is the tilt angle of the pinhole mask plane. d denotes the focal length of the microscope objective. m_0 represents the lateral magnification on the optical axis. h_p is the focal coordinate at the tilted focal plane. H_p is the pinhole coordinate in the tilted pinhole-mask plane, where $p = 1, 2, \dots, n$ represent the indices of the pinhole aperture-image pairs. γ and θ are the local tilt angles of the focus-pinhole pairs.

It can be seen that eq.(C.1) and eq.(C.3) have no analytical solution in general, but it is possible to solve these two equations numerically. Thereafter, the pinhole coordinate (H_p) can be obtained using eq.(C.2) and eq.(C.4). In conclusion, the Geometry approach is quite direct but the calculation is relatively laborious. This approach has no analytical solution, so its application is limited to some extent.

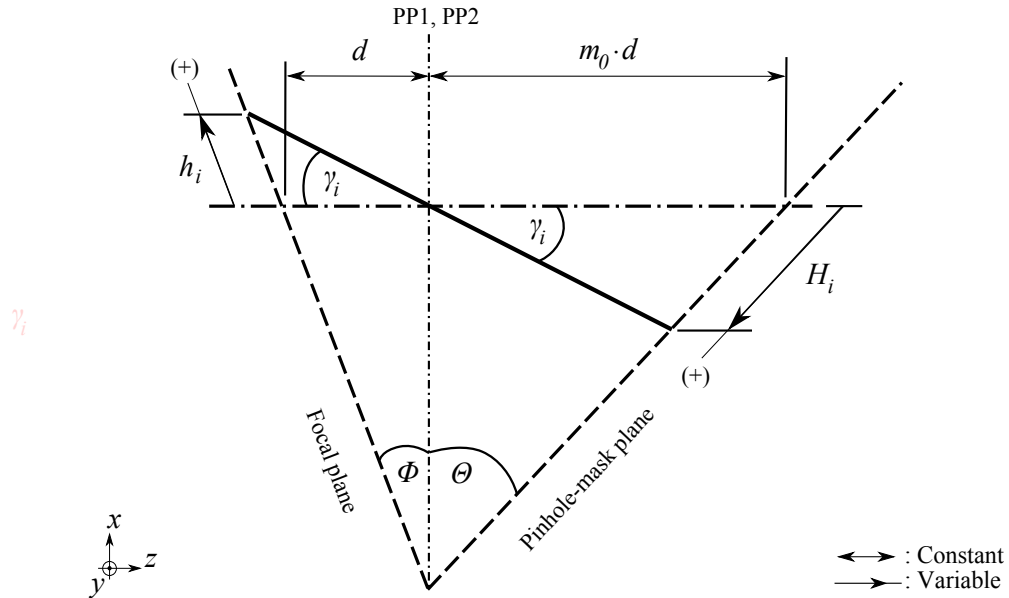


Figure C.2: The first case of the similar triangles. In this case, the h_i and H_i are in positive sign, and γ_i is the local tilt angle of the focus-pinhole pair, where $i = 1, 2, \dots, m$ and $p = 1, 2, \dots, m, m + 1, \dots, n$ represent the indices of the pinhole aperture-image pairs.

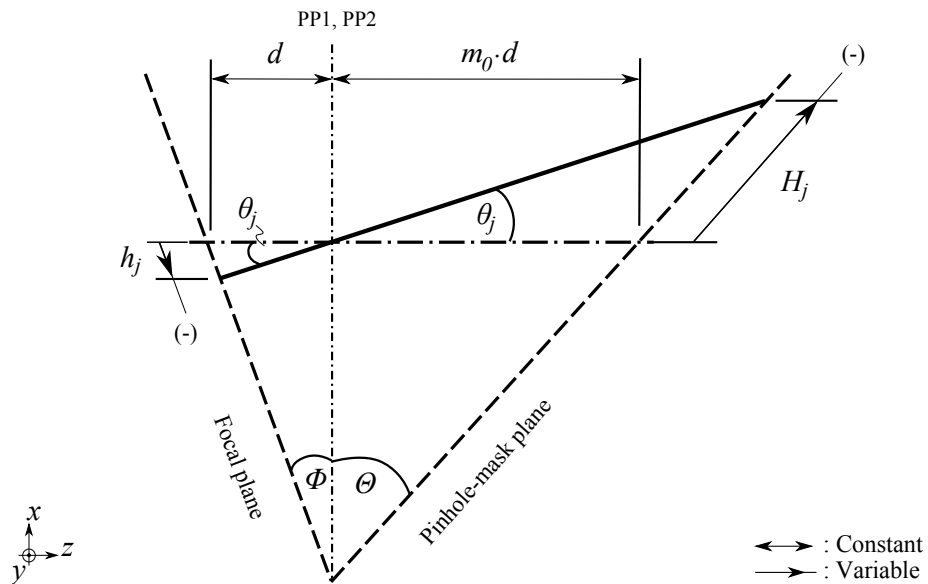


Figure C.3: The second case of the similar triangles. In this case, the h_j and H_j are in negative sign, and θ_j is the local tilt angle of a focus-pinhole pair, where $j = m, m + 1, \dots, n$ and $p = 1, 2, \dots, m, m + 1, \dots, n$ represent the indices of the pinhole aperture-image pairs.

Appendix D

Gaussian-Lens-Equation Approach for Pinhole Design

This appendix presents the main derivation of the magnification in a tilted plane system. The result of this derivation is of importance for the pinhole pattern design (see Chapter 3), to incorporate uncorrected keystone distortion inherent in the system of the CLSS in the pinhole design.

The pinhole coordinate (H_p) are derived as a function of five variables:

$$H_p = H_p(h_p, m_{x_p}; m_0, \Phi, \Theta), \quad (\text{D.1})$$

where (;) separates constants and variables. If the function is $f(x_1, x_2; x_3, x_4)$, x_1 and x_2 represent the constants, while x_3 and x_4 denote the variables. h_p is the variable of the focal coordinate. m_{x_p} represents the lateral magnification in the tilted focal plane, where $p = 1, 2, \dots, n$ denote the indices of the pinhole aperture-image pairs. m_0 is the lateral magnification on the optical axis. Φ and Θ are the tilt angles of the focal plane and the pinhole mask plane, respectively.

Referring to Figure D.1, the well-known Gaussian Lens Equation, with the paraxial and thin lens approximations, is given by

$$\frac{1}{f} = \frac{1}{s_o} + \frac{1}{s_i}. \quad (\text{D.2})$$

Consequently, the Newtonian form of the thin-lens equation can be expressed as

$$f^2 = g_o \cdot g_i, \quad (\text{D.3})$$

where $g_o = s_o - f$ and $g_i = s_i - f$.

Following the Scheimpflug's rule [82], a tilted image plane is formed from a tilted object plane by an imaging system. The imaging system means either a singlet-lens system or a compound lens system. As mentioned before, the shifting of the principal planes can be accomplished by the optical arrangement in a compound lens system. When the principal planes are shifted, the object and image

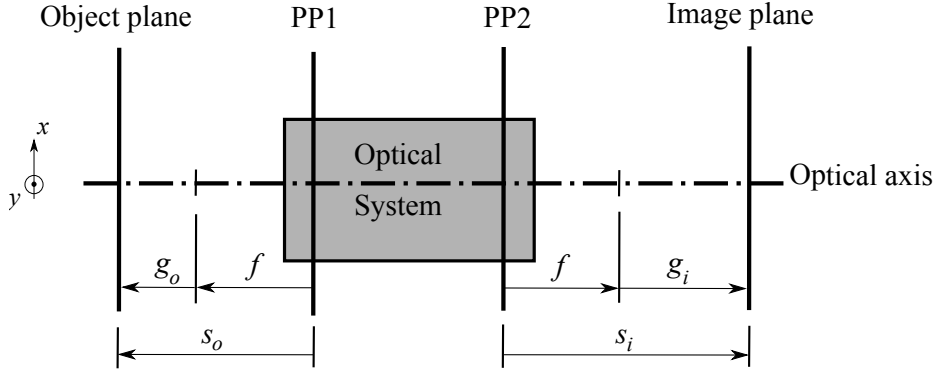


Figure D.1: Schematic of an imaging system, where PP1 is the first principal plane and PP2 is the second principal plane. f is the effective focal length of the imaging system. s_o is the object distance measured from PP1. s_i is the image distance measured from PP2. g_o and g_i are the object and image distances with respect to the effective focal points.

distances vary, so does the magnification, without the physical movement of the object.

In order to shift the principal planes from positive (*direct keystone*) to infinity (*corrected keystone*) and to negative direction (*reverse keystone*), a compound lens system should be employed, (see Chapter 3 for the definition of all cases of the keystone distortion). In practice, a singlet-lens system can only generate the *direct keystone* distortion. In contrary, a compound lens system in the CLSS comprising of a field lens, a tube lens and a microscope objective are used to form the *reverse keystone* distortion at the tilted focal plane.

In this derivation, the tilted the focal plane is considered as a tilted object, and the tilted image plane is formed at the tilted pinhole-mask plane, shown in Figure D.2. Here, the optical system is assumed to be a singlet-lens system, which directs the derivation to the *direct keystone* case. However, the result can practically be applied in all cases of the keystone distortion.

The relation of the tilt angles of the object plane and the image planes, shown in Figure D.2, can be written by

$$m_0 = \frac{\tan(\Theta)}{\tan(\Phi)}. \quad (\text{D.4})$$

As the lateral magnification is the ratio of the image distance (or size) to the object distance (or size) [33], the lateral magnification in the system of Figure D.2 takes the form

$$m_{x_p} = -\frac{H_p \cos(\Theta)}{h_p \cos(\Phi)} = -\frac{s_{i_p}}{s_{o_p}}, \quad (\text{D.5})$$

where the minus sign means that the image is inverted from the object.

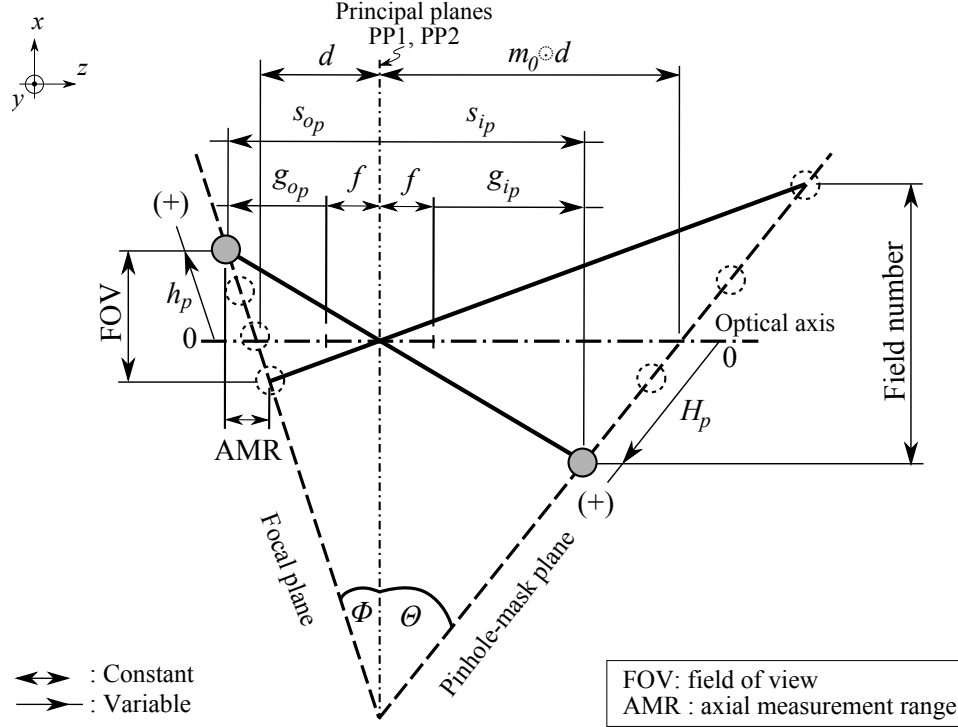


Figure D.2: Schematic illustration of the Gaussian-lens-equation approach for the derivation of the magnification in a tilted plane system. Θ is the tilt angle of the focal plane. Φ is the tilt angle of the pinhole mask plane. d is the microscope objective focal length. m_0 is the lateral magnification on the optical axis. f is the effective focal length of an imaging system. s_{op} and s_{ip} are object and image distances with respect to the principal planes, PP1 and PP2, respectively. g_{op} and g_{ip} are the local object and image distances with respect to the effective focal points. h_p is the focal coordinate along the tilted focal plane. H_p is the pinhole coordinate along the tilted pinhole-mask plane, where $p = 1, 2, \dots, n$ denote the indices of pinhole aperture-image pairs.

By substituting $s_{ip} = m_0 \cdot d - H_p \sin(\Theta)$ and $s_{op} = d + h_p \sin(\Phi)$ into eq.(D.5), m_{x_p} becomes

$$m_{x_p} = -\frac{s_{ip}}{s_{op}} = -\frac{m_0 \cdot d - H_p \sin(\Theta)}{d + h_p \sin(\Phi)}, \quad (\text{D.6})$$

where $p = 1, 2, \dots, n$ represent the indices of the pinhole aperture-image pairs. Then, Eq.(D.6) represents the lateral magnification along the tilted image plane, where the lateral plane means the $x - y$ plane. Note that m_0, d, Φ, Θ are considered constant throughout the thesis.

By substituting these fractions, $\sin \Theta / \sin \Theta$ and $\sin \Phi / \sin \Phi$, into eq.(D.5),

the lateral magnification becomes

$$m_{x_p} = \frac{H_p \cos(\Theta) \frac{\sin(\Theta)}{\sin(\Theta)}}{h_p \cos(\Phi) \frac{\sin(\Phi)}{\sin(\Phi)}} = \frac{H_p \sin(\Theta)}{h_p \sin(\Phi)} \cdot \frac{\tan(\Phi)}{\tan(\Theta)}. \quad (\text{D.7})$$

After rearranging eq.(D.7), $H_p \sin(\Theta)$ appears as

$$H_p \sin(\Theta) = m_{x_p} \cdot m_0 \cdot h_p \sin(\Phi). \quad (\text{D.8})$$

The lateral magnification in eq.(D.6) can be simplified further by substituting $H_p \sin(\Theta)$ into eq.(D.6), which leads to

$$m_{x_p} = -\frac{m_0 \cdot d}{d + h_p (1 + m_0) \sin(\Phi)}. \quad (\text{D.9})$$

Therefore, eq.(D.9) is a simplified form of the lateral magnification at the tilted image plane. Now consider the total magnification across the tilted image plane, where the axial magnification (z axis) is included. According to Hecht [33], the axial magnification is given by

$$m_{z_p} = -\frac{dg_{i_p}}{dg_{o_p}}. \quad (\text{D.10})$$

By differentiating $g_{i_p} = m_0 d - f - H_{p_z}$ and $g_{o_p} = d - f + h_{p_z}$ to obtain dg_{i_p} and dg_{o_p} , Eq.(D.10) has the form

$$m_{z_p} = -\frac{dg_{i_p}}{dg_{o_p}} = \frac{dH_{p_z}}{dh_{p_z}}. \quad (\text{D.11})$$

The minus sign is eliminated in eq.(D.11), as the direction of h_{p_z} and H_{p_z} are the same, whereas g_{i_p} and g_{o_p} are opposite each other, depicted in Figure D.2. On substituting $m_{z_p} = -m_{x_p}^2$ [33] into eq.(D.11) and integrating this formula, the equation now becomes

$$H_{p_z} = -\int_0^{h_{p_z}} m_{x_p}^2 dt, \quad (\text{D.12})$$

where t is a dummy variable. Consequently, $h_{p_z} = h_p \sin(\Phi)$ can be differentiated to obtain

$$dh_{p_z} = \sin(\Phi) dh_p. \quad (\text{D.13})$$

By substituting eq.(D.13) in eq.(D.12), H_{p_z} is now

$$H_{p_z} = -\int_0^{h_p} m_{x_p}^2 \sin(\Phi) dT, \quad (\text{D.14})$$

where T is a dummy variable. The integration is carried out with respect to T from zero to h_p ; hence, eq.(D.14) takes the form

$$H_{p_z} = -m_x \cdot m_0 \cdot \sin(\Theta) \cdot h_p. \quad (\text{D.15})$$

The sign convention of H_{p_x} and h_{p_z} in the positive direction are presented in Figure D.2.

Then, the pinhole coordinate (H_p) along the tilted pinhole-mask plane is obtained in terms of a scalar product of two orthogonal elements by

$$H_p = \sqrt{H_{p_x}^2 + H_{p_z}^2}. \quad (\text{D.16})$$

By substituting H_{p_x} and H_{p_z} into eq.(D.16), H_p as a function of h_p is given by

$$H_p = h_p \cdot m_{x_p} \sqrt{\cos^2(\Phi) + m_0^2 \sin^2(\Phi)}. \quad (\text{D.17})$$

Consequently, the pinhole coordinate (H_p) can be calculated as a function of the focal coordinate (h_p).

Finally, the total magnification along the tilted image plane can be written by

$$m_p = m_{x_p} \sqrt{\cos^2(\Phi) + m_0^2 \sin^2(\Phi)}. \quad (\text{D.18})$$

It is interesting to point out that this expression can predict all significant cases of the keystone distortion. The most direct one is the *direct keystone* distortion, in which case m_p is varied across the tilted image plane following the laws of geometry, shown in Figure D.2. However, the square root product in eq.(D.18) is a constant if a given tilt angle of the focal plane (Φ) is also constant. In consequence, when the principal planes are shifted approaching infinity the lateral magnification (m_{x_p}) will be uniform across the tilted image plane, so does the total magnification (m_p), leading to the *corrected keystone* case. Moreover, when the principal planes are shifted to the negative direction, the sign convention of m_{x_p} then m_p are reversed, resulting in the *reverse keystone* case.

Bibliography

- [1] *Journal of the Royal Microscopical Society, Volume 60*. Royal Microscopical Society, 1929, ch. 9, p. 123.
- [2] M. Abramowitz and M. W. Davidson, “Köhler microscope illumination,” [http : //micro.magnet.fsu.edu/primer/anatomy/kohler.html](http://micro.magnet.fsu.edu/primer/anatomy/kohler.html), Olympus America, Inc. and National High Magnetic Field Laboratory.
- [3] A. C. Aplin, S. R. Larter, M. A. Bigge, G. Macleod, R. E. Swarbrick, and D. Grunberger, “Confocal microscopy of fluid inclusions reveals fluid-pressure histories of sediments and an unexpected origin of gas condensate,” *Geology*, vol. 28, pp. 1047–1050, 2000.
- [4] B. Bhushan, *Principles and Applications of Tribology*. Wiley-Interscience, 1999.
- [5] A. A. Blaker, *Handbook for scientific photography*. Focal Press, 1989.
- [6] M. Born and E. Wolf, *Principles of Optics*. Cambridge University Press, UK, 1999, ch. 8.
- [7] —, *Principles of Optics*. Cambridge University Press, UK, 1999.
- [8] —, *Principles of Optics*. Cambridge University Press, UK, 1999, ch. 9.
- [9] G. Bradski and A. Kaehler, *Learning OpenCV: Computer Vision with the OpenCV Library*. O’Reilly Media, 2008, ch. 6, p. 150.
- [10] E. Brigham, *Fast Fourier Transform and Its Applications*. Prentice Hall, 1988.
- [11] S. Cha, P. C. Lin, L. Zhu, P.-C. Sun, and Y. Fainman, “Nontranslational three-dimensional profilometry by chromatic confocal microscopy with dynamically configurable micromirror scanning,” *Applied Optics*, vol. 39, no. 16, pp. 2605–2613, June 2000.
- [12] S. Chanbai, J. Valentin, M. Weber, and G. Wiora, “Device i.e. line scanner, for monitoring measuring points on object surface to be measured, has

- focus plane displaceable parallel to object surface, where object surface is displaceable lateral to focus plane,” German Patent DE102 008 031 412 A1, 2010.
- [13] S. Chanbai and M. Weber, *Encyclopedia of Tribology*. Springer, ch. Accuracy of surface topography characterization tools.
- [14] S. Chanbai, G. Wiora, and M. Weber, “A novel confocal line scanning sensor,” *Proc. SPIE*, vol. 7378, p. 737822, 2009.
- [15] S. Chanbai, G. Wiora, M. Weber, and H. Roth, “Fast-Fourier-transform for tilted planes based on numerical integration,” in *Focus on Microscopy 2009 (FOM)*, 2009, p. 124.
- [16] T. R. Corle, C.-H. Chou, and G. S. Kino, “Depth response of confocal optical microscopes,” *Optics Letters*, vol. 11, no. 12, pp. 770–772, December 1986.
- [17] T. R. Corle and G. S. Kino, *Confocal Scanning Optical Microscopy and Related Imaging Systems*. Academic Press, 1996.
- [18] T. R. Corle, “Studies in scanning confocal microscopy,” Ph.D. dissertation, Stanford University, 1989.
- [19] V. R. Daria, J. J. Miranda, and C. Saloma, “High-contrast images of semiconductor sites via one-photon optical beam-induced current imaging and confocal reflectance microscopy,” *Appl. Opt.*, vol. 41, no. 20, pp. 4157–4161, 2002.
- [20] A. Diaspro, Ed., *Confocal and Two-Photon Microscopy: Foundations, Applications and Advances*. Wiley-Liss, 2001.
- [21] A. Elwazri, P. Wanjara, and S. Yue, “Measurement of pearlite interlamellar spacing in hypereutectoid steel,” *Materials Characterization*, vol. 54, no. 4-5, pp. 473–478, 2005.
- [22] F. Ericson and J. A. Schweitz, *Handbook of Micro/Nano Tribology*. CRC Press, 1998, ch. 15.
- [23] D. T. Fewer, S. J. Hewlett, E. M. McCabe, and J. Hegarty, “Direct-view microscopy experimental investigation of the dependence of the optical sectioning characteristics on pinhole-array configuration,” *J. Microscopy*, vol. 187, pp. 54–61, 1997.
- [24] R. F. Fischer, B. Tadic-Galeb, and P. Yoder, *Optical System Design*. McGraw-Hill Companies, 2008, ch. 5, p. 92.
- [25] M. Fleischer, R. Windecker, and H. J. Tiziani, “Theoretical limits of scanning white-light interferometry signal evaluation algorithms,” *Appl. Opt.*, vol. 40, pp. 2815–2820, 2001.

- [26] O. Giraud and O. Dugne, "Characterization of materials by confocal microscopy," in *MC95. International Metallography Conference*, 1996, pp. 23–28.
- [27] J. W. Goodman, *Introduction to Fourier Optics*. Roberts & Company, 2004.
- [28] H. Gross, *Handbook of Optical Systems, Volume 3, Aberration Theory and Correction of Optical Systems*, H. Gross, Ed. Wiley-VCH, 2007.
- [29] M. Gu, *Advanced Optical Imaging Theory*. Springer Verlag, Heidelberg, 1999.
- [30] M. Gu, D. Day, O. Nakamura, and S. Kawata, "Three-dimensional coherent transfer function for reflection confocal microscopy in the presence of refractive-index mismatch," *J. Opt. Soc. Am. A*, vol. 18, no. 8, pp. 2002–2008, August 2001.
- [31] M. Gu, T. Tannous, and J. R. Sheppard, "Effect of an annular pupil on confocal imaging through highly scattering media," *Optics Letters*, vol. 21, no. 5, pp. 312 – 314, March 1996.
- [32] Q. Hao, "Alternative algorithm for evaluation of the intensity distribution of the confocal microscope," Presentation, WEMESURF internal meeting, March 2007.
- [33] E. Hecht, *Optics*. Addison Wesley, 1998.
- [34] A. R. Hibbs, G. MacDonald, and K. Garsha, *Handbook of Biological Confocal Microscopy*. Springer, 2006, ch. 36.
- [35] S. B. Howell, *Handbook of CCD Astronomy*. Cambridge University Press, 2006.
- [36] J. Illingworth and J. Kittler, "A survey of the hough transform," *Computer Vision, Graphics, and Image Processing*, vol. 44, no. 1, pp. 87–116, 1988.
- [37] M. Instruments, "Introduction to CCD imaging," <http://ccd.mii.cz/art?id=303&lang=409>, February 2008, CCD camera for astronomy.
- [38] X. Jiang, P. S. D. Whitehouse, and L. Blunt, "Paradigm shifts in surface metrology. part ii. the current shift," *Proc. R. Soc. A*, vol. 463, no. 2085, pp. 2071–2099, September 2007.
- [39] B. Jähne, H. Scharr, and S. Körkel., *Handbook of Computer Vision and Applications, Volume 2*. Academic Press, 1999, ch. Principles of Filter Design, pp. 125–151.

- [40] H. J. Jordan, M. Wegner, and H. J. Tiziani, “Highly accurate non-contact characterization of engineering surfaces using confocal microscopy,” *Meas. Sci. Technol.*, vol. 9, pp. 1142–1151, 1998.
- [41] J. Kim, D. Kang, and D. Gweon, “Spectrally encoded slit confocal microscopy,” *Opt. Lett.*, vol. 31, no. 11, pp. 1687 – 1689, June 2006.
- [42] G. S. Kino and G. Q. Xiao, *Confocal Microscopy*. Academic Press, London, 1990, ch. 14.
- [43] C. J. Koester, S. M. Khanna, H. D. Rosskothien, R. B. Tackaberry, and M. Ulfendahl, “Confocal slit divided-aperture microscope: applications in ear research,” *Appl. Opt.*, vol. 33, no. 4, pp. 702 – 708, February 1994.
- [44] A. Köhler, “Gedanken zu einem neuen beleuchtungsverfahren für mikrophotographische zwecke,” *Z. Wiss. Mikrosk.*, vol. 10, pp. 433–440, 1893.
- [45] E. Y. Lam, X. Zhang, H. Vo, T. C. Poon, and G. Indebetouw, “Three-dimensional microscopy and sectional image reconstruction using optical scanning holography,” *Appl. Opt.*, vol. 48, no. 34, pp. H113–H119, 2009.
- [46] P. C. Lin, P.-C. Sun, L. Zhu, and Y. Fainman, “Single-shot depth-section imaging through chromatic slit-scan confocal microscopy,” *Appl. Opt.*, vol. 37, no. 28, pp. 6764–6770, 1998.
- [47] V. K. Madisetti, *The digital signal processing handbook: video, speech, and audio signal processing and associated standards*. Crc Pr Inc, 2009.
- [48] F. Marinello, P. Bariani, L. D. Chiffre, and H. N. Hansen, “Development and analysis of a software tool for stitching three-dimensional surface topography data sets,” *Meas. Sci. Technol.*, vol. 18, pp. 1404–1412, 2007.
- [49] B. R. Masters, *Confocal Microscopy and Multiphoton Excitation Microscopy: The Genesis of Live Cell Imaging*. SPIE Press, 2006.
- [50] —, “David maurice’s contributions to optical ophthalmic instrumentation roots of the scanning slit clinical confocal microscope,” *Exp. Eye Res.*, vol. 78, no. 3, pp. 315–326, 2004.
- [51] B. Matsumoto, P. T. Matsudaira, and L. Wilson, Eds., *Cell Biological Applications of Confocal Microscopy: 38 (Methods in Cell Biology)*. Academic Press Inc, 1993.
- [52] K. Matsushima, H. Schimmel, and F. Wyrowski, “Fast calculation method for optical diffraction on tilted planes by use of the angular spectrum of plane waves,” *J. Opt. Soc. Am. A*, vol. 20, no. 9, pp. 1755–1762, 2003.

- [53] J. McCarthy, J. Fairing, and J. Bucholz, “Confocal tandem scanning reflected light microscope,” US Patent 4,802,748, February 7, 1989.
- [54] W. J. Merline and S. B. Howell, “A realistic model for point-sources imaged on array detectors: The model and initial results,” *Exp. Astron.*, vol. 6, pp. 163–210, 1995.
- [55] M. Minsky, “Microscopy apparatus,” US Patent 3 013 467, 1961.
- [56] —, “Memoir on inventing the confocal scanning microscope,” *Scanning*, vol. 10, pp. 128–138, 1988.
- [57] G. Molesini, G. Pedrini, P. Poggi, and F. Quercioli, “Focus wavelength encoded optical profilometer,” *Opt. Commun.*, vol. 49, pp. 229–233, 1984.
- [58] NanoFocus, “Product,” <http://www.nanofocus.de>, NanoFocus AG.
- [59] H. Naora, “Microspectrophotometry and cytochemical analysis of nucleic acids,” *Science* 14, vol. 114, no. 2959, pp. 279–280, 1951.
- [60] P. Nipkow, German Patent DE30 105, 1884.
- [61] A. Nussbaum and R. A. Phillips., *Contemporary optics for scientists and engineers*. Prentice-Hall, 1976, ch. 10, p. 265.
- [62] A. V. Oppenheim and R. W. Schaffer, *Digital Signal Processing*. Prentice Hall, US ed edition, 1975.
- [63] B. R. Organization, “Stray light analysis in ASAP,” Breault Research Organization, Inc., Tech. Rep., 2007.
- [64] S. W. Paddock, “Tandem scanning reflected light microscopy of cell substratum adhesions and stress fibres in swiss 3T3 cells,” *J. Cell Sci.*, vol. 93, pp. 143–146, 1989.
- [65] J. A. Parker, R. V. Kenyon, and D. E. Troxel, “Comparison of interpolating methods for image resampling,” *IEEE Medical Imaging*, vol. 2, pp. 31–39, 1983.
- [66] J. Pawley, Ed., *Handbook of Biological Confocal Microscopy*. Springer, 2006.
- [67] M. Petran, M. Hadravsky, J. Benes, R. Kucera, and A. Boyde, “The tandem scanning reflected light microscope. part 1 - the principle, and its design,” *Proc. R. Microscop. Soc.*, vol. 20, pp. 125–129, 1985.
- [68] M. Petráň, A. Boyde, and M. Hadravský, *Confocal Microscopy*. Academic Press, London, 1990, ch. 9, p. 257.
- [69] M. Petráň and M. Hadravský, Czechoslovakian Patent 7720, 1966.

- [70] ———, “Tandem-scanning reflected-light microscope,” *J. Opt. Soc. Am.*, vol. 58, no. 5, pp. 661–664, 1968.
- [71] M. Priest and C. M. Taylor, “Automobile engine tribology - approaching the surface,” *Wear*, vol. 241, no. 2, pp. 193–203, 2000.
- [72] L. Rayleigh, “Investigations in optics, with special reference to the spectroscope,” *Phil. Mag. series (5)*, vol. 8, pp. 261–274, 1879.
- [73] E. E. N. report, “Dynamic height of easily deformable surfaces.” Bio Health Newsletter, October 2010, boletín CESEAND Perfiles Tecnológicos.
- [74] F. Roberts and J. Young, “The flying-spot microscope,” *Proc. IEE - Part IIIA: Television*, vol. 99, pp. 747 – 757, 1952.
- [75] A. K. Ruprecht, T. F. Wiesendanger, and H. J. Tiziani, “Signal evaluation for high-speed confocal measurements,” *Appl. Opt.*, vol. 41, pp. 7410–7415, 2002.
- [76] ———, “Chromatic confocal microscopy with a finite pinhole size,” *Opt. Lett.*, vol. 29, no. 18, pp. 2130 – 2132, September 2004.
- [77] T. Rymarczyk, “Untersuchung konfokaler auswertalgorithmen, internal technical report,” NanoFocus, Tech. Rep., 2007.
- [78] J. Sasian, “Image plane tilt in optical systems,” *Opt. Eng.*, vol. 31, pp. 527–532, 1992.
- [79] J. M. Sasian, “How to approach the design of a bilateral symmetric optical system,” *Opt. Eng.*, vol. 33, no. 6, pp. 2045–2061, 1994.
- [80] H. Sax, “Stepper motor driving,” SGS-THOMSON Microelectronics, Tech. Rep., 1995.
- [81] J. Scheers, M. Vermeulen, C. D. MarÃ©, and K. Meseure, “Assessment of steel surface roughness and waviness in relation with paint appearance,” *Int. J. Mach. Tool. Manu.*, vol. 38, no. 5-6, pp. 647–656, 1998.
- [82] T. Scheimpflug, “Improved method and apparatus for the systematic alteration or distortion of plane pictures and images by means of lenses and mirrors for photography and for other purposes,” British Patent GB 1196/1904, 1904.
- [83] ———, “Verfahren und apparat zur methodischen verzerrung ebener bilder auf photographischem wege mit beliebigen objektiven.” Austria Patent AT20 299 (B), 1905.

- [84] S. Scherer, "Fokus-variation zur optischen 3d messung im mikro- and nanobereich," in *Handbuch zur Industriellen Bildverarbeitung*. Fraunhofer IRB Verlag, 2007, pp. 198–202.
- [85] J. J. Sheehan, *Business & Corporate Aviation Management : On Demand Air Travel*. McGraw-Hill Professional, 2003.
- [86] C. J. R. Sheppard and M. Gu, "Aberration compensation in confocal microscopy," *Applied Optics*, vol. 30, no. 25, pp. 3563–3568, September 1991.
- [87] —, "Edge-setting criterion in confocal microscopy," *Appl. Opt.*, vol. 31, no. 22, pp. 4575–4577, 1992.
- [88] C. J. R. Sheppard and X. . Q. . Mao, "Confocal microscopes with slit apertures," *J. Mod. Opt.*, vol. 35, no. 7, pp. 1169–1185, 1988.
- [89] C. J. R. Sheppard and T. Wilson, "Depth of field in the scanning microscope," *Opt. Lett.*, vol. 3, no. 3, pp. 115–117, 1978.
- [90] —, "Effects of high angles of convergence on $v(z)$ in the scanning acoustic microscope," *Appl. Phys. Lett.*, vol. 38, pp. 858–859, 1981.
- [91] C. J. R. Sheppard, "Aberrations in high aperture conventional and confocal imaging systems," *Applied Optics*, vol. 27, no. 22, pp. 4782–4786, November 1988.
- [92] C. J. R. Sheppard, M. Gu, K. Brain, and H. Zhou, "Influence of spherical aberration on axial imaging of confocal reflection microscopy," *Applied Optics*, vol. 33, no. 4, pp. 616 – 624, February 1994.
- [93] K. Shi, P. Li, S. Yin, and Z. Liu, "Chromatic confocal microscopy using supercontinuum light," *Optics Express*, vol. 12, no. 10, pp. 2096–2101, May 2004.
- [94] W. Smith, *Modern Optical Engineering*. McGraw-Hill Professional, 2007.
- [95] J. P. Southall, *The principles and methods of geometrical optics*. BiblioLife, 2009, ch. 8, pp. 244–245.
- [96] C. M. Sparrow, "On spectroscopic resolving power," *Astrophys. J.*, vol. 44, pp. 76–86, 1916.
- [97] K. R. Spring, H. E. Keller, and M. W. Davidson, "Microscope objectives introduction," [http : //www.olympusmicro.com/primer/anatomy/objectives.html](http://www.olympusmicro.com/primer/anatomy/objectives.html), Olympus America Inc.
- [98] K. J. Stout and L. Blunt, *Three-dimensional surface topography*. Butterworth Heinemann, 2000.

- [99] K. J. Stout and L. A. Blunt, "Application of 3-d topography to bio-engineering," *Int. J. Mach. Tool. Manu.*, vol. 35, pp. 219–229, 1995.
- [100] B. N. Taylor and C. E. Kuyatt, "Guidelines for evaluating and expressing the uncertainty of NIST measurement results. Technical report, NIST technical note 1297," U.S. Government Printing Office, Washington, DC, Tech. Rep., 1994.
- [101] H. J. Tiziani, R. Achi, and R. N. Krämer, "Chromatic confocal microscopy with microlenses," *J. Mod. Opt.*, vol. 43, no. 1, pp. 155–163, 1996.
- [102] H. J. Tiziani and H. M. Uhde, "Three-dimensional image sensing by chromatic confocal microscopy," *Appl. Opt.*, vol. 33, no. 10, pp. 1838–1841, 1994.
- [103] H. J. Tiziani and H.-M. Uhde, "Three-dimensional analysis by a microlens-array confocal arrangement," *Appl. Opt.*, vol. 33, no. 4, pp. 567–572, February 1994.
- [104] H. J. Tiziani, M. Wegner, and D. Steudle, "Confocal principle for macro- and microscopic surface and defect analysis," *Opt. Eng.*, vol. 39, no. 1, pp. 32–39, 2000.
- [105] —, "Confocal principle for macro- and microscopic surface and defect analysis," *Opt. Eng.*, vol. 39, no. 1, pp. 32–39, January 2000.
- [106] T. Tommasi and B. Bianco, "Computer-generated holograms of tilted planes by a spatial frequency approach," *J. Opt. Soc. Am. A*, vol. 10, no. 2, pp. 299–305, 1993.
- [107] N. Vadeboncoeur, G. Schajer, A. Johnson, and D. Rickard, "Separate-sided surface height measurement using a handheld profiling device," *Forest products journal*, vol. 58, pp. 72–76, September 2008.
- [108] N. Wax, *Noise and stochastic processes*. Dover Publications, New York, 1964.
- [109] M. Weber, "Device and method for high-intensity uniform illumination with minimal light reflection for use in microscopes," European Patent EP2 010 953 (A1), 2009.
- [110] —, "Method for generating a universal pinhole pattern for use in confocal microscopes," US Patent US2 009 207 468 (A1), 2009.
- [111] D. J. Whitehouse, *Handbook of Surface Metrology*. Taylor & Francis, 1994.
- [112] —, "Surface metrology," *Meas. Sci. Technol.*, vol. 8, pp. 955–972, 1997.
- [113] K. Wiley and S. Chambers, *Digital Astrophotography: The State of the Art*, D. Ratledge, Ed. Springer, 2005.

-
- [114] T. Wilson, *Confocal Microscopy*. Academic Press, London, 1990, ch. 1.
- [115] —, *Confocal Microscopy*. Academic Press, London, 1990, ch. 3.
- [116] T. Wilson and A. R. Carlini, “Size of the detector in confocal imaging systems,” *Opt. Lett.*, vol. 12, no. 4, pp. 227–229, 1987.
- [117] —, “The effect of aberrations on the axial response of confocal imaging system,” *J. Microscopy*, vol. 154, pp. 243–256, 1989.
- [118] G. Wiora, M. Weber, and J. Valentin, “Oberflächencharakterisierung mit optischer messtechnik vom meter bis zum nanometer,” in *Photogrammetrie, Laserscanning, Optische 3D-Messtechnik, Beiträge der Oldenburger 3D-Tage*, 2008, pp. 236–243.
- [119] J. C. Wyantb and J. Schmit, “Large field of view, high spatial resolution, surface measurements,” *Int. J. Mach. Tool. Manu.*, vol. 38, no. 5, pp. 691–698, 1998.
- [120] G. Q. Xiao, “Confocal optical imaging systems and their applications in microscopy and range sensing,” Ph.D. dissertation, Stanford University, 1990.
- [121] G. Q. Xiao, T. R. Corle, and G. S. Kino, “Real-time confocal scanning optical microscope,” *Appl. Phys. Lett.*, vol. 53, no. 8, pp. 716–718, 1988.
- [122] L. Yang, A. M. Raighne, E. M. McCabe, L. A. Dunbar, and T. Scharf, “Confocal microscopy using variable-focal-length microlenses and an optical fiber bundle,” *Applied Optics*, vol. 44, no. 28, pp. 5928–5936, October 2005.
- [123] J. Young and F. Roberts, “A flying-spot microscope,” *Nature*, vol. 167, no. 4241, p. 231, February 1951.